

Photonics-enabled very high capacity wireless communication for indoor applications

Citation for published version (APA):

Zhang, X. (2020). *Photonics-enabled very high capacity wireless communication for indoor applications*. [Phd Thesis 1 (Research TU/e / Graduation TU/e), Electrical Engineering]. Technische Universiteit Eindhoven.

Document status and date:

Published: 30/06/2020

Document Version:

Publisher's PDF, also known as Version of Record (includes final page, issue and volume numbers)

Please check the document version of this publication:

- A submitted manuscript is the version of the article upon submission and before peer-review. There can be important differences between the submitted version and the official published version of record. People interested in the research are advised to contact the author for the final version of the publication, or visit the DOI to the publisher's website.
- The final author version and the galley proof are versions of the publication after peer review.
- The final published version features the final layout of the paper including the volume, issue and page numbers.

[Link to publication](#)

General rights

Copyright and moral rights for the publications made accessible in the public portal are retained by the authors and/or other copyright owners and it is a condition of accessing publications that users recognise and abide by the legal requirements associated with these rights.

- Users may download and print one copy of any publication from the public portal for the purpose of private study or research.
- You may not further distribute the material or use it for any profit-making activity or commercial gain
- You may freely distribute the URL identifying the publication in the public portal.

If the publication is distributed under the terms of Article 25fa of the Dutch Copyright Act, indicated by the "Taverne" license above, please follow below link for the End User Agreement:

www.tue.nl/taverne

Take down policy

If you believe that this document breaches copyright please contact us at:

openaccess@tue.nl

providing details and we will investigate your claim.

Photonics-enabled very high capacity wireless communication for indoor applications

PROEFSCHRIFT

ter verkrijging van de graad van doctor aan de
Technische Universiteit Eindhoven, op gezag van de
rector magnificus, prof.dr.ir. F.P.T. Baaijens, voor een
commissie aangewezen door het College voor
Promoties in het openbaar te verdedigen
op donderdag 30 juni 2020 om 16.00 uur

door

Xuebing Zhang

geboren te Hebei, China

Dit proefschrift is goedgekeurd door de promotoren en de samenstelling van de promotiecommissie is als volgt:

Voorzitter:	prof.dr.ir. M.J. Bentum
Promotor:	prof.ir. A.M.J. Koonen
Co-promotor:	dr.ir. Z. Cao
Leden:	prof.dr. D. O'Brien (University of Oxford)
	prof.dr.ir. S. Yu (University of Bristol)
	prof.dr. S. Huang (Beijing University of Posts and Telecommunications)
	Prof.dr.ir. S.M. Heemstra de Groot
	dr. J. van der Tol

Het onderzoek of ontwerp dat in dit proefschrift wordt beschreven is uitgevoerd in overeenstemming met de TU/e Gedragscode Wetenschapsbeoefening.

A catalogue record is available from the Eindhoven University of Technology Library.

ISBN: 978-90-386-5069-2

NUR: 959

Title: Photonics-enabled very high capacity wireless communication for indoor applications

Author: Xuebing Zhang

Eindhoven University of Technology, 2020.

Keywords: Indoor networks / Wireless communication / Photonic integrated circuits / Beam steering / Mode-division multiplexing / line-of-sight / Non-line-of-sight

Copyright © 2020 Xuebing Zhang

All rights reserved. No part of this publication may be reproduced, stored in a retrieval system, or transmitted in any form or by any means without the prior written consent of the author.

Typeset using L^AT_EX, printed in The Netherlands.

Dedicated to my parents and siblings

SUMMARY

Over the last 10 years, wireless traffic has greatly increased, particularly in indoor scenarios. The number of connected devices is predicted to be more than three times the world's population in 2023, growing from 18.4B to some 29B in 2023, of which half concerns machine-to-machine connections growing at 30% CAGR. To satisfy the growing demand for faster and better wireless connectivity, two main types of technologies have been extensively developed: radio frequency (RF) wireless communication and optical wireless communication (OWC). This Ph.D. research is aiming to design and realize photonics as a means to create dynamically reconfigurable wireless access points fed by a low-cost indoor fibre-optic network, and beam-steering techniques for short-range wide-band low-power radio- and optical-wireless connections.

For RF wireless communication, the main research issue is how to establish large-capacity power-efficient millimetre-wave (mm-wave) wireless communication. The required low-loss/broadband time-delay or phase shift is hard to be realized in a CMOS platform due to the limitations of its technical characteristics. Photonics-enabled techniques with their inherently low loss and broad bandwidth can be used to solve this problem. Compared to methods using bulk-optics-components, methods based on photonic integrated circuits (PIC) are more attractive due to their stable system performance and compact system integration. In my Ph.D. research, two major technologies needed in radio wireless communication have been researched and implemented by using PIC-based techniques, namely optically-controlled mm-wave beam steering and optically-controlled RF orbital angular momentum (RF-OAM) multiplexing. For mm-wave wireless communication, a 38-GHz mm-wave wireless beam steering system with a steering angle of 186° is experimentally demonstrated by using our proposed integrated looped-back arrayed waveguide grating-based (AWG-base) optical mm-wave beam-former (delay error $<8.8\%$). A data-rate of 4-Gbit/s is implemented over a 28-cm wireless link by utilizing QAM-4 signal. The looped-back AWG module is a stepwise delay network with discrete time delays. To increase the number of delay time steps per area on-chip, a wavelength-tuned bidirectional integrated beamformer with a doubled delay time resolution is designed as the core delay system unit, which is more beneficial for remotely-controlling the beam steering. Additionally, size-reducing designs on the device-level are implemented as well. Firstly, employing the compact silicon integration technique, a silicon-on-insulator-based (SOI-based) transmission-type AWG is demonstrated experimentally utilizing the advantages of this technology. Next, a more compact reflection-type AWG is proposed and implemented using the advantages of both the compact Indium-phosphide Membrane on Silicon (IMOS) technology and a footprint-reduced architecture. This structure design enables an extra 35% size-reduction and only 1.1-dB extra loss compared with the transmission-

type AWG. Moreover, a single-element tunable broadband bidirectional optical true-time-delay network (OTTDN) is proposed and its proof-of-concept is experimentally implemented in IMOS platform with a 20-GHz double-sided bandwidth and a ± 13 -ps delay range. It can be applied to both optically-controlled mm-wave beam steering and optically-controlled RF-OAM multiplexing.

As to RF-OAM multiplexing, except for OTTDN-based methods, a wider-bandwidth phased array is proposed, designed, and realized. An optical passive 90° -hybrid-based multi-OAM-mode generator is proposed by using an on-chip-filter-based mode selector. A multi-mode OAM generator is designed which by changing the wavelength of the signal can switch between three OAM modes (0 and ± 1 order modes) at ~ 18 GHz. Furthermore, a thermally-controlled 1-by-4 tunable optical mm-wave phased array with an on-chip optical filter for both mm-wave OAM multiplexer and demultiplexer is proposed and fabricated. Two types of required dual-port filters are implemented as well, which are a λ tuned cascaded MZI-based filter and a thermally-controlled optical interleaver.

Next to RF indoor communication, another main theme of this Ph.D. thesis is indoor OWC. The research work addresses two aspects: I) line-of-sight (LOS) OWC; II) non-line-of-sight (NLOS) OWC. For LOS OWC, a novel crosstalk-mitigated transmission scheme in an AWG-based 2D infrared (IR) beam-steered OWC system is proposed by creating polarization orthogonality between the odd and even AWG channels. This technique can mitigate the inter-channel spectral overlap and a wavelength misalignment between AWG and laser. A 20-Gbit/s IR OWC transmission with PAM-4 signal has been experimentally demonstrated over a 1.2-m free-space link. Besides, an optical receiver with a field-of-view of 18° -by- 360° is experimentally investigated by using the proposed concept of cyclically arranged optical beam steering. A 40-Gbit/s data-rate is successfully transmitted over 1-km single-mode fibre and a 0.5-m free-space link. Another significant topic of the OWC research is indoor diffused NLOS ultra-high-capacity OWC using techniques from basic physics. For the first time, an energy-efficient NLOS OWC scheme (at $\lambda=1550$ nm) has been designed and implemented experimentally whereby light is steered around obstacles after reflecting off a diffuse surface. The diffusely reflected light to the receiver can be power-enhanced by >17 -dB and steered within an angular range of 20° , which breaks the NLOS limitation of OWC. Moreover, an 8-times faster NLOS OWC system with a 3-dB-FOV of $>50^\circ$ has been established. A further record-breaking NLOS data-rate of 40 Gbit/s is implemented with an extended double-sided angular range of $>80^\circ$ over a 25-cm diffuse link by using the faster Transmission Matrix algorithm. These technical schemes boost the development of high capacity indoor wireless access networks.

Finally, a free-space optical field measurement system is designed and is verified in an optical far-field measurement of on-chip optical gratings.

CONTENTS

Summary	vii
List of Abbreviations	xii
1 Introduction	1
1.1 Indoor wireless communication I: Current systems	2
1.1.1 Mobile communication systems	3
1.1.2 WiFi	6
1.2 Indoor wireless communication II: Advanced technologies	7
1.2.1 mm-wave beam steering	8
1.2.2 Terahertz communications	8
1.2.3 Radio frequency orbital angular momentum	9
1.2.4 Optical wireless communications	9
1.3 Organization and contributions of the dissertation	11
2 Photonics-enabled indoor wireless communication: technologies and state-of-the-art	13
2.1 Radio-frequency wireless communication	14
2.1.1 RF-OAM	14
2.1.2 Mm-wave beam steering	17
2.2 Optical wireless communication	22
2.2.1 Visible light communication using LED lighting	23
2.2.2 Light-fidelity (LiFi)	24
2.2.3 IR light communication using steered beams	25
2.2.4 Non-line-of-sight optical wireless communication	30
2.3 Chapter Summary	31
3 Optically controlled radio frequency OAM multiplexing	32
3.1 Ring phased array for OAM generation	32
3.2 Single-element-tuned bidirectional optical delay network	33
3.2.1 Working Principles	33
3.2.2 Chip design	35
3.2.3 Experimental setup	37
3.2.4 Results and discussion	38
3.3 Optical phase shift network for RF-OAM	38
3.3.1 Multi-OAM-mode generator I: Passive phased array	39
3.3.2 Multi-OAM-mode generator II: Direct optical synthesis phased array	43

3.3.3	Discussion	44
3.4	Chapter Summary	45
4	Optically wavelength-controlled mm-wave beam steering	46
4.1	Looped-back AWG-based beamformer on-chip	46
4.1.1	Device-level design I: SOI-based transmission-type AWG . . .	47
4.1.2	Device-level design II: IMOS-based reflection-type AWG . . .	49
4.1.3	System-level resolution-doubled beamformer I: spatially switch	55
4.1.4	System-level resolution-doubled beamformer II: wavelength tuning	59
4.2	38-GHz mm-wave transmission system	62
4.2.1	Experimental setup	62
4.2.2	Results and discussions	64
4.3	Chapter summary	66
5	Line-of-sight beam-steered indoor optical wireless communications	68
5.1	Crosstalk-mitigation scheme for AWGR-based optical beam steering	68
5.1.1	Operational principles	70
5.1.2	Benefits	71
5.1.3	Experimental setup	74
5.1.4	Experimental results and discussions	75
5.1.5	Conclusion	78
5.2	2D beam steerer on-chip using high port-count AWGR	79
5.3	Cyclically arranged optical beam steering	80
5.3.1	Principle of cyclically arranged 1D grating	81
5.3.2	Cyclically arranged optical receiver	82
5.3.3	Experimental setup and results	83
5.3.4	Conclusion	86
5.4	Chapter summary	87
6	Non-line-of-sight indoor optical wireless communication	88
6.1	First generation beam-reconfigurable indoor NLOS OWC	88
6.1.1	Operational principles	89
6.1.2	Experimental setup	91
6.1.3	Results and analysis	94
6.1.4	Discussions	99
6.1.5	Conclusion	100
6.2	Second generation beam-reconfigurable indoor NLOS OWC	101
6.2.1	Transmission matrix algorithm	101
6.2.2	Experimental setup	102
6.2.3	Results and discussions	103
6.2.4	Conclusion	106
6.3	Chapter summary	106

7	Free-space optical field measurement system	107
7.1	System design	107
7.2	Characterization	109
7.3	Chapter Summary	110
8	Summary and future outlook	111
8.1	Summary	111
8.2	Future outlook	114
	References	119
	List of publications	132

LIST OF ABBREVIATIONS

1G	First Generation
2G	Second Generation
3G	Third Generation
4G	Fourth Generation
5G	Fifth Generation
6G	Sixth Generation
1D	One Dimensional
2D	Two Dimensional
3D	Three Dimensional
AWG	Arrayed Waveguide Grating
AWGe	Arbitrary Waveform Generator
AWGR	AWG Router
APD	Avalanche Photodiode
AM	Amplitude Magnificent
AMPS	Advanced Mobile Phone System
BER	Bit Error Rate
Bi-ODN	Bi-directional ODN
BHC	Bidirectional Hybrid Coupler
BRDF	Bi-directional Reflectance Distribution Function
CAA	Circular Antenna Array
CAGR	Compound Annual Growth Rate
CDMAOne	Code-division multiple access/Interim Standard 95
CAP	Carrier-less Amplitude and Phase
CW	Continuous Wave
CF	Cleaved Single-mode Fibre
CMOS	Complementary Metal-oxide-semiconductor
CPC	Compound Parabolic Concentrator
CPSS	Complementary Phased Shifted Spectra
CS	Continuous Sequential
CAO-Tx	Coherent Array Optical Transmitter
CAO-BS	Cyclically Arranged Optical Beam Steering
CP	Cyclic Prefix
DPO	Digital Phosphor Oscilloscope
DC	Direct Current
D-AMPS	Digital AMPS
DI	Delay Interferometer
DVS-BCB	Divinylsiloxane-bis-benzocyclobutene
EDFA	Erbium-Doped Fiber Amplifier

EM	Electromagnetic
ESA	electrical spectrum analyzer
EVM	Error Vector Magnitude
EA	Electrical Amplifiers
ECL	External Cavity Laser
FoV	Field-of-View
FPR	Free Propagation Region
FSOC	Free Space Optical Communication
FTTH	Fiber-to-The-Home
FSR	free spectral range
FFT	Fast Fourier Transform
FWHM	Full Width Half Maximum
FDTD	Finite-difference Time-domain
GC	Grating Coupler
GSM	Global System for Mobile Communications
GPRS	General Packet Radio Service
IM-DD	Intensity-Modulation Direct-Detection
IMOS	Indium-phosphide-Membrane-on-Silicon
IoT	Internet-of-Things
ITU	International Telecommunication Union
IL	Insertion Loss
I/O	Input/Output
IFFT	Inverse Fast Fourier Transform
LD	Laser Diode
LED	Light-Emitting Diodes
LiFi	Light Fidelity
LOS	Line-of-Sight
LTE	Long-Term Evolution
LCSLM	Liquid Crystal Spatial Light Modulator
LF	Lensed Single-mode Fibre
MZM	Mach-Zehnder Modulator
M2M	Machine-to-Machine
MIMO	Multiple-Input Multiple-Output
mm-wave	Milimeter Wave
MZI	Mach-Zehnder-Interferometer
MWP	Microwave Photonics
MEMS	Micro-electro-mechanical System
MMI	multimode Interferometer
MPW	Multi-Project-Wafer
NLOS	Non-Line-of-Sight
NA	Numerical Aperture
NMT	Nordic Mobile Telephone
OAM	Orbital Angular Momentum

OC	Optical Coupler
OCC	Optical Camera Communication
ODN	Optical Delay Network
OFDM	Orthogonal Frequency Division Multiplexing
OOK	On-Off Keying
OTDL	Optical Time Delay Line
OTTD	Optical True-Time Delay
OWC	Optical Wireless Communication
OFDMA	Orthogonal Frequency Division Multiple Access
OPS	Optical Phase Shifter
ORR	Optical Ring Resonator
OBTB	Optical Back-to-back
OLO	Optical Local Oscillator
OSA	Optical Spectrum Analyzer
PAM	Pulse-Amplitude Modulation
PBC	Polarization Beam Combiner
PBS	Polarization Beam Splitter
PC	Polarization Controller
PD	Photodiode
PON	Passive Optical Networks
PIC	Optics Integrated Circuits
PAA	Phased Array Antenna
P2P	Point-to-Point
P2MP	Point-to-multipoint
PLC	Programmable Logic Controller
PRBS	Pseudo-random Binary Sequence
PCR	Photonic Crystal Reflector
QAM4	4-ary Quadrature Amplitude Modulation
QAM16	16-ary Quadrature Amplitude Modulation
RF	Radio Frequency
RF-OAM	OAM on radio frequency
RGBY	Red+Green+Blue+Yellow
R-AWG	Reflection-type AWG
Rx	Receiving Antennas
SDM	Spatial Division Multiplexing
SLM	Spatial Light Modulator
SOI	Silicon-On-Insulator
SSBI	Signal-to-Signal Beat Interference
SSC	Spot-Size Converter
SNR	signal-to-noise ratio
SPP	Spatial Phase Plate
SSMF	Standard Single-mode Fibre
THz	Terahertz

TTD	True-Time Delay
TACS	Total Access Communication System
TDMA	Time-division Multiple Access
TD-SCDMA	Time Division-Synchronous Code Division Multiple Access
TE	Transverse Electric
TM	Transverse Magnetic
T-AWG	Transmission-type AWG
Tx	Transmitting Antennas
UV	Ultraviolet
VOA	Variable Optical Attenuator
VL	Visible Light
VLC	Visible Light Communication
VR	Virtual Reality
VNA	Vector Network Analyzer
WiFi	Wireless Fidelity
WLAN	Wireless Local Area Network
WDM	Wavelength Division Multiplexing
W/	With
W/o	Without
WG	Waveguide

CHAPTER 1

INTRODUCTION

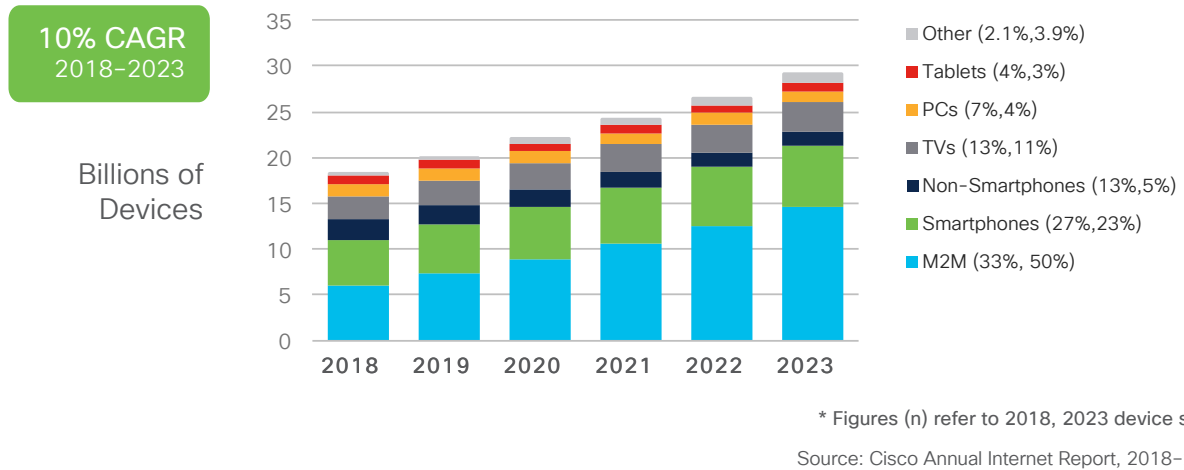


Fig. 1.1 Global devices and connections growth in Cisco Visual Networking Index [1].

With the fast development of smart terminals such as smartphones, tablet computers, laptops, etc., and emerging new applications (e.g., Internet of Things (IoT), virtual reality (VR), video streaming and other real-time services), wireless data traffic has increased at over 50% per year according to the newest Cisco Visual Networking Index (2018-2023) [1]. Fig. 1.1 shows the forecast of global devices and connections growth from CISCO. Globally, the number of devices and connections are growing fast with a compound annual growth rate (CAGR) of 10 percent, where machine-to-machine (M2M) connections and smartphones will be the two fastest-growing categories. This demand is expected to increase as the IoT becomes a reality, and the predicted number of connected devices grows to 100 billion by 2025 [2] as presented in Fig. 1.2.

By 2021 more than half of 17 billion connected devices will be mobile, 65% of the IP traffic will be from mobile devices, 80% of the internet traffic will be video. Current wireless networks cannot adequately meet the quickly rising demand for wireless connectivity. In 2020, CISCO made the forecast for the global mobile devices connection growth rates as described in Fig. 1.3. By 2023, there were 8.8 billion global mobile devices and connections in 2018, which will grow to 13.1 billion by 2023 with 8.7 billion handheld or personal mobile-ready devices and 4.4 billion M2M connections at a CAGR of 8%. Mobile devices are evolving to higher-generation network connectivity (forth-generation (4G) LTE and now also fifth-generation-and-beyond (5G-and-beyond)). The global mobile 4G connections will grow from 3.7 billion in 2018 to 6.0 billion by 2023 at a CAGR of 10% as shown in Fig. 1.4. 5G

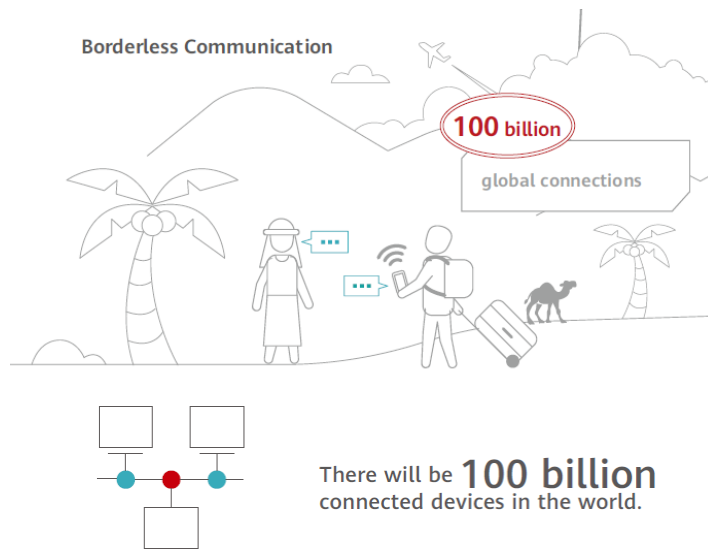
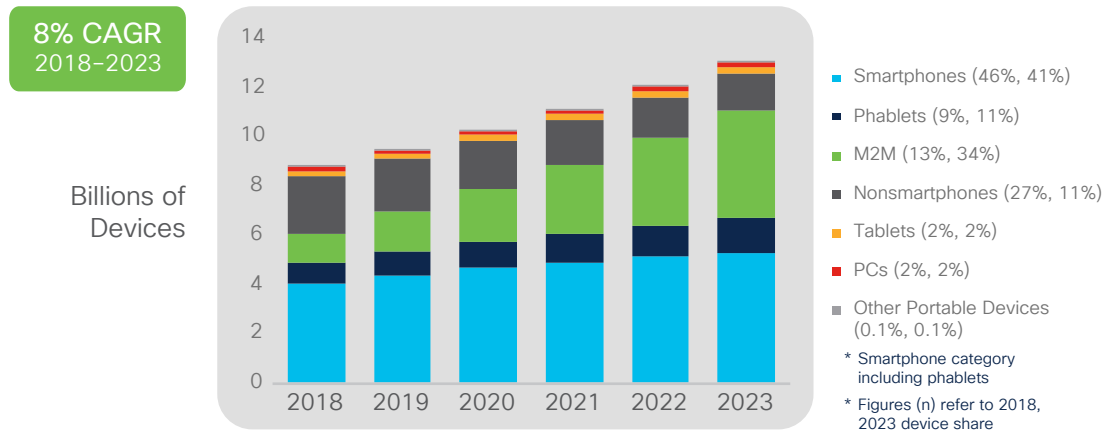


Fig. 1.2 The connected devices by 2025 provided by Huawei [2].

connections will appear on the scene in 2019 and will grow over 100-fold from about 13 million to 1.4 billion by 2023. Combining device capabilities with faster and more intelligent networks will contribute to increased wireless traffic. Wireless communication is becoming more demanding than ever before.

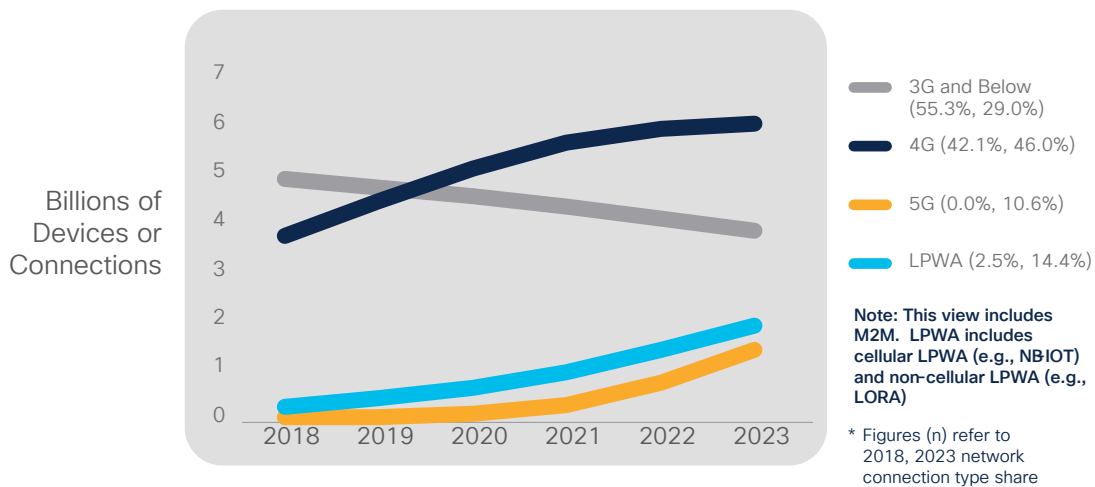


Source: Cisco Annual Internet Report, 2018-2023

Fig. 1.3 Global mobile device and connection growth according the statistics from CISCO [1].

1.1 Indoor wireless communication I: Current systems

As a significant application domain of wireless communication, indoor scenario is attracting more and more attention. With the advent of the Information age, the way



Source: Cisco Annual Internet Report, 2018–2023

Fig. 1.4 higher-generation network connectivity growth according the statistics from CISCO [1].

in which we work and live is changed entirely, having more advanced technologies for the improvement of the working environment such as remote video meetings and using more smart mobile devices for both work and entertainment. It generates huge wireless data traffic loads notably in indoor environments. According to the statistics from IEEE Future Networks, nearly 80% of the mobile traffic volume is generated indoors [3]. Conceivably, the percentage of indoor wireless traffic will be even higher in the near future. Current wireless communication systems that can cover indoor applications are the mobile 4G LTE communication system and IEEE 802.11 Wireless Fidelity (WiFi) systems.

1.1.1 Mobile communication systems

Mobile wireless communication has started its technology origination, revolution, and evolution since early 1970. The first generation (1G) mobile communication mainly supplied telephone calls, by analog cell phones with a speed up to 2.4 kbit/s. 1G includes Nordic Mobile Telephone (NMT), Total Access Communication System (TACS), and Advanced Mobile Phone System (AMPS) offering handover and roaming capability. But it has small capacity and poor voice links [4, 5]. The second-generation (2G) mobile wireless communication was launched in the early 1990s, and is based on digital technologies offering digital voice and simple text and picture messages. 2G comprises several mobile systems such as Global System for Mobile Communications (GSM), Digital AMPS (D-AMPS) and Code-division multiple access/Interim Standard 95 (CDMAOne) [6]. As the first 2G system, the GSM standard uses Time-division Multiple Access (TDMA) technique and is operated in the 900 and 1800 MHz bands. By using the General Packet Radio Service (GPRS) based on GSM technology, 2G can provide data rates from 56 kbit/s up to 384

kbit/s (normally <0.5 Mbit/s). The third-generation (3G) mobile communication supports a ubiquitous wireless communication standard for all countries under the coordination of the International Telecommunication Union (ITU). Two main types of 3G systems are CDMA2000 and WCDMA, which have been developed from CDMA and GSM systems, respectively. The other standard uses Time Division-Synchronous Code Division Multiple Access (TD-SCDMA). In this system, the mobile broadband communication is implemented with optimized audio- and video- streaming. The 4G mobile communication includes Long-Term Evolution (LTE) and LTE advanced, aims to provide faster and better mobile broadband experiences. The Orthogonal Frequency Division Multiple access (OFDMA) technique is implemented in 4G by dividing the channel in narrowbands to transmit data packets with better robustness against channel impairments and greater efficiency [7]. The LTE services were first launched by major North American carriers in September 2010 [8].

For the upcoming 5G mobile communication, there are higher requirements, such as higher capacity, massive connectivity, lower latency, low energy-consumption, high data security, high user quality-of-experience, and high reliability. The key requirements of 5G are listed below [9]:

High data rate: 5G mobile networks must have the capability to support a 10-Gb/s peak data rate, which is several orders of magnitude higher than 4G.

High-density connectivity: 5G will support connectivity to massive amounts of mobile devices; 10 to 100 times more devices will be connected compared to the 4G network [10]. The mobile data volume per area will be 1000 times higher than that of the 4G wireless networks.

Low energy-consumption: Consuming less energy will be a significant request in 5G networks. More than 90% reduction in energy-consumption is required compared to current 4G networks [10].

Low latency: The end-to-end latency will have to be in the one-millisecond level compared to the average latency of around 50 ms for 4G.

In the next decades, our society will be more and more information-driven, aided by nearly unlimited wireless connectivity [11]. As a result, the 5G-beyond network has to be much faster than the current 4G/5G mobile networks. Besides, the next-generation mobile network needs to support different types of applications enabled by advanced technologies. Fig. 1.5 presents potential applications, trends, and supported technologies. With the advanced requirements such as wireless brain-computer interactions, more stringent new requirements will be put on data volumes, connectivity, energy-consumption, and latency. Besides, The mobile network is typically the outdoor public network. For fast increasing demand for indoor wireless connectivity, next to the mobile network, there also needs to be indoor wireless local area networks (WLANS). Thus the mobile network will need to have some special types of characteristics to support the next-generation wireless communication.

As a vision of the future, some new trends are analyzed as follows:

IoT networks: As the main enablers of the IoT, 5G is being deployed all over the

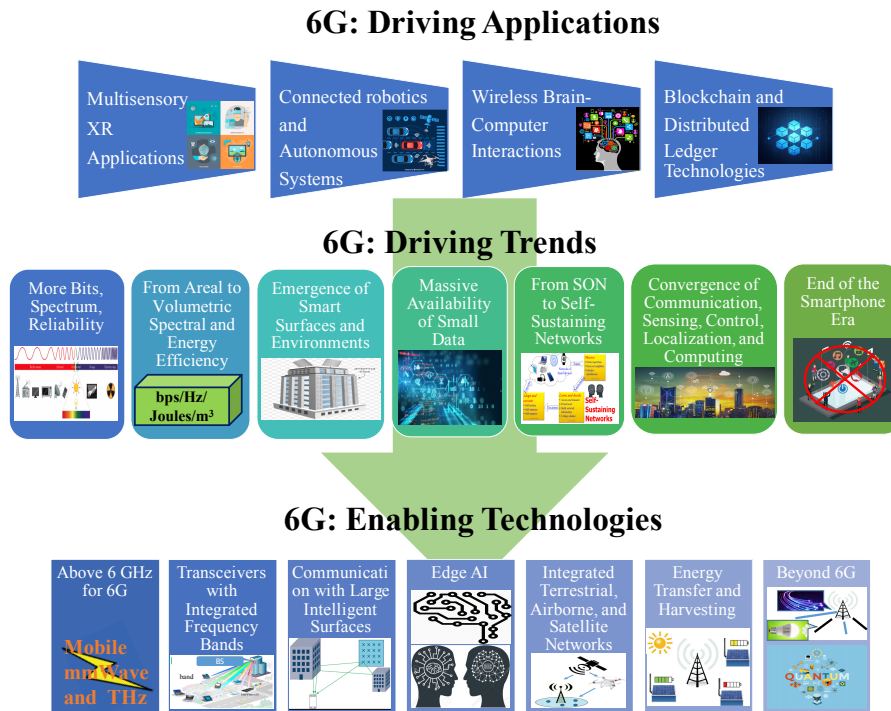


Fig. 1.5 6G vision: Applications, trends, and technologies introduced by Walid Saad et al. in [1].

world. Hence, the IoT networks are expected to be a significant characteristic of 5G-beyond. A large number of devices such as smartphones, laptops, wiring equipment, and personalized health sensors will connect to the network.

Tiny-cell networks: The high-dense tiny-cell networks have been proposed as one of the core characteristics to obtain the continued growth in wireless capacity. These tiny cells allow a much larger number of connected devices and have a higher utilization ratio of spatial and spectral resources.

Ultra-high speed: 5G-beyond systems are also expected to be $\times 100$ or $\times 1000$ faster than current 5G by using multiple techniques such as massive multiple-input and multiple-output (MIMO) algorithms, advanced coding and modulation schemes, spatial division multiplexing (SDM) and so on. To tackle the almost exhausted radio spectrum, new spectrum bands are being opened, e.g. sub-THz ones stretching the spectrum up to 300 GHz.

Less energy-consumption: The next-generation mobile network is required to be more energy-efficient due to the ultra-large number of user devices and the extremely high wireless data capacity. The consumed energy per bit of information should be largely reduced as we know that the current 5G network should use 90% less energy per bit than 4G. Nevertheless, this does mean the 5G mobile network will consume less power. In contrast, the total energy consumption will increase due to the much larger data rate, exponentially-increasing number of user devices, and IoT networks. New technologies from both physical-level and network-level are desired to continuously improve energy efficiency.

Offloading of the heavy traffic to indoors: According to the research of IEEE Future Networks, nearly 80% of the mobile traffic volume is generated indoors [3]. Offloading this volume of data to indoor environment by WLANs will be an important characteristic of 5G-beyond networks.

Even though the 5G-beyond (e.g. 6G) specifications have not yet been exactly identified, many researchers have started working on it [11–15]. The 5G-beyond mobile network will attract a great deal of attention soon. Some organizations and countries already started 6G research projects. For example, in April 2018, the Academy of Finland announced a research program, “6Genesis-the 6G-Enabled Wireless Smart Society & Ecosystem” to develop the areas such as wireless connectivity and distributed intelligent computing as well as other novel applications through a joint effort of the University of Oulu and Nokia [16]. Addressing also the upcoming privacy concerns, the European Commission has invested in studies into the potential techniques capabilities in of quantum technology technologies studies for 6G and beyond [17].

As mentioned above, most wireless connectivity will occur in an indoor environment. One of these significant research issues is the next-generation indoor wireless network. Next to the mobile network, an indoor WLAN is also promising solution as an extension for the mobile coverage indoor, such as the one that uses lightwaves. Therefore, advanced techniques that can provide faster wireless connectivity are worth being researched.

1.1.2 WiFi

WiFi is a family of wireless networking technologies which, which is commonly used for local area networking of devices and Internet access. Unsurprisingly, over 50% of all wireless data typically goes through a WiFi hotspot. As a widely-used and also a cost-efficient indoor wireless connectivity means, WiFi has been continuously evolving – typically resulting in faster speed and wider coverage since it was first released to the market in 1997 [18]. Almost at the same time, two WiFi standards were released, namely 802.11b and 802.11a. As the original 802.11 standard, 802.11b uses the 2.4-GHz frequency band and supports a theoretical maximum data-rate of 11 Mbit/s with complementary code keying modulation format covering a range up to 150 feet [19]. The components’ cost is low, but the standard is the slowest of all the 802.11 standards. 802.11a introduces the orthogonal frequency division multiplexing (OFDM) technique for the wireless signal generation [20]. It allows a much larger bandwidth than 802.11b with a theoretical maximum speed of 54 Mbit/s. Besides, it employs the less crowded 5-GHz frequency band, and has more channels with a bandwidth of 16.6 MHz, thus making it less prone to interference. To balance the cost and speed, a new standard 802.11g was then introduced at the same speed as 802.11a (54 Mbit/s) but at lower-cost [21]. It operates in the more crowded 2.4-GHz band with higher power and higher-quality coverage. In 2009, WiFi became even faster and more reliable in order to meet the ever-increasing demand for indoor wireless data traffic. A more advanced WiFi standard, namely

802.11n, supports a theoretical maximum transfer rate of 300 Mbit/s (and can go up to 600 Mbit/s when using four antennas) operating in both the 2.4-GHz and 5-GHz bands [22]. In the 802.11n standard, the more powerful MIMO technique together with an antenna array at one or at both ends of the link is utilized. In 2013, the current version of the WiFi standard 802.11ac was published with a speed ranging from 433 Mbit/s up to several gigabits per second in the 5-GHz band [23]. To meet the rapid growth of wireless data traffic, more spatial streams (up to 8) are supported and the channel-bandwidth has been doubled to 80 MHz (160 MHz optional). More importantly, the concept of beamforming was first applied, where the radio signal could be directed at a specific area. Now the more advanced IEEE 802.11ax-2019 is being proposed and will succeed both IEEE 802.11n-2009 and IEEE 802.11ac-2013 as the next high-throughput Wireless Local Area Network (WLAN) amendment [24]. For dense deployments, throughput speeds are 4 times higher than IEEE 802.11ac, with a 75% latency reduction.

In 2018, to simplify the names of different WiFi standards, the WiFi Alliance took steps to rename the used WiFi-versions as WiFi 1 to WiFi 5. This classification is supposed to help make it easier for consumers to understand. However, the demand for higher data rate never stops, what is the future of WiFi? The IEEE 802.11ad protocol was published in 2012 operating in the 60-GHz band and supports an ultra-high-speed connection within a room [25]. It is seen as a complement to existing low-frequency WiFi. Similarly, the IEEE802.15.3c standard has been defined to enable data rates in excess of 5 Gb/s using the 60 GHz band [26]. All these versions of the faster WiFi relay on the development of the physical-level techniques. Therefore, no matter mobile communication systems or WiFi systems, advanced technologies are needed to support a faster wireless communication standard.

1.2 Indoor wireless communication II: Advanced technologies

Indoor wireless services occur in a room, such as homes, offices, classrooms, industrial manufacturing halls, and shopping malls. Up to now, nearly 80% of the mobile traffic volume is generated indoors [3, 27]. Hence, indoor wireless communication already plays a significant role in daily life and this role will become ever more important. However, the current wireless communication networks supporting indoor applications, no matter using mobile communication systems or WiFi systems, are being challenged due to the overall increased demand for higher quality wireless services including higher data speeds and higher data volumes. More advanced techniques from different levels such as new frequency resources and advanced coding methods are needed to improve the current wireless systems. In this section, we review a number of promising advanced physical-level wireless technologies.

1.2.1 mm-wave beam steering

With the rapid evolution of our information-society, the limited spectrum allocated to current radio communication will be exhausted very quickly. New radio spectrum bands are being opened such as millimeter-wave (mm-wave), Terahertz (THz) signals. Mm-wave with large bandwidth from 30 GHz to 300 GHz is being proposed for multi-gigabit per second wireless communication services [28]. Actually, the attention was fixed on 28 GHz, 38 GHz, 60 GHz, 71-76 GHz, and 81-86 GHz [29–31]. A large amount of unoccupied spectrum has been of particular interest for next-generation ultra-high-speed transmission. However, mm-waves propagate only by line-of-sight (LOS) paths. They are not reflected by the ionosphere nor do they travel along with the earth as ground waves like lower frequency radio waves do [32]. At typical power densities, they are blocked by building walls and suffer significant attenuation passing through foliage. [32, 33]. Absorption by atmospheric gases is a significant factor throughout the band and increases with frequency. To overcome these inherent problems, advanced massive MIMO combined with beamforming antenna array technologies have been introduced [34]. And it is expected to play a key role in 5G wireless communication systems. The antenna-array-based beamforming using narrow mm-wave beams can steer the mm-wave signals only there where and when needed. On one hand, mm-wave beamforming improves energy efficiency by utilizing the steered beams. On the other hand, it minimizes spatial interference and therefore improves the spatial capacity. In 2014, Samsung proposed and demonstrated a mm-wave communication empowered by beam-steering [35], which is based on electronic devices. For broadband beam-steering, true-time delay (TTD) is required to minimize beam squint. However, the required low-loss and broadband TTD at mm-waves are hard to be implemented using electronic integrated circuits in the CMOS platform, which is limited by the high loss of silicon at high frequencies and the narrow bandwidth. Photonic methods e.g. using optical true-time delay (OTTD) with inherent low loss and broad bandwidth is applied to solve the problems both on integrated circuit-level [36–40] and system-level [41–43]. Compared to the bulk-optics components-based optical true time delay lines (OTDLs), integrated OTDLs are more attractive because of their stable performance and compact system integration [38]. Currently, many methods based on integrated optics are investigated such as the ring resonator-based tunable OTDL [39, 44] and the OTDLs based on optical switches [36, 45]. Photonics-enabled mm-wave beamforming/steering will be a promising candidate for indoor wireless solutions.

1.2.2 Terahertz communications

With radio wireless communication shifting towards beyond-mm-wave frequencies, ultra-high-speed THz communication has a strong potential to support the tremendous increase in the demand for wireless bandwidth. The THz frequency band ranges from 0.1 to 10 THz, which is the last span of the radio spectrum and is generally considered as the THz-gap. The THz band is envisioned to be able to pro-

vide users with up to Tbit/s data speeds to satisfy extremely high throughput, low latency and completely new application scenarios [46–48]. It is expected to become a reality within the next 5–10 years [49]. Due to the tight spectrum regulation, with most bands below 300 GHz already allocated, the yet unregulated bandwidth above 300 GHz appears to be attractive for accommodating ultra-high-speed, short-range, indoor THz communication systems [50, 48].

1.2.3 Radio frequency orbital angular momentum

A promising way for opening a new spatial multiplexing degree of freedom, next to the utilization of a higher frequency, is the orbital angular momentum (OAM) multiplexing technique which is proposed to further boost the capacity-increase for radio wireless communication [51, 52]. It builds on the basic physical properties of electromagnetic (EM) fields, and can support in principle an infinite number of spatial channels. Thus it has the potential to greatly extend the capacity of radio wireless communication without requiring more radio spectrum. The concept of using OAM in wireless connectivity was first proposed in 2004 [53]. Further OAM technology investigations and its applications in optical wireless communication (OWC) have since then received much interest. In 2011, high-volume optical OAM multiplexing was proposed to realize terabit data transmission [54, 55]. Meanwhile, OAM in the radio frequency domain (RF-OAM) also shows promising application prospects. Almost at the same time, RF-OAM has been studied simulations and generated by a circular antenna array (CAA) by using electrical phase shifters [56]. However, limitations caused by electrical devices such as the limited spectral width, high loss, and the limited resolution of the phase-shift are still causing problems [57, 58]. Thanks to the advanced photonic methods, broadband RF-OAM modes can be generated by an OTTD system together with a CAA [59, 60]. Photonics-based OAM multiplexing in the radio domain is another promising candidate for solving the indoor wireless communication congestion.

1.2.4 Optical wireless communications

In general, RF-based wireless communication is limited by the limited radio spectrum available, by strong interference effects, strict regulations and so on. Just RF-based wireless communication technologies are insufficient to satisfy the demand of the higher-volume wireless services. Therefore, researchers are working hard on opening up a new spectrum that can fulfill the exponential growth. Ultra-wide bandwidth optical communication is considered to be a promising solution. In the optical domain, without requiring licensing fees, the vast frequency regions are available, which can be disclosed by optical wireless communication (OWC) technology. OWC is a form of optical communication in which ultraviolet (UV), visible and infrared light is used to carry a communication signal in free space [61, 62]. UV is rarely applied in indoor scenarios, amongst others due to eye safety issues and lack of suitable fast sources and detectors. According to wavelength,

indoor OWC can be divided into two main types: visible light (VL) and infrared (IR) light wireless communications [62, 63]. OWC in the VL spectrum spans over a range between 400 nm (750 THz) and 700 nm (430 THz) [64–66]. OWC operating in the IR spectrum commonly centers at 850 nm (353 THz), 1310 nm (229 THz) and 1550 nm (193 THz) in a Point-to-Point configuration, and is widely reported [62, 63]. In terms of practical system implementation, which combines various technologies and wavelength domains in one system, OWC can be divided into four main technologies, namely visible light communication (VLC), light fidelity (LiFi) building on illumination light sources, optical camera communication (OCC), and free-space optics communication (FSOC) [9, 64, 67, 68, 62]. VLC normally uses light-emitting diodes (LEDs) as transmitters and photodetectors (PDs) as receivers. Only VL is used as the communication carrier with broadcasting or sub-broadcasting indoor coverage. Beyond 10-Gbit/s data rate has been realized using LED-based wavelength division multiplexing. [69]. Similar to WiFi technology, LiFi provides wireless connectivity at sub-Gbit/s speeds, but along with illumination using LEDs or diffuse laser diodes (LDs) as transmitters and PDs as receivers [9, 67]. For the wireless downlink, VL is mandatory, while the uplink can be VL or IR light. Due to the lack of high-power LEDs in most user equipment, e.g. smartphones, the uplink communication in both VLC and LiFi cannot perform at high data rates [67]. OCC uses a LED-array/-lamp as a transmitter and a camera or an imaging sensor as the receiver [70]. The OCC technique has attracted particular interest for indoor functions such as localization, motion capture, IoT communication, and intelligent transportation systems. As a supplementary technique to high-speed OWC based on photo-detectors, communication through image sensors as receivers does not need much modification of the current infrastructure, which reduces the implementation complexity and cost. The normally-used communication medium is VL or IR light. However, all the above technologies are mainly based on the broadcast mode and can only support short-reach and up to a few gigabits per second data rate. The broadcast connections determine that the source's energy cannot be fully captured at the receiver. To achieve higher capacity and energy-efficiency, a narrow-beam-based (normally pencil-beam) FSOC together with accurate beam steering techniques has been proposed and experimentally researched. Several research activities have been reported to carry above 100 gigabits per second speed for indoor OWC transmission with high energy-efficiency [71, 62, 72–74].

Currently, many advanced techniques such as mm-wave beam steering, RF-OAM, and OWC are aiming at a higher speed, lower energy consumption, low cost, and higher safety, privacy and reliability. And a large number of problems need to be solved to realize this. In this thesis, new solutions from several aspects mentioned above are proposed to boost indoor high-speed wireless connectivity.

1.3 Organization and contributions of the dissertation

In general, indoor wireless communication networks are evolving towards a higher speed. It is almost impossible that a single technique can support ultra-high-speed wireless communication alone. An indoor wireless communication system is a complicated network that requires the integration of separate technologies. For example, the lower frequency spectrum (like WiFi) may be used for indoor large-scale coverage and low-speed but reliable connections. The high-frequency domain such as mm-wave and optical-wave can aim at providing high-speed transmission. Hence, different ways of extending wireless connectivity are to be explored. This dissertation focuses on the wireless capacity extension by utilizing photonics-enabled physical-level technologies. The photonics-enabled methods not only provide broadband and low-loss solutions for wireless communication, but they are compliant with the well-established fibre networks as well, and can therefore build on the wealth of mature proven fiber-optic technologies.

The main contributions of this thesis are organized in a number of chapters and sections, according to the technology types, as follows below.

Chapter 2 presents an overview of the photonics-enabled indoor wireless communication technologies. Further discussions are given from two aspects: RF techniques including OAM multiplexing, mm-wave beam-steering, THz, and optical methods such as VLC, LiFi, IR light beam steering. The state-of-the-art of these schemes, demonstrated in recent publications, is introduced.

Chapter 3 discusses the proposed RF-OAM multiplexing technology. OAM generation enabled by optical true-time delay networks and an optical phased array are presented, respectively. For the former, a single-element-tuned bidirectional optical delay network (ODN) is proposed and implemented in the IMOS platform. Furthermore, the concept of a broad bandwidth optical multiple RF-OAM-mode generator using an optical phased array is proposed. Two types of integrated designs, namely passive phased array and active phased array, are introduced in silicon on an insulator (SOI) platform (from IMEC).

Chapter 4 introduces the optically-controlled mm-wave beam steering technique. A 38-GHz integrated mm-wave wireless beamformer and the beam steering system are proposed and experimentally characterized by using the novel integrated looped-back arrayed waveguide grating-based (AWG-based) ODN. Moreover, the key element — an AWG is further studied. An normal transmission-type AWG is designed and realized in the SOI platform, and a reflection-type AWG in the IMOS platform is demonstrated for the first time, which enables a size-reduced beamformer.

Chapter 5 presents LOS indoor OWC solutions for communication performance improvement. A novel crosstalk-mitigated scheme for the AWG-based 2-D IR beam-steered OWC system is experimentally discussed by creating polarization orthogonality between the odd and even AWG channels. This technique can tolerate the crosstalk from the inter-channel spectral overlap and the wavelength misalign-

ment between AWG and laser. Besides, a cyclically arranged optical beam steering concept is proposed by introducing the concept of “Rotating 1-D grating”. A novel optical receiver architecture is experimentally demonstrated with a field-of-view of 18° -by- 360° .

Chapter 6 starts from the long-term challenge of non-line-of-sight (NLOS) OWC for indoor applications. For the first time, an energy-efficient NLOS OWC scheme has been designed and implemented experimentally whereby light is steered around obstacles after reflecting off a diffuse surface. The diffuse light to the receiver can be intensity-enhanced by >17 -dB and steered in an angular range of 20° . In the second stage of the research, further experimental establishment of a record-breaking 40-Gbit/s NLOS beam-steered OWC is presented. An average 18-dB-power-enhancement and a double-side-range of $> 80^\circ$ are employed over a 25-cm free-space link. The 8-times faster Transmission Matrix algorithm is introduced and implemented.

Chapter 7 describes a free-space optical field measurement system. First, motivation is explained. Then the system design including functional specifications and detailed parameters is shown. Further measurement for a free-space-spread optical grating antenna is conducted. This system can be used for free-space-radiated optical far-field characterization.

Finally, **Chapter 8** summarizes the findings of this thesis and includes a section that discusses the possible areas for improvements, which could be further pursued in future work on the photonics-enabled indoor wireless communication techniques.

**PHOTONICS-ENABLED INDOOR WIRELESS
COMMUNICATION: TECHNOLOGIES AND
STATE-OF-THE-ART**

Indoor networks, being a significant part of 5G-and-beyond networks, are becoming more and more congested due to the ever-increasing number of connected smart devices. They have to carry a large variety of services, with widely differing needs regarding, e.g., bandwidth, latency, burstiness, quality of service, and security. On the other hand, they also need to support both wire-bound and wireless connectivity at low cost and low energy consumption levels [75]. Moreover different from access networks that are owned by a network operator and need to be installed by professionals conforming to standards such as those in passive optical networks (PON), an indoor network, is mainly privately owned and is required to be easy to install. Without requiring professionals, the users decide which equipment to install and bear all the relevant costs. Hence, the design and the technical implementation of indoor networks are quite different from those of operator-owned outdoor networks.

Indoor networks are predominantly a mixture of different network technologies such as coaxial cable networks, WiFi networks, and the upcoming LiFi networks. However, the coexistence of different types of networks has brought many limitations on installation and maintenance, on upgrading to new services, and on the interoperation between multiple platforms [75]. Moreover, these networks are bandwidth-limited, which seriously hinders the development of 5G-and-beyond for indoor applications. As we know, optical fibre has arrived at the doorsteps of our homes and offices in fiber-to-the-home (FTTH) access networks, but it has not made significant inroads yet the indoor networks. This means its huge capabilities are yet to be extended up to users' devices. The bandwidth demand of the indoor networks is exponentially increasing and may even exceed the demand in access lines, for example, the ultra-high-speed data transfer of an extremely high-definition video. A novel converged indoor network architecture is required to tackle these problems.

An optical fibre-based broadband network architecture is regarded as an encouraging solution owing to the fibre's inherent characteristics of low cost, high bandwidth, low loss, light weight, small diameter, and immunity to electromagnetic interference [76]. Optical fibre is to be deployed into our rooms. Then, making the link from fibre to the users' devices, the connection can be established using either wired or wireless methods. For the wire-bound cases, the connection is usually serving the less-frequently moving devices such as televisions, printers, and desktops. While, with the fast increase of the numbers of smart mobile devices/sensors in the upcoming 5G-and-beyond and the afterward IoT networks, wireless connectivity

may dominate the indoor data communication. Thus investigations on this issue need to be done both academically and industrially [1, 27, 67]. Currently, indoor wireless networks are evolving towards faster data transfer using well-established fibre-optic networks. However, today's reality is that almost all current mobile terminals are electronic devices, implying a huge bandwidth gap between the optical signal (optical fibre) and the radio signal (users' devices). Signals in the optical domain need to be down-converted to the RF domain. Hence, how to extend the indoor wireless capacity utilizing high-bandwidth photonic methods will be a long-term goal for researchers.

The wireless bandwidth can be significantly extended by using advanced multiplexing schemes and higher carrier frequencies, where photonic techniques can play a significant role in overcoming the bandwidth bottleneck. The main idea is to move more bandwidth-limited procedures, e.g., the signal processing (delay or phase shift), to the optical domain or to use optical links instead of RF links [57, 58]. Until now, two main types of high-speed solutions — I) RF-based; II) light-wave-based wireless solutions, have been widely investigated. And many advanced solutions have been proposed and experimentally verified.

2.1 Radio-frequency wireless communication

Upgrading current RF systems may be the most direct way of achieving a higher bandwidth. The improvements can be done by using advanced (de)multiplexing methods such as spatial division multiplexing, spectrally multiplexing higher frequency waves, and new coding/modulating techniques. In this section, my research is focused on the physical-layer RF-solutions, reviewing new techniques and analyzing challenges.

2.1.1 RF-OAM

The OAM, as the inherent physical property of EM fields, describes the spatial distribution of the EM field [77]. OAM modes lie within an unbounded mode space with each mode orthogonal to all of the others. The physical orthogonality could potentially provide a low computational-complexity compared to the conventional MIMO technique using digital signal processing. The concept of OAM mode division multiplexing for wireless communication was first proposed for OWC [53]. Then the OAM-based OWC attracted great interest due to its potential of providing infinite numbers of spatial channels. Normally, EM beams carrying OAM can be described in the spatial azimuthal phase term $\exp(il\varphi)$ ($l=\pm 1$), in which φ refers to the azimuth angle and l determines the topological charge of the OAM mode [78]. In 2011 and 2012, high-capacity optical OAM transmission was experimentally demonstrated by J. Wang and his colleagues, respectively [54, 55]. Since then, a large variety of effort was paid in optical OAM (de)multiplexing. Meanwhile, researchers realized that it is possible to implement the RF-OAM (de)multiplexing

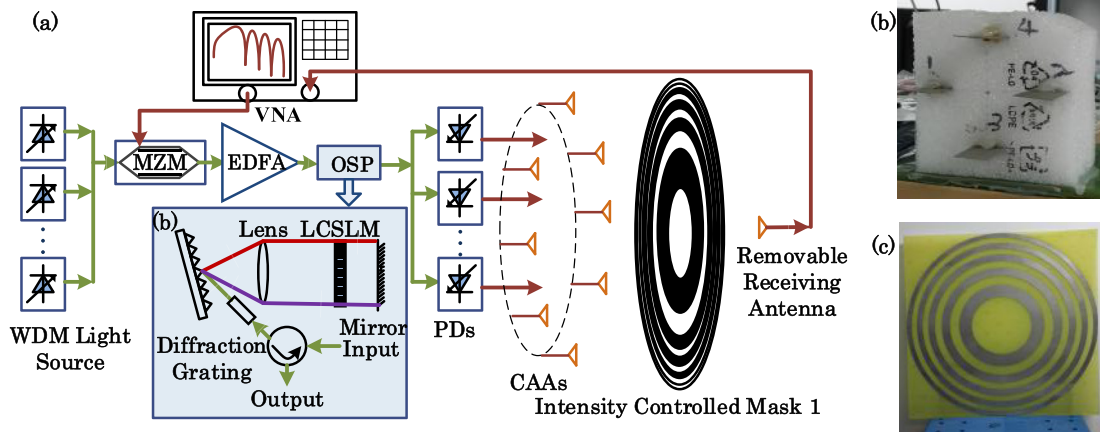
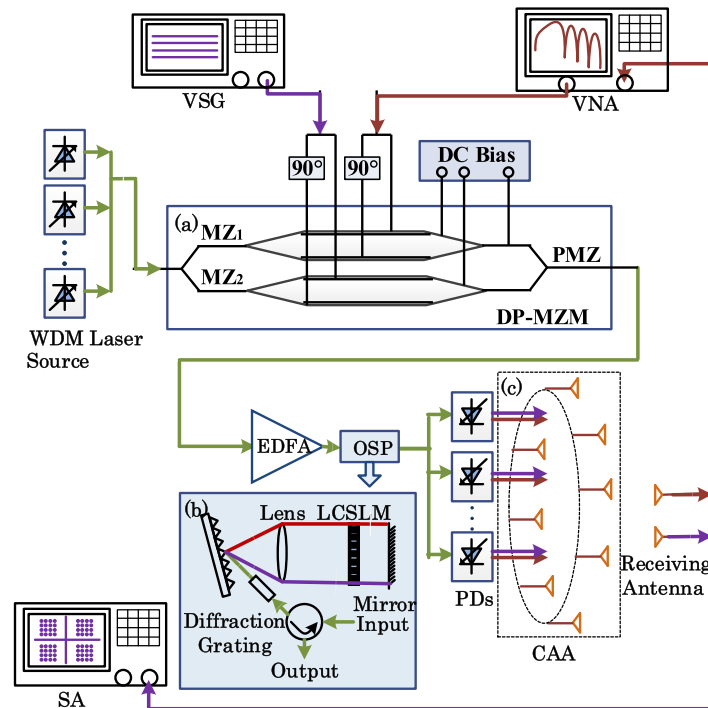


Fig. 2.1 (a) Experimental setup of the OAM radio beam collimating by the intensity controlled mask; (b) Photograph of the real array antennas with four elements; (c) Photograph of the real intensity controlled mask [78].

due to the same physical properties as light. The first simulation work on RF-OAM multiplexing was done in 2010, which was carried out by a CAA using electronic methods [56]. Then further experimental implementations were reported with different radio frequencies such as 5.8 GHz, 10 GHz, and 60 GHz [79–82]. Normally, there are two main types of antennas to generate the RF-OAM modes, namely the phase-mask-based method and the CAA-based scheme. With the first method by passing through or reflecting off a phase mask, the induced angular phase differences between parts of the RF beam could produce the RF-OAM modes using a commercial antenna as the source [52]. Due to the fixed phase mask, the OAM mode is not reconfigurable. In the second method, a CAA with specific phase differences induced between the antenna elements is utilized to obtain the RF-OAM beams [56], which enables a reconfigurable multimode-generator. Hence, the CAA-based RF-OAM multiplexing gives a more promising prospect. To generate RF-OAM modes, an accurate broadband phase shift is required, which means all frequencies should be with the same phase [79]. However, due to the limited bandwidth, high loss, and the low resolution of phase-shift, it is not an easy task for electronic technology alone to support the broadband RF-OAM multiplexing [57, 58].

In 2013, X. Gao et al. proposed, theoretically analyzed and numerically simulated a photonics-based RF-OAM generation [59]. From there, OTTDs were first applied in the realization of electrical phase shifters for RF-OAM modes excitation. OTTD has advantages of low loss, small size, lightweight, and immunity to electromagnetic interference. In 2014, they implemented the first experimental verification of a CAA-based RF-OAM generator by using OTTDs as shown in Fig. 2.1 [78]. This scheme employs a four-antenna CAA generating a 20-GHz OAM radio beam with the OAM topological charge of +1. Four OTTDs composed of bulk-optics components provide high-resolution time delays for the CAA by tuning a liquid crystal spatial light modulator (LCSLM). First, the four wavelengths carried the same signal are diffracted into different directions by means of an optical grating. By adding a



In 2019, they extended their work, generating double RF-OAM modes based on the same principles as presented in Fig. 2.2 [83]. By utilizing an improved experimental architecture – a newly introduced dual-parallel Mach-Zehnder modulator carrying 17-GHz and 19-GHz RF signals simultaneously, the dual-mode RF-OAM could be radiated through a single CAA. Meanwhile, the experiment also implemented the beam steering of RF-OAM beams. The 17-GHz OAM beam with topological charge $L = 1$ is continuously steered to two dimensional (2D) directions $(:, 0^\circ, 0^\circ)$, $(:, 0^\circ, 1.70^\circ)$, $(:, 0^\circ, 3.87^\circ)$, $(:, 0^\circ, 6.17^\circ)$, and $(:, 0^\circ, 7.80^\circ)$, with good vortex properties. The 19-GHz OAM beam with topological charge $L = -1$ is steered from $(:, 0^\circ, 0^\circ)$ to $(:, 0^\circ, -6.72^\circ)$. This is an important improvement in the photonic RF-OAM generation. But it still has some limits on reconfigurable multi-mode generation due to its frequency-dependence. It is difficult to control the time delay of different modes individually. In 2015, B. Liu et al. experimentally investigated the RF-OAM demultiplexer based on X. Gao's work [84]. 10-GHz RF-OAM signals with OAM topological charges of 0, 1 and 2 were recovered with a sidemode suppression ratio of -20 dB. The separately studied RF-OAM multiplexing and de-multiplexing prove the effectiveness of the OTTD method.

In 2019, J. Huang and his colleagues introduced the optical phase shifter (OPS) to broadband RF-OAM mode generation and the mode quality of the CAA-based OAM was evaluated as well [85]. This work enables a higher-quality spatial distribution of the OAM modes. As described above, the OTTD-based OAM excitation is not broadband phase shift, thus the bandwidth is still limited. OPS can produce higher-quality RF-OAM modes, which enables lower inter-mode crosstalk. In this scheme, a dual-arm I/Q modulator acts as the key phase shift component, where one arm is for data modulation, while the other is non-data-loaded. By changing the phase on one arm, the phase difference in the optical domain will finally transfer to RF signals.

Compared to the above bulk-optics components-based OTDL/OPS, integrated OTDL/OPS, however, is more attractive because of their stable performance and compact system integration [38]. This dissertation will investigate further improvements using photonic integrated circuit (PIC) technologies, which are detailed in **Chapter 3**.

2.1.2 Mm-wave beam steering

In addition to multiplexing methods, increasing the carrier frequency towards mm-wave is another effective way of exploring the huge bandwidth for indoor applications [86, 35]. There are two main technical challenges for indoor communication at mm-wave frequencies: one is the high penetration loss through walls, which makes inter-room connection/coverage difficult (but on the other hand also reduces crosstalk between rooms and improves privacy); the other is the small electrical aperture inherent to the high antenna gain needed [38, 33]. For the former, fibre-wireless systems with low-loss fibres connected to different rooms and multiple remote antennas linking fibre to free-space can solve the inter-room wireless coverage problem. In terms of the required high antenna gain, advanced beam-forming/-steering techniques based on antenna arrays are able to break this bottleneck [75, 35]. Communication using mm-waves integrated with energy-efficient beam steering technology has been widely studied [87, 88].

In today's networks, the wireless signal is typically radiated into all directions in a given area. No matter whether there is a terminal user in this direction, the energy is always delivered. By spatially focusing the radio signal only into a narrow direction where and when needed, the required energy consumption for data transmission can be effectively reduced. Moreover, RF interference can be minimized, which enables that the parallel data streams transmitted into different directions are carried on the same frequency carrier. A phased array antenna (PAA) with beam steering can provide fast and energy-efficient indoor mobile wireless connections. To take the advantages of broadband mm-wave beam steering communications, TTD is required to enable a squint-free beam steering [89]. However, electronic integrated circuits (for instance complementary metal-oxide-semiconductor (CMOS) circuits) suffer from a high loss at high frequencies. OTTD with its inherent low loss and broad bandwidth can be used to solve these problems [36, 37, 90]. Compared to the tunable

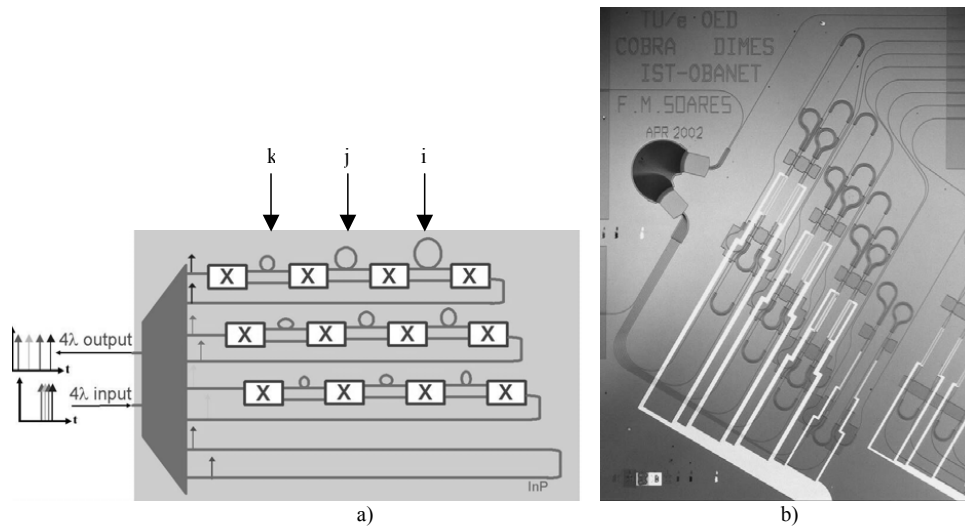


Fig. 2.3 (a) Implementation of the integrated beamformer and (b) a photograph of the fabricated beamformer [91].

OTDLs composed of bulk-optics components, which may limit the applications due to their large size and reduced stability, the integrated tunable OTDLs are more attractive because they can be integrated into a single chip [38].

Currently, several types of optically controlled mm-wave beamformers using PICs are being investigated based on: I) switched delay lines; II) optical ring resonators (ORRs); III) complementary phased shifted spectra (CPSS); VI) looped-back AWG. The concept of switched tunability is simple and easy to implement. In 1996, E. J. Murphy et al. proposed the half-integrated switched OTDLs. In this design, the optical switches were put on separate lithium niobate chips, which are interconnected by precisely manufactured lengths of polarization-maintaining fibres with delays in multiples of 44 ps [92]. In 2004, F. M. Soares and his colleagues designed, fabricated and characterized an integrated switched optical beamformer for a four-element PAA in an InP platform (COBRA) [91]. The fully integrated beamformer is shown in Fig. 2.3. Four wavelengths are first demultiplexed to different switched delay units via an AWG. Hereafter, each wavelength goes through a sequence of four cascaded Mach-Zehnder-Interferometer (MZI) switches connected to each other by three bypass-lines and three delay-lines with a length ratio of 1:2:4. The lengths of the delay-lines are linearly increasing for the different wavelengths. In this way, the time delay can be set separately for each wavelength. Finally, the four optical signals will feedback and combine into an output waveguide through the same AWG.

Benefitted by simple and reliable architecture, the switched delay networks were further developed in different platforms for performance improvement. For example, in 2013, R. L. Moreira experimentally demonstrated a 4-bit programmable delay line with an ultra-low loss in the Si₃N₄ platform [94]. Soon, J. Xie et al. reported an even higher 7-bit reconfigurable OTDL using the standard CMOS fabrication processes on a SOI wafer, which was shown in Fig. 2.4 [93]. Variable optical attenuators were

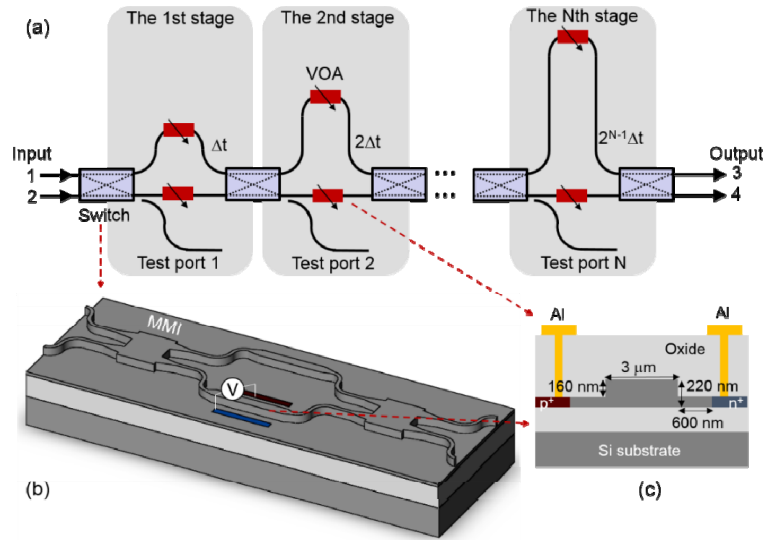


Fig. 2.4 (a) Topologic structure of the silicon N-bit OTDL. (b) 3D view of the single-armmodulated MZI used as an optical switch. (c) Cross-sectional view of the p-i-n diode for optical phase tuning and optical power attenuation [93].

embedded to suppress the inter-symbol crosstalk caused by the finite extinction ratio of switches. In 2017, a further tunability-improved switched OTDL was realized on a 60-nm-thick silicon waveguide platform [95]. By combining an ORR array and an MZI switch array, the OTDL could provide continuous tunability.

Different from the switch-based OTDLs that only provide limited tuning resolution, ORR-based OTDLs can support a continuously tunable time delay for mm-wave beam steering. The basic ORR structure has a single-bus layout, which contains a recirculating waveguide coupled in parallel to a straight waveguide. The group delay response of ORRs, which is periodic and bell-shaped, generates a narrowband time delay window [96, 97]. The time delay can be varied by tuning the coupling coefficient between the straight and ring waveguide. In 2006, the first ORR-based optical beam steering network was proposed and analyzed in principle [39]. In this scheme, based on the cascaded ORR architecture, a 1-by-8 binary tree topology ODN was reported as described in Fig. 2.5.

In 2007, L. Zhuang in the same research group experimentally demonstrated the on-chip ORR-based ODN for mm-wave beam steering [44]. Group delay responses at each output of the network were measured and a linearly increased delay was obtained as well. In 2014, a completed mm-wave beam steering communication system was implemented [98]. Fig. 2.6 depicts the schematic of the microwave photonics (MWP) beam steering system. The proposed beamformer not only demonstrated an ORR-based beamformer but also designed an optical sideband manipulator. N. M. Tessema et al. realized a tunable integrated ORR-based ODN for satellite communication in the 20-GHz band with 5-GHz RF delay bandwidth in the year of 2016 [99]. The true time delay circuit consists of an optical side band filter for single side band modulation and an optical ring resonator for broadband time delay.

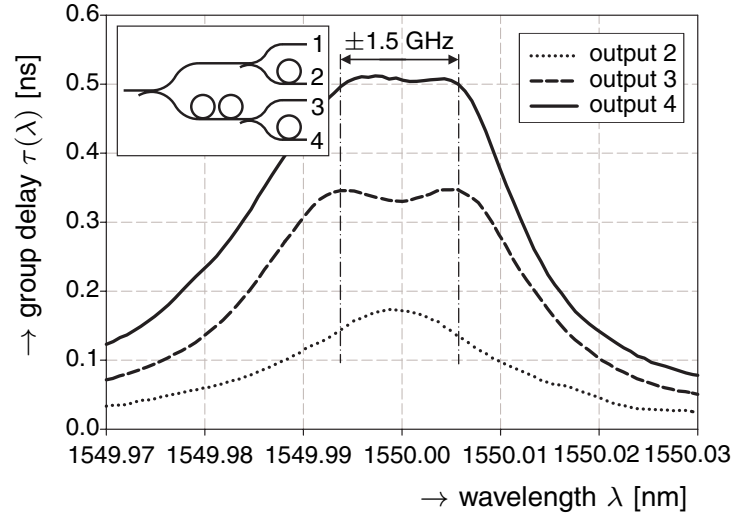


Fig. 2.5 Group delay measurement results of a 1-by-4 binary tree optical beamformer network (Inset: topology of the network) [39].

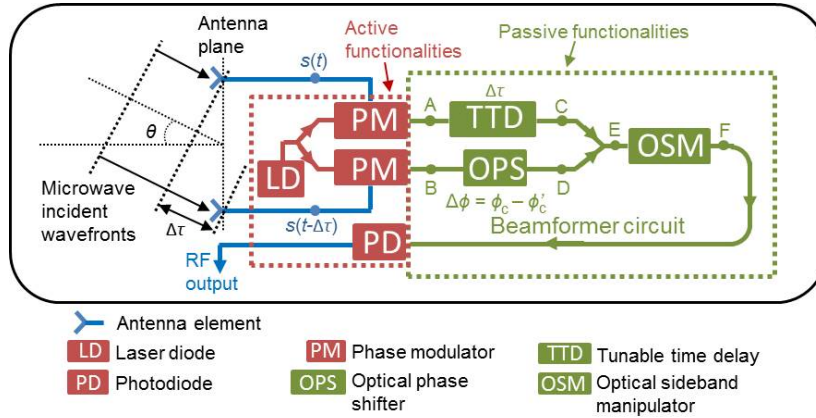


Fig. 2.6 A schematic of the MWP beamformer system proposed by L. Zhuang in [98].

Two methods of optical delay tuning are investigated: 1) optical wavelength and 2) thermo-optic delay tuning. The wavelength controlled tuning enables a large delay tuning range and can be done remotely from a distant location. The close to a linear phase measurements can be used for full beam-scanning of radio signals with frequencies in the 20 GHz band. The thermal control results in a 5 GHz RF delay bandwidth. A proof-of-concept 2×1 beamforming is demonstrated in the 20 GHz band. The design presented here can be employed to realize multi-beams for multi-users serviced by multiple satellites.

In 2019, L. Blik et al. realized the automatic delay adjustment of the ORR-based photonic beamformer [100]. In a real beam steering system, the large number of actuators makes manual tuning practically impossible. This work showed a demo solution, which is essential for real-life applications.

Recently, a novel integrated OTDL was reported by the researchers from ETH Zurich [101]. Their design relies on the splitting and combining of complementary

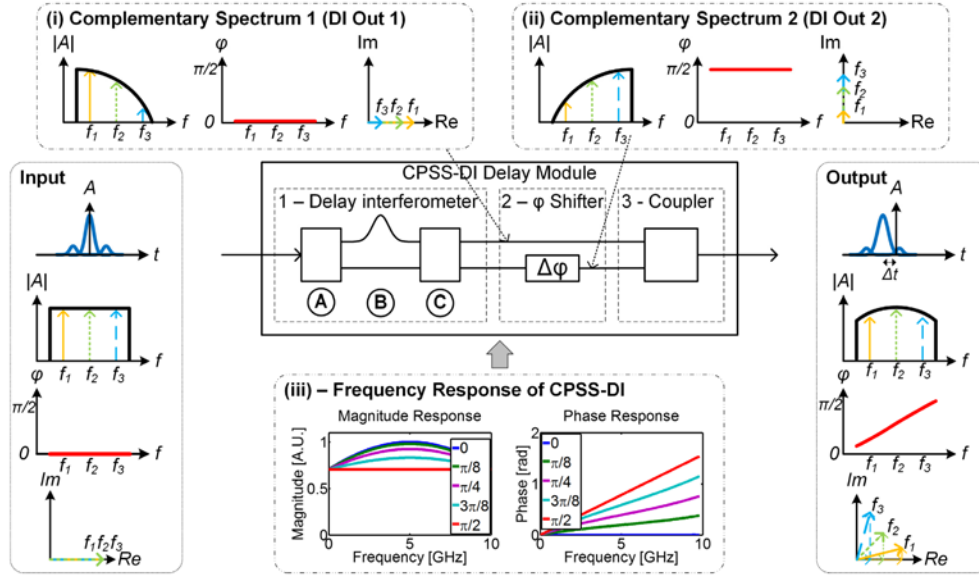


Fig. 2.7 Implementation of a TTD by a CPSS module based on a delay interferometer (DI). A signal is split into two complementary spectra (i) and (ii) by a DI. The inset (iii) shows the magnitude and phase responses of this configuration for different CPSS phases.[101].

phased shifted spectra (CPSS), allowing a large bandwidth and a low complexity. Moreover, the ultra-short settling time in the order of tens of picoseconds was achieved by using high-speed phase modulators. Fig. 2.7 presents an on-chip CPSS-based tunable OTDL with a three-stage architecture. First of all, a delay interferometer-based 1-by-2 optical filter is used to generate complementary spectrum 1 and 2 at its two outputs, respectively. Then two complementary spectra recombine through a 3-dB optical coupler. Its output signal will generate the required time delay by changing the phase of one complementary spectrum (1 or 2). In 2016, an ultra-fast mm-wave beam steering system with a settling time of <50 ps was experimentally demonstrated using the proposed CPSS-based OTDLs [102]. This dual-element antenna beam steering system proves the effectiveness of the CPSS-based beamformer.

However, all the techniques mentioned above require active tuning elements at the antenna (or beamformer) site to achieve a reconfigurable beamformer. Such active adjustment may complicate the design of the beamformer. To simplify the architecture of the antenna and also to provide flexible connection control, in 2014, a centralized and remotely-tuned scheme was proposed for optically controlled 2-D radio beam steering as shown in Fig. 2.8 [37]. The concept features steering the beam in the 2-D area by tuning just one parameter, namely the wavelength λ of the input light. By using an integrated optical circuit that uses jointly TTD elements with a large free spectral range (FSR) and TTD elements with a small FSR, the single-parameter tuning can be implemented. The used TTD element is a looped-back AWG supporting flexible delay tuning. The antenna site thus can be compact and robust, requiring minimum installation effort. Besides, the fully passive does not

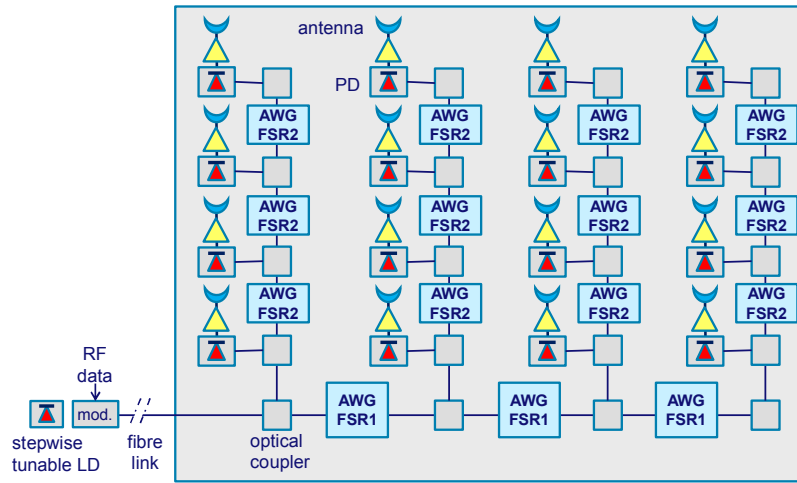


Fig. 2.8 Wavelength-tunable 2D beam steering using a combination of TTD stages with a large FSR and TTD stages with a small FSR [37].

contain active elements and thus requires very little to no maintenance. Moreover, the remotely-tuned method eases the control algorithms for fast beam steering and releases the burden of comprehensive electronic signal processing at the antenna site. So far, the AWG-based integrated delay lines are reported, but the required on-chip delay networks and the associated issues such as the size-reduction and the delay resolution improvement, have not been addressed. In this dissertation, the novel solutions for the advanced delay element design, the system design, and further implementations will be discussed in **Chapter 4**.

2.2 Optical wireless communication

The idea of OWC became very interesting by making use of earlier achievements in optical components, with the invention of the laser [103], IR Light Emitting Diode (LED) [104], and fiber optics in the 1960's. In the 90's, optical communication using visible light lasers, was widely investigated in the communication between satellites and the earth's ground [105]. After the year 2000, FSOC gained interest and was applied to many different areas employing wavelengths from 1 up to 10 μm [106–109]. More recently, due to its prominent bandwidth advantage, OWC is seen as an access technology, complementary to radio for high-speed short-range communication in 5G-and-beyond networks [110]. Generally, there are four types of OWC, which are VLC, LiFi, FSOC, and OCC [62]. For indoor applications, only the first three types are extensively researched and implemented. The related technologies will be reviewed in the following sections.

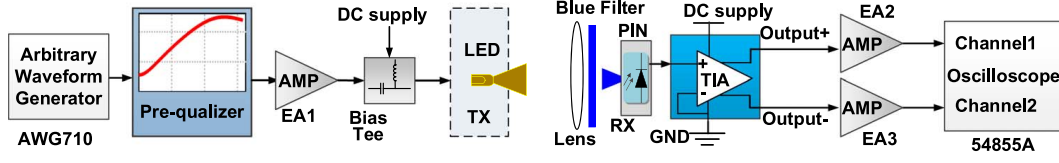


Fig. 2.9 Experimental setup of VLC system in [111].

2.2.1 Visible light communication using LED lighting

The VLC technology combines both communication and illumination by piggy-backing communication on the existing lighting infrastructure based on LEDs. It was driven by the progress of white LEDs for solid-state lighting [112]. In 1999, G. Pang et al. reported an audio broadcast transmission from a 441-LED-composed (visible light) transmitter [113]. Also, Y. Tanaka and T. Komine did the VLC experiments using white LED in 2001 and 2004, respectively [114, 115]. In 2015, X. Huang et al. did a 2.28-Gbit/s VLC transmission with a white LED over a 1.5-m free-space link [111] as shown in Fig. 2.9. In their experiment, an extended modulation bandwidth of 600 MHz was obtained by using a pre-equalization circuit. Also, adaptive bit loading, power allocation, and OFDM signals were introduced to boost the capacity. The transmission distance can go up to 3 m with 1-Gbit/s data rate.

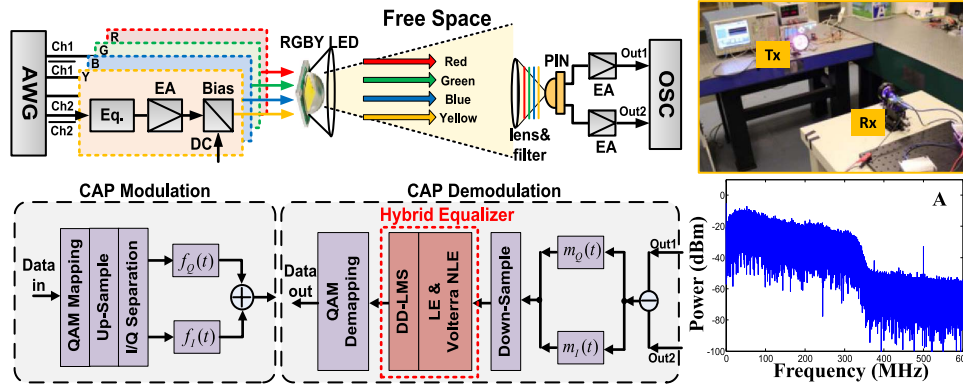


Fig. 2.10 Experimental setup of the WDM VLC system employing high-order CAP and the hybrid post equalizer [116].

Another technical realization is based on the technique of Wavelength Division Multiplexing (WDM) using Red+Green+Blue+Yellow (RGBY) LEDs. An 8-Gbit/s WDM VLC transmission using Carrier-less Amplitude and Phase (CAP) modulation were employed by Y. Wang et al. in 2015 [116]. A commercial four-wavelength LED (RGBY) was used to transfer a WDM signal over a 1-m indoor free-space distance. Fig. 2.10 describes the system setup. By using a passive equalizer, the modulation bandwidth was improved from 25 MHz to 320 MHz. A reflection cup with a 60° divergence angle was applied to the RGB LED to decrease the beam angle of the LED for longer transmission distance.

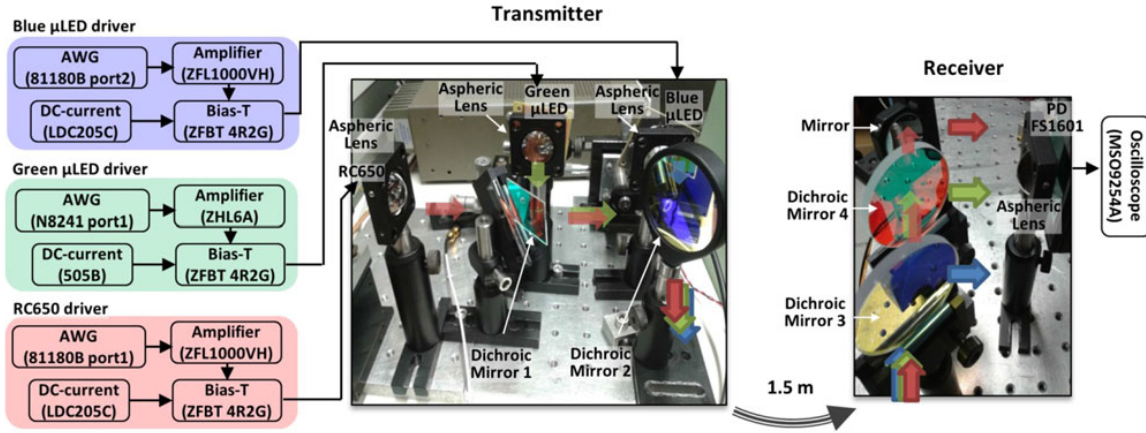


Fig. 2.11 Dichroic mirror-based WDM-VLC experimental set-up in [69].

In 2016, a record speed of 11.28 Gbit/s (net bit rate 10.4 Gb/s) at an illumination level of 984 lx was demonstrated by H. Chun et al. with RGB LEDs (Red RC-LED with 4 Gbit/s, Green LED with 2.558 Gbit/s and Blue LED with 4.724 Gbit/s) over 1.5-m reach as depicted in Fig. 2.11 [69]. In this work, the impact of different color combinations on VLC WDM was investigated for the first time. In other words, it took into account the color properties of the generated light and realized simultaneous WDM reception. The -3 -dB bandwidth of each LED is approximately 100 MHz. Also in 2016, a record transmission data rate of 5 Gbit/s with OFDM modulation format and by employing a single micro-LED, was reported by R.X.G. Ferreira [117] over an approximately 75-cm apart. These blue-emitting micro-LEDs were shown to have very high electrical-to-optical modulation bandwidths, exceeding 800 MHz.

2.2.2 Light-fidelity (LiFi)

As mentioned above, VLC uses LEDs to transmit data wirelessly by using intensity modulation at the transmitter and direct-detection photodiode at the receiver. This fits in the IEEE standard 802.15.7 for short-range OWC in local and metropolitan area networks [119]. VLC has been conceived as a point-to-point (P2P) data communication technique – essentially as a cable replacement. Light-fidelity (LiFi) in contrast describes a complete wireless networking system [120]. It includes bi-directional multiuser communication, i.e. point-to-multipoint and multipoint-to-point communication. LiFi also involves a multiple-access-points-based wireless network with very small optical attocells and a seamless handover. This means that LiFi enables full user mobility, and therefore forms a new layer within the existing heterogeneous wireless networks [118, 120]. Fig. 2.12 illustrates the principal techniques that are needed to create LiFi networks [118]. At the core are novel devices such as micro-LEDs and single-photon avalanche diodes. These are embedded in optical front-ends and subsystems which are basically the research area of VLC. LiFi also requires other supporting layers including the channel model, link-level algorithms,

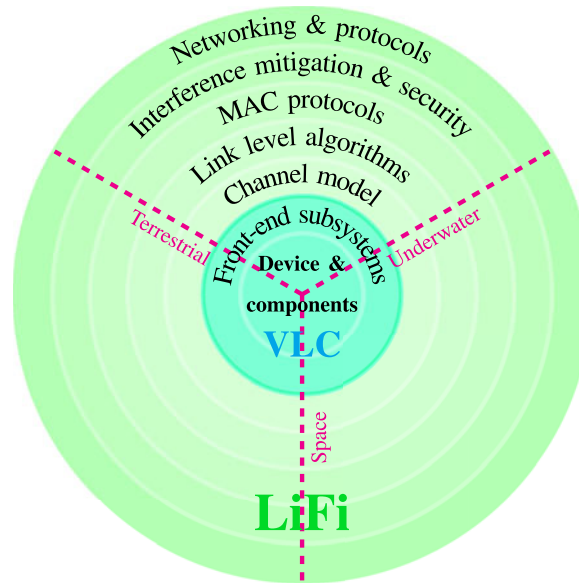


Fig. 2.12 The principal building blocks of LiFi and its application areas proposed by Harald Haas [118].

Medium access control (MAC) protocols, interference mitigation & security, and networking & protocols to extend VLC (point-to-point) into a fully networked system. Therefore, LiFi is an advanced bi-directional full-duplex system solution. Currently, Fraunhofer HHI already presents the next-generation of Gigabit VLC modules for indoor LiFi systems [121]. Outstanding features are the smaller form factor, lower energy consumption, enhanced coverage, and multi-user access. The peak data rate can go up to 1 Gbit/s.

2.2.3 IR light communication using steered beams

The spectrum of infrared light used for high-speed optical fibre communication, roughly from 1500 nm to 1600 nm, has a bandwidth of 12.5 THz. For the IR light, a wealth of mature high-speed optical devices are available (e.g. laser diodes, photodetectors, optical modulators) for optical fibre communication systems. Optical wireless communication can build on this legacy. Besides, infrared light used for fibre communication is relatively 'eye-safe'. For a Class 1 laser, the allowed maximum continuous wave (CW) power for visible light is about 0.5 mW, whereas, for infrared light beyond 1400 nm, the number can go up to 10 mW [122]. Eye safety regulations allow infrared light beams to carry much higher power than visible light beams in optical free-space area [122]. As we know, light in vacuum has a higher speed than any other media with a speed of 299792458 m/s . Compared with beams guided in an optical waveguide such as a silica fibre, free-space optical beams experience a lower latency and can offer higher bandwidth. Besides, many other advantages provided by its ability of being confined to narrow light beams [123]. By using a collimated light beam, the spatial reach can be largely extended. Also because of the utilization of directed narrow beams, only the user who sent the request can receive the light

signal, which enables higher data privacy and higher energy efficiency. Due to the avoidance of the broadcast access, the power of a transmitter can be significantly higher than the radiated way. Thus its SNR is much better. Moreover, compared to comprehensive phased array antenna structures supported by complex signal processing, especially the so-called massive MIMO antennas in 5G networks, simple optical lens or concave mirrors can easily yield >40dB gain than massive electrical antennas.

To obtain a clear view of different types of OWC, an overview comparison is done. LiFi is a network design, which is different from the physical P2P or point-to-multipoint (P2MP) communications such as VLC and IR light communication. The comparison only between VLC and the IR beam-steered communication has been made. This work is done by Prof. A. M. J. Koonen from the Eindhoven University of Technology in [124] as shown in Fig. 2.13. For VLC, the capacity per user (can be up to 10.4 Gbit/s) is shared due to its broadcast connectivity, while the IR beam-steered communication does not need to share the capacity and speeds up to 112 Gbit/s have been shown. In terms of the reach, VLC is normally applied to short to medium distance (several meters), which is shorter than that of IR light communication (can be from several meters to a very long distance). It should be pointed out that both of them are suited for short-reach indoor applications. Then the energy consumption is compared. VLC normally requires high radiated power (watt-level) which is definitely beyond the limit regulated by eye safety, while an IR beam is only below 10 mW, which is limited by the eye-safety regulation [125]. When comparing carrier frequency and average bandwidth, it is obvious that VLC has a higher carrier frequency in the wavelength range of 400-700 nm, with a 320-THz bandwidth, which is much higher than 20.9 THz of IR light communication (the carrier is from 1460 to 1625 nm). Such two bandwidths are large enough for supplying the high-speed indoor connectivity. As to the safety aspects, normally the VLC can penetrate eyes, which is less safe than the IR beam (does not penetrate eyes). Both visible light and IR light have a good privacy level. Compared to IR light communication, VLC can be embedded into the well-established LED illumination systems, which will largely reduce the cost of the infrastructure. The IR beam steering system, however, requires a new indoor (fiber) infrastructure. Currently, VLC being standardized by IEEE for further practical applications (IEEE 802.15.7). And the first generation of products is already available on the market. In contrast, the IR optical wireless communication has not been regulated yet and the study is still in the laboratory-stage.

In general, the IR beam-steered optical wireless communication can provide a more effective solution for high-speed, high-security, energy-efficient indoor wireless connections. A large amount of research has been reported for advanced IR beam steering schemes and further transmission systems. In this section, the beam-steered optical wireless systems proposed in the recent past will be presented.

Mirror-steered beam steering:

	VLC	IR beam-steered communication
Capacity per user	Shared 10.4 Gbit/s over 1.5 m ☹	Unshared Very high (Up to 112 Gbit/s per beam) ☺
Reach	Short - medium (few m)	Medium (<10 m) – long
Energy consumption	High (Watts); illumination on ☹	Low (per beam <10 mW, on-demand only) ☺
Carrier frequency	400 - 700 nm ☺	1460 - 1625 nm (S+C+L band) ☺
Average bandwidth	Width 320 THz ☺	Width 20.9 THz ☺
Safety aspects	Penetrates eye; If collimated: <<1mW	Does not penetrate eye; Collimated <10mW ☺
Privacy	Good - moderate (contained by walls; not by windows) ☹	Good (contained by walls; windows may be coated) ☺
Infrastructure	Share LED illumination ☺	New indoor (fiber) infra ☹
Standardization	First steps made, IEEE 802.11 LC study group ☹	Not yet ☹
Utilization	First products on the market ☹	Laboratory phase ☹

Fig. 2.13 The comparison between VLC and IR light beam-steered communication [124].

The first type of beam-steered OWC system is the mechanically-steered mirror-based beam steering, which was first demonstrated in the year 2010 by K. Wang and his colleagues. In this system, a hybrid optical-radio wireless system was proposed for incorporating a high bandwidth LOS FSO system and RF localization [126] as shown in Fig. 2.14, where IR light is for the duplex data transmission (uplink and downlink) and the RF frequency is used for localization. The 2.5-Gbit/s data transmission over 1.2 m distance using a Compound Parabolic Concentrator (CPC) receiver showed the feasibility of the mirror-based beam steering system in an indoor environment. Based on the same mechanism, in 2011 and 2015, K. Wang et. al further improved the system from a four-wavelength (1550.12 nm, 1550.92 nm, 1551.72 nm, and 1552.52 nm) WDM downlink transmission with 4-by-12.5 Gbit/s [127] to full-duplex communication with 10-Gbit/s downlink (1550.92 nm) and 2-Gbit/s uplink (850 nm) data rate using micro-electro-mechanical system (MEMS) based steering mirrors [128]. The earlier MEMS-based optical beam steering experiment was reported by P. Brandl et al. in 2013 as described in Fig. 2.15. They proposed the MEMS-based beam steering together with an adaptive focus in order to steer and to control the divergence of the beam [129]. By using a directly-modulated VCSEL laser and a receiver chip, a 3-Gbit/s wireless transmission over a 7-m free-space link was implemented.

Spatial-light-modulator-based beam steering:

A. Gomez et al. from the University of Oxford, in 2015, proposed a 2D bi-directional beam-steered system at 1550 nm by using Spatial Light Modulators (SLMs) and WDM techniques (with seven wavelengths) as shown in Fig. 2.16 [74]. A steering angle of 3° was achieved by tuning the SLM alone and the coverage can be further extended to $\pm 30^\circ$ with a novel angle magnifier. The SLM will generate a blaze profile to change the beam direction. Their transmission took six wavelengths to deliver a maximum of 224 Gbit/s over a 3-m free-space link. In 2016, they made a

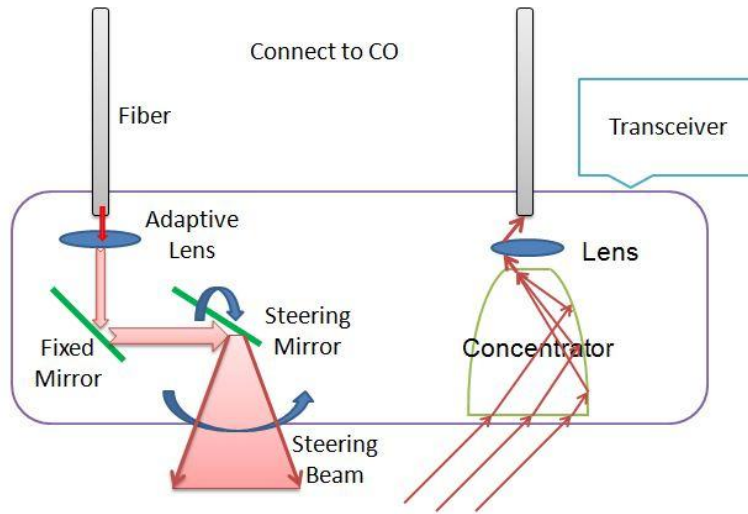


Fig. 2.14 The proposed structure of transceiver at the ceiling in [126].

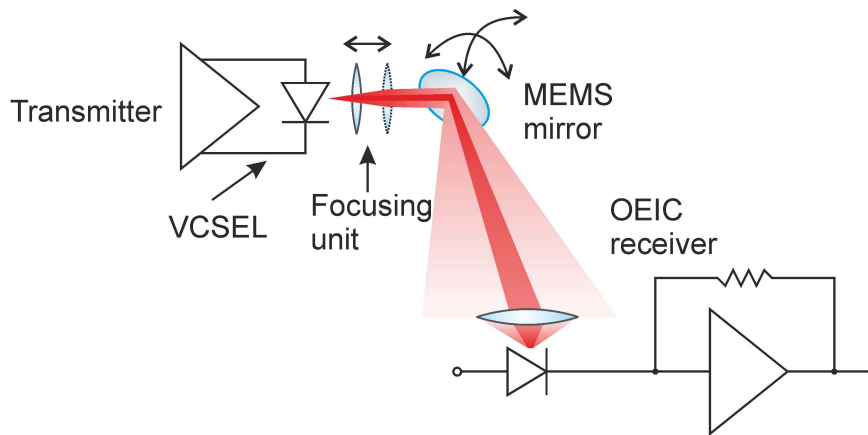


Fig. 2.15 Simplified schematic of the optical wireless communication system in [129].

performance-improved optical beam steering system with a record capacity of 416 Gbit/s [71].

Diffraction grating-based beam steering:

Different from the above two types of IR beam-steered communications (mirror-steered and SLM-based), which require an active control either mechanical adjustment or voltage change, the diffraction grating-based beam steering is a fully passive scheme, using wavelength tuning. In the years 2004 and 2013, the wavelength-tuned beam steering communication system was experimentally demonstrated using a single grating by K. Liang and C.W. Oh, respectively [130, 131]. K. Liang et al. proposed the concept of wavelength space-division multiplexing in their scheme. By changing the wavelength of the light illuminated on the dispersive grating, the beam can be steered in a 1D direction with a dispersive angle of $\sim 10^\circ$ over a range of 30 nm (1530 nm - 1560 nm). 1-Gbit/s data rate over a 4.5-m free-space link with a receiver field-of-view (FoV) of 12° was achieved. C.W. Oh et al. extended this work

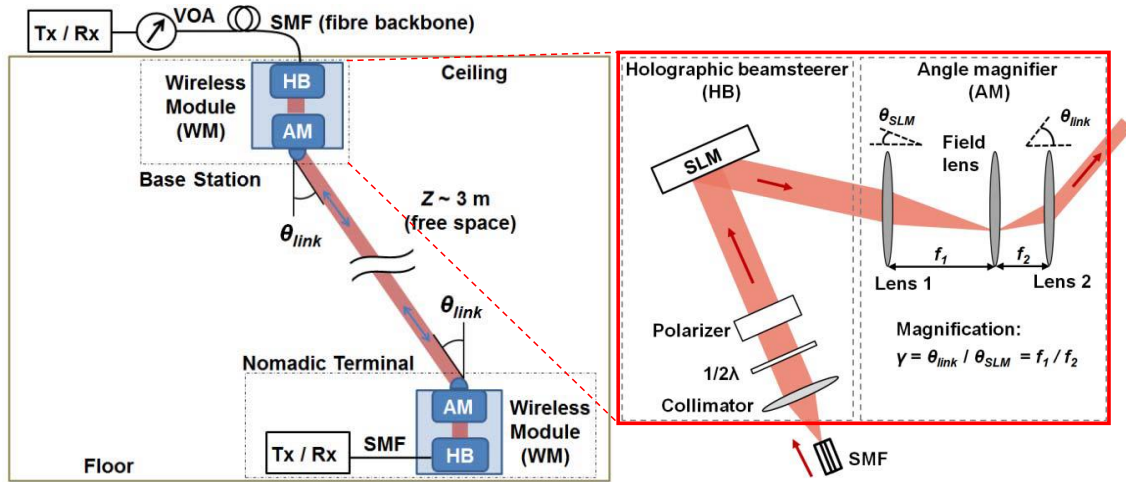


Fig. 2.16 The proposed system schematic and the wireless modules [74].

with a higher capacity of 10 Gbit/s and a larger steering angle of 17.16° . In 2015 and 2016, C.W. Oh, A. M. J. Koonen and their colleagues did further work on developing 2D beam steering systems [132, 133]. By using two 2D cascaded gratings acting as the steering module, a capacity of 42.8 Gbit/s per-channel was achieved over 2.5 m distance with a steering angle of $5.61^\circ \times 12.66^\circ$ (wavelength tuning between 1529 nm and 1611 nm). The maximum path loss is 14.6 dB. Then the performance was improved with an optical path loss of <6.15 dB by using a transmission grating and a reflection grating. Fig. 2.17 presents the beam steering system.

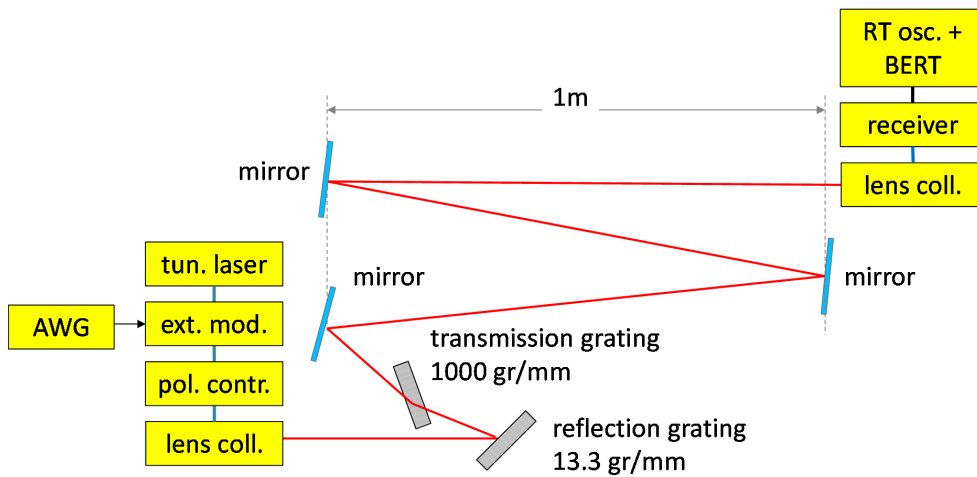


Fig. 2.17 2D beam-steered system experiment proposed in [133].

AWG router-based beam steering:

Recently, an advanced beam steering approach that requires less alignment effort was proposed by using AWG router (AWGR) modules which are readily available commercially as shown in Fig. 2.18 [134–137]. Enabled by a passive high port count

AWG feeding a 2D fibre array (N-by-M) and a lens, a large area coverage can be accomplished in an indoor IR light beam steering system. The N-by-M output fibres of the AWGR are arranged in an N-by-M 2D fiber array, which is put in the object plane of a lens. The position of the fibre in the object plane determines in which 2D direction its corresponding beam is emitted after the lens. The first concept was introduced by Prof. A.M.J. Koonen from the Eindhoven University of Technology in 2016 [134] and a transmission system is experimentally implemented with a data rate of 10 Gbit/s over 2.4-m free-space distance [135]. Soon they improved systems' performance with a capacity increasing from 10 Gbit/s to 35 Gbit/s (OOK signal) [138] and further to 112 Gbit/s (PAM-4 signal) [73]. And in 2018, a size-reducing scheme of the beam steering module was proposed and analyzed by Prof. A.M.J. Koonen et al. with defocusing the fiber array [137].

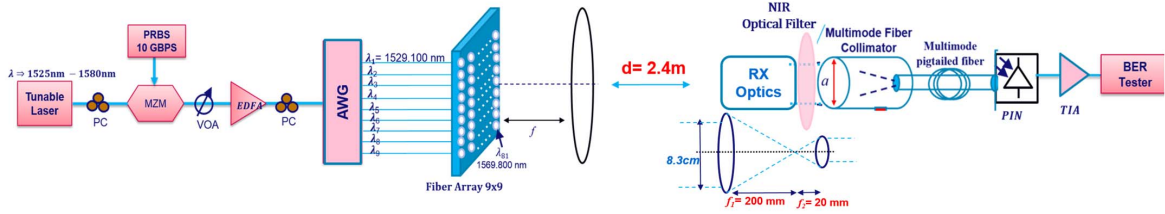


Fig. 2.18 The AWGR-based beam steering system in [135].

However, for these methods proposed above, the issues of increasing the capacity with higher spectral efficiency, designing a new receiver with wider field-of-view, and reducing the size of the steering modules with higher system stability are still challenges. In this dissertation, new solutions will be proposed for the LOS problems and a detailed discussion of experiments is given in **Chapter 5**.

2.2.4 Non-line-of-sight optical wireless communication

OWC has been proposed to support a faster indoor wireless connectivity due to its immunity to EM interference, high level of privacy, relatively-easy installation, and a huge license-free spectrum. Moreover, it can offer a large aggregated capacity by means of spatial re-use. However, an essential limitation of the OWC systems is the blocking of direct transmission by obstacles, named as the NLOS OWC. Until now, many NLOS OWC solutions for indoor applications have been based on broadcast (or sub-broadcast) wireless communication using LED-sources/LD-sources in visible light/infrared light wavelength domain, diffuse reflection links via rough surfaces, and free-space photodiodes [139–141]. For these types of NLOS OWC, the transmission speed is usually at a relatively low level mainly due to the multi-path condition (multi-reflection) and the low signal-to-noise-ratio (SNR) [140]. In 2018, a state-of-art MIMO OWC system including the NLOS-link evaluation for a smart factory is demonstrated by researchers from Fraunhofer Heinrich-Hertz-Institute with a relatively stable connection speed of only 1 Mbit/s [142]. In general, the proposed solutions for the NLOS environment do not address the diffusion mechanism itself

but instead focus on the compensation of diffuse losses by increasing the system power, using multiple streams, and selecting the highly-sensitive detectors. But the transmitted optical power could not be unlimited due to the eye-safety regulations [125]. Also, energy-efficiency is hard to be guaranteed. These inherent problems will be a long-standing challenge for ultra-high capacity and power-efficient NLOS OWC. In **Chapter 6**, a breakthrough method will be proposed, analyzed, experimentally demonstrated and discussed for the energy-efficient NLOS.

2.3 Chapter Summary

In this chapter, photonics-enabled indoor wireless communication technologies are reviewed from two aspects, namely RF wireless communication and light-wave wireless communication. In the RF area, OAM multiplexing and mm-wave beam steering, as the promising solutions, are introduced. Moreover, in **Chapter 3** and **Chapter 4**, new advanced solutions will be proposed and discussed. For OWC, the state-of-the-art of the widely studied VLC, LiFi, and IR beam-steered communication is given. Through the technical comparison between VLC and the IR beam steering, we know that the IR beam steering has the potential of providing energy-efficient ultra-high-speed indoor wireless connectivity. Then in **Chapter 5** and **Chapter 6** many advanced solutions have been proposed and experimentally verified.

CHAPTER 3

OPTICALLY CONTROLLED RADIO FREQUENCY OAM MULTIPLEXING

As a new multiplexing dimension, OAM by means of radio frequency can provide a potentially huge wireless capacity by providing infinite spatial channels. OAM is associated with the helicoidal phase profile in the plane perpendicular to the propagation direction. Different OAM modes are orthogonal to each other. Therefore, in optics and radio regimes, OAM has recently been widely considered for high-capacity communications [143, 60]. In this chapter, the issue of RF-OAM multiplexing is discussed by using the CAA technique. Then the optical integrated delay network and the phase shift network are investigated on chip-level.

3.1 Ring phased array for OAM generation

In the microwave regime, a CAA can be used to excite OAM modes as described in **Chapter 2**. Compared with methods using a spatial phase plate (SPP), which can only generate a single OAM mode per SPP, a CAA can support a transformation between multiple OAM modes by correctly setting the phase differences between the antenna elements. A CAA-based method is more flexible and feasible in RF-OAM applications. The principle of OAM mode generation using a CAA is explained in [51, 56, 85]. Here, the requirement for a CAA is briefly explained. A geometric configuration of an N-element CAA for RF-OAM excitation is shown in Fig. 3.1. N ideal antennas with progressive phases are distributed equidistantly around a circle. In principle, the number of antenna elements (N) determines the largest OAM mode (l_{max}) and can be expressed as:

$$N > 2 |l_{max}| \quad (3.1)$$

A progressive phase shift is added to different branches of an RF signal before being launched to a CAA, as shown in Fig. 3.1. The step phase shift is given by:

$$\Delta\varphi = -2\pi l / N \quad (3.2)$$

where l is the index of the excited OAM mode. In a 4-element CAA system, the allowed OAM modes are $l=0$ and $l=\pm 1$, totally three modes. For the fundamental mode, each antenna should have the same phase. For $l=+1$ and $l=-1$, the required step phase shift is -90° and 90° , respectively. The 4-antenna system is discussed in detail in **Section 3.3**.

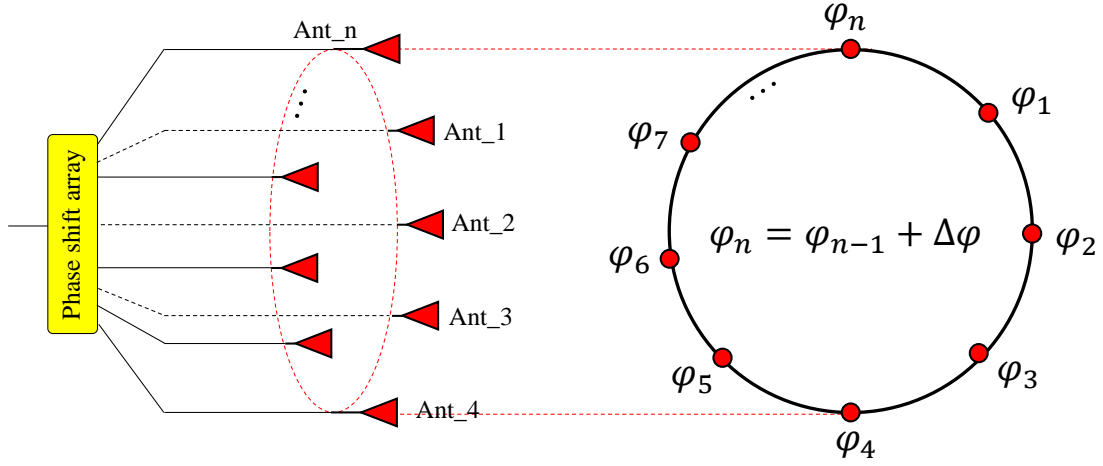


Fig. 3.1 The geometry of an N-element circular antenna array used for RF-OAM generation/detection.

3.2 Single-element-tuned bidirectional optical delay network

As described in [59], OTDLs, especially integrated OTDLs, can produce broadband time delay when converting the signal from the optical domain to the electrical domain. For an RF signal, this time delay can work as phase shift within a certain bandwidth range. R. Bonjour et al. proposed a novel broadband tunable OTDL that relies on the splitting and combining of CPSS [101]. It is a promising technique for broadband OAM generation. However, this design is a single delay line, not a compact multiport network which is more frequently used in practical applications. Normally, the required delay array is realized by simply merging individual delay lines. In this part, a more compact two-port optical delay network is proposed and demonstrated. A tunable bidirectional optical time delay can be achieved by tuning a single phase-element.

3.2.1 Working Principles

Figure 3.2 (a) shows a conventional CPSS-based optical RF phase shifter, which is composed of three parts, namely the delay interferometer, the phase (φ) shifter, and the coupler (1-by-2 coupler). A detailed analysis has been done in [101]. This design can be regarded as a 1-by-1 network, whose matrix transfer function can be presented as follows without taking the loss into consideration:

$$H_{CPSS} = \begin{bmatrix} \frac{1}{\sqrt{2}} & \frac{1}{\sqrt{2}} \end{bmatrix} \cdot \begin{bmatrix} 1 & 0 \\ 0 & e^{j\varphi} \end{bmatrix} \begin{bmatrix} \frac{-j}{\sqrt{2}} & \frac{1}{\sqrt{2}} \\ \frac{1}{\sqrt{2}} & \frac{-j}{\sqrt{2}} \end{bmatrix} \begin{bmatrix} 1 & 0 \\ 0 & e^{-j2\pi\Delta tf} \end{bmatrix} \begin{bmatrix} \frac{1}{\sqrt{2}} \\ \frac{1}{\sqrt{2}} \end{bmatrix} \quad (3.3)$$

But in my design, the output port is added to two by replacing the 1-by-2 coupler with a 2-by-2 coupler at the output side, and changing the input 50:50 coupler into a tunable coupler as shown in Fig. 3.2 (b). Its expression is shown as:

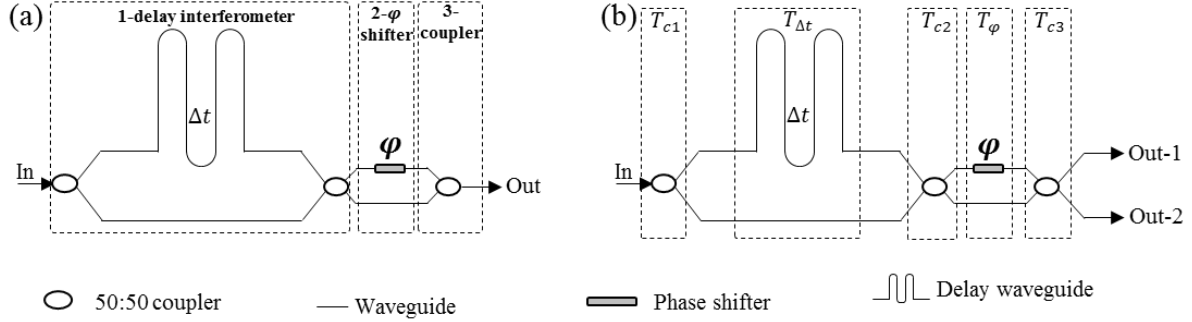


Fig. 3.2 (a) The conventional CPSS-based optical tunable delay line; (b) the architecture of the proposed optical time delay array.

$$H_{2_port} = T_{c3} \cdot T_{\varphi} \cdot T_{c2} \cdot T_{\Delta t} \cdot T_{c1} = \begin{bmatrix} \frac{-j}{\sqrt{2}} & \frac{1}{\sqrt{2}} \\ \frac{1}{\sqrt{2}} & \frac{-j}{\sqrt{2}} \end{bmatrix} \cdot \begin{bmatrix} 1 & 0 \\ 0 & e^{j\varphi} \end{bmatrix} \cdot \begin{bmatrix} \frac{-j}{\sqrt{2}} & \frac{1}{\sqrt{2}} \\ \frac{1}{\sqrt{2}} & \frac{-j}{\sqrt{2}} \end{bmatrix} \cdot \begin{bmatrix} 1 & 0 \\ 0 & e^{-j2\pi\Delta t f} \end{bmatrix} \cdot T_{c1} \quad (3.4)$$

where, T_{c1} is the transmission matrix (2-by-1) of the tunable coupler. We set T_{c1} as

$$T_{c1} = \begin{bmatrix} a_1 \\ a_2 \end{bmatrix} \quad (3.5)$$

where, $a_1^2 + a_2^2 = 1$. Then equation 3.4 can be wrote as

$$H_{2_port} = \frac{1}{2} \begin{bmatrix} -a_1 - ja_2 \cdot e^{-j2\pi\Delta t f} + e^{j\varphi} \cdot (a_1 - ja_2 \cdot e^{-j2\pi\Delta t f}) \\ -ja_1 + a_2 \cdot e^{-j2\pi\Delta t f} - e^{j\varphi} \cdot (ja_1 + a_2 \cdot e^{-j2\pi\Delta t f}) \end{bmatrix} \quad (3.6)$$

When $a_1 = a_2 = \frac{1}{\sqrt{2}}$, the same setting as that in [101], the simulation responses of the two outputs (Ch1 and Ch2) are shown in Fig. 3.3. Here, the FSR is defined as the inverse of Δt (FSR=1/Δt). Fig. 3.3 (a) presents the intensity responses of Ch1 and Ch2. They are complementary in the frequency domain. When changing the phase of φ from 20° to 80°, the bandwidth of Ch2 increases a little bit, but Ch1 changes rapidly (bandwidth decrease) with the fast growth of power loss. Their phase responses have a similar changing trend when increasing time delay. The linear area of the phase response of Ch1 trends to be narrower when increasing φ . Therefore, Ch1 and Ch2 cannot be broadband simultaneously. Such a direct dual-port design cannot support broadband applications.

However, by changing the power splitting ratio of the input 1-by-2 coupler, a broadband dual-port bidirectional tunable delay network can be implemented by using single-element adjustment. When $a_1 : a_2$ is set as 1:3, the simulation results according to equation 3.6 are presented in Fig. 3.4. When tuning φ , the time delay

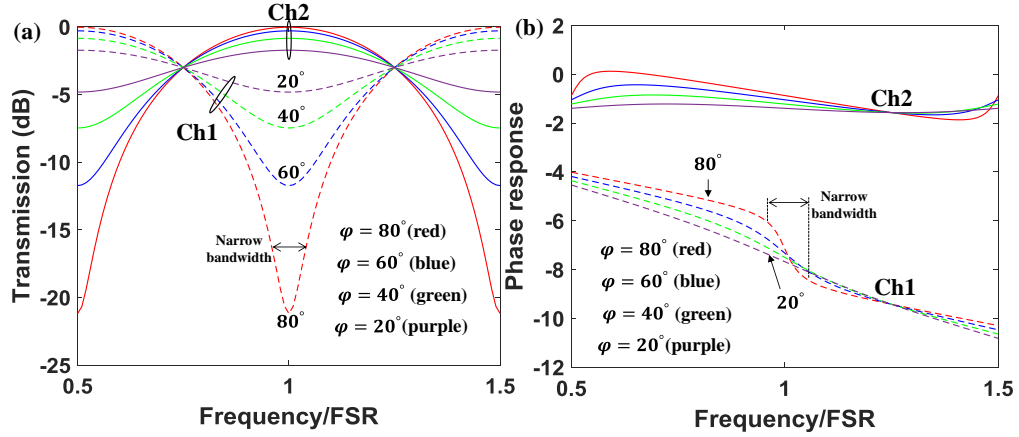


Fig. 3.3 (a) The intensity response (b) the phase response of the direct dual-port design of the CPSS-based ODN.

of Ch2 changes much faster than that of Ch1 as described in Fig. 3.4 (b). The different changing trends enable an increase of their relative time delay between two output ports, which implements the concept of a dual-port tunable delay network. As for the intensity response, Ch2 has similar bandwidth as that in Fig. 3.3, but the narrow bandwidth of Ch1 in Fig. 3.3 is significantly extended due to its flat intensity response. Both of the two channels can support broadband applications with a maximum 8.3-dB power imbalance in principle in Fig. 3.4 (a). It should be pointed out that this power imbalance can be reduced by selecting a higher power splitting ratio of a:b, but the bandwidth may be reduced as well. Besides, the idea of bidirectional time delay can be achieved by tuning the same phase factor φ . Simulation results in Fig. 3.4 (c) and (d) depict the exchanged responses between Ch1 and Ch2 by tuning the phase to a different range (from 210° to 185°). If we define the delay in Fig. 3.4 (b) is positive, then the time delay in Fig. 3.4 (d) is negative.

3.2.2 Chip design

Design in principle:

As analyzed above, the bidirectional tunable dual-port ODN can be realized via power-splitting control. Here, a complete design is given in Fig. 3.5. An MZI-based tunable power splitter is introduced for phase tuning (φ_1). Its matrix transfer function is

$$H_{splitter} = \begin{bmatrix} \frac{-j}{\sqrt{2}} & \frac{1}{\sqrt{2}} \\ \frac{1}{\sqrt{2}} & \frac{-j}{\sqrt{2}} \end{bmatrix} \cdot \begin{bmatrix} 1 & 0 \\ 0 & e^{j\varphi_1} \end{bmatrix} \cdot \begin{bmatrix} \frac{1}{\sqrt{2}} \\ \frac{1}{\sqrt{2}} \end{bmatrix} = \frac{1}{2} \begin{bmatrix} -j + e^{j\varphi_1} \\ 1 - j \cdot e^{j\varphi_1} \end{bmatrix} \quad (3.7)$$

where, φ_1 means a tunable phase shifter, which can be a thermally-controlled metal heater or a fast phase modulator. From the results, we know that the two output

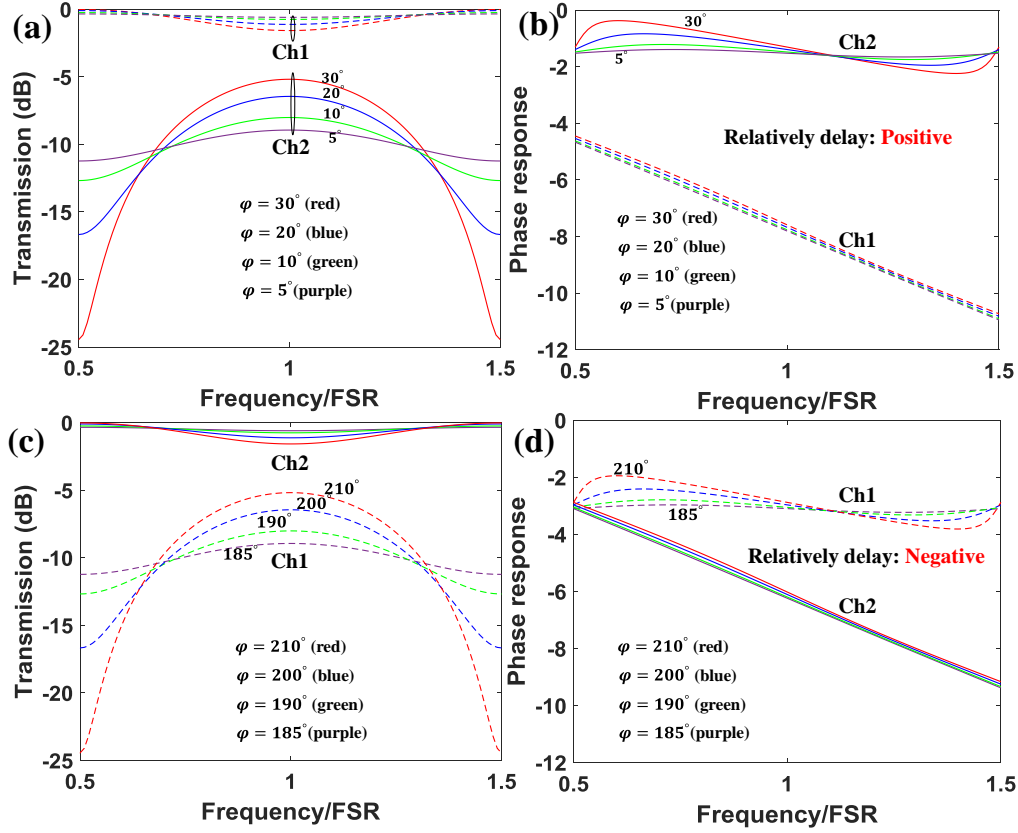


Fig. 3.4 (a)-(b) The simulated intensity and phase responses of the proposed broadband time delay network with positive delays; (c)-(d) The simulated intensity and phase responses of the proposed broadband delay network with negative delays.

signals are in phase but with different amplitudes, which satisfy the requirement for the amplitude/phase response in equation 3.5.

IMOS chip:

Then the idea is verified experimentally by using an on-chip design in Indium-phosphide-Membrane-on-Silicon (IMOS) platform as shown in Fig. 3.6. IMOS technology is explained in **Chapter 4**. In this design, an alternative design is used to implement the proof-of-concept of the ODN. Different from the scheme that using a tunable coupler mentioned above, here, we make use of power loss of the on-chip delay path to obtain the required imbalanced power setting. As presented in the topological structure, a normal 50:50 optical coupler is used to split the input light into different paths. By utilizing the inherent higher loss in the delay path, an imbalanced power ratio between two paths (the Blue path has lower power and the Red path has higher power) can be obtained. These two signals will pass afterward modules of T_{c2} , $T_{\Delta t}$, and T_{c3} , which are the same as the theoretical analysis above. An alternative chip is depicted according to its topological structure. In the beginning, this chip is designed for a cascaded ORR-based optical delay network. Meanwhile, it can be used to prove our idea. First, the input light is split into two parts (the Blue one and the Red one). Then the Red one is fed into the coupler of T_{c2}

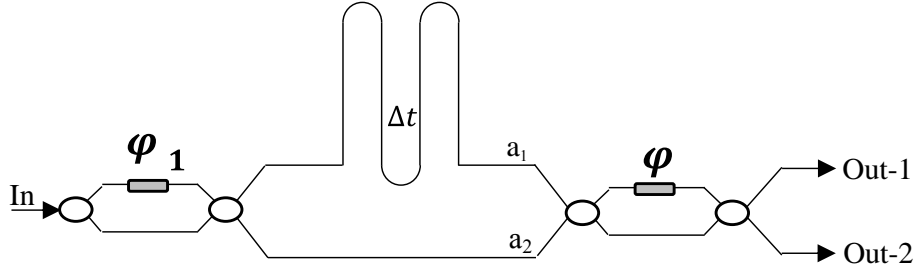


Fig. 3.5 A complete design of the proposed dual-port bidirectional tunable time delay network.

directly and the Blue one goes into the delay unit $T_{\Delta t}$, which brings higher power loss than the Red channel. The loss comes from the cascaded rings, the waveguides (~ 20 dB/cm caused by imperfect fabrication), and the unused power (-3 dB in principle). To implement a concept of the waveguide-based time delay, the light in Blue channel is controlled to go through directly without going into the ORR rings by properly setting the phase φ_1 and φ_2 . Finally, the delayed signal is fed into the coupler of T_{c2} as well. This delayed path is topologically equal to a delayed waveguide with relatively high loss. Thanks to the power loss in the delay path, the required power assignment is maintained. The bidirectional tunable ODN can be achieved by changing the phase factor of T_φ .

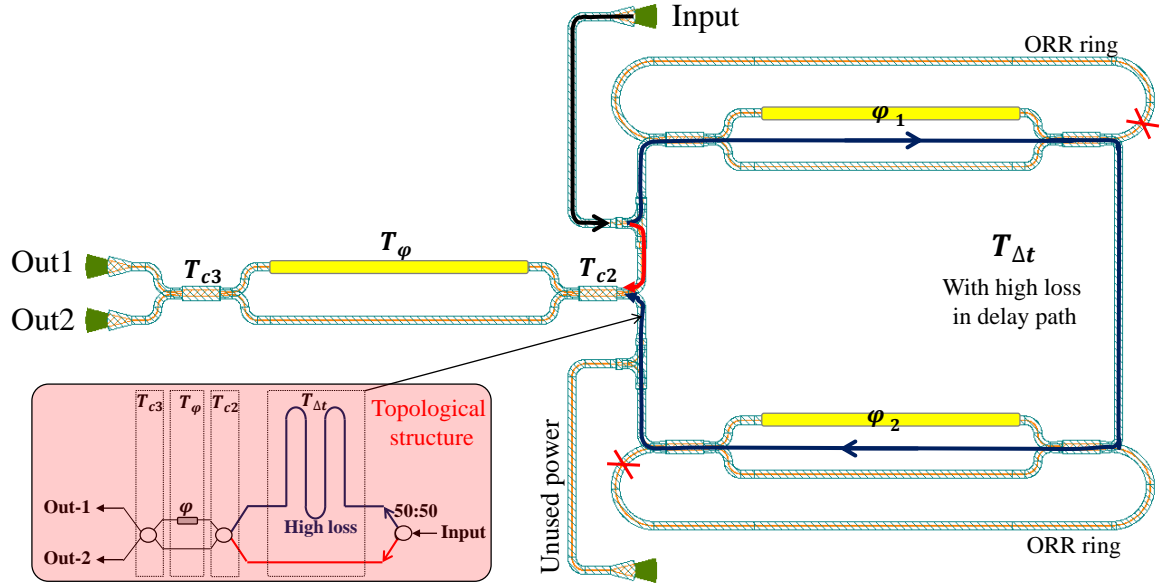


Fig. 3.6 The mask layout of the alternative bidirectional delay network.

3.2.3 Experimental setup

Fig. 3.7 presents the experimental setup. An optical carrier is first fed into a 40-GHz Mach-Zehnder modulator (MZM) via a polarization controller (PC-1) which yields

a power-optimized input. The MZM is modulated by a radio signal generated by a vector network analyzer (VNA) and is biased at the quadrature point (~ 2.0 V). An erbium-doped fiber amplifier (EDFA) is used to amplify the optical signal. Another PC (PC-2) is employed to align the polarization state to the transverse electric polarization. Then the light is vertically coupled in and out via a pair of cleaved single-mode fibre (CF). The proposed dual-port bidirectional time delay network is thermally biased/controlled by a heater controller. The two output ports are measured by mechanically moving the position of the output CF. Finally, the light is detected by a photodetector and is fed back to the VNA. The VNA sweeps a frequency range from 1 GHz to 10 GHz.

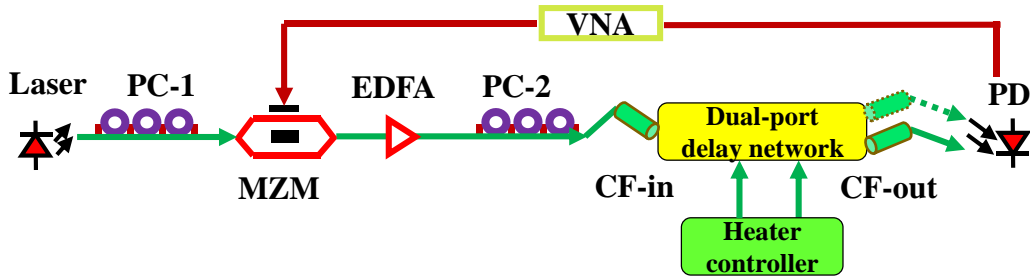


Fig. 3.7 The experimental setup.

3.2.4 Results and discussion

This part will discuss the experimental results. Fig. 3.8 (a) and (b) describe the measured optical spectra at Out1 and Out2 when changing the phase of φ via applying different voltages to a heater. The used optical light is at $\lambda=1530.95$ nm. When increasing the voltage from 0.87 V to 0.97 V with a 0.02-V increment, the measured optical power of Ch1 decreases from -3.9 dB to -5.2 dB (1.3-dB fluctuation). While the power of Ch2 increases from -9.9 dB to -5.6 dB. Thus the maximum optical power imbalance between Ch1 and Ch2 is around 6 dB. The measured intensity responses of the two channels well match the trends in simulation analysis. Then the bidirectional delay performance is given in Fig. 3.8 (c) and (d). When the voltage is between 0.87 V and 0.97 V, Ch2 exists a negative time delay compared to Ch1. The relative time delay will exchange if the voltage is set in the range from 1.26 V to 1.33 V. The measured continuous delay ranges are +13.3 ps and -13.1 ps respectively. This experiment proves the effectiveness of the proposed single-element-tuned bidirectional dual-port ODN.

3.3 Optical phase shift network for RF-OAM

For broadband RF-OAM multiplexing, the broadband phase shift is needed. Moreover, it is the multi-port phase shift network that supports the required phase settings

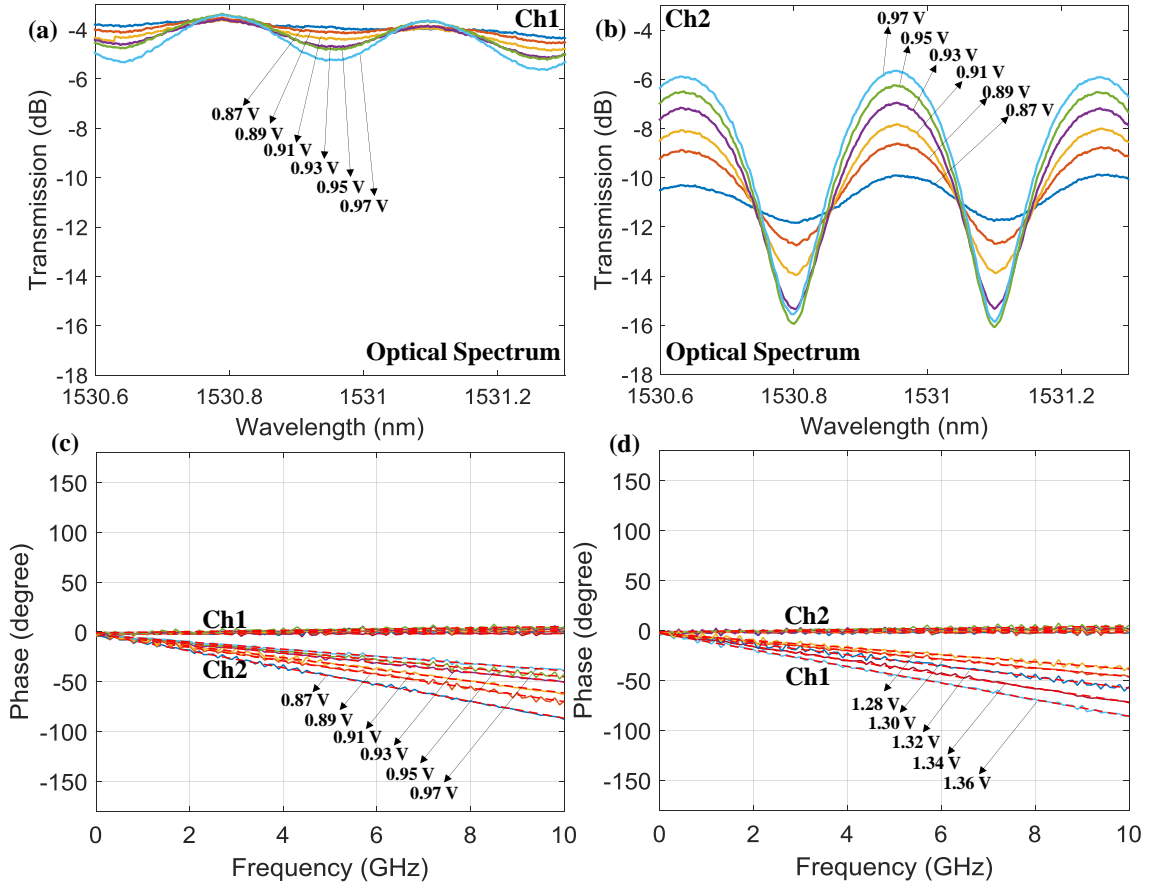


Fig. 3.8 (a)-(b) The measured optical spectra of Ch1 and Ch2; (c)-(d) the measured phase responses of Ch1 and Ch2 with positive and negative time delays.

for a CAA. However, it is very hard work to generate accurate phased arrays using bulk-optics components such as fibre-based systems. The phased array on a single chip is considered as a promising solution due to its accurate phase control using photonic integrated technologies. In this section, novel integrated phased arrays for RF-OAM generation including wavelength-controlled and thermally controlled schemes are presented.

3.3.1 Multi-OAM-mode generator I: Passive phased array

Principles:

Based on a CAA structure, a reconfigurable passive phased array is proposed for multi-OAM-mode generation. This passive generator aims at realizing a 4-element CAA system, which can support three OAM modes, namely, the fundamental (0 order) mode and the ± 1 order mode. By tuning the optical wavelength, the produced OAM mode can be switched between the three modes without any active control at the antenna side (including a CAA and a photonic phased array). The idea is presented in Fig. 3.9. An on-chip phased array is composed of two stages: I)

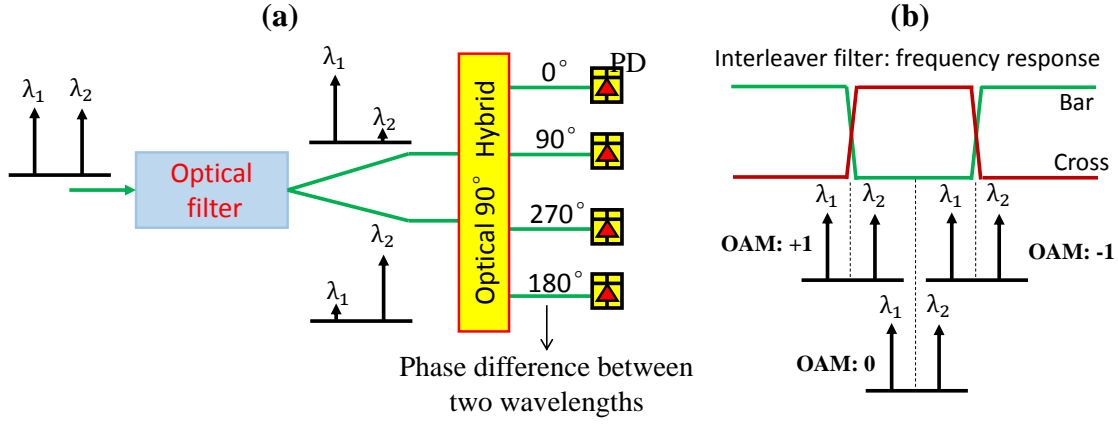


Fig. 3.9 The wavelength-switched three-mode OAM generator.

two-port optical filter; II) 2-by-4 passive optical phased array. For the first stage, the frequency responses at two output ports should be complementary and have a very sharp filter-shape to split two closed wavelengths. As shown in Fig. 3.9 (a), two phase-locked wavelengths (λ_1 and λ_2) with a certain frequency spacing (This depends on the application.) are fed into an optical filter and are wavelength-split to different paths with greatly suppressing the unwanted wavelength (e.g. < -20 dB). Then each output is delivered to an input port of an optical 90° hybrid, which is widely used in a current optical coherent receiver [144, 145]. The 90° hybrid can be a 4-by-4 multimode interferometer (MMI) only using channel 1 (Ch-1) and channel 3 (Ch-3) as input ports. When the electric field of the two signals (E_{λ_1} and E_{λ_2}) are set as the input components of the 4-by-4 MMI coupler, each output field of the coupler is represented by using the phase relationship as shown in Fig. 3.8 [146].

$$\begin{bmatrix} E_1 \\ E_2 \\ E_3 \\ E_4 \end{bmatrix} = \sqrt{k_{4 \times 4}} \cdot \begin{bmatrix} 1 & 0 & e^{-j(\pi/4)} & 0 \\ e^{j(3\pi/4)} & 0 & 1 & 0 \\ e^{-j(\pi/4)} & 0 & 1 & 0 \\ 0 & 0 & e^{j(3\pi/4)} & 0 \end{bmatrix} \cdot \begin{bmatrix} E_{\lambda_1} \\ 0 \\ E_{\lambda_2} \\ 0 \end{bmatrix} \quad (3.8)$$

where $\sqrt{k_{4 \times 4}}$ indicates the power splitting coefficient of the 4-by-4 MMI coupler. Suppose the coupler has an ideal power splitting and subtract any constant phase offset, the output phase relationship between the signal E_{λ_1} and the signal E_{λ_2} is $E_{\lambda_1} + E_{\lambda_2}$, $E_{\lambda_1} + jE_{\lambda_2}$, $E_{\lambda_1} - jE_{\lambda_2}$, and $E_{\lambda_1} - E_{\lambda_2}$ for the output from Ch-1 to Ch-4, respectively. Thus after a photodiode, the normalized phases of detected four RF signals are 0° , 90° , 270° , and 180° , which are then fed to a 4-element CAA. A non-hop phase can be implemented by exchanging Ch-3 and Ch4 using the wire bonding technology. In this case, a CAA can provide the OAM mode of $+1$ order. When exchanging the order of E_{λ_1} and E_{λ_2} (E_{λ_1} for Ch-3 and E_{λ_2} for Ch-1), the obtained normalized phase is 0° , -90° , -270° , and -180° , respectively. Accordingly, the OAM mode is -1 (as shown in Fig. 3.9 (b)). This operation can be achieved by

shifting the two wavelengths simultaneously to a different frequency domain of the two-port filter, which can be an interleaver filter as described in Fig. 3.9 (b). When the two signals go into the same path of the filter, they will experience the same optical phase change. Thus there is no phase difference between four detected RF signals. This case respects the fundamental OAM mode.

Chip design I: interleaver & 4-by-4 MMI:

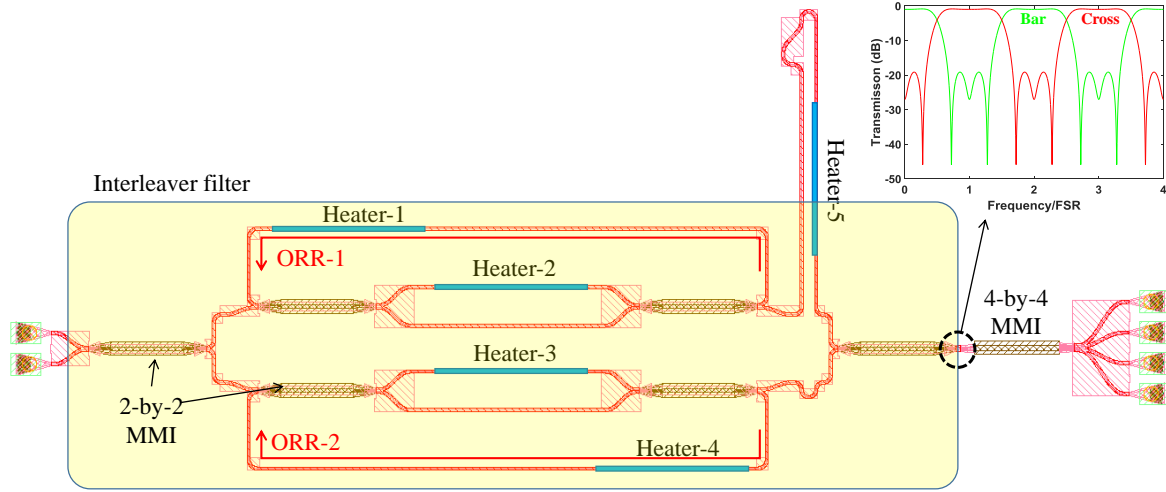


Fig. 3.10 The mask layout of the 90°-hybrid-based OAM generator.

A 90°-hybrid-based OAM generator is designed and fabricated using silicon technology in IMEC platform as shown in Fig. 3.10. It is composed of two parts, namely the two-port interleaver filter and the 4-by-4 MMI. For the first part, a verified architecture of embedding ORRs into an MZI is utilized [147, 148]. An input signal is first to split into two parts via a 2-by-2 MMI, each of which is fed into an ORR (ORR-1 or ORR-2). The ORR uses a typical reconfigurable design, with a heater (Heater-1) for ring phase shift and a heater (Heater-2) for the adjustment of the coupling coefficient. In the lower path of the MZI, the same ORR structure (ORR-2) is introduced. Then the two ORR outputs are recombined via a delayed interference waveguide with an extra heater (Heater-5) for phase shift. The delayed waveguide is required to be half-lengthed of the ring. The outputs of the interleaver filter are named as the bar port and the cross port. By properly controlling heaters (set the phase shift), the spectrally complementary responses at bar and cross ports can be obtained. The phase shift caused by heaters can be implemented by changing the index of the waveguide via tuning the temperature of the Tungsten heater [148]. Simulated interleaver frequency responses at two outputs are presented in the inset of Fig. 3.10. The coupling ratios of ORRs used are 0.96 and 0.94 with 0.2 power loss in the ring, respectively. The phase shifts in ORRs (Heater-1 and Heater-2) and delayed waveguide (Heater-5) are set as 0°, 180°, and 0°. Then the split signals are fed into the port 1 and 3 of a 4-by-4 MMI, which will provide the required phases for a 4-element CAA.

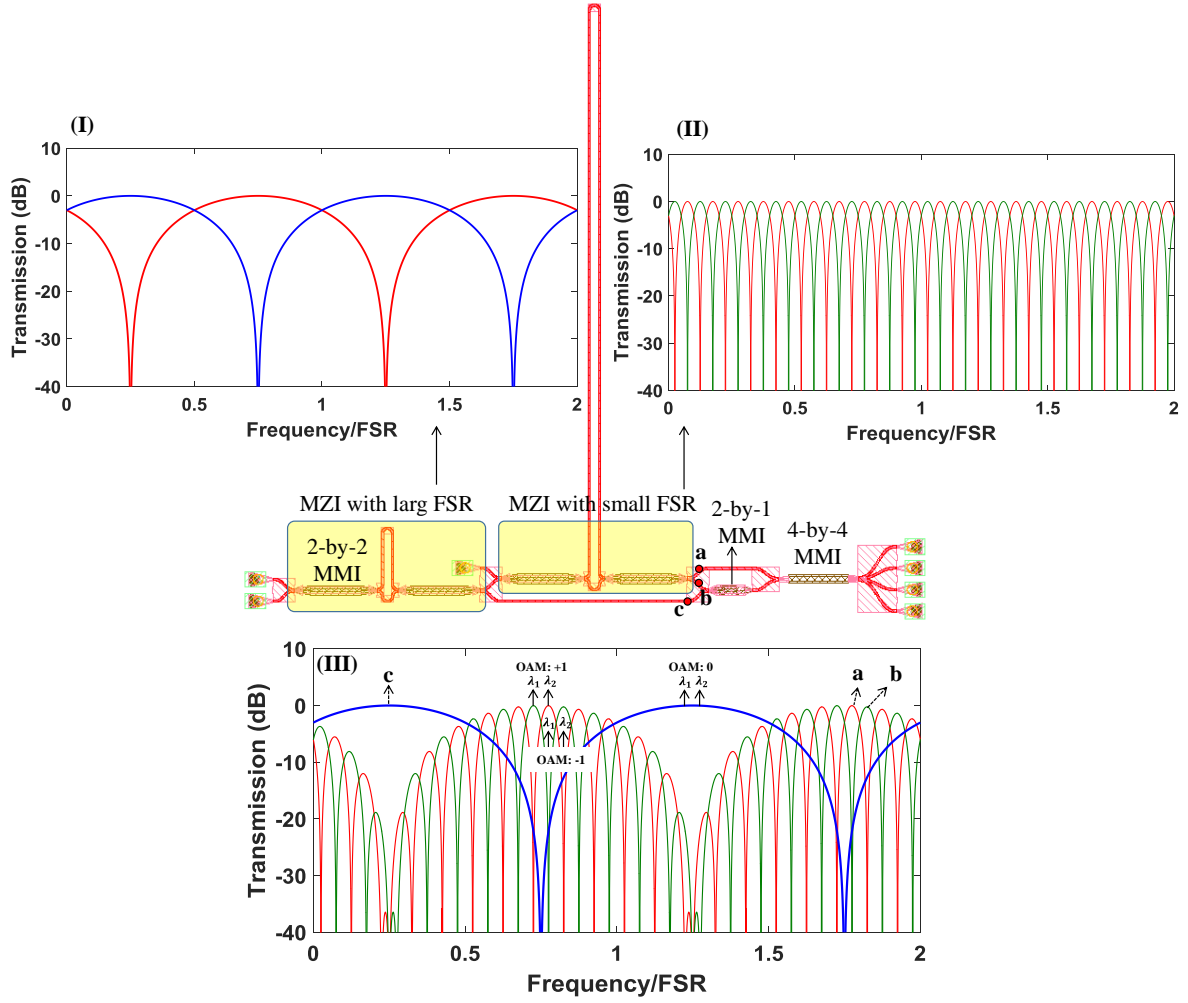


Fig. 3.11 The mask layout of the passive 3-mode OAM generator.

Chip design II: Cascaded MZI & 4-by-4 MMI:

Different from an interleaver filter that requires thermal control at the antenna side, an MZI-based passive filter is proposed to simplify the phased array. Fig. 3.11 describes the mask layout of the passive OAM generator. It utilizes cascaded MZI filters with different FSRs, in which the MZI with small FSR is for the switch between the fundamental mode and higher modes (± 1) while the MZI with large FSR is for the switch between modes of $l=1$ and $l=-1$. The lengths of the delayed waveguides in different MZI stages are set as $200\ \mu\text{m}$ and $2200\ \mu\text{m}$, with which the filter can split two 18-GHz-spacing wavelengths. In this design, the target signal bandwidth is 2 GHz @18-GHz carrier. The filter's FSR can be changed according to the target RF carrier. The insets I and II show the frequency responses of MZI filters (I for MZI with large FSR, II for MZI with small FSR). Inset III describes the spectral responses at points of a (red), b (green), and c (blue). When λ_1 and λ_2 are delivered to the point a and b respectively, the obtained phase relationship of the four outputs (MMI)

can generate the OAM mode of $l=+1$. Then shift the wavelength by a half smaller FSR (left or right), λ_1 and λ_2 will exchange the output ports (from a/b to b/a). The relative OAM mode is also changed to $l=-1$. To obtain the fundamental OAM mode, the used two wavelengths are required to be delivered to point c simultaneously. Thus no phase difference exists between the four RF signals.

3.3.2 Multi-OAM-mode generator II: Direct optical synthesis phased array

Principles:

However, an MMI-based optical passive phased array cannot be phase-changed once being fabricated and it can only support a 4-element CAA system. Besides, it may suffer from the fabrication error, which can cause phase errors. As a complementary scheme, the direct optical synthesis phased array that can provide any phase shift is proposed to support a larger-element-count CAA and mitigate phase errors. Enabled by a mental heater, the required broadband phase shift can be realized as shown in Fig. 3.12. First, the input two wavelengths are split into two paths (Path-1 and Path-2) via an optical interleaver filter (shown above). Then the wavelength in Path-1 will go through a phase shift system, which is composed of four heaters and a four-port power splitter. The heaters here act as phase shifters ($0-2\pi$) by using the thermally-caused index change. To reduce the energy consumption of the heaters, the cascaded architecture is utilized. This design allows phase accumulation from multi-stage heaters, thus it can spread the required phase shift to different heating elements, releasing the pressure on a single heater. The other signal in Path-2 will be split into four in-phase parts in principle and each one will combine with the corresponding signal that originated from Path-1. The optical phase relationship ($0^\circ, 90^\circ, 180^\circ$, and 270° ,) between the two wavelengths will be passed to RF signals. Different from the passive waveguide-based scheme, this fully reconfigurable method can provide continuously tunable phases for OAM activation and can mitigate phase errors caused by fabrication. Meanwhile, there are two ways of OAM-mode switching. The first one is the pure thermally-controlled phased array, which can provide the continuous phase shift from 0 to 2π . The other type is the wavelength-tuned switch that is mentioned in Section 3.3.1.

Chip design:

Fig. 3.13 presents the mask layout of the proposed heater-based phased array. Here, a 4-output phased array using an on-chip interleaver filter is introduced as an example. The thermally-controlled phased array is composed of two similar 1-by-4 optical splitters using three 1-by-2 MMIs. The simpler one equals to a 1-by-4 power splitter with in-phase outputs. The other one introduces four heaters for phase tuning. Finally, the eight signals are combined in pairs via four 1-by-2 MMIs to generate four outputs. Besides, as mentioned above, the interleaver filter can be replaced by a simpler cascaded MZI-based filter.

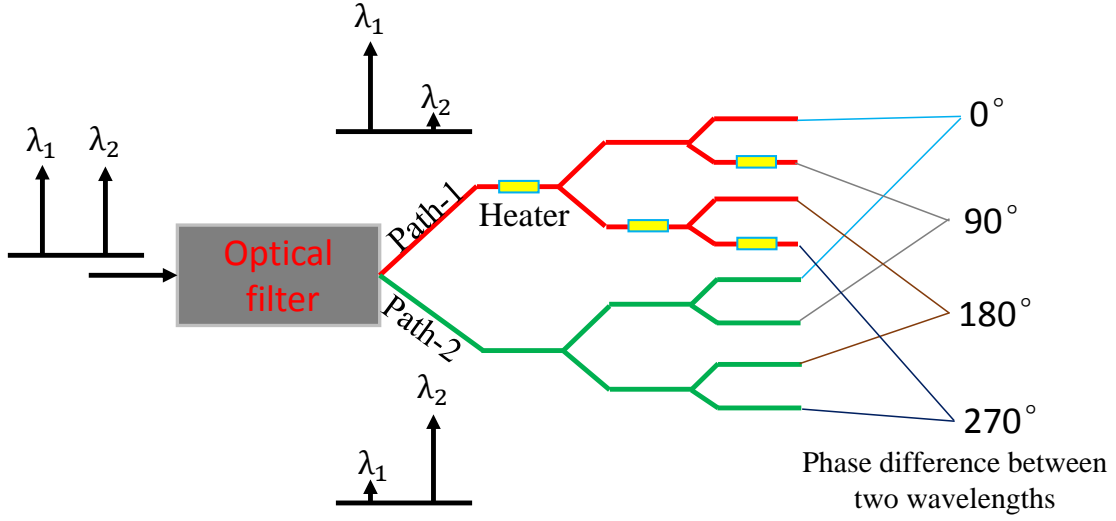


Fig. 3.12 The thermally-tuned optical phased array for OAM generation.

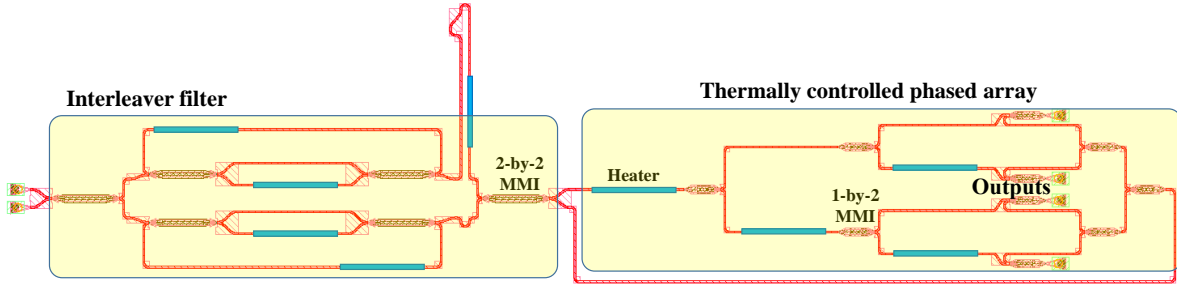


Fig. 3.13 The mask layout of the thermally-tuned optical phased array.

3.3.3 Discussion

In this section, several optical phased arrays are proposed for broadband RF-OAM multiplexing. The chip is fabricated using a silicon photonic technology. For a passive phased array, the expected phase error can be below five degrees, which is reasonable performance and has been proved experimentally [146]. Active designs can eliminate these phase errors by carefully setting the voltage of phase shifters. But such adjustment will introduce extra unstable factors to the system, which requires more effort such as algorithmic control to keep stable. The passive method enables a simpler/lower-cost architecture but supports only three OAM modes. In contract, the active method can easily enlarge the supported quantities of OAM modes and eliminate phase errors in the passive scheme with sacrificing system complexity. They are complementary methods and can be selected according to practical applications. As for the filter type, we can expect a similar conclusion - a passive filter presents a simpler and interruption-less system but it has a narrow bandwidth due to its gradually filtering shape. An interleaver filter can provide a very sharp filter with a bandwidth-extended 'flat-top' response. But its system complexity increases.

In terms of the real implementation including system control and chip fabrication, a completed passive scheme (a passive filter and a phased array) is more technically practical for the first-generation RF-OAM application. Upgraded active design with higher performance and a more complicated architecture will be then considered.

3.4 Chapter Summary

RF-OAM provides new freedom of mode multiplexing, which can definitely extend indoor wireless capacity. This chapter discusses the integrated-photonics-enabled RF-OAM activation using a reconfigurable CAA method. To provide the required phase shift, two ways – optical time delay-based generation and the generation utilizing an optical phased array, are investigated. In the first scheme, a novel single-element-tuned bidirectional ODN is proposed, simulation proved, and experimentally demonstrated. Enabled by an imbalanced power-control, a compact dual-port broadband delay array is achieved with a 20-GHz double-sided bandwidth and a ± 13 -ps continuous tunable delay range. The bidirectional tunable time delay between two outputs is implemented by selecting different phase shift areas. Moreover, to obtain broadband OAM modes, a phased array is needed. A series of integrated phased array designs are proposed - an optical 90° hybrid-based passive phased array and a thermally-controlled phased array. The passive design could support the switch of three OAM modes of $l=0$ and $l=\pm 1$ by changing the optical wavelength. Meanwhile, as a complementary scheme to support a higher-count antenna system and mitigate phase errors from fabrication, the thermally-tuned phased array is proposed. It can provide two types of OAM mode switch – the pure thermal control and the wavelength control. These integrated-photonics-enabled time delay arrays and phased arrays provide new solutions for the applications of RF-OAM mode multiplexing.

**OPTICALLY WAVELENGTH-CONTROLLED
MM-WAVE BEAM STEERING**

As described in **Section 2.3**, the wavelength-tunable 2D beam steering is of many advantages. On the one hand, no active tuning elements at the antenna side are required, which reduces the complexity, the interference, and the installation efforts of antennas. On the other hand, by using the well-established indoor fibre-wireless networks, multiple wavelengths can be delivered from a control center to antennas to tune beam directions. This physical-layer procedure releases the burden of the comprehensive calculation and control of antennas. For a control center, the fast beam steering could be done by using fast tunable or switched laser diodes. My research is mainly focused on photonics-enabled RF phased arrays, in which the integrated optical mm-wave beamformer is especially significant. In this chapter, I will first explain the working principle of the key tunable delay module – looped-back AWG. Then novel on-chip delay networks are reported and discussed. In addition, advanced AWG architecture design is presented as well.

4.1 Looped-back AWG-based beamformer on-chip

First of all, as the most significant element, a looped-back AWG is described in principle in Fig. 4.1. It is composed of a regular AWG and four feedback waveguide paths connecting inputs and outputs. An extra pair of input/output waveguides is selected as the bidirectional in-port and out-port. This architecture is topologically equivalent to two AWGs in series where the AWG acts as both a wavelength multiplexer and a de-multiplexer. Thus it is an almost half-sized and fabrication-tolerant design. Its delay is t_0 with respect to the wavelength of λ_0 , which will go directly to the out-port. It names as the through path. The corresponding feedback paths are set in an increment of Δt . The delay response respecting to the spectrum of the looped-back AWG is also shown (measured time delay at out port) on the right part. Due to AWG's spectrally cyclic characteristic, the time delay response of a looped-back AWG is also cyclic. Within one free spectral region (FSR), each wavelength (from λ_0 to λ_4) is split into a different feedback loop according to the inherent wavelength-division feature of the AWG [149] and experiences an individual time delay (from t'_0 to $t'_0 + 3\Delta t$). However, the inherent large delay difference ($t'_0 - t_0$) between the through-path and the looped-back path causes the spatially-discontinuous beam steering. In practical ODNs, a specially designed optical interface before each output port is necessary for delay calibration. By changing the input wavelength, a step-wise time delay can be obtained.

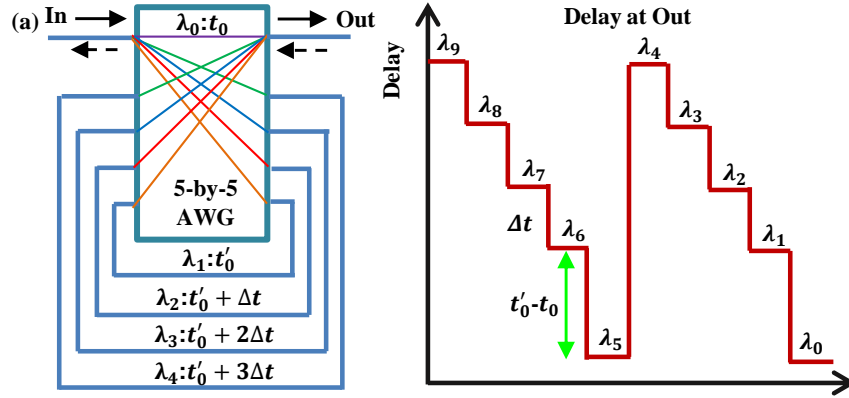


Fig. 4.1 The looped-back AWG

The looped-back AWG is a stepwise tunable time delay module and its time delay resolution (the number of discrete delays) is determined by the number of looped-back paths. Normally, a higher delay resolution means a more flexible beamformer. For realistic applications, it is the ODN (system) that is frequently used, which normally takes a large area on a photonic chip. The size of the designs is becoming more concerned especially in the monolithic integration, which tends to require a much smaller architecture. Therefore, the delay resolution per area on-chip is an essential evaluating factor and it is positively correlated with the performance of an ODN. To obtain a higher time delay resolution per area, two methods are utilized - reducing chip size and increasing delay density. Reducing the chip size especially the size of an AWG will increase the integration scale and system stability. Thus sized-reduced AWGs are first investigated in this section. In general, there are two types of solutions. The first one is selecting a more compact integration technology, and the other one is designing a novel architecture that allows a smaller footprint. They are discussed separately. As to the increase of the delay density, a system-level design is demonstrated.

4.1.1 Device-level design I: SOI-based transmission-type AWG

As described above, a more compact integration technology will help reduce the size of the looped-back-AWG-based delay module. SOI technology is a promising compact integration solution due to its high-density integration, excellent passive performance, high-quality devices (modulators and photodiodes), and low-cost properties. This silicon integration platform leverages the existing complementary metal-oxide-semiconductor (CMOS) ecosystem, including front-end and back-end processes. Furthermore, silicon is a transparent material with wavelengths of $1.3 \mu\text{m}$ and $1.55 \mu\text{m}$ and is therefore particularly compatible with InP lasers and SMF fibres. In this section, the transmission-type AWG in the SOI platform is discussed.

The typical single-mode waveguide:

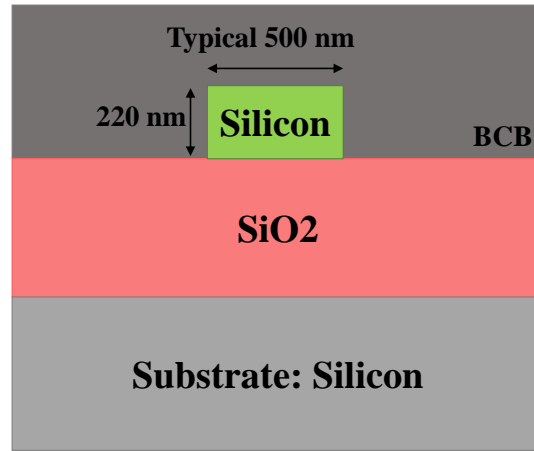


Fig. 4.2 The cross-section of the standard SOI passive waveguide.

Due to the ultra-high index difference between the waveguide core and cladding, a high confinement structure can be implemented with a bending radius being as small as $2\ \mu\text{m}$ [150]. Fig. 4.2 describes the cross-section of the used standard SOI passive waveguide. The top layer is a silicon membrane embedded into the benzocyclobutene (refractive index=1.54), which is the cladding layer. Passive waveguides/architectures are fabricated in the silicon layer. A standard single-mode waveguide has a width of $500\ \text{nm}$ and a thickness of $220\ \text{nm}$. Then a thick SiO_2 layer is used to confine the light in the waveguide (silicon). The bottom layer is the substrate (Silicon). A passive waveguide is fabricated by using EBL and dry etching technologies. Because of the ultrahigh δ and ultras-small cross-section of Si nanowires, the AWG performance (especially the crosstalk) is very sensitive to the size variation of waveguides. A very small thickness variation ($<5\ \text{nm}$) will cause remarkable phase errors. And the accumulated phase error consequently leads to large crosstalk [150]. Thus it is not an easy task to obtain a high-performance AWG.

The mask layout of the AWG:

Fig. 4.3 presents the mask layout of the AWG in SOI platform. This chip is fabricated by the researchers from Sun Yat-sen University, Guangzhou, China. This is a 6-by-6 on-chip transmission-type AWG with an asymmetric design. For each input/output port, a grating coupler (optimized at TE mode) is utilized for the coupling from the chip to a single-mode fibre. In order to reduce the radiation mode activation, a $400\text{-}\mu\text{m}$ taper is introduced to guide the light from $0.5\ \mu\text{m}$ to $12\ \mu\text{m}$. The oriented coupling angle is designed at around 8° . The asymmetric design of the input/output aperture size aims at obtaining a flat-top AWG response [149]. The input aperture size is $4.02\ \mu\text{m}$ and the output is set as $2.52\ \mu\text{m}$. FPR is ~ 110.4 micrometers long with Roland-Circle-shaped configuration, which is widely used in current AWGs [151]. The AWG has a whole size of $\sim 367\ \mu\text{m} \times 540\ \mu\text{m}$. 31 arrayed waveguides are utilized to obtain an accurate image on the output plane.

Measurement results:

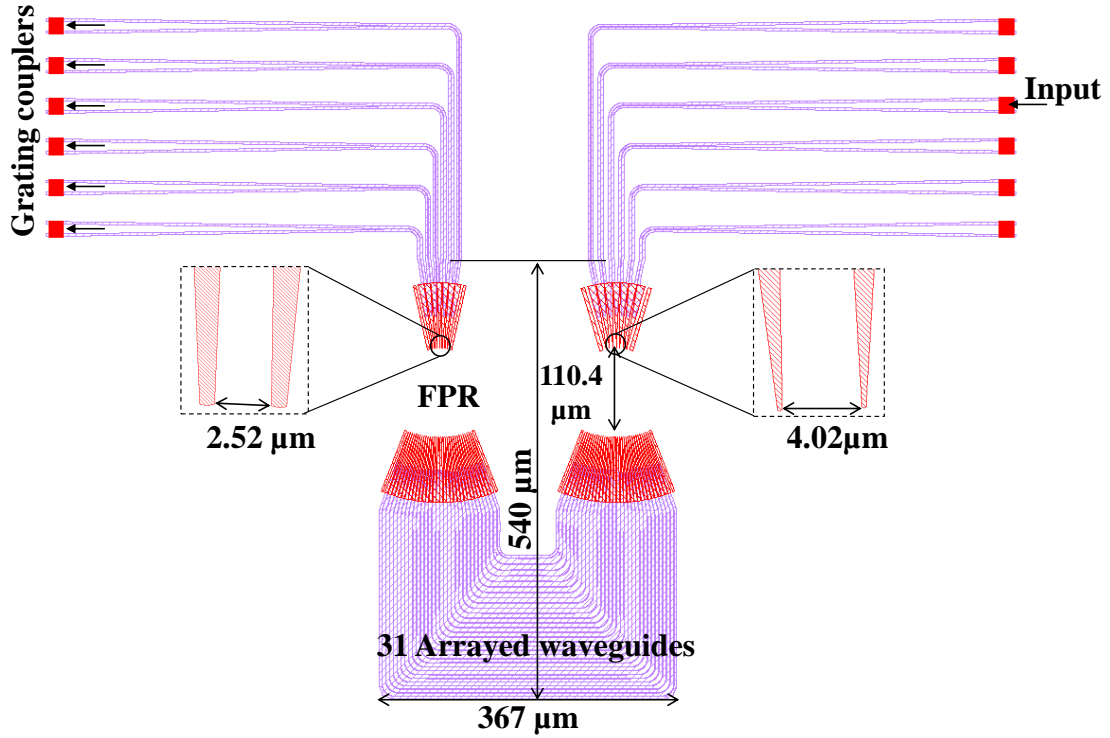


Fig. 4.3 The mask layout of the AWG.

Fig. 4.4 (a) shows the measurement setup. An amplified spontaneous emission light source that covers the whole C-band (1530 nm to 1565 nm) is polarization-filtered by a polarization beam splitter (PBS). The polarization state of the filtered light is further aligned to the TE mode by using a PC and is fed into a chip system including two vertically coupling single-mode fibres and a device under-tested (DUT) (a chip). An optical spectrum analyzer is utilized to measure the frequency response of the AWG. The normalized amplitude response of the transmission-type AWG using 3rd waveguide on the right side as the input port is depicted in Fig. 4.4 (b). The measured power loss is around 2.6 dB (the two highest channels) with an acceptable 2.9-dB power imbalance between the six channels. The measured channel spacing is ~ 3.5 nm. Inter-channel crosstalk is around -13.6 dB for the third channel. The implemented performance is acceptable.

4.1.2 Device-level design II: IMOS-based reflection-type AWG

To reduce the size of AWGs, selecting a more compact integration technology and designing a novel architecture that allows a smaller size, as mentioned above, will help increase the delay resolution per area. Addressing these two aspects in a scheme, a reflection-type AWG (R-AWG) (de)multiplexer in an advanced Indium-phosphide-Membrane-on-Silicon (IMOS) platform is proposed and experimentally demonstrated for a becoming-smaller target. IMOS technology is a quite new photonic integration platform, which enables a much higher density integration

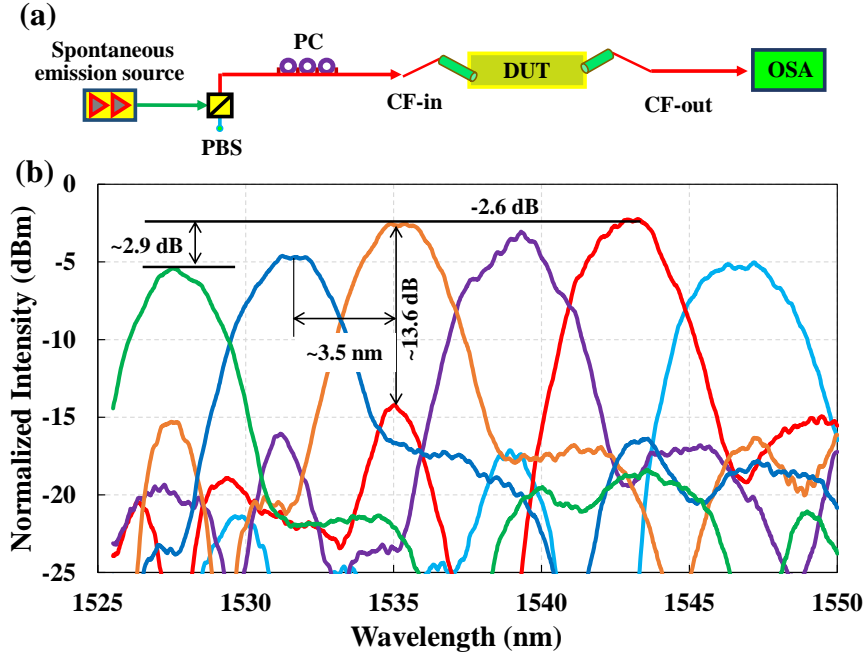


Fig. 4.4 (a) The measurement system; (b) the measured 3rd-port-input AWG response.

than the traditional InP platform. Meanwhile, the idea of using reflection in arrayed waveguides could provide a half-sized AWG in principle. Therefore, this scheme meets the requirements of the technology and the architecture, simultaneously. By using high reflection photonic crystal reflectors (PCRs), the first IMOS R-AWG is implemented. It enables a 35% size-reduced footprint at a cost of 1.1-dB extra loss compared with the traditional transmission-type AWG (T-AWG) that has the same spectral parameters. Compared with silicon-nanowire R-AWGs, an acceptable performance ($680 \mu\text{m} \times 190 \mu\text{m}$, 6.7-dB loss, and 10-dB crosstalk) is obtained. The ultra-small $5.4\text{-by-}0.7 \mu\text{m}^2$ PCR can realize $> 90\%$ reflectivity. Besides, the length reduction of the arrayed waveguide will contribute to minimizing the accumulated phase error caused by the variation-sensitive waveguides.

Technology:

First, I simply introduce the advanced IMOS technology. The detailed information can be found in [152]. With the rising requirements of higher bit-rate data transport and massive computing, the electronic integrated circuits alone cannot support [153]. In order to deal with these challenges, photonic integrated circuits have been created using different materials. A popular one is the SOI technology, which has attracted wide attention and many high-quality photonic devices such as high-speed modulators and photodetectors are implemented [154, 155]. However, due to the indirect bandgap feature of silicon, the integration of optical sources and amplifiers cannot be easily realized on such chips. Several approaches are proposed to solve this problem such as using an off-chip light source, designing III-V lasers/amplifiers/detectors, and coupling light between these devices and silicon waveguides [156–158]. How-

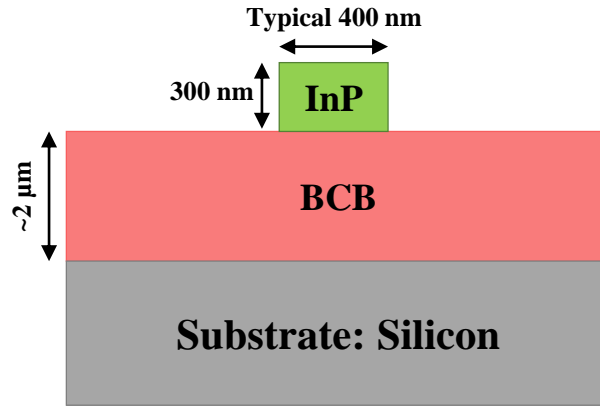


Fig. 4.5 The cross-section of a standard IMOS passive waveguide

ever, in monolithic integration, the size of devices on-chip is required to be much smaller. Thus the coupling between III–V sections and silicon waveguides is inefficient [152]. To solve these problems, the novel IMOS platform has been proposed [152, 159, 160], in which the silicon membrane for waveguide on SOI platforms is replaced by an InP-membrane. Monolithic integration of active and passive components is possible by using a single III–V membrane. This technique can solve many problems such as the coupling between active and passive components and the alignment with respect to the underlying silicon circuits [159]. Moreover, passive devices such as typical single-mode waveguides (width: $0.4 \mu\text{m}$) and waveguide bends (minimum radius: $5 \mu\text{m}$) can realize comparable footprint as the ones in SOI platforms, which support very high-density integration. Currently, many passive and active components in IMOS platform have been demonstrated with a fully acceptable performance [152]. Fig. 4.5 describes the cross-section of a standard IMOS passive waveguide. The top is an InP-based membrane photonic layer, in which both IMOS passive waveguides and active lasers/semiconductor optical amplifiers have been fabricated [159]. A standard single-mode waveguide has a width of 400 nm and a thickness of 300 nm. The divinylsiloxane-bis-benzocyclobutene (DVS-BCB, refractive index=1.5) is used as the adhesive polymer with a thickness of $\sim 2 \mu\text{m}$. The bottom layer is the substrate (Silicon). Passive waveguides are fabricated by using Electron-beam lithography (EBL) and dry etching technologies.

Operational principles:

Fig. 4.6 (a) explains the working principle of the R-AWG. In terms of the layout, a T-AWG is usually symmetrical such as the architecture as shown here. The input light will go through two identical half-layouts. Thus the same function can be achieved by using the half layout and reflectors at the end of each arrayed waveguide as presented in the right part of Fig. 4.6 (a). Because the light in R-AWG passes the same structure twice, which is logically equivalent to a T-AWG. The R-AWG allows a more flexible adjustment of the grating order [149]. Fig. 4.6 (b) shows the schematic configuration of the proposed IMOS-based R-AWG (de)multiplexer. This device is fabricated in one of the IMOS Multi-Project-Wafer (MPW) runs carried out by our

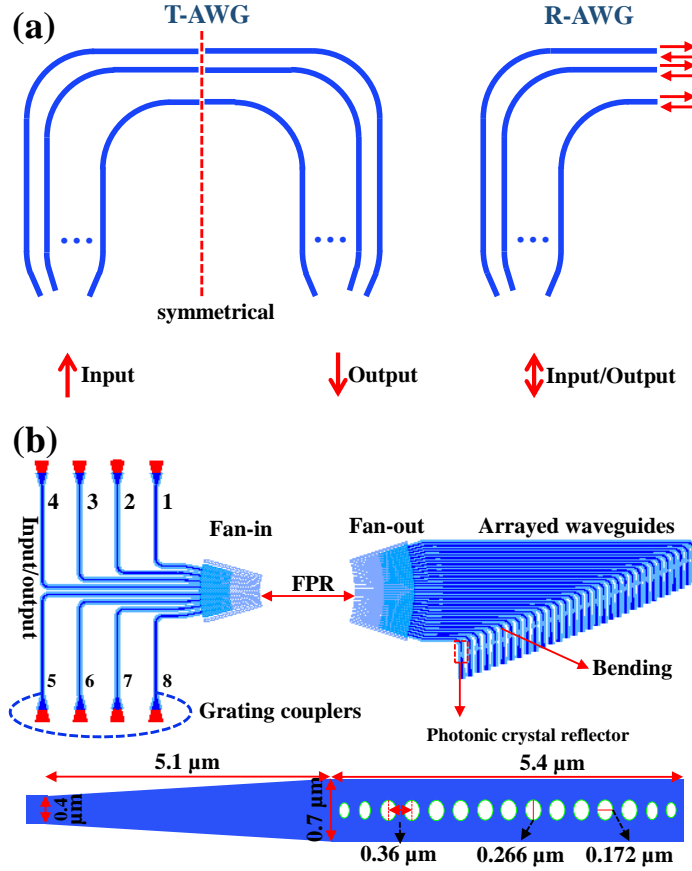


Fig. 4.6 (a) The layout comparison between a T-AWG and a R-AWG; (b) The schematic configuration of the proposed IMOS-based R-AWG (de)multiplexer. FPR: free propagation region.

research department - Institute for Photonic Integration, Eindhoven University of Technology. The R-AWG contains 8 input/output waveguides, in which anyone can be selected as the input port. The vertically-coupled light via a surface grating will be firstly fed into a fan-in area which is composed of a taper array. The fan-in architecture helps increase the power coupling efficiency from a single-mode rectangle waveguide (400-nm width) to a slab waveguide, which is called the free propagation region (FPR). Then the light will be coupled to a fan-out structure followed by a plurality of arrayed waveguides, waveguide bends, and PCRs. Finally, a taper is used to minimize the end reflection of the transmission light. The radius of the bending is 10 μm . In fact, the waveguide bends can be removed and thus it contributes to minimizing the accumulated phase error. Here, the bends are reserved to analyze the performance of PCRs in the comparison in Fig. 4.8 (a).

Reflector:

The key component of realizing an R-AWG is the ultra-small PCR which is a standard building block in IMOS platform. As presented in Fig. 4.6 (b), the size of the PCR is 0.7- μm wide and 5.4- μm long, with 15 deep-etched holes along the central axis. The inter-hole spacing is set at 0.36 μm and the minor and major axis diameters

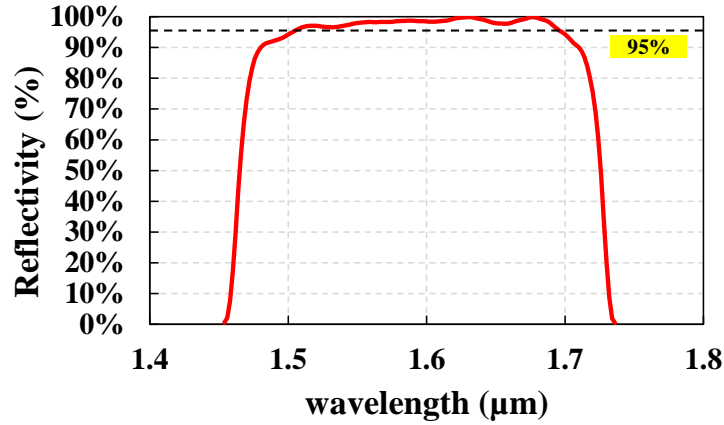


Fig. 4.7 The reflectivity of the reflecting structure (including the photonic crystal reflector, taper and the single-mode waveguide)

of ellipse-shaped holes is $0.266 \mu\text{m}$ and $0.172 \mu\text{m}$, respectively. At each end, the hole is slowly getting smaller in order to reduce the scattering at the interface (from the waveguide to PCR). In our design, the light is coupled into the proposed PCR (width: $0.7 \mu\text{m}$) from a typical single-mode waveguide ($0.4 \mu\text{m}$), thus a simple linear taper is employed in between to suppress radiation modes. The similar PCRs in the IMOS platform have been reported as high reflectivity mirrors for laser cavities [159]. The simulation results using Lumerical three dimensional (3-D) finite-difference time-domain (FDTD) method (mesh accuracy is set as 6) are depicted in Fig. 4.7. The reflectivity can be $> 90\%$ in a broad wavelength range of $>200 \text{ nm}$, especially in the C band (1530 nm - 1565 nm), $> 95\%$ light can be reflected.

Results and discussions:

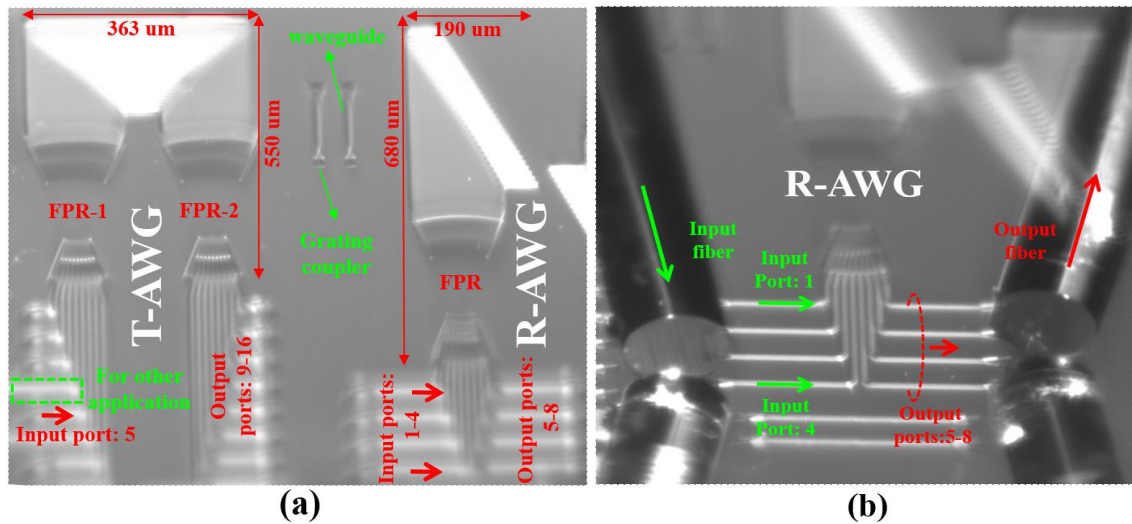


Fig. 4.8 (a) Photo of the fabricated IMOS-based T-AWG and R-AWG (de)multiplexers; (b) Photo of the measurement of the designed R-AWG using vertically-aligned fibres.

To demonstrate the effectiveness of the designed IMOS R-AWG by using PCRs, a set of T-AWG, and R-AWG with the same spectral parameters are fabricated on the same chip. In both designs, end spacing between adjacent input/output waveguides is $3.7\ \mu\text{m}$ and the length of FPR is $130\ \mu\text{m}$. The spacing between fan-out waveguides and the number of arrayed waveguides is $2.5\ \mu\text{m}$ and 32 respectively. In terms of frequency response, the designed central wavelength is set at $1550\ \text{nm}$ with 4-nm channel spacing and a 32-nm FSR. Fig. 4.8 (a) presents the fabricated T-AWG and R-AWG on the InP-membrane. It is obvious that the size of the R-AWG ($129200\ \mu\text{m}^2$) has been reduced compared with $8\text{-by-}8$ T-AWG ($199650\ \mu\text{m}^2$). By halving the FPR area and the length of arrayed waveguides, 35% of the size is reduced. The separate waveguides with a grating coupler on each end (next to the AWGs) are used to calibrate the coupling loss of the grating couplers. In the T-AWG, because the 4^{th} input waveguide is designed for other applications, the 5^{th} input waveguide is selected as the input port in our measurement. While, in the R-AWG, the 1^{st} and 4^{th} input waveguides are input ports. Fig. 4.8 (b) shows the measurement of the R-AWG. The input/output cleaved single-mode fibres are aligned vertically and their coupling angle is about 9.5° . Due to the limitation of the measurement system, only 5^{th} - 8^{th} input/output waveguides are measured according to the two input ports.

Fig. 4.9 (a) shows the measurement setup. An amplified spontaneous emission light source that covers the whole C-band ($1530\ \text{nm}$ to $1565\ \text{nm}$) is polarization-filtered by a PBS. The polarization state of the output light is further aligned to the TE mode by using a PC and is fed into the chip measurement system including two vertically coupling single-mode fibres and the DUT. An optical spectrum analyzer (OSA) is utilized to measure the frequency response of the AWGs. The normalized amplitude response of the T-AWG using 5^{th} waveguide as the input port is depicted in Fig. 4.9 (b). The power loss is $5.6\ \text{dB}$ (including the couple-in/-out loss) with an acceptable 3-dB power imbalance between the central and edge channels as shown in Fig. 4.9 (c). The measured channel spacing ($4\ \text{nm}$) perfectly matches the designed value. While the FSR experiences 1-dB increase from the designed $32\ \text{nm}$ to the fabricated $33\ \text{nm}$. Inter-channel crosstalk is around $-11.4\ \text{dB}$. The size-reduced R-AWG implements the same 4-nm channel spacing, 3-dB output amplitude variation, and 10-dB crosstalk. Only 1.1-dB extra loss is introduced after fabrication. Because the input port number is 4 (5 in T-AWG), there is a wavelength blue shift of 4-nm (one channel spacing) compared to the T-AWG's response. The response is noisier than the relative T-AWG. One possible contribution to the response is the higher-order mode excitation due to the non-vertical sidewalls in the fabricated photonic crystal reflector. When the input port is changed to the first, the cyclic response can be observed as shown in Fig. 4.9 (d). Usually, the power loss increases with the distance increase off the central input waveguide. Here the loss is $9.4\ \text{dB}$ with a 2.8-dB increase. The wavelength blue shift is $12\ \text{nm}$ and the cross talk is $11.4\ \text{dB}$. Other parameters such as the channel spacing ($4\ \text{nm}$), the power uniformity (3

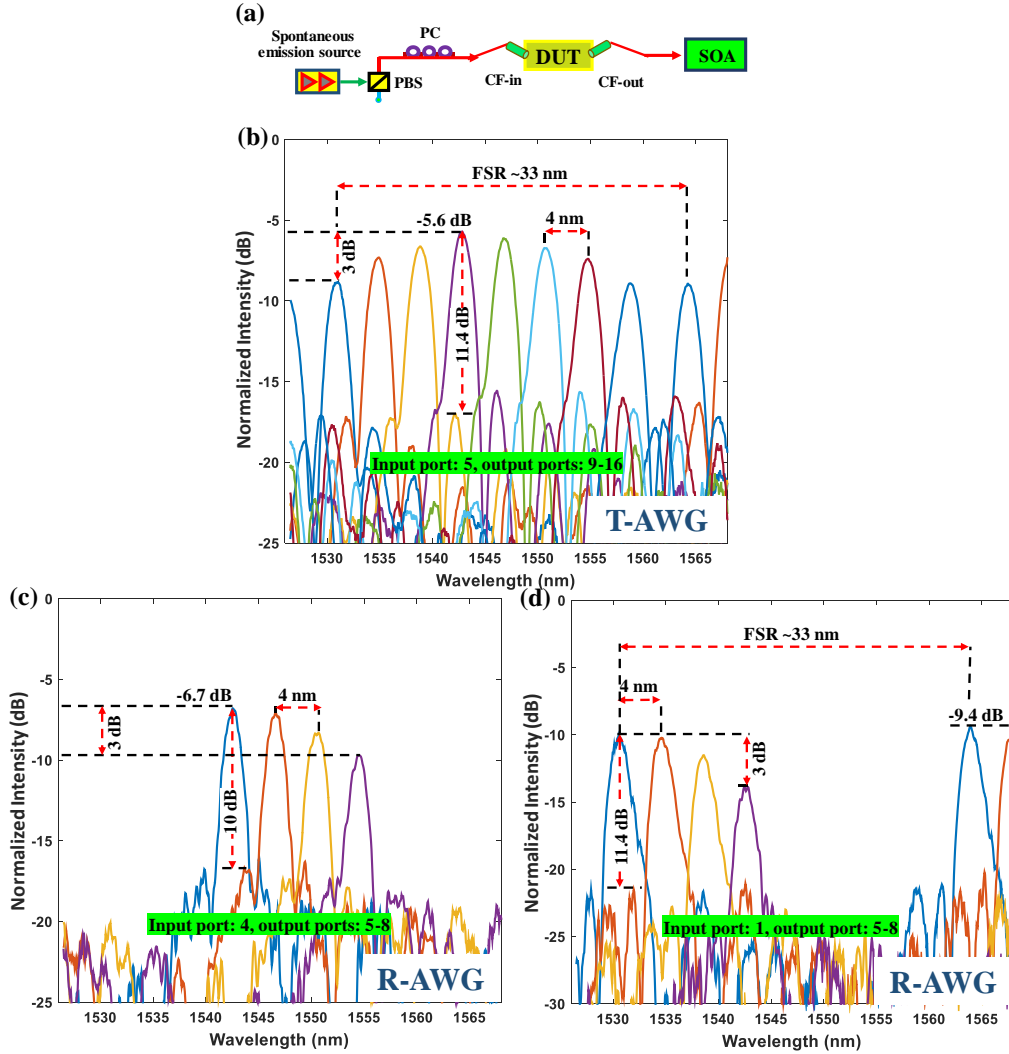


Fig. 4.9 (a) The measurement system; (b) the measured 5th-port-input T-AWG response; (c) the measured 4th-port-input R-AWG response; (d) the measured 1st-port-input R-AWG response.

dB), and the FSR (33 nm) are maintained. The R-AWG proves an effective way of reducing the footprint.

4.1.3 System-level resolution-doubled beamformer I: spatially switch

At the system level, optical delay networks with a higher delay density are demonstrated. Based on a looped-back AWG, a spatially-switched integrated tunable optical mm-wave beamformer is proposed and experimentally demonstrated with a doubled delay resolution. This beamformer is a fully integrated ODN, which does an important exploration on the on-chip system-level. Meanwhile, it provides a new way of doubling the time delay resolution without changing the complex time

delay component. Here, the delay resolution is defined as the number of available discrete time delays. Actually, increasing the delay resolution and thus increasing the number of steered spatial channels is always a problem. Generally speaking, the delay resolution is determined by the number of feedback loops inside a looped-back AWG. Once a looped-back AWG is fabricated completely, the available stepwise time delays cannot be changed anymore. Therefore, this scheme is a significant improvement for the limited discrete-time delays. Enabled by extending the positive delay to its negative counterpart, a specially designed bi-directional ODN (Bi-ODN) can provide a doubled delay resolution. This integrated Bi-ODN is fabricated in a generic InP platform and experimentally characterized. The measured insertion loss (IL) of the 2-by-2 Bi-ODN is <17.5 dB that contains the losses of a looped-back AWG (6.4 dB), a bidirectional hybrid coupler (BHC, 7.94 dB) and a multimode interferometer (MMI, 3 dB). An imbalance of ~ 1 -ps between positive and negative delays has been implemented. This technique also supports single-wavelength tuning for steering multiple beams. Moreover, two passive BHCs are experimentally investigated as well.

Principles:

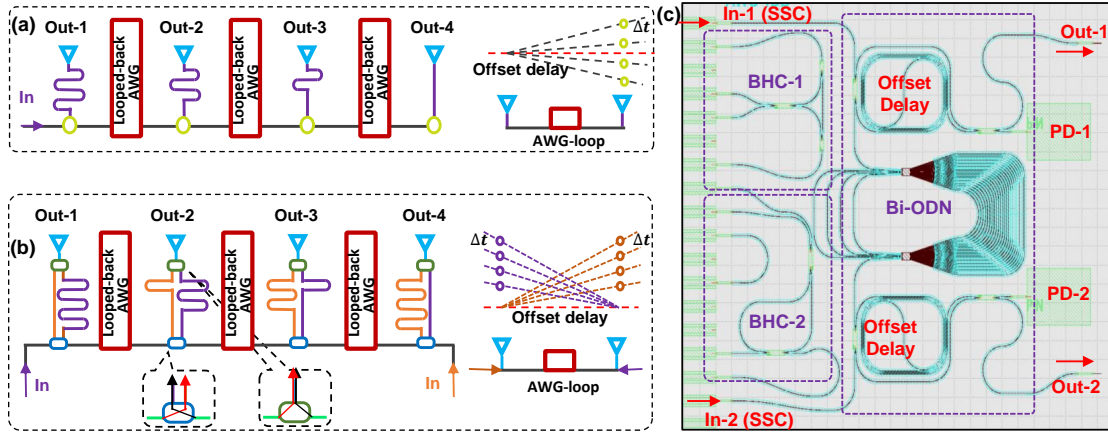


Fig. 4.10 (a) the positive-delayed ODN; (b) the principle of the Bi-ODN; (c) the mask layout of the Bi-ODN.

The principle of Bi-ODN for mm-wave beam steering is schematically shown in Fig. 4.10. Fig. 4.10 (a) presents the regular positive ODN, where the delay of each output is successively increased. This is a 1-by-4 network and each output is put in a separate offset delay line. When a signal is fed into the right port, the delays at the four outputs are disordered due to the mismatched offset delays, which means it only supports a one-way working mode. The right part of Fig. 4.10 (a) describes the delay response of a 1-by-2 ODN. The offset delay of Out-1 is set between t'_0 and $t'_0 + 3\Delta t$, here it is set as $t'_0 + 1.5\Delta t$. Then the relative delays of Out-2 are $0.5\Delta t$, $-0.5\Delta t$, $1.5\Delta t$, and $-1.5\Delta t$, respectively. Thus the delay resolution is 4. In contrast, the resolution-doubled Bi-ODN is shown in Fig. 4.10 (b). A specially designed passive BHC with bidirectional offset delay line structure replaces the regular couplers in Fig. 4.10 (a). The dual-input ODN not only doubles the resolution without changing

the looped-back AWG but also supports simultaneous multi-beam steering using a single wavelength. From the delay response of the 1-by-2 network, the delay resolution grows from N ($N=4$) to $2N$ by extending the negative delays. Here N is the number of discrete delays in a looped-back AWG. When signals are separately fed into the ODN from different inputs at the same time, the ODN's output is the so-called radio multi-beam steering. Fig. 4.10 (c) describes the mask layout of the 1-by-2 Bi-ODN. Two spot-size converters (SSCs) at the chip input are used to enable better lateral fibre coupling. The coupled light is then split into two paths by a BHC, which includes two 2-by-2 MMIs. One path is for PD-1 (Out-1) with an offset delay. The other branch goes into the looped-back AWG and its output is also split via another MMI-based BHC. The output of PD-2 (Out-2) experiences a different offset delay. The symmetrical design allows a bidirectional operation. Out-1 and Out-2 are optical ports reserved for measurement, which can be removed in the final design.

Chip measurement:

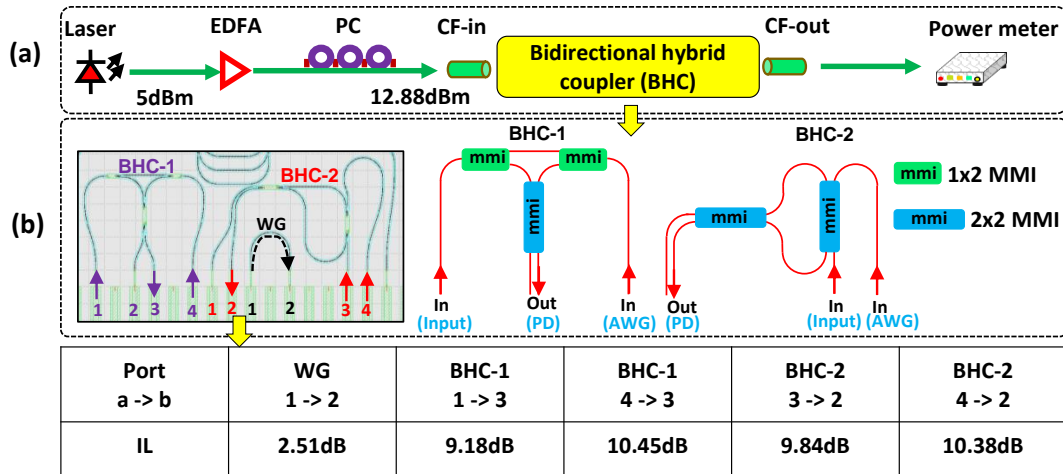


Fig. 4.11 (a) the measurement setup; (b) the mask layout and the simplified logically mapping of the BHCs.

In this part, the measured results are shown and technically analyzed. Fig. 4.11 (a) presents the measurement setup of the two BHCs. 5.00-dBm optical power generated by a laser is first amplified to 12.88 dBm via an Erbium-doped fibre amplifier (EDFA). A PC is employed to enable a pure transverse electric (TE) or transverse magnetic (TM) polarization state in order to get the minimum insertion loss. Then the light is laterally coupled into a waveguide through a cleaved single-mode fibre (CF). The same CF is placed aiming to couple light from the chip to a fibre. Finally, the light is launched into a power meter. The mask layout of the measured structures is shown in Fig. 4.11 (b) and the tested ILs are given in the table at the bottom of Fig. 4.11 (b). First of all, the waveguide (WG) including two SSCs is measured as the reference and its IL is 2.51 dB. Then move to the BHC-1, which is composed of two 1-by-2 MMIs and one 2-by-2 MMI. Since port 2 and 3 are functionally equivalent, we select port 3 as the output. The ILs from 1 to 3 and 4 to 3 is 9.18 dB and 10.45 dB, with a 1.27

dB power difference. Similarly, in the BHC-2 design using two 2-by-2 MMIs, the ILs from 3 to 2 and 4 to 2 are 9.84 dB and 10.38 dB, with a smaller power imbalance ($0.54 \text{ dB} < 1.27 \text{ dB}$). Excluding SSC's IL, the pure losses are 6.67 dB and 7.94 dB for BHC-1, and 7.33 dB and 7.87 dB for BHC-2. Therefore, BHC-2 has better performance. In Fig. 4.11 (b), the right part shows their simplified structures that logically mapped to our designs. This imbalance is mainly caused by the 2-by-2 MMI connected to outputs (PD and Out-1). In fact, in the final design, it can be replaced by 1-by-2 MMI, which provides better bidirectional performance.

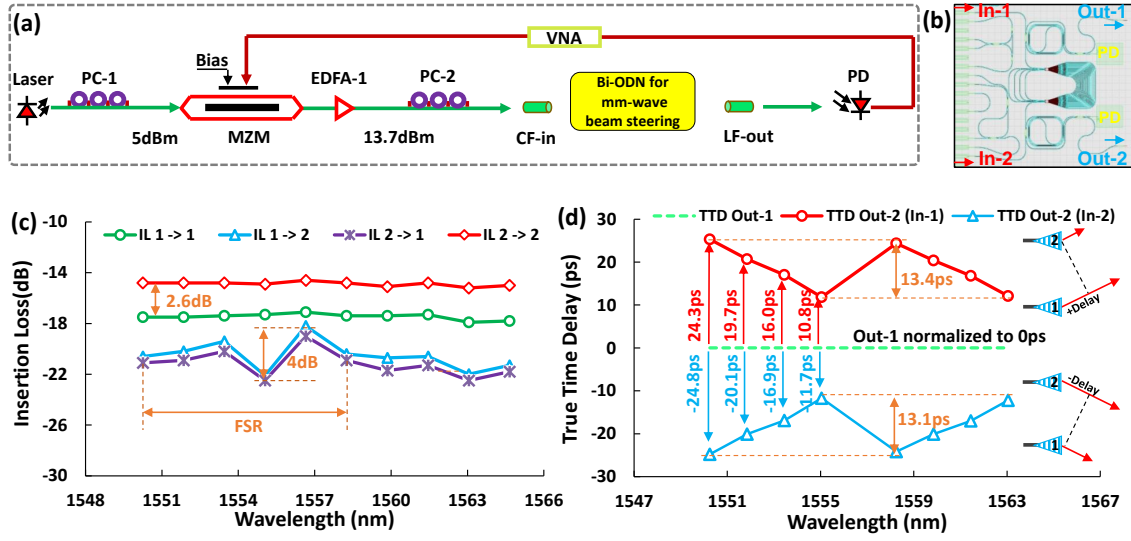


Fig. 4.12 (a) the measurement setup; (b) the mask layout of the Bi-ODN; (c) the measured insertion loss of the ODN; (d) the measured delay response of the Bi-ODN.

The measurement setup of the proposed Bi-ODN is shown in Fig. 4.12 (a). A 5.00-dBm optical carrier is first fed into a 40-GHz Mach-Zehnder modulator (MZM) through PC-1 which yields a power-optimized input. The MZM is modulated by a radio signal generated by a vector network analyzer (VNA) and biased at the quadrature point ($\sim 2.0 \text{ V}$). An EDFA is used to boost the power to 13.70 dBm. PC-2 is employed to align the polarization state. Then the light is laterally coupled into a waveguide through a CF. At the output port, a lensed single-mode fibre (LF) replaces the CF aiming to optimize the coupling. Finally, the light is detected by a PD and fed back to the VNA. The VNA sweeps a large frequency range from 1 GHz to 20 GHz. The spectrum center of the AWG is designed at 1550 nm and its free spectral range is 8 nm (1000 GHz) with a 1.6-nm (200-GHz) channel spacing. The measured loss of the Bi-ODN (shown in Fig. 4.12 (b)) is depicted in Fig. 4.12 (c). From the results, there is a 2.6-dB loss difference between the path from In-1 to Out-2 ($\sim 17.5 \text{ dB}$) and the path from In-2 to Out-2 ($\sim 14.9 \text{ dB}$). This difference is mainly caused by the mismatch of the two offset delay lines. The loss-fluctuation of the cross paths (In-1 \rightarrow Out-2 and In-2 \rightarrow Out-1) is less than 4 dB. Moreover, they have highly-consistent loss curves with a $< 1\text{-dB}$ difference, which is well-matched with our design. Excluding the CF-chip-LF loss (usually $> 5 \text{ dB}$), the measured loss of the through path (In-1

-> Out-1) is 10 dB including the 6-dB loss of an MMI and the 2.25-dB loss of an offset delay waveguide. The cross path (In-1 -> Out-2) experiences a <17-dB loss which is comprised of the losses of MMIs (9 dB), a looped-back AWG (6.4 dB), and waveguides. Fig. 4.12 (d) provides the measured normalized TTD of the ODN. First of all, the delay of Out-1 (for Antenna-1) is normalized to 0 ps. When a signal is fed into the ODN from In-1, the stepwise relative delays between Out-1 and Out-2 (for Antenna-2) are 24.3 ps, 19.7 ps, 16.0 ps, 10.8 ps. The maximum tuning range of Out-2 is 13.4 ps which is a little bit higher than designed (12.5 ps). When changing the input port to In-2, the stepwise relative delays between Out-1 and Out-2 are -24.8 ps, -20.1 ps, -16.9 ps, -11.7 ps. The tuning range is 13.1 ps. The extended positive and negative delays can realize resolution-doubled mm-wave beam steering as shown in Fig. 4.12 (d) (dual-antenna system). An imbalance of ~ 1 ps is experimentally implemented.

4.1.4 System-level resolution-doubled beamformer II: wavelength tuning

It should be pointed out that the design above only shows an initial concept. The completely passive-based wavelength-controlled bidirectional mm-wave beamformer needs to improve further. In the next part, an upgraded design is proposed for the passive target. An entirely wavelength-controlled integrated Bi-ODN for mm-wave beam steering utilizing a specially designed bidirectional optical interface, a looped-back AWG delay line, and an AWG router. By including a positive delay in addition to its negative counterpart, the delay resolution is also doubled. Thanks to the AWG router, a passive single-input Bi-ODN is built, which potentially supports multi-port wavelength-switching of a scaled-up network.

Principles:

In the upgraded Bi-ODN as shown in Fig. 4.13, an AWG router switches the input signal to different output waveguides with respect to its wavelength. And each output channel spectrally covers at least an FSR of the looped-back AWG (>32 nm). Then the wavelengths are split into two groups I) λ_1 to λ_4 for channel-I; II) λ_6 to λ_9 for channel-II. Therefore, the Bi-ODN not only doubles the resolution via the same looped-back AWG but also supports completely wavelength tuning. This means, at the local side, no active tuning element is required and thus there is no controlling information delivery, which allows a more reliable and flexible network.

Chip measurement:

Fig. 4.14 (a) shows the mask layout of the 1-by-2 Bi-ODN. One spot-size converter on-chip is used to optimize the lateral fibre-to-chip coupling. The coupled light is first λ -switched to Path-1 or Path-2 via an AWG router. Then it is split into two paths by a BHC (as shown in Fig. 4.11, which contains two 2-by-2 multimode interferometers (MMIs) and two offset delay waveguides. One path is for the electrical Out-1 (or the optical Out-1) through an offset delay waveguide. The other branch is guided into the looped-back AWG followed by another BHC. The parameters of this AWG are

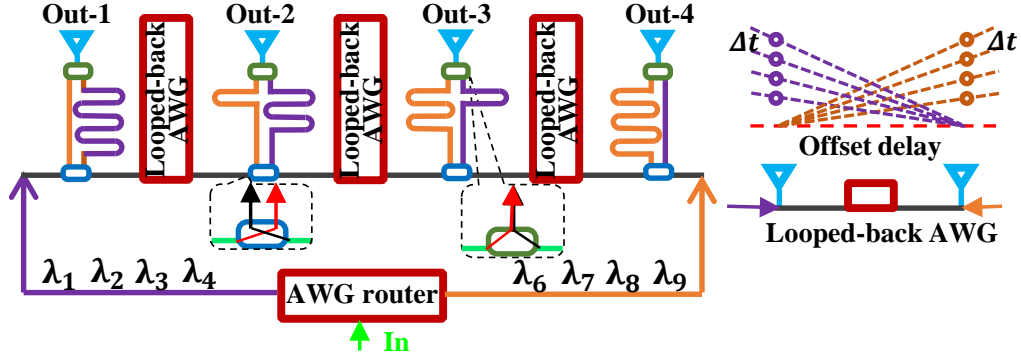
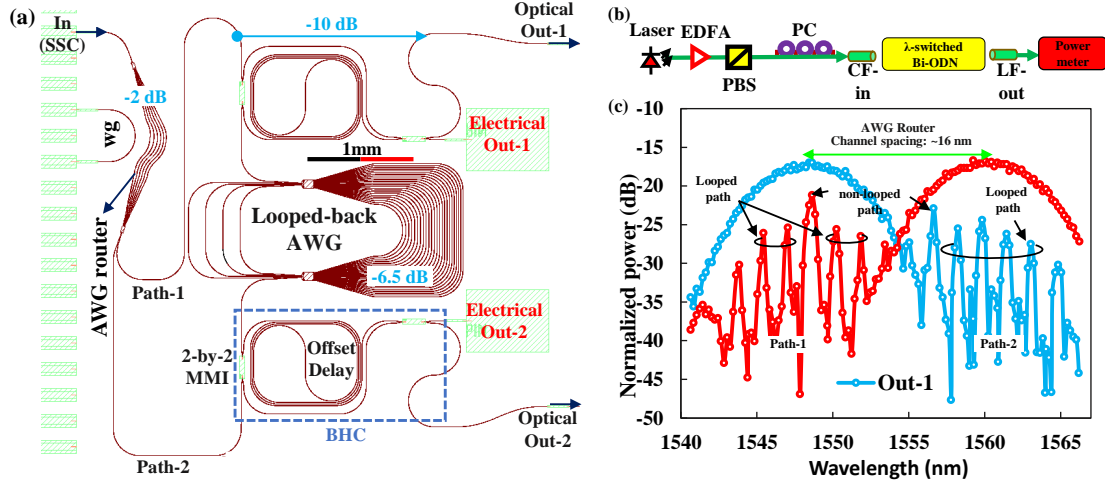


Fig. 4.13 (The principle of the wavelength-tuned Bi-ODN)

Fig. 4.14 (a) The mask layout of the λ -switched Bi-ODN; (b) The measuring system of the structure on chip; (c) The measured amplitude response of two optical outputs.

as follows: 8-nm FSR with 1.6-nm channel spacing. It should be pointed out that the optical outputs will be removed in practical applications. Thus the measured optical loss will be reduced by 3 dB as well. Two electrical outputs are used to convert the optical signal to mm-wave signals. The individual optical waveguide ('wg' in Fig. 4.14 (a)) is used for power normalization. The intensity response is measured using the setup shown in Fig. 4.14 (b) and the results' analysis is depicted in Fig. 4.14 (c). In this section, an optical power loss respecting to the wavelength at two output waveguide ends is measured. First of all, a 5-dBm optical source is amplified to 13 dBm by using an EDFA and then is fed into a PBS. Here, the PBS acts as a polarization state filter to eliminate unwanted signals. Furthermore, a fibre PC is utilized to optimize the optical fibre-to-grating coupling by tuning its polarization state to the TE mode. Then the light is laterally coupled into an SSC through a CF. Because optical outputs are standard single-mode waveguides, not SSCs. A lensed fibre is required to compensate for the relatively higher loss caused by the waveguide-to-fibre mode mismatching. Finally, the light is collected by an optical power meter.

The measured normalized intensity as a function of the wavelength is shown in Fig. 4.14 (c). It is clear that the channel spacing of the proposed AWG router is ~ 16 nm and each channel spectrally covers at least six sub-channels which corresponds to the wavelength range of a looped-back AWG. The central wavelengths of 1543.85 nm, 1545.45 nm, 1547.05 nm, 1548.65 nm, 1550.25 nm, 1551.85 nm are switched to the upper output path (Path-1) of the AWG router, and the measured losses are -30.2 dB, -26.1 dB, -25.4 dB, -21.2 dB, -25.6 dB and -26.5 dB respectively. The losses of the wavelengths switched to Path-2 (1556.65 nm, 1558.25 nm, 1559.85 nm, 1561.45 nm, 1563.05 nm and 1564.65 nm) are -22.9 dB, -25.5 dB, -24.4 dB, -26.2 dB, -27.5 dB and -30.2 dB. The two power-highest wavelengths (1548.65 nm and 1556.65 nm) correspond to non-looped AWGR paths and the others with relatively lower powers are looped-back paths. The measured loss includes the -5.5-dB fibre-to-waveguide coupling loss and the AWG router's filtering loss which can be mitigated by designing a larger port-bandwidth. Excluding the -10-dB loss from Path-1 to Out-1 (including two MMIs and an offset delay waveguide) and the -5.5-dB coupling loss, the insertion loss of the AWG router is only -2 dB. The looped-back AWG has a ~ 6.5 -dB power loss. For the 1-by-2 ODN measurement, the minimum peak-to-null intensity difference is ~ 14.3 dB. One main contributor is the interference impact. Because the looped-back architecture is different from the normal AWG module in [40]. For a given wavelength, the light is first split into different channels (same as non-looped AWG), and the signal loops back and combines again, thus the measured light signal is the addition of vector signals from several neighboring paths (mainly two adjacent paths). When a wavelength located in the overlapping area of adjacent channels' responses, the interference effect becomes stronger. Besides, the polarization state and the wavelength-sweeping resolution may also affect the measurement. However, it should be pointed out that these measured values (e.g. 14.3 dB) are not the channel crosstalk of AWG. The crosstalk is still < -25 dB [40]. This result is used to show the location of each looped sub-channel and its corresponding power loss.

By selecting a certain wavelength, a relative delay can be obtained. The measured time delay response of the proposed Bi-ODN is shown in Fig. 4.15. In Fig. 4.15 (a), a 5-dBm optical carrier is first fed into a 40-GHz MZM via PC-1 which yields a power-optimized input. The MZM is modulated by a radio signal generated by a VNA and is biased at the quadrature point (~ 2.0 V). An EDFA is used to boost optical power to 13 dBm. PBS and PC-2 are employed to align the polarization state as described in Fig. 4.15 (b). Then the light is laterally coupled in and out through a pair of CF and LF. Finally, the light is detected by a photodetector and fed back to the VNA. The VNA sweeps a frequency range from 1 GHz to 10 GHz. Fig. 4.15 (b) provides the measured normalized true-time delay of the Bi-ODN. First of all, the time delay of Out-1 (optical Out-1) is normalized to 0 ps. When the selected wavelength is located in Path-1 of the AWG router, Out-2 has a positive time delay compared to Out-1, and the relative delay is 10.00 ps (1547.05 nm), 16.94 ps (1545.45 nm), 19.69 ps (1551.85 nm), 23.60 ps (1550.25 nm), and -47.48 ps (1548.65 nm), respectively.

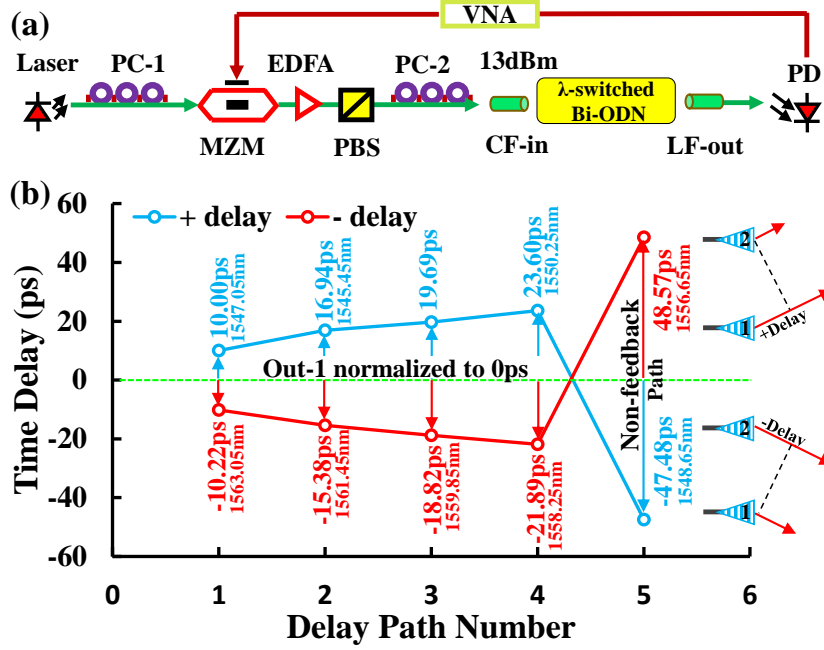


Fig. 4.15 (a) The measuring setup of the time delay response; (b) The measured time delay of the two optical output ports.

The largest opposite delay comes from the non-feedback path where the light goes through the AWG once time. Similarly, by tuning the wavelength to Path-2, the light will firstly go to Out-2 then Out-1 and thus the relative time delay is negative. The accomplished stepwise delays are -10.22 ps (1563.05 nm), -15.38 ps (1561.45 nm), -18.82 ps (1559.85 nm), -21.89 ps (1558.25 nm), and 48.57 ps (1556.65 nm). The designed tuning range is 12.5 ps. The measured values are 13.60 ps and -11.68 ps with errors of 8.80% and 6.56%, respectively. The extended positive and negative delays can realize resolution-doubled mm-wave beam steering as shown in Fig. 4.15 (b) (dual-antenna system).

4.2 38-GHz mm-wave transmission system

After discussing the beamformer on-chip, its performance is evaluated in a 38-GHz mm-wave beam steering system. The beamformer used is the proposed purely wavelength-tunable Bi-ODN, which is a 1-by-2 network allowing a dual-antenna beam steering system.

4.2.1 Experimental setup

As the resolution-doubled concept is already proved on chip-level in **Section 4.1.2**, in this part, the system experiment only tests the positive time delays in order to simplify the system operation. The proof-of-concept 38-GHz mm-wave beam steering system is depicted in Fig. 4.16. A 10-dBm optical carrier is first fed into

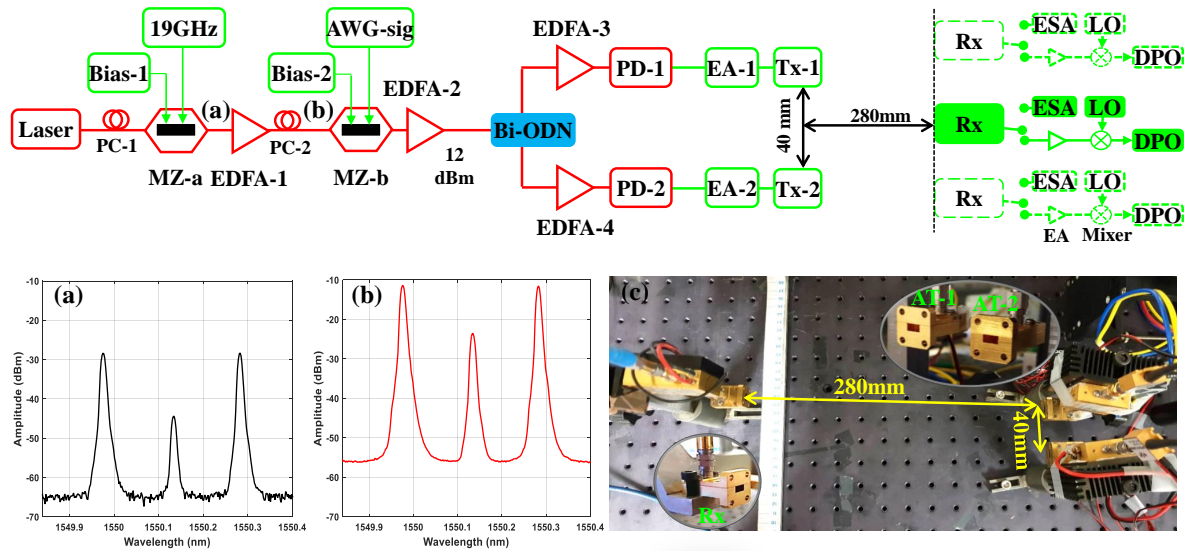


Fig. 4.16 The proof-of-concept experimental setup of the 38-GHz mm-wave fibre-wireless link. (a) The optical spectrum before EDFA-1; (b) The optical spectrum after EDFA-1; (c) photos of the mm-wave wireless link.

a 40-GHz MZM (MZM-a) via PC-1 which yields the power-optimized input. The MZM-a drove by a 19-GHz clock signal is biased at the null point to generate optical carrier suppression. Then the 38-GHz mm-wave carrier can be obtained by beating the two 19-GHz sidebands as shown in Fig. 4.16 (a). After power compensation enabled by EDFA-1 (presented in Fig. 4.16 (b)) and polarization state optimization via PC-2, a 2-GSa/s baud rate QAM-4 signal with a 2-GHz radio carrier is modulated onto the optical domain by a 10G-class MZM. This radio signal is generated by an arbitrary waveform generator (AWG-sig in Fig. 4.16). Before being delivered to the proposed Bi-ODN, the signal is pre-amplified to 12 dBm due to the high chip-loss. Two EDFAs (EDFA-3 and EDFA-4) are employed to make power-balanced mm-wave signals, which are then detected by a pair of photodetectors. The required 38-GHz carrier frequency is obtained after the optical-to-electrical conversion. The converted signals are amplified by two 40-GHz bandpass amplifiers (EA-1 and EA-2, bandwidth 36 GHz - 40 GHz). EA-1 and EA-2 separately connect to two identical 38-GHz aperture antennas (Tx-1 and Tx-2) to spread the data signals wirelessly. The center-to-center distance between Tx-1 and Tx-2 is set at 40 mm and the receiving antenna (Rx) is put at the forward distance of 280 mm. By moving the Rx antenna laterally, the measurement at different lateral distances can be implemented. The power is measured by an electrical spectrum analyzer (ESA, 0-67 GHz) without amplification. For the data transmission part, the received QAM-4 signal is firstly amplified by a 38-GHz amplifier and is down-converted to baseband enabled by a mixer and a 38-GHz local oscillator with 23-dBm output power. Finally, the baseband signal is analyzed by a digital phosphor oscilloscope (DPO) to calculate the error vector magnitude (EVM). Fig. 4.16 (c) presents the 38-GHz mm-wave wireless communication link.

4.2.2 Results and discussions

In this section, the detailed experimental results will be shown and discussed. Firstly, the mm-wave power distribution of each antenna only transmitting 38-GHz single-frequency carrier is measured in order to obtain the spatial coverage of each antenna and the overlapping area in-between in the lateral direction. As shown in Fig. 4.17, the measured main lobe of the antenna spreads around 17 cm and the overlapping area is 14 cm. Thus in mm-wave beam steering measurement, the selected measuring span is 15 cm (From -7.5 cm to 7.5 cm). For each antenna, the average received electrical power in the main lobe is ~ -28.65 dBm.

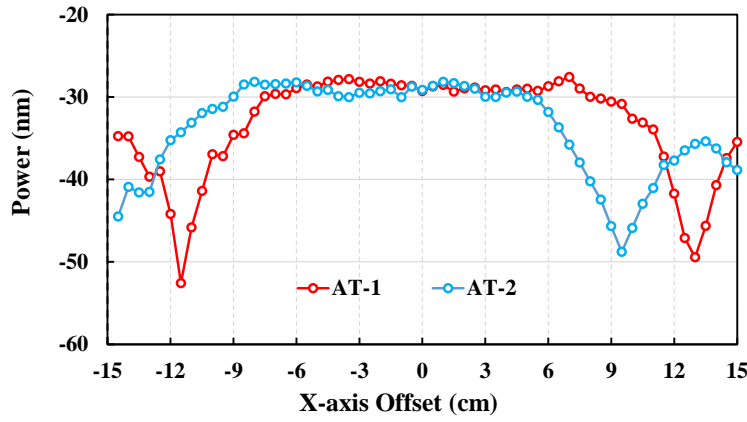


Fig. 4.17 The measured power distribution of the two antennas

For an arrayed antenna wireless system, the basic expression of the array factor can be described as [38]:

$$AF(\theta) = \sum_{n=1}^N I_n \times e^{(-j \times \beta \times n \times d \times \sin \theta)} \quad (4.1)$$

where θ is the arriving angle from Tx to Rx. N is the number of Tx antennas. β is the propagation constant and d is the spacing of Tx antennas. The assumption behind Eq. (1) is that the forward distance is much longer than the element antenna distance d , which results in the same arrival angle (θ). In our wireless link, the forward distance (280 mm) is not that long for the antenna spacing (40 mm). Thus the extra phase compensation is added in the simulation. The engaged aperture antennas can be considered as semi-omnidirectional antennas. In our experiment, the distance of 40 mm between Tx antennas is much larger than one half of the wavelength (3.95 mm). Thus the side lobes of the phased array antennas exist, resulting in more than one peak in the beam profile. It should be pointed out that the side lobes can be easily avoided by using patch antennas.

Fig. 4.18 (a)-(b) present the simulated and measured 38-GHz mm-wave power versus the lateral offset (referred to as 'X-axis offset') curves transmitting a single-frequency signal (38-GHz carrier) without loading QAM-4 signal. In the simulation, the amplitude coefficients are set to 1 and 0.92 respectively according to the practical

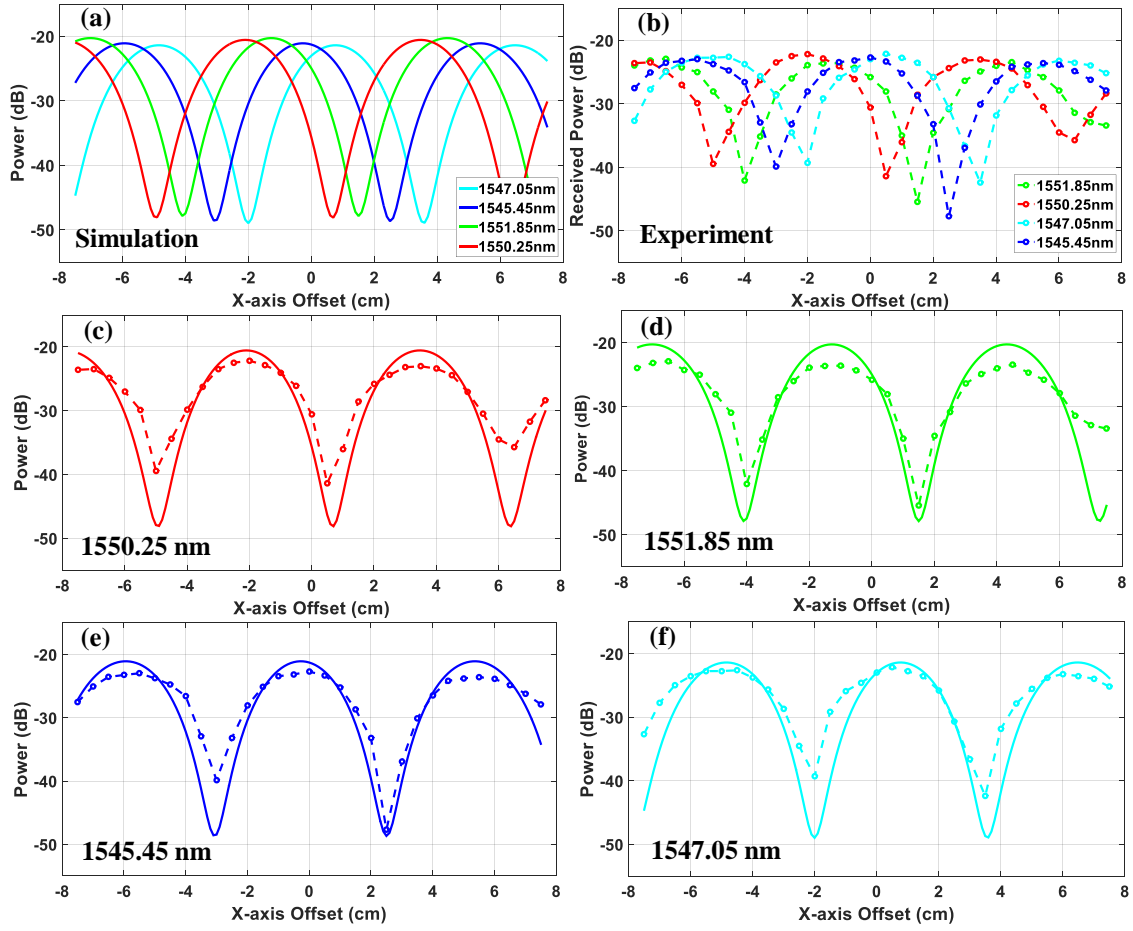


Fig. 4.18 The received power versus x-axis offset curves

radio powers, and the average power is normalized to the received average values in the experiment. The lateral beam distribution spatially shifts when changing the phase difference converted from the time delay of the Bi-ODN. The phase shifts of the 38-GHz mm-wave are 67.57° , 132.54° , and 186.02° respecting the relative delays of 6.94 ps, 9.69 ps, and 13.60ps respectively. The peak moves from right side (x-axis = 0.5 cm) to left side (x-axis = -2 cm). The power difference between peak and null points is around 17 dB and the measured average peak power is -22.50 dBm with 5.85 dB higher than the single antenna case, which perfectly matches the theoretical gain of 6 dB. We can clearly see that the phase shift between the measured red curve (1547.05 nm) and the green one (1550.25 nm) is almost π , which matches well with the simulation result (186.1° shift for 38-GHz mm-wave). Thus a very high accurate mm-wave beam steering system can be experimentally demonstrated by utilizing our designed Bi-ODN. In Fig. 4.18 (c)-(f), the simulated and experimental results are separated to allow a better illustration of the trends. The measured power versus x-axis offset curve (dot) and its simulated counterpart (line) are presented one by

one according to the wavelength. The experimental results match well with the simulated results in terms of peak/null locations and their periodicities.

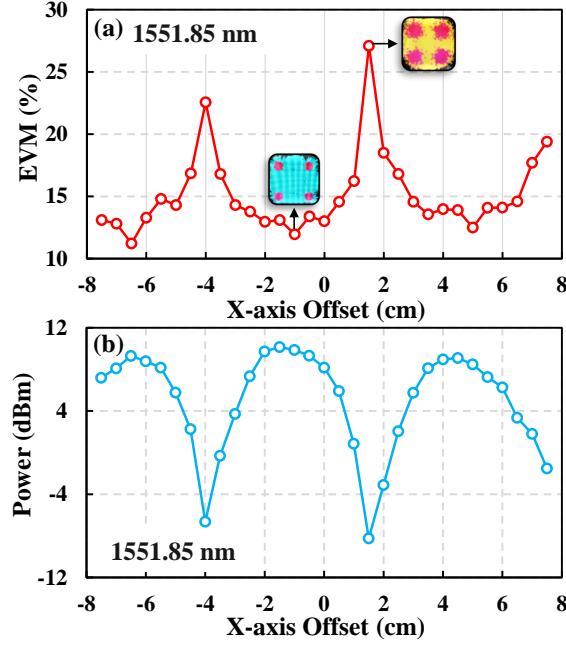


Fig. 4.19 The received power versus x-axis offset curves

Then the data transmission performance is evaluated by loading a QAM-4 signal and introducing an extra electrical pre-amplifier. Measured EVM values of the QAM-4 signal on a 38-GHz mm-wave using 1551.85 nm are shown in Fig. 4.19 (a). Fig. 4.19 (b) is the measured power distribution after amplification. We can clearly see that the EVM curve agrees well with the power curve, indicating that the beam steering induced power variance affects the quality of the received QAM-4 signal enormously. When the mm-wave beam goes directly to the receiving antenna, the EVMs can be 11.9% (x-axis = -1 cm) and the constellations are well converged as shown in the inset photo next to this point. As shown in Fig. 4.19 (b), an around 18-dB power drop at the null point (x-axis = 1.5 cm) compared with the peak value. The received power is -8.2 dBm and the corresponding EVM number is reduced to 27.1%. The data rate of the QAM-4 signal is 4 Gbit/s.

4.3 Chapter summary

In this chapter, the photonics-enabled mm-wave beam steering communication is experimentally implemented, in which the totally integrated looped-back AWG-based beamformer is designed and tested in a 38-GHz mm-wave beam steering system with accurate time delays (error < 10%). Moreover, to achieve compact ODN integration, the size-reduced R-AWG is investigated in a novel platform - IMOS.

These works contribute to the improvement of the indoor mm-wave beam steering on both integrated system-level and component-level.

**LINE-OF-SIGHT BEAM-STEERED INDOOR
OPTICAL WIRELESS COMMUNICATIONS**

IR light wireless communication using steered narrow beams is regarded as an emerging approach for high-speed indoor wireless connectivity. Different from the broadcast-based VLC, the energy-efficiency is significantly improved by using narrow beams and bringing them where and when needed. In addition, the IR laser with a narrow linewidth enables a large modulation bandwidth, which is the basis of a large-capacity transmission. Meanwhile, the aggregate capacity can be extremely extended via frequency re-use in separate, dense tiny communication cells. While there are still many technical problems that need to be solved. In this chapter, new solutions from the levels of the transmission-scheme design and the FoV-extension design will be proposed.

5.1 Crosstalk-mitigation scheme for AWGR-based optical beam steering

To satisfy the exponential bandwidth increase in indoor wireless networks, beam-steered indoor IR light OWC employing narrow pencil beams is of increasing interest. Recently, A. M. J. Koonen et al. propose an easier assembling and less alignment passive-steering scheme - a wavelength-controlled 2D IR beam steering system using a high port-count AWGR [136]. In this scheme, the AWGR module determines the spatial resolution and the spectral efficiency of the beam steering system. Fig. 5.1 (a) shows the schematic architecture of the proposed system. The low-cost intensity modulation/direct detection (IM-DD) is used, which is common in access networks. An electrical signal is modulated onto an optical carrier provided by a tunable laser via an MZM. After power adjustment (by an EDFA), the output fibres of the AWGR are arranged in a 2D fibre array that is located in the focal plane of a lens. The position of a fibre in the focal plane determines the 2D direction in which the corresponding beam is steered through the lens. In other words, the light from each output port of the AWGR covers a certain area at a certain angle. Such a λ -switched system has a simple architecture and more importantly it is a remotely tuning architecture that benefits centralized network management. With the increase of the spatial coverage and transport capacity per channel, an AWGR with a higher port-count and a wider channel bandwidth is of great demand. Considering a limited spectral range (e.g. 35 nm for C band), the port count (or spatial resolution) is compromised with the channel bandwidth. Fig. 5.1 (b) presents a normal AWGR response. It is

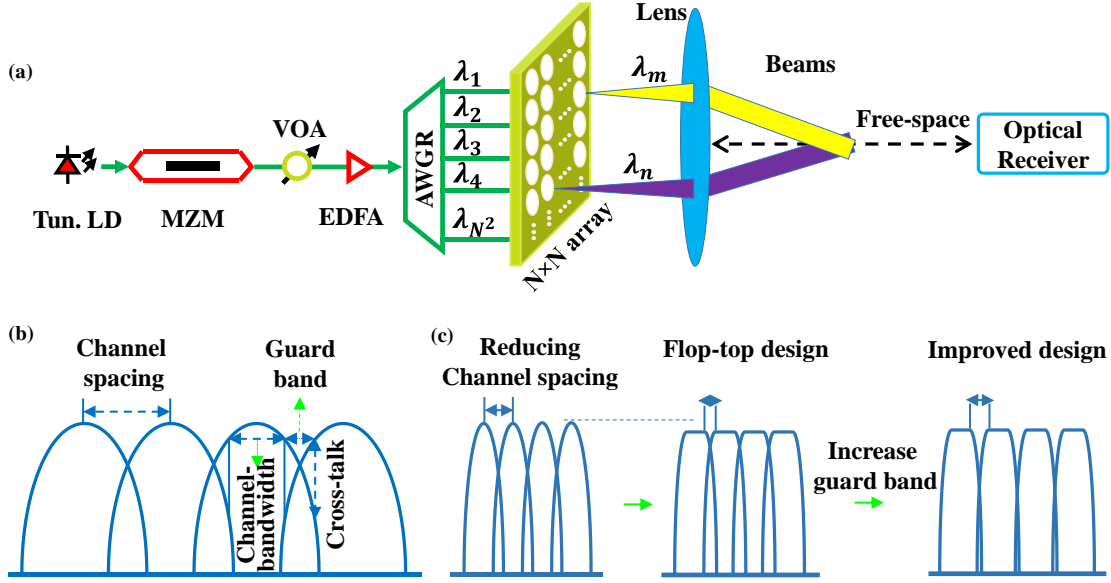


Fig. 5.1 (a) AWGR-based 2-dimensional IR beam steering system; (b) the normal AWGR response; (c) the improved 'Flat-top' design.

clear that the most direct way of increasing the port-count is to reduce the channel spacing. Meanwhile, to avoid the inter-channel crosstalk, a spectral guard band is inserted between adjacent AWGR channels, which inevitably causes the waste of spectral resources. Thus the channel bandwidth is further shrunk. Currently, a general solution is to reduce the AWGR's channel grid (e.g. from a 50-GHz grid to 12.5-GHz grid) and at the same time, to shape the channel response from 'Gaussian' to 'Flat-top' to increase the available channel bandwidth as depicted in Fig. 5.1 (c) [149, 161–163]. The 1-dB bandwidth can be extended from 31% to $> 65\%$ of the channel spacing [149]. Nevertheless, this 'Flat-top' design leads to higher crosstalk which requires a larger guard band between adjacent channels to mitigate, thus the improved spectral efficiency is weakened again. As to the Gaussian-shaped AWG, the guard band for crosstalk reduction cannot be avoided either.

To solve these problems, the following concept is proposed. By creating polarization orthogonality between odd and even channels, a very high crosstalk tolerance between spectrally overlapping AWGR channels can be achieved because two signals with orthogonal polarization states will not beat with each other upon the detection. The signal with the crosstalk on the orthogonal polarization state will not generate a mixing product and direct current (DC) crosstalk can be deleted by an ac-coupled detector. Hence, such overlap means higher spectral efficiency. The technique can also resist the wavelength misalignment between AWGRs and light source outputs. The constraint on high wavelength-stability tunable lasers is also relieved. Moreover, in items of AWGR design, the higher port-count can be implemented simply by reducing the spatial gap between output waveguides on a chip, which allows a low-complexity and high port-count AWGR design.

5.1.1 Operational principles

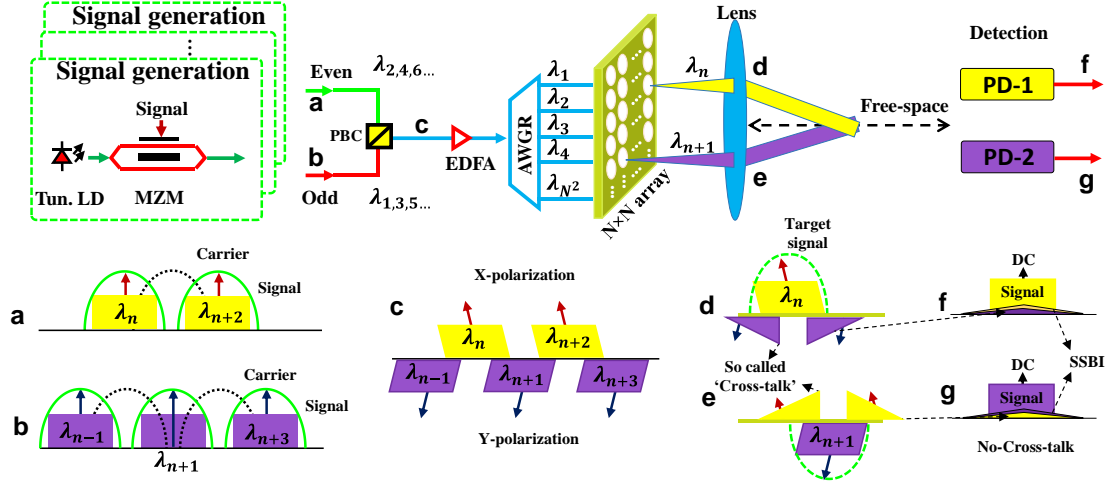


Fig. 5.2 The operating principle of the AWGR-based 2D IR beam steering no-crosstalk transmission scheme; (a) the input optical spectrum of the PBC even channel; (b) the input optical spectrum of PBC odd channel; (c) the combined optical spectrum after PBC; (d)-(e) the optical spectrum of channel n and $n+1$; (f)-(g) The electrical spectra of detected photocurrent. Tun. LD: tunable laser; PBC: polarization beam combiner; PD: photodiode

In traditional IR beam-steered OWC systems, the signal that is fed into the AWGR module is not specially polarization-designed and non-spectrally-overlapped to avoid the inter-channel crosstalk of an AWGR. To increase the spectral efficiency and the port-count of an AWGR, the crosstalk mitigated method is employed. Fig. 5.2 shows the operational principle. A low-cost IM-DD transmission method with a single polarization state is utilized. In this scheme, an input signal is split into two groups - even and odd channels according to the spectral response of the AWGR as shown in Fig. 5.2 (a) and (b). The adjacent channels are set to be spectrally overlapped to show the crosstalk. While the polarization states of even and odd groups are orthogonally set enabled by a polarization beam combiner (PBC). Fig. 5.2 (a)-(c) present the spectra before and after the PBC. Due to the filtering of the AWGR, the signal is λ -split and then steered to different directions by a lens. For the channels of λ_n and λ_{n+1} , they contain the target signal and the so-called optical 'crosstalk' from adjacent channels with the orthogonal polarization state as shown in Fig. 5.2 (d)-(e). Then the received signal is detected by a photodiode and the photocurrent can be presented as (for a unity responsivity detector)

$$I_n = \left| E_{c,n,x} + E_{s,n,x} + \tilde{E}_{c,n+1,y} + \tilde{E}_{s,n+1,y} + \tilde{E}_{c,n-1,y} + \tilde{E}_{s,n-1,y} \right|^2 \quad (5.1)$$

where, $E_{c,n,x}$ and $E_{s,n,x}$ is the carrier and signal in n^{th} (with x-polarization state) channel, respectively. $\tilde{E}_{c,n+1,y}$ and $\tilde{E}_{s,n+1,y}$, $\tilde{E}_{c,n-1,y}$ and $\tilde{E}_{s,n-1,y}$ are the crosstalk

(including carriers and signals with the y-polarization state) between $(n + 1)^{th}$ channel and $(n - 1)^{th}$ channel. Because two orthogonal polarization states do not affect each other upon detection, we have

$$\begin{aligned}
 I_n &= |E_{c,n,x} + E_{s,n,x}|^2 + \left| \tilde{E}_{c,n+1,y} + \tilde{E}_{s,n+1,y} + \tilde{E}_{c,n-1,y} + \tilde{E}_{s,n-1,y} \right|^2 \\
 &= |E_{c,n,x}|^2 + |E_{s,n,x}|^2 + 2\Re\{E_{s,n,x}E_{c,n,x}^*\} \\
 &\quad + \left| \tilde{E}_{c,n+1,y} \right|^2 + \left| \tilde{E}_{s,n+1,y} \right|^2 + 2\Re\{\tilde{E}_{s,n+1,y}\tilde{E}_{c,n+1,y}^*\} \\
 &\quad + \left| \tilde{E}_{c,n-1,y} \right|^2 + \left| \tilde{E}_{s,n-1,y} \right|^2 + 2\Re\{\tilde{E}_{s,n-1,y}\tilde{E}_{c,n-1,y}^*\} \\
 &\quad + 2\Re\{\tilde{E}_{s,n+1,y}\tilde{E}_{c,n-1,y}^*\} + 2\Re\{\tilde{E}_{s,n+1,y}\tilde{E}_{s,n-1,y}^*\} \\
 &\quad + 2\Re\{\tilde{E}_{c,n+1,y}\tilde{E}_{c,n-1,y}^*\} + 2\Re\{\tilde{E}_{c,n+1,y}\tilde{E}_{s,n-1,y}^*\}
 \end{aligned} \tag{5.2}$$

From the final expression of the photocurrent, the first item ($|E_{c,n,x}|^2$) is DC generated by the target carrier, which does not affect the signal. The second item $|E_{s,n,x}|^2$ is the inherent signal-to-signal beat interference (SSBI) generated by the target signal, and the third item $2\Re\{E_{s,n,x}E_{c,n,x}^*\}$ is the recovered signal. The SSBI item is the noise that reduces the signal-to-noise ratio of the system. In a typical IM-DD system, the optical carrier is high-power-biased to suppress itself inherent SSBI [164]. Thus $E_{c,n} \gg E_{s,n,x}$. The other items are crosstalk, in which the DC components of $\left| \tilde{E}_{c,n+1,y} \right|^2$ and $\left| \tilde{E}_{c,n-1,y} \right|^2$ are easy to be removed. Due to the filtering of the AWGR, the cross signal is smaller than the target signal ($E_{s,n,x} > \tilde{E}_{s,n+1,y}$, $E_{s,n,x} > \tilde{E}_{s,n-1,y}$). The cross SSBI items of $\left| \tilde{E}_{s,n+1,y} \right|^2$ and $\left| \tilde{E}_{s,n-1,y} \right|^2$ are also suppressed to a very low level that can be neglected. Similarly, $2\Re\{\tilde{E}_{s,n+1,y}\tilde{E}_{s,n-1,y}^*\}$ can be ignored. $2\Re\{\tilde{E}_{c,n+1,y}\tilde{E}_{c,n-1,y}^*\}$ is located at the frequency of twice channel spacing, which will not impact the baseband signal. In addition, the cross carriers (the central wavelengths) are filtered to a very low power-level compared to the target carrier ($E_{c,n,x} \gg \tilde{E}_{c,n+1,y}$, $E_{c,n,x} \gg \tilde{E}_{c,n-1,y}$, normally >20 dB). The left four beating crosstalk items, are at least 20-dB lower than the target signal component ($2\Re\{\tilde{E}_{s,n,x}\tilde{E}_{c,n,x}^*\}$). Therefore, compared to the traditional IM-DD system, all electrical crosstalk items can be controlled at a very limited level. For λ_{n+1} channel, similar results can be obtained.

5.1.2 Benefits

By introducing the crosstalk-mitigated transmission method into an AWGR-based IR beam-steered OWC system, many improvements and technical advantages can be obtained.

Spectral efficiency improvement:

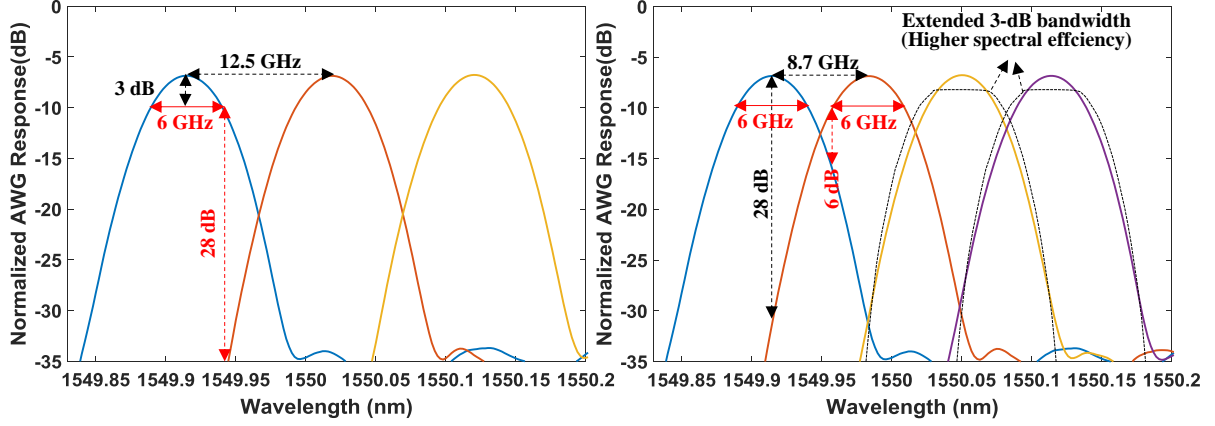


Fig. 5.3 (a) The traditional AWGR response with large spectral guard band; (b) The Guard-band-reduced AWGR response for crosstalk-mitigated IR beam steering system.

Fig. 5.3 (a) presents the spectral response of a commercial AWG [165]. The crosstalk limit is set at -28 dB and the measured 3-dB bandwidth is 6 GHz. From 1549.85 nm to 1550.2 nm, there are three AWG channels with 12.5-GHz channel spacing. Usually, the energy of a signal is mainly in the passband (e.g. 3-dB bandwidth) but there is still spectrum leakage such as the sideband of the signal and the frequency offset of the signal in real communication systems. To reduce crosstalk (here is -28 dB), the spectral guard band requires to be large enough, which inevitably causes a waste of spectral resources. However, by creating polarization orthogonality between odd and even channels, the so-called optical crosstalk can be mitigated in the electrical domain with a largely reduced optical guard band as presented in Fig. 5.3 (b). To suppress the crosstalk components, adjacent cross carriers should be highly suppressed, here a -28-dB suppression ratio is maintained. With the decrease of the inter-channel spectral guard band, optical crosstalk will increase to -6 dB. For the traditional method, this optical crosstalk cannot be canceled but using a large guard band. However, for the proposed orthogonally-designed scheme, crosstalk can be neglected. It is clear that the available 3-dB bandwidth is not reduced when decreasing the channel spacing to 8.7 GHz, which means higher spectral efficiency (an increase from 48% to 69%). Meanwhile, a compact spectrum can support a higher port-count AWGR, which directly increases the spatial resolution of the IR steered OWC system. In Fig. 5.3 (b), an extra port can be added within the same spectral region of 0.45 nm. Besides, the 3-dB bandwidth can be further extended when a flat-top design is utilized, which potentially allows higher spectral efficiency.

A low-complexity solution of the high port-number AWGR:

Fig. 5.4 (a) shows the mask layout of an AWGR. It contains input and output waveguides, free propagation regions (FPRs) and arrayed waveguides [166]. The tapered waveguides are utilized between typical narrow waveguides and an FPR to obtain proper input/output apertures. The input light is firstly fed into a FPR, propagates in this slab waveguide, and couples into arrayed waveguides as shown

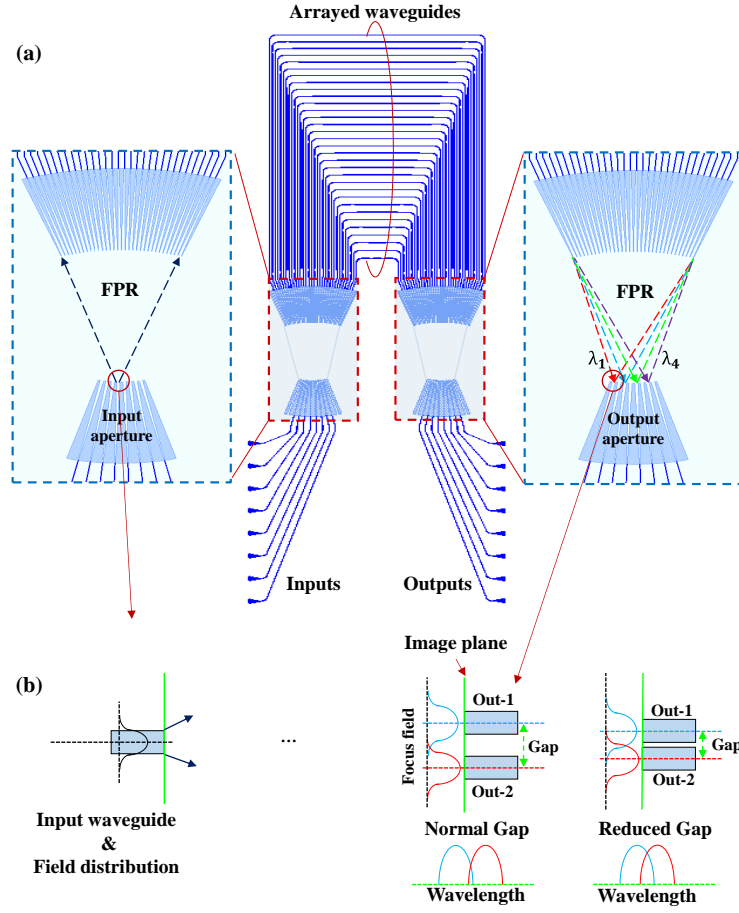


Fig. 5.4 (a) The mask layout of a U-shaped AWG; (b) the connection between the crosstalk and adjacent waveguide spacing. FPR: free propagation region.

in the left inset figure. Through a set of arrayed waveguides with a constant length difference which determines the diffraction order of the grating, the light field distribution at the input aperture will be recovered in the image plane according to the wavelength as described in the right inset figure. As presented in Fig. 5.4 (b), the input mode profile will finally image on the image plane. And because the focusing field has a certain width, the single-wavelength light may couple into adjacent output waveguides (or even farther waveguides) when the gap is not large enough, which causes spectral crosstalk. Thus the gap in current AWGRs cannot be too small to move closer.

Generally speaking, a higher port-count AWGR has many requirements such as a larger FPR, more arrayed waveguides, a higher diffraction order, and so on [149]. So using a widely proved AWGR design (layout and parameters) can reduce complexity and improve reliability. In AWGR design, reducing the spatial distance between input/output waveguides on the image plane is a direct way to increase port-count. Fortunately, for the proposed method, higher optical crosstalk is not a problem anymore. Although the same AWGR layout is used, the port number can be further

increased by reducing the gap between I/O waveguides. Thus well-established AWGR designs can be still used for adding more I/O ports, without causing extra designing and fabricating problems. This technique provides a low-complexity solution of the high port-count AWGR.

Wavelength misalignment:

The wavelength misalignment between an AWGR and a laser is an important issue that may affect system performance. It is caused by many reasons such as the laser wavelength shift, the AWGR's thermally-caused spectral-shift and the mismatch due to fabrication error. The frequency mismatch can be up to several GHz [165] (e.g. Kyla AWG/25GHz, the channel center offset 1.25 GHz and thermal offset ~ 6.25 GHz). For a large channel spacing (e.g. 100 GHz or 200 GHz), the impact is very limited. But when the channel spacing becomes smaller (e.g. 25 GHz or 50 GHz), the performance will be sensitive to such wavelength mismatch. The proposed crosstalk-mitigation is a promising method for solving this problem.

5.1.3 Experimental setup

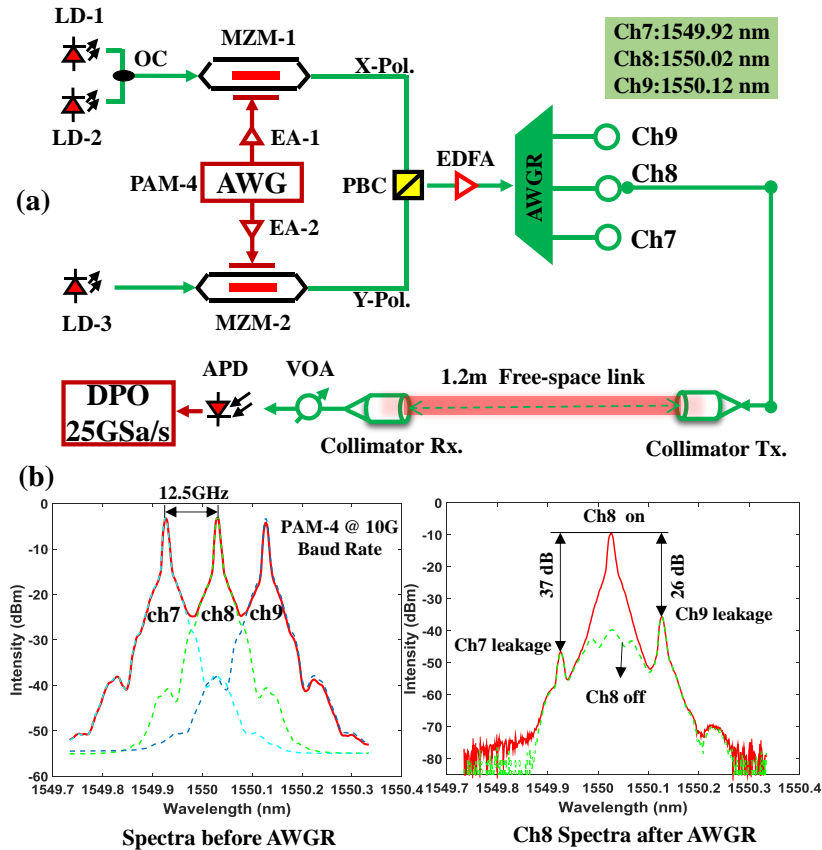


Fig. 5.5 (a) Experimental setup; (b) spectra before and after AWGR. LD: tunable laser; MZM: Mach-Zehnder modulator; AWG: arbitrary waveform generator; EA: electrical amplifier; OC: optical coupler; PBC: polarization beam combiner; X/Y-Pol.; X/Y-polarization; PC: polarization controller; VOA: variable optical attenuator.

Fig. 5.5 (a) shows the schematic setup. For the experimental demonstration of the proposed scheme, a 4-level pulse amplitude modulation (PAM-4) signal is used. Three adjacent AWGR channels (1549.92 nm, 1550.02 nm, and 1550.12nm) named Ch7 to Ch9 are utilized, in which Ch8 will be discussed in detail. For the two side channels, two individual tunable lasers (LD-1 and LD-2) are combined through an optical coupler (OC) and then are fed into MZM-1 driven by a PAM-4 signal. The central channel utilizes a third LD (LD-3) and a second MZM (MZM-2) to de-correlate adjacent signals. The PAM-4 signal is generated by an arbitrary waveform generator (AWGe) running at 10 GSa/s, and amplified by an electrical amplifier (EA). The double-sideband main lobe bandwidth and the data rate is 20 GHz and 20 Gbit/s, respectively. The modulated signal is λ -switched to two input ports of a PBC. And they carry odd and even channels of the AWGR. The combined signal is amplified by an EDFA. Then the specially designed signal is split into different channels and sent to a 1.2-m free-space link (~ 2.5 -dB loss) via a collimator. The receiver consists of a collimator followed by a commercial avalanche photodiode (APD, DSC-R402). A variable optical attenuator (VOA) is introduced only for performance measurement. It can be removed in real applications. The detected signal is sampled by a digital phosphor oscilloscope (DPO) at a sampling rate of 25 GSa/s. Fig. 5.5 (b) shows the optical spectra before and after the AWGR. Ch8 is the target channel with a channel-spacing of 12.5 GHz. The spectra of Ch8 after AWGR show the signal and the crosstalk strength by switching the LD on and off. The strength of carrier leakage is -26.3 dB (Ch9) and -37.0 dB (Ch7), respectively. This is mainly caused by the spectral response of the AWGR as shown in Fig. 5.6 (a).

5.1.4 Experimental results and discussions

A Gaussian-shaped commercial AWGR is used to evaluate the effectiveness of our crosstalk-mitigated transmission scheme as shown in Fig. 5.6 (a). The AWGR has 12.5-GHz channel spacing with a 6.7-dB loss. Three channels are selected in this experiment, and the used optical carrier is set at the center of each channel. For two adjacent carriers, the measured crosstalk into Ch8 is -36.4 dB (from Ch7) and -27.3 dB (from Ch9), respectively, which is well-matched to the crosstalk in Fig. 5.6 (b). Then we fix the wavelengths and 10-GBaud/s modulation baud rate in our measurement. By changing received optical power, the bit error rate (BER) versus received power curves are measured to evaluate the system performance. To discuss the relationship between crosstalk and the polarization state, an OC is employed as a combiner before AWGR. An extra PC is introduced to shift the relative polarization state to the same or the orthogonal state. The results are shown in Fig. 5.6 (b). The crosstalk is rather high when adjacent channels have the same polarization state, which is much higher than that has an orthogonal state. There is an apparent error flow in the curve with a high BER level ($7 \times 10^{-2} - 2 \times 10^{-2}$). For the orthogonal state, crosstalk is largely reduced and thus BER is improved to $\sim 5 \times 10^{-4}$, which allows a 20-Gbit/s data transmission. This proves that an orthogonal polarization state can significantly mitigate crosstalk. But an OC cannot enable the stable crosstalk mitigation due to its

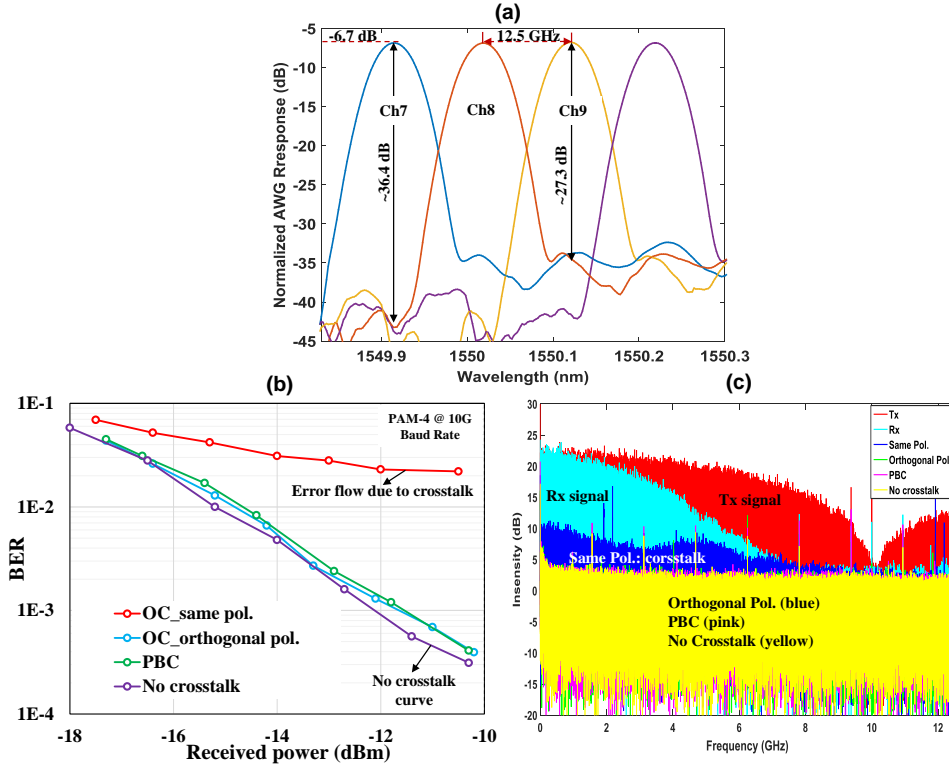


Fig. 5.6 (a) The AWGR response used in this experiment; (b) the measured BER versus received power curves with and without crosstalk mitigation; (c) the electrical spectra under each condition. BER: bit error rate; Tx signal: transmitted signal; Rx signal: received signal. pol.: polarization.

polarization-sensitivity to external interference. A PBC is used in our scheme, and its performance is measured as well. From the results, using a PBC has a very close BER performance to that using an OC in the orthogonal condition. Moreover, we also compare the crosstalk mitigation method with that without crosstalk (turn off Ch7 and Ch9). A very limited BER decrease is obtained, which means the vast majority of crosstalk is mitigated. To further validate the effectiveness of this method, more intuitive pieces of evidence (received electrical spectra) are presented in Fig. 5.6 (c). The red one is our transmitted PAM-4 signal, and after the transmission, the received signal (cyan) is filtered mainly by the AWGR. When turning off Ch8, a very high crosstalk component (blue) can be obtained, leading to the performance drop. However, after the crosstalk mitigation, the crosstalk component is only a little bit higher than the no crosstalk case.

Different modulation rates are also explored as shown in Fig. 5.7. 10 GBaud/s, 8 GBaud/s, and 6 GBaud/s is measured separately. The BER performance of a PBC-based system improves along with the decrease of baud rate, obtaining 3-dB (from 10 GBaud/s to 8 GBaud/s) and 2.2-dB (from 8 GBaud/s to 6 GBaud/s) receiver responsivity improvement at the BER level of 1×10^{-3} , respectively. This improvement is mainly due to the less AWGR filtering, which allows less signal distortion. In contrast, the improvement without crosstalk mitigation is very limited.

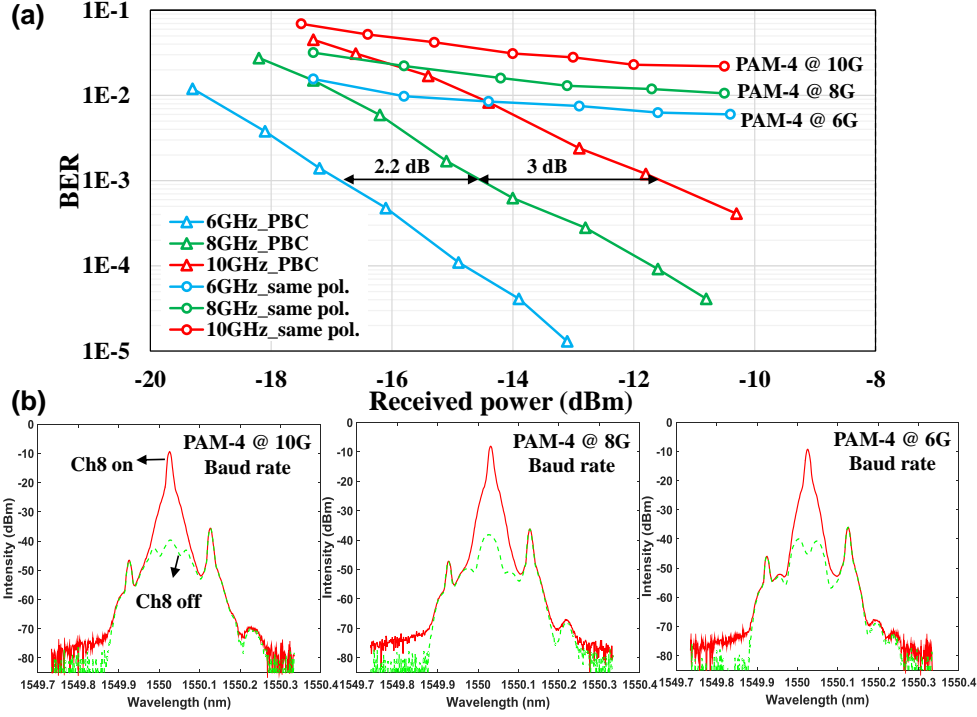


Fig. 5.7 (a) The measured BER performance using 10 GBaud/s, 8 GBaud/s, and 6 GBaud/s, respectively; (b) the measured spectra after AWGR with Ch8 on and off, respectively.

The performance improvement in cases with the crosstalk mitigation is much faster than that without mitigation when signal bandwidth is reduced. Fig. 5.7 (b) depicts the optical spectra under Ch8-on/-off cases using different bandwidths. For a 10-GBaud/s PAM-4 signal, the crosstalk comes from both the main lobe and the first side lobe of two adjacent PAM-4 signals. The crosstalk of an 8-GBaud/s signal is mainly caused by the two first side lobes. While the source of crosstalk in a 6-GBaud/s system is the first and second side lobes.

Two 4.4-GHz electrical filters are introduced before electrical amplifiers to analyze the influence of side lobes of a PAM-4 signal. As shown in Fig. 5.8 (c), the insets are the transmitted electrical spectra with and without a filter. After filtering, the side lobes of the PAM-4 signal are significantly reduced but the main lobe has limited impact. For each condition, the same and orthogonal polarization state setting is measured, respectively as shown in Fig. 5.8 (a). When a filter is applied, the BER performance without crosstalk mitigation is improved from $\sim 6 \times 10^{-3}$ to $\sim 3 \times 10^{-4}$ at a -11-dBm power level. In contrast, the performance with crosstalk mitigation has a responsivity decrease of 0.1 dB, which is caused by the impact of slightly filtering. Fig. 5.8 (b) describes the optical spectra with and without the filter. ~ 9.7 -dB crosstalk drop is achieved due to the filtering. The detailed electrical spectra are presented in Fig. 5.8 (c). It is clear that the filter reduces some crosstalk. However, the residual crosstalk still apparently reduces the transmission performance compared with the

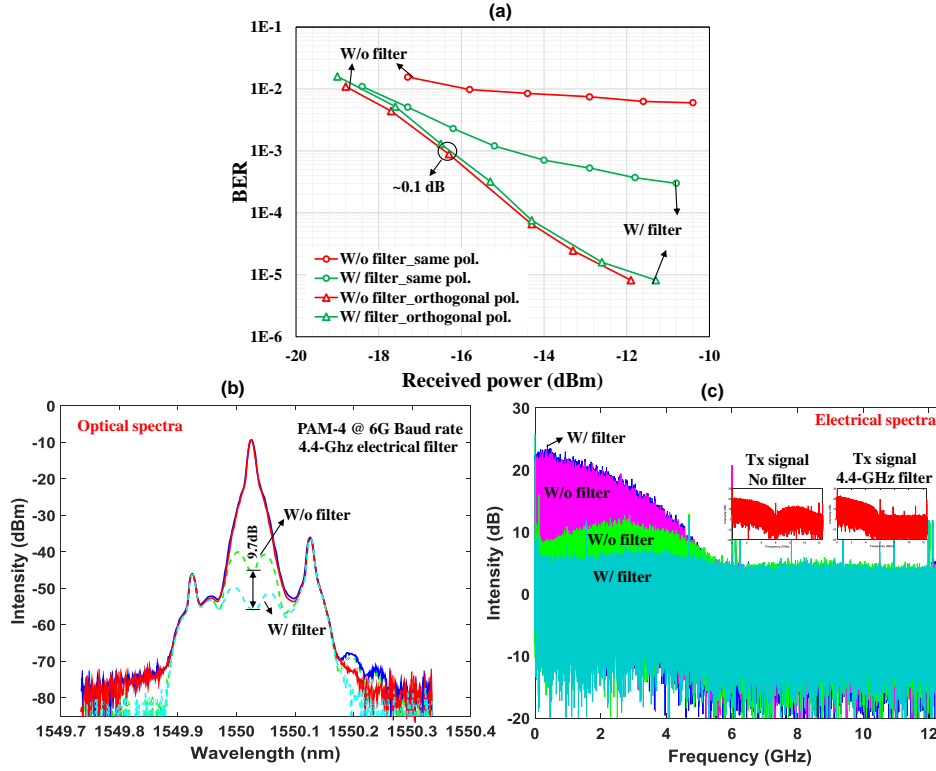


Fig. 5.8 (a) The measured BER performance with (W/) and without (W/o) filter; (b) the measured optical spectra of Ch8 with and without filter; (c) the electrical spectra with and without filter.

proposed crosstalk mitigation method, especially in the high signal-to-noise region (high received power).

5.1.5 Conclusion

Current AWGR-based OWC systems have a low spectral efficiency, which limits the number of users. This dissertation proposes to create polarization orthogonality between adjacent AWGR channels to produce a very high crosstalk tolerance. As two signals with orthogonal polarization states will not beat with each other in a photodiode. The optical crosstalk on the orthogonal polarization state will not generate a mixed beat note after detection and thus crosstalk in the electrical domain can be largely mitigated. By reducing the spectral guard band or even setting spectral overlap, such a tradeoff between a higher port number and a large channel bandwidth of an AWGR is broken. Moreover, the port number can be increased by simply shortening the spatial gap between adjacent output waveguides on a chip. The proposed method can also tolerate the wavelength misalignment between an AWGR and a laser, which relaxes the pressure of designing low crosstalk AWGRs and high wavelength stable lasers. A 20-Gbit/s data rate OWC system using PAM-4 format has been experimentally demonstrated over a 1.2-m free-space link. Experimental results show that our proposed scheme can significantly reduce inter-channel

crosstalk. This method not only can be used in our AWG-based beam-steered OWC system but also can be applied in traditional WDM access networks.

5.2 2D beam steerer on-chip using high port-count AWGR

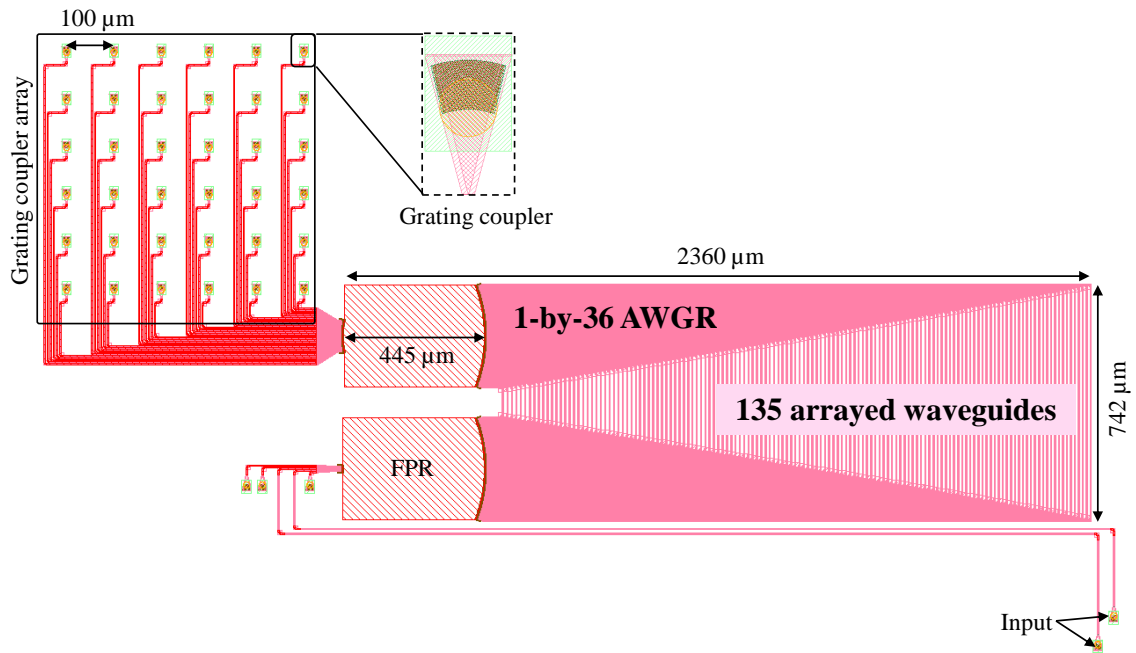


Fig. 5.9 The on-chip AWGR-based beam steerer.

As mentioned above, a 2D beam steerer using a high port-count AWGR and a fibre array followed by a lens can realize a remotely-controlled passive optical beam steering system. But so far, such a system is based on bulk-components, especially the rectangular fibre array. On the one hand, this will be sensitive to vibration, which may change the physical axis. The position change will further impact the coverage of each beam, thus the system performance may not be maintained. On the other hand, the beam steerer or transmitter is still large. A more compact architecture is of demand for practical applications. Integrated photonic technology is introduced to implement an on-chip beam steerer.

Fig. 5.9 presents the mask layout of the on-chip AWGR-based beam steerer in the SOI platform. This is a collaboration project between Eindhoven University of Technology (TU/e), The Netherlands, and Ghent University (UGent), Belgium. The design is fabricated using the IMEC Multi-project wafer (MPW) run, in which we (from TU/e) propose the idea, lead the system and mask layout design, and finalize the verification of the beam steering system. The researchers from UGent provide the large port-count AWGR modules in the IMEC platform. This on-chip

system contains a 5-by-36 AWGR and a 6-by-6 rectangular grating coupler array. Two central AWGR ports are selected as the inputs of the beam steerer. A standard grating coupler building block in IMEC platform is used for light couple-in/-out. Due to the large port-count (36), the AWGR is also large with a length of $\sim 2360 \mu\text{m}$, a width of $\sim 742 \mu\text{m}$, and an FPR length of $\sim 445 \mu\text{m}$. Meanwhile, 136 arrayed waveguides are utilized to obtain an accurate image on the output plane and to reduce power loss. The outputs of the AWGR connect to a 36-element grating array, where each element is a focusing grating coupler optimized at the TE mode. The spacing in between is $100 \mu\text{m}$. The light is radiated to free space with a certain oriented angle from the perpendicular direction.

Because the output is originally designed for the coupling from grating to single-mode fibre, the suggested mode field and coupling efficiency need to be re-evaluated. Fig. 5.10 shows the simulated far-field distribution @1550 nm of the grating coupler using the Lumerical FDTD solution with a mesh accuracy of 5. The oriented angle is at around 8° . Then the radiated light is steered to different directions via a lens.

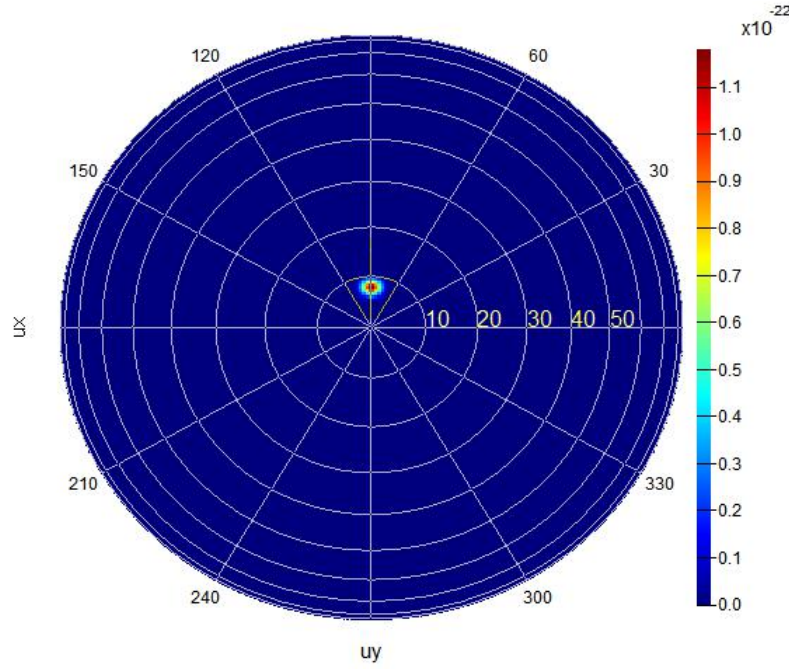


Fig. 5.10 The far-field of the grating coupler.

5.3 Cyclically arranged optical beam steering

As mentioned above, OWC using narrow steered beams can boost the aggregate capacity for indoor mobile wireless connectivity. To guarantee an uninterrupted data connection, large angular coverage of transmitters/receivers is of demand.

Therefore, reconfigurable transmitters/receivers with a large FoV is a promising solution. An SLM could steer an optical beam without mechanical movement, which has been applied to indoor IR light beam steering systems [167, 168, 74]. Compared to other means, an SLM has highly repeatable performance, high tolerance from the device and atmosphere. An SLM also does not limit the signal's bandwidth [167]. So far, A. Gomez et al. already extend the FoV from 3° (only using an SLM) to 60° by introducing an extra lens system as an angle magnifier (AM) [74]. Such an AM concept is attractive since it can directly increase the FoV of different kinds of systems. However, until now, most SLM-based methods implement 2D beam steering by using the concept of a 2D grating in the Cartesian coordinate, such as the beam steering using regular gratings. For a simple 1D grating, if we assume its number of grating lobes is N , when extending it to 2D, the number of grating lobes is $N \times N$. As the number increase, its power efficiency decreases. The covered range of grating lobes or the FoV is traded off with power efficiency. Additionally, it is not easy to implement beam steering at (quasi-) continuous angle due to the discrete diffraction orders of a simple grating and the fixed pixel size of an SLM. This results in only certain discrete angles in a steering area. Here, we proposed another 2D beam steering scheme named cyclically arranged optical beam steering (CAO-BS) to break the trade-off between FoV and power efficiency. Traditional 2D gratings extend optical beam in Cartesian coordinate (1D grating in horizontal + 1D grating in vertical), while CAO-BS extends optical beam in polar coordinate (1D grating + angular rotation). Since only 1D grating is engaged, the power efficiency increases with the decrease of the number of grating lobes. In polar coordinate, the angular rotation in an SLM is quasi-continuous in a range of full 2π . Even though the idea of CAO-BS has never been explored for indoor OWC systems, a similar idea to use rotation as the freedom for beam steering is studied in Risley Prisms [169, 170]. Based on the CAO-BS concept, an FoV of 18° is experimentally demonstrated by using a reflective SLM and a simple 1D grating. The OWC transmission using a 40-Gbit/s OOK data is also experimentally implemented over a 1-km standard single-mode fibre and 0.5-m free space. This quasi-continuous $\pm 9^\circ$ FoV greatly releases the pressure on alignment and thus provides a promising solution for indoor OWC systems.

5.3.1 Principle of cyclically arranged 1D grating

Fig. 5.11 shows the concept of SLM-based 2D CAO-BS. The general diffraction pattern is presented in Fig. 5.11 (a). By changing the grating pitch, we can alter the pointing direction of the first order beam, which is the common meaning of 1D beam steering as shown in Fig. 5.11 (b). In terms of the 1D case, the operational principle of CAO-BS is the same as a conventional method. As shown in Fig. 5.11 (c), for a traditional 2D beam steering, a 1D grating is extended to a 2D grating, while for CAO-BS, a cyclical rotation is applied to a 1D grating as shown in Fig. 5.11 (d). This avoids further power splitting in another dimension, which enables higher power efficiency.

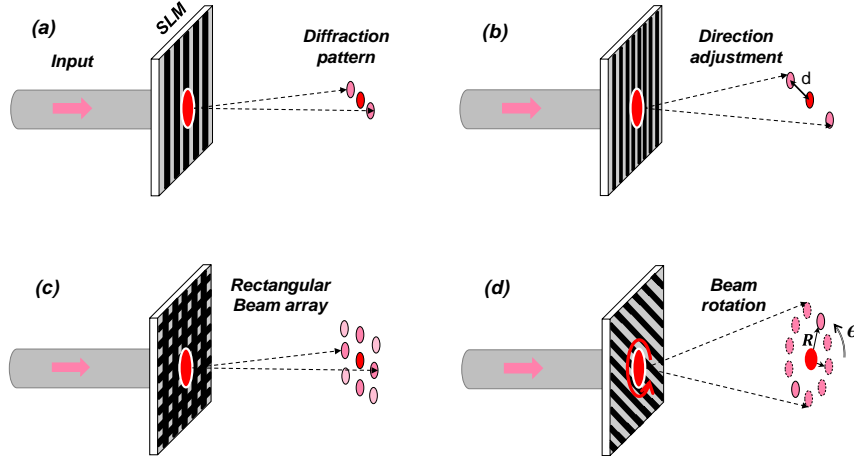


Fig. 5.11 The concept of SLM-based cyclically arranged optical beams steering; (a) the general 1D grating diffraction; (b) grating pitch adjustment; (c) 2D beam steering using 2D grating; (d) cyclically arranged optical 2D beam steering. SLM: spatial light modulator; d: The distance between central and first order spots.

Even though a 1D grating can be quasi-continuously rotated in the angle dimension, the angle of a 1D grating is still discrete due to the limitation of the pixel size of the SLM, leading to some unreachable directions. As suggested in [74], for an SLM, the maximum deflection angle α of the first order in full angle is determined by pixel pitch Δ of an SLM and a laser wavelength λ , which is presented as $\alpha = \lambda/\Delta$. In the reported system in [74], Δ of SLM device is $\sim 20 \mu\text{m}$ and the wavelength is 1060 nm. Thus the maximum α is ~ 3.04 degree. In practice, once the SLM is selected, Δ cannot be changed. To avoid the gap between two discrete angles, a new structure that can meet this requirement is proposed as shown in Fig. 5.12.

5.3.2 Cyclically arranged optical receiver

Fig. 5.12 (a) illustrates a general diffraction pattern used in optical beam steering. L is the distance between an SLM and a receiver, which is an essential factor in our scheme. As we discussed above, we could clearly see an unreachable area between central spot and first-order grating lobes. However, when we reduce L to L' ($L' \ll L$), for instance around 10 mm in our experiment, the grating lobes can be quite close to the central spot as shown in Fig. 5.12 (b). If we decrease L further, the uniformness will be better. When all grating lobes are close enough to fall in the coupling region (aperture) of a collimator, a wide-FoV receiver without obvious blind spots can be realized as shown in Fig. 5.12 (c). Optical beams in different directions (illustrated by different colors) are projected to the grating. Elliptical rings with different colors represent input signals at different angles. When the angle of the input signal changes along one direction (eg. horizontal direction in Fig. 5.12 (c)), a linear beam will shift a certain angle in the same direction as well. But a part of the beam still falls in the coupling area of the collimator. This radiated beam ensures a

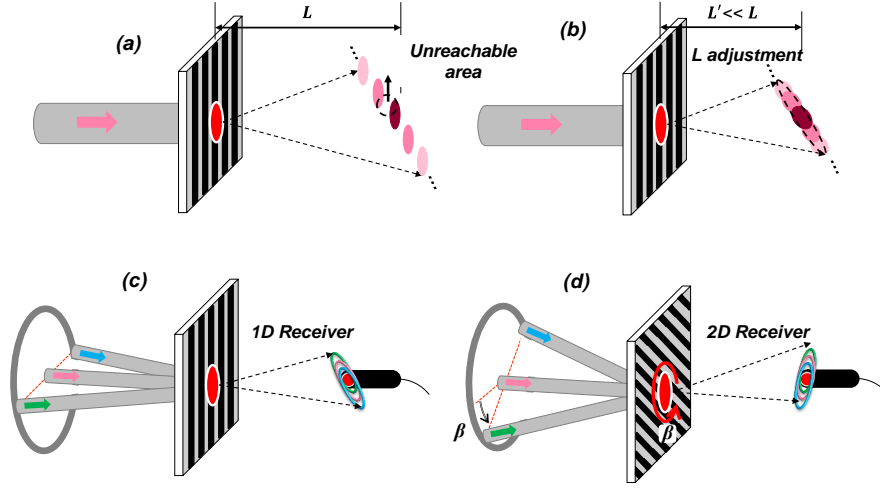


Fig. 5.12 The principle of the SLM-based receiver that supports 2D continuous-angle beam steering (a) general grating diffraction; (b) demonstration of the continuous beam; (c) 1D receiver; and (d) 2D receiver. L : The distance between the diffraction beam and grating; β : The angle between the incident plane and the horizontal plane.

stable optical connection without a blind area in a certain angular range. Fig. 5.12 (d) shows the 2D principle. For arbitrary input light within the FoV of the 1D grating, the grating is rotated to match the input direction by updating the phase profile of the SLM. For instance, when an incident plane rotates β degree anticlockwise, the grating angle should have the same rotation to make sure it is perpendicular to the new incident plane as shown in Fig. 5.12 (d). In this experiment, we demonstrate an optical receiver based on a reflective SLM produced by HOLOEYE (PLUTO Phase Only SLM). It should be pointed out that for our receiving structure, the reflective SLM is the same as the transmission-type in terms of function.

5.3.3 Experimental setup and results

The experimental setup is illustrated in Fig. 5.13 (a). A laser with a narrow bandwidth (<100 kHz) is employed for the optical carrier with a wavelength of 1550 nm. A 40-Gbit/s OOK signal is generated from a commercial transmitter (SHF10000B) and is amplified by a boosting amplifier (EDFA-1) before being delivered over a 1-km single-mode fibre. The 1-km standard single-mode fibre (SSMF) stands for the distance from a central controlling room to a user room in an indoor scenario. The SLM used here is a polarization-sensitive device. So a PC is introduced to align the polarization state to optimize the modulation efficiency of the SLM. The light is fed into a transmitting collimator (NA=0.28) and transmitted over 0.5-m free space before illuminating the SLM. The incident angle can be tuned as shown in Fig. 5.14. This free space link is used to emulate the distance between an access point and a terminal user. A lens with a focal length of 200 mm is employed to adjust the spot size. A compact receiver can be achieved by using a specially designed lens

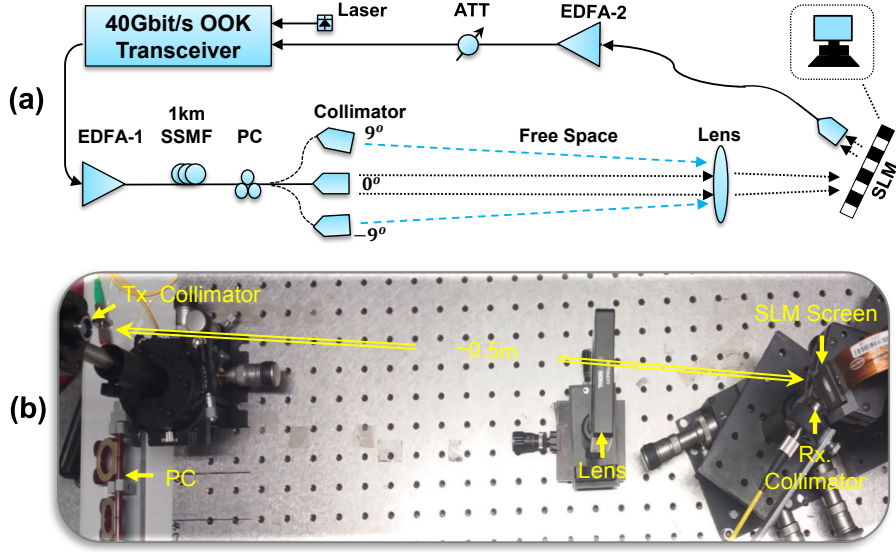


Fig. 5.13 Experimental setup (a) the whole transmission system and (b) the real free-space link. ATT: optical attenuator; EDFA: erbium-doped fibre amplifier; SSMF: standard single-mode fibre; PC: polarization controller.

system. The reflective SLM has 1920×1080 active pixels and an $8\text{-}\mu\text{m}$ pixel pitch. The spatially modulated light wave is collected by a smaller collimator ($\text{NA}=0.16$) and then coupled into a single-mode fibre. The distance between this collimator and screen is 10 mm. To compensate for the insertion loss including the imperfect alignment loss, a pre-amplifier (EDFA-2) is used. An optical attenuator is introduced to measure the BER versus received optical power curves.

The experimental results are analyzed as shown in Fig. 5.14, 5.15, and 5.16. As discussed in Fig. 5.12 (d), the uniformness of reflective beams are evaluated by a movable multimode fibre (as a receiver) with a small aperture ($\phi = 62.5\text{ }\mu\text{m}$). Such a small aperture allows a relatively accurate measurement of the power distribution. The location and angle of the receiver (multimode fibre) are adjusted while fixing the transmitting collimator. The adjusting step of the location is 0.5 mm within a range of ~ 10 mm. A tiny angular adjustment is needed to optimize the power collection. The results are shown in Fig. 5.14. We set the input power is 9 dBm, and the measured power is between -34.5 dBm and -37.8 dBm. The variation is less than 3.3 dB, which presents a quite uniform power distribution along a line. As expected, there is no apparent blind spot.

Then a receiving collimator with a $\text{NA}=0.16$ replaces the multimode fibre. The other conditions are fixed, including input power and configurations of the free-space optical system. The transmitting collimator is then tuned to five different angles of -9° , -4.5° , 0° , 4.5° and 9° . The corresponding received power is -25.01 dBm, -23.1 dBm, -19 dBm, -25.6 dBm, and -22.7 dBm respectively as shown in Fig. 5.15. The power variation is less than 6.6 dB, which proves that the proposed method can provide relatively stable connectivity within an 18° angular range. In our experiment, the power loss is 33 dB, which is mainly due to the limited overlap

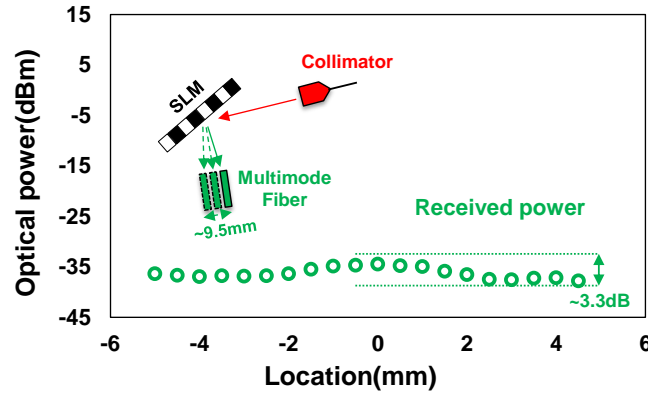


Fig. 5.14 Power distribution of the linear beam.

area between the converted beam and the receiving aperture. This power loss can be significantly reduced by increasing the active area of a collimator or replacing a collimator with a photodetector. Besides, an imperfect optical alignment can also contribute to such high loss. A well-designed/-optimized optical system is required for further loss-reduction.

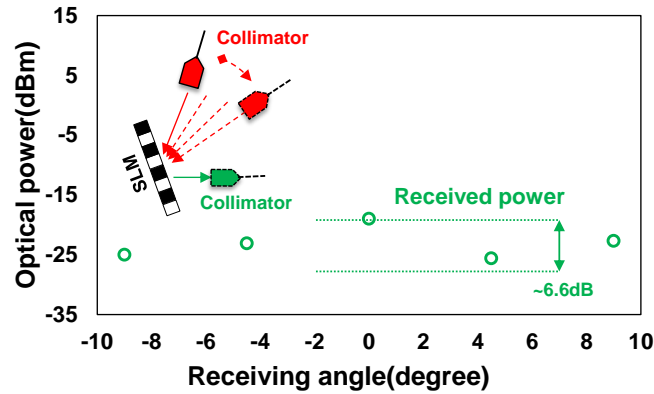


Fig. 5.15 Received power versus receiving angle curves.

The BER performance of the system is tested by transmitting a 40-Gbit/s OOK signal. In this experiment, we select -9° , 0° , and 9° input angles to evaluate the system transmission performance. The measured BER curves are shown in Fig. 5.16. At the limit of $\text{BER}=1 \times 10^{-9}$, the received power at the angle of -9° , 0° , and 9° is -7.8 dBm, -7.4 dBm, and -7.0 dBm respectively. As a reference, the corresponding received power of the optical back-to-back (OBTB) case is -9.2 dBm. The received sensitivity at the angle of 0° is the highest among the three transmissions. It shows 1.4-dB degradation compared with an OBTB condition. This is mainly caused by the noise from the boosting amplifier (EDFA-1) and the pre-amplifier (EDFA-2). The difference in receiving sensitivity between the angle of 0° and 9° is 0.4 dB. The receiving sensitivity at -9° is 0.8-dB lower than that at 0° . This coincides well with the power imbalance shown in Fig. 5.15. Such imbalance may be caused by the

angle-dependent properties of an SLM. As shown in the lower part of Fig. 5.16, the eye diagrams in the cases of OBTB, -9° , 0° , and 9° are all measured at 0 dBm. No drastic change in rising/falling edges is observed, which suggests that an optical link does not affect the electrical bandwidth significantly.

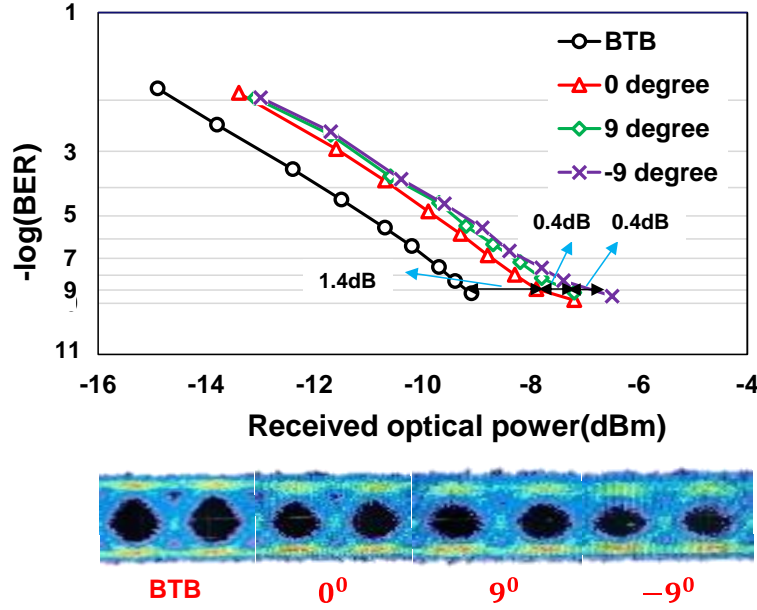


Fig. 5.16 Received power versus receiving angle curves and measured eye diagrams.

5.3.4 Conclusion

To conclude, a novel 2D beam steering scheme named CAO-BS is proposed to break the trade-off between FoV and power efficiency in grating applications. Different from traditional 2D gratings, CAO-BS extends the optical 1D beam steering to 2D in polar coordinate (1D grating + angular rotation). Since only 1D grating is engaged, the power efficiency increases with the reduction of the number of grating lobes. Moreover, in polar coordinate, an angle rotation in an SLM is quasi-continuous in a range of full 2π . Based on this concept, a wide FoV receiver is demonstrated utilizing an SLM and a conventional collimator. An FoV of 18° -by- 360° is realized without using mechanical movement. It can be further extended to $\sim 140^\circ$ -by- 360° when an angle magnifier mentioned in section 5.3.2 is applied. In addition, a 40-Gbit/s bit-rate OOK transmission experiment is demonstrated over a 1-km standard single-mode fibre and a 0.5-m free-space link. We believe this technique can provide a promising solution for indoor OWC systems.

5.4 Chapter summary

In this chapter, two novel LOS OWC solutions are proposed for indoor applications. One is the advanced transmission scheme with larger indoor spatial coverage and higher spectral efficiency. By creating polarization orthogonality between adjacent AWGR channels, an ultra-high crosstalk-tolerant OWC transmission in an AWGR-based beam steering system is experimentally investigated. The other is a novel rotating-1D-grating-based OWC receiver. The concept is introduced by comparing it with a traditional 2D grating solution. It can significantly reduce power consumption. And a further FoV-extended receiver is proposed with an FoV of 18° . These improvements provide new technical solutions for an indoor beam-steered OWC.

NON-LINE-OF-SIGHT INDOOR OPTICAL WIRELESS COMMUNICATION

As discussed in **Chapter 5**, wireless communication by means of light (a.k.a. OWC) can bring a breakthrough in communication capabilities, both in terms of ultra-high capacity per user and in terms of electromagnetic interference-free communication. However, one fundamental challenge for OWC arises when the direct pathway between a transmitter and a receiver is obstructed by an obstacle. In indoor applications, an NLOS link could potentially be established using light that is diffusely reflected off a scattering material (e.g., a ceiling or a wall). When an optical beam is incident on a rough surface, the light is scattered in a disordered manner, resulting in the near-isotropic, speckled intensity distribution of the diffusely reflected light. Therefore, at the receiver end, the intensity of the diffused light is inherently much lower than that of a collimated incident light beam arriving directly at the receiver. As described in **Chapter 2**, most current solutions for this issue are based on a broadcast connection and have a low transmission speed. As a long-standing challenge, such diffuse losses critically hinder a wide application of OWC. In this chapter, the work is focused on the first experimental implementation of NLOS OWC and its further performance improvement.

6.1 First generation beam-reconfigurable indoor NLOS OWC

In this section, a novel solution for this challenge is presented. We enhance the light intensity of a diffuse NLOS link by means of wavefront shaping [171, 172], which is a well-known technique in the field of scattering optics with applications in, for instance, deep-tissue microscopy [173, 174], micro-manipulation [175] and quantum secure authentication [176]. This technique allows light to be focused through and inside opaque materials by controlling the wavefront of the light using an SLM, greatly enhancing the light intensity at a desired location (or direction). Here, we use wavefront shaping to establish a diffuse NLOS free-space link by spatially controlling the wavefront of the light incident on a diffuse reflector, maximizing the diffuse optical power at an OWC receiver. The diffuse NLOS link is directionally adjustable, which is essential in an indoor beam-steered OWC system. We are the first to introduce wavefront shaping to address NLOS issues in an OWC system to the best of our knowledge. We demonstrate this technique experimentally, which we have dubbed ‘coherent array optical transmitter’ (CAO-Tx). Using the proposed

CAO-Tx, a record data rate of 30 Gbit/s is implemented over a diffuse link with an angular range of 20° . First, the operation principle of the CAO-Tx is explained, and then an experimental setup is detailed. Experimental results are shown and analyzed in the next part. Finally, practical challenges are discussed for future applications.

6.1.1 Operational principles

In Fig. 6.1 (a), an indoor use case for CAO-Tx is depicted. From the access point (CAO-Tx), the narrow light beams loaded with user data are sent to the wireless terminals. Usually, the user data is transmitted from an information server to an access point via an indoor fibre network. In some cases, a direct high-speed connection between CAO-Tx and a terminal can be established via a LOS path. However, when the direct pathway is obstructed, the light can instead be directed to a diffuse reflection ceiling/wall to establish an indirect NLOS pathway to the device (right example: diffuse reflection in Fig. 6.1). However, the light incident on a diffusely reflecting object will be scattered in many different directions, as shown in Fig. 6.1 (b). Therefore, an OWC detector at a long distance from the diffuse reflector will collect a small part of the diffused light.

To overcome this problem, CAO-Tx integrated an SLM allows the control over the phase of the field E_a , which is incident on a diffuse reflecting surface. The SLM is divided into N different segments and each of which can be separately controlled. Now, the scattered field reaching a detector can be described by:

$$E_b = \sum_a^N t_{ba} E_a \quad (6.1)$$

where t_{ba} is an element of the scattering matrix T , connecting the N number of incident field segments E_a to the detected field E_b . Here, all elements of the matrix T are assumed to be random complex variables, and as a result, all scattered waves $t_{ba} E_a$ will have a random phase [172, 177]. All of these randomly scattered waves interfere, forming a complex intensity pattern known as a speckle pattern.

Assuming that the scattering material does not change during the optimization, we can modulate the phase of E_a to optimize the intensity at the detector. To maximize the intensity $|E_b|^2$, we use the stepwise sequential wavefront-shaping algorithm [172, 177], where the phases of the incident field segments are modulated between 0 and 2π in a stepwise fashion. As a result, the intensity measured at the detector will vary as a function of θ_a , the phase of a single input segment a :

$$I_b(\theta_a) \equiv |E_b|^2 = \left| E_{ref} + t_{ba} E_a e^{i\theta_a} \right|^2 \quad (6.2)$$

with reference field

$$E_{ref} \equiv \sum_{a' \neq a}^N t_{ba'} E_{a'} \quad (6.3)$$

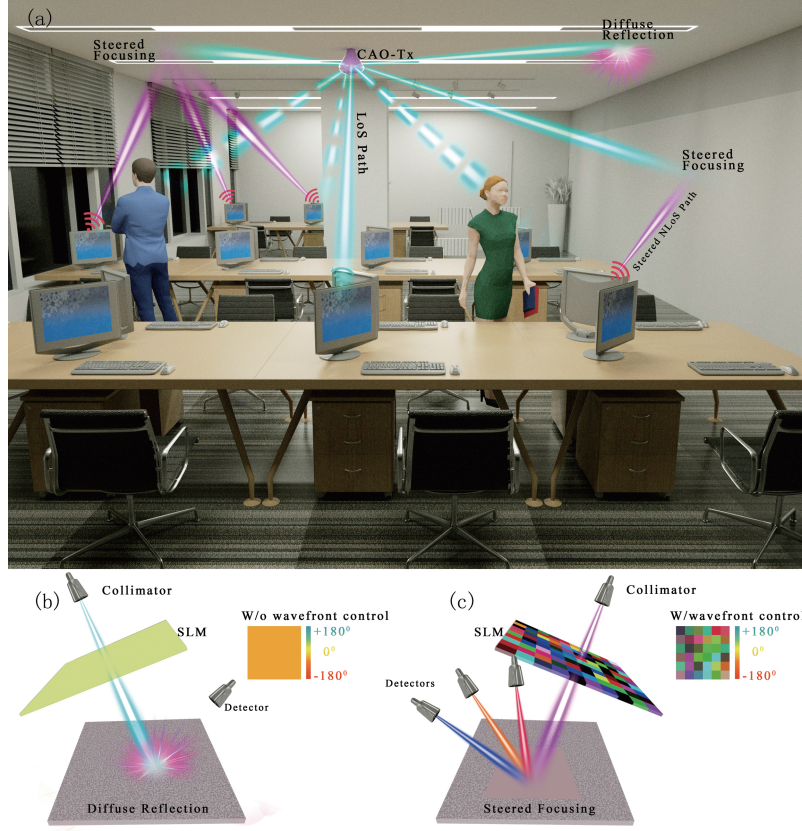


Fig. 6.1 (a) Indoor use case of the coherent array optical transmitter. In the absence of a direct LOS path, diffusely reflected light can be focused to the OWC detector of the wireless device. (b) Basic principles of wavefront shaping: a diffuse reflecting surface is illuminated with a flat wavefront, and the light is randomly scattered in all directions. Only a small fraction of the light reaches the detector. (c) By means of an SLM, the phases of different segments of the incident light are modulated to maximize the intensity at the detector.

The intensity at the detector is maximized when E_{ref} and $t_{ba}E_a e^{i\theta_a}$ are in phase, i.e., $\theta_a = \arg(E_{ref}) - \arg(t_{ba}E_a)$. This procedure is repeated for all input field segments, and finally the optimized phase of all incident field segments is applied to the SLM, resulting in an enhancement of the light intensity at the position of the detector (see Fig. 6.1 (c)). To enhance the light intensity at a different detector position, the algorithm is performed again to find the new ideal phase pattern.

The diffusely reflected light can be focused to any location in the room as long as the OWC detector is capable of measuring the intensity of the SLM-modulated light during the optimization process. The scattered light can also be focused on multiple detectors simultaneously by superimposing multiple ideal phase patterns on the SLM [177]. The theoretical intensity enhancement at the detector is independent of the properties of the scattering material. The only limiting factor is the SNR at the receiver [178]. The losses of the diffuse link over large distances can be compensated by optimizing for a larger number of SLM segments since the intensity enhancement increases linearly with N [172]. Once the diffuse link with required optical power is

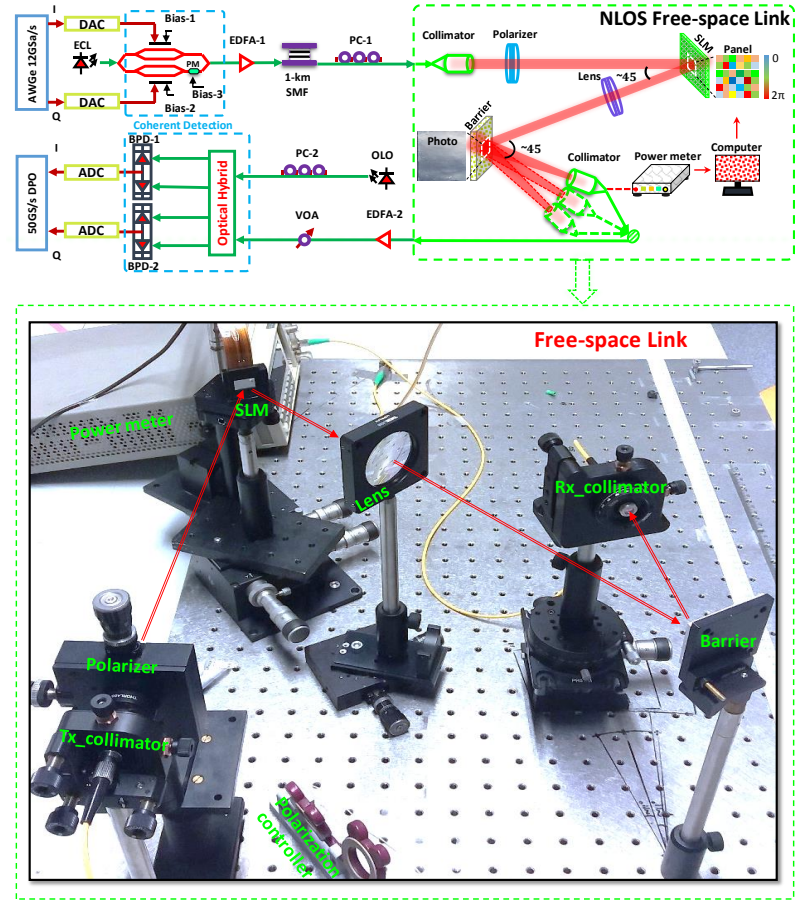


Fig. 6.2 (a) Schematic drawing of the experimental setup;(b) the photo of free-space link. AWGe: arbitrary waveform generator; EDFA: Erbium-doped Fibre Amplifier; PC: polarization controller; SLM: spatial light modulator; OLO: optical local oscillator; BPD: Balanced Photodiodes; VOA: variable optical attenuator; ADC/DAC: analog-to-digital converter/digital-to-analog converter; DPO: digital phosphor oscilloscope

obtained using the proposed CAO-Tx, high-speed OWC signals can be transmitted to the receiver.

6.1.2 Experimental setup

The schematic of the transmission system:

The description of a 30-Gbit/s indoor NLOS beam reconfigurable OWC system enabled by the CAO-Tx method is to proceed. Fig. 6.2 depicts the experimental setup and detailed parameters. In our experiment, a widely used electrical 30-Gbit/s OFDM signal is generated by an AWGe. DSP flow and parameters can be found in the part of **Digital Signal Processing**. This OFDM signal is then modulated onto an optical carrier via an optical transmitter including an extra cavity laser and an optical IQ modulator (It is introduced **Section 1.1.2**). The optical signal is amplified via an EDFA (EDFA-1). A 1-km bend-insensitive single-mode fibre is used to emulate the distance for an indoor application. Afterward, a PC (PC-1) is used to align the

polarization state of the optical signal to the polarization axis of the SLM before a collimator. The collimated Gaussian beam is then incident on the SLM (HOLOEYE, PLUTO Phase Only SLM). The angle between an incident beam and a reflected beam is 45° . To match the size of the Gaussian beam, 1024×1024 pixels are activated, which are further grouped into segments of 128×128 pixels, yielding a total of 8×8 segments. All pixels in a segment are simultaneously modulated from 0 to 2π in the increment of $\pi/4$. After the phase modulation of these segments, a lens ($f = 200$ mm) focuses the modulated beam onto a diffuse reflection barrier, which emulates the rough surface (ceilings or walls) in indoor scenarios. Here, two types of scattering samples are tested: I) a Thorlabs polystyrene screen (EDU-VS1/M); II) a sandblasted aluminum film. The angle between the SLM-modulated beam and the normal of the barrier is -22.5° , and we define the principal reflection angle as $+22.5^\circ$, (i.e., the angle of reflection equals the angle of incidence).

To collect the diffusely reflected optical signal, the light is coupled into a fibre using a collimator. The receiving fibre is mounted on a movable stage, allowing the receiving angle/distance to be varied. An optical power meter is used to provide feedback for the wavefront-shaping algorithm to enhance the light intensity at the receiver. The received optical signal is pre-amplified via a second EDFA (EDFA-2) before being detected by an optical coherent receiver. Finally, the detected signal is sampled by a real-time oscilloscope operating at a 50-GSa/s sampling rate. The sampled signal is then processed through an offline digital signal-processing algorithm, and the binary signal is ultimately recovered.

The transmitter/receiver of optical coherent OFDM:

An electrical OFDM signal is generated by an AWGe with a 12-GSa/s sampling rate. Its bandwidth is ~ 9.2 GHz with 16-ary quadrature amplitude modulation (16QAM), and the net bit rate is 30 Gbit/s. The detailed calculation of the net bit rate is presented in the part of "Digital signal processing". Through an optical IQ modulator, an OFDM signal is modulated onto an optical carrier provided by an external cavity laser (ECL). Here, the optical spectrum-efficient quadrature amplitude modulation is employed. The in-phase (I) and quadrature (Q) components are separately modulated onto the optical carrier enabled by 3 bias voltages, in which Bias-1 and Bias-2 are used for a carrier-suppression modulation [144] and Bias-3 is to obtain a 90° phase shift for generating the quadrature carrier. The central wavelength of the optical carrier can be flexibly set. The coherent detection is employed to obtain higher responsivity and spectrum efficiency [145]. A variable optical attenuator (VOA) is placed between EDFA-2 and the receiver to adjust the received power. An extra ECL with 14-dBm power is used as an optical local oscillator (OLO). Another PC (PC-2) is utilized to align the signal polarization state and the OLO polarization state. Through an optical hybrid component, the four outputs are detected by two balanced photodiodes. The phase difference between the signal and OLO of the four outputs (top-to-bottom) is 0° , 180° , 90° , and 270° , respectively [145].

Digital signal processing

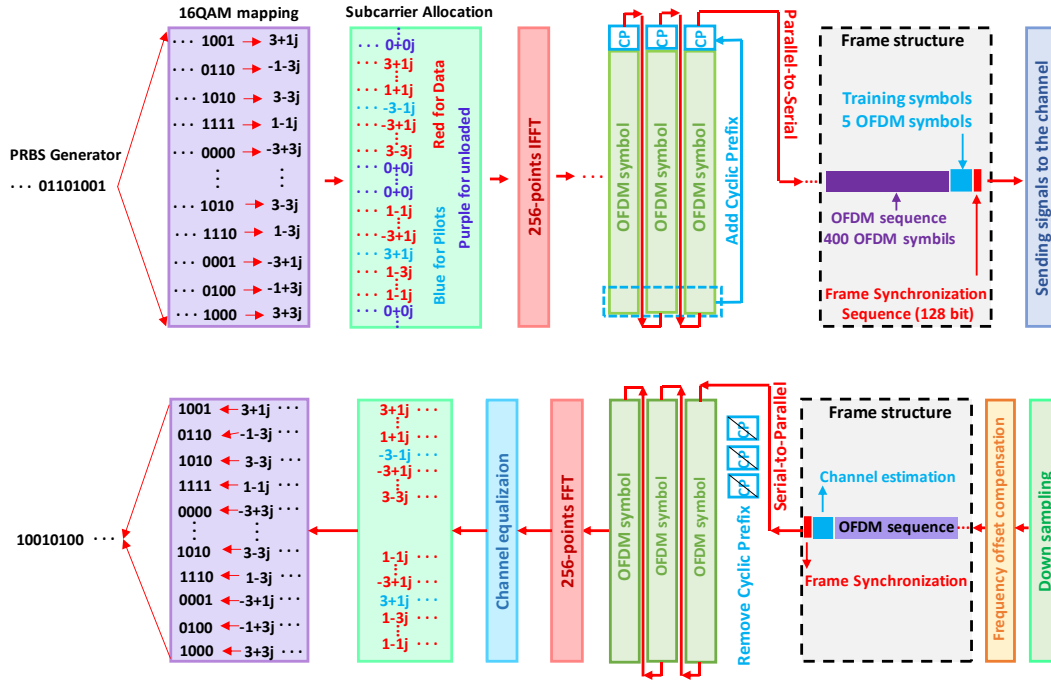


Fig. 6.3 Offline digital signal processing.

Fig. 6.3 presents the offline DSP. A pseudo-random binary sequence (PRBS) is used as a data source. The data is mapped to complex number symbols for data-loaded subcarriers. Here, a 16QAM mapping method is employed due to the data capacity and channel quality. Then the signal is converted from the frequency domain to the time domain by utilizing a 256-point inverse fast Fourier transform (IFFT), in which 188 subcarriers are loaded with data and seven subcarriers are unloaded to avoid the DC and low-frequency interference. Two subcarriers are selected as pilots for phase noise estimation and the other 59 subcarriers on the edges are also data-unloaded. Thus the bandwidth of the OFDM-16QAM signal is [144]

$$12 \times (188 + 7 + 2)/256 \approx 9.23(\text{GHz}) \quad (6.4)$$

where 12 means the 12-GSa/s sample rate of the AWGe, 256 stands for the total number of subcarriers.

A cyclic prefix (CP) is inserted between two OFDM symbols and its length is 1/16 IFFT size. Parallel-to-Serial conversion is to convert the signal into a data sequence. Five OFDM training symbols are periodically inserted in front of each frame, which is followed by 400 payload symbols. Finally, a 128-bit sequence for time synchronization is added. The net bit rate is:

$$12 \times 186/256 \times 0.93 \times (15/16) \times (400/405) \times 4 \approx 30.35(\text{Gbit/s}) \quad (6.5)$$

where 0.93 is the net bit rate excluding the FEC overhead. The terms of 15/16 and 400/405 stands for the net information eliminating the CP redundancy and the

training symbol redundancy, respectively. 4 means 4 bit per symbol for the 16-QAM signal.

To demodulate the signal, the same procedure and distortion compensation algorithms are performed in reverse. A received signal is firstly down-sampled, then frequency offset needs to be compensated. A frame synchronization algorithm is used to extract a frame of the OFDM signal for offline processing. Training symbols are used for channel estimation. Afterwards, Serial-to-Parallel conversion, CP removal, FFT are employed to convert the signal into the frequency domain and channel equalization is utilized to compensate channel impairment. Pilot subcarriers are aimed at compensating phase noise. Aided by these procedures, the 16-QAM signal is recovered and then is de-mapped to binary data.

6.1.3 Results and analysis

Material discussion:

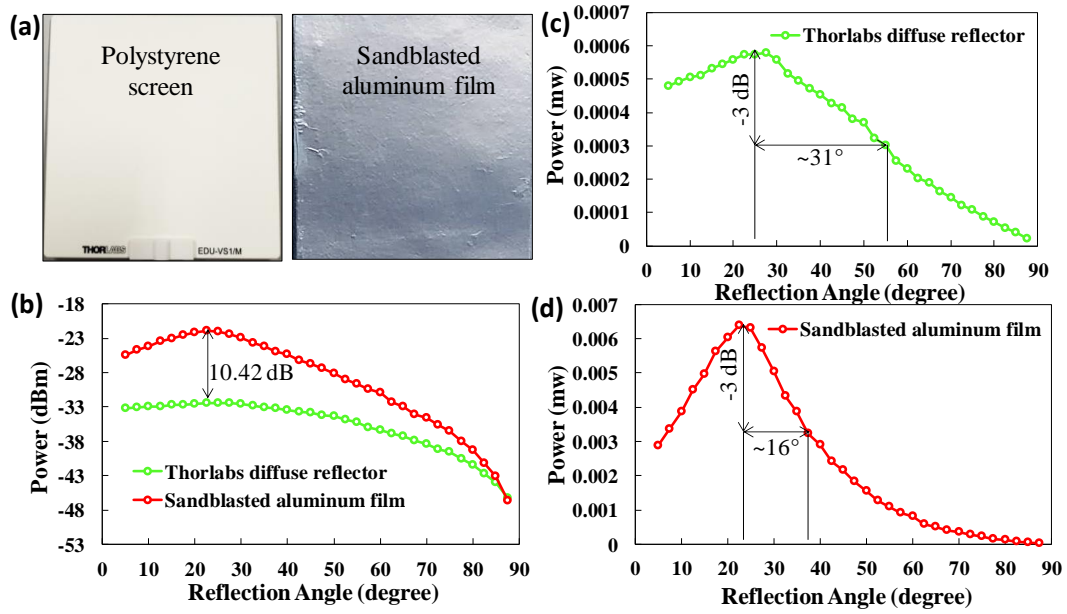


Fig. 6.4 Reflectors/materials. (a) the photos of the two proposed samples; (b) comparison of the measured BRDFs of both samples in logarithmic scale; (c) and (d) are the measured BRDFs in mW, respectively.

In my diffuse NLOS communication system, the angular coverage is mainly determined by the scattering angle range of the diffuse reflector. In the experiments, we tested our method using two different materials: I) a polystyrene screen (Thorlabs EDU-VS1/M) and II) a sandblasted aluminum film. Photos of the scattering samples are shown in Fig. 6.4 (a). To characterize the scattering response of these materials, we measured the bi-directional reflectance distribution function (BRDF) for an incident angle of -22.5° . BRDF describes how much optical power is back scattered into a given reflection angle. We measure BRDFs of the two samples by using an optical power meter with a round active area (3-mm diameter) at a distance of 70

mm from the sample. The laser power incident on the sample was set to 9 dBm at the wavelength of 1550 nm. The measured BRDFs for the polystyrene screen and the sandblasted aluminum film are shown in Fig. 6.4 (c) and Fig. 6.4 (d), respectively. A comparison in between is presented in Fig. 6.4 (b). Here, the measured angle is offset to the normal direction of the diffuse reflector. As shown in Fig. 6.4 (c), the polystyrene screen scatters the diffuse reflected light in a wide range of reflection angles ($\pm 31^\circ$). But the received power within this angular range is relatively low (~ -33 dBm). In contrast, the sandblasted aluminum sample has a much higher received power (10.42-dB increase at peak point), while sacrificing angular coverage ($\pm 16^\circ$). These results demonstrate a tradeoff between angular coverage and received power.

Enhancement of received power:

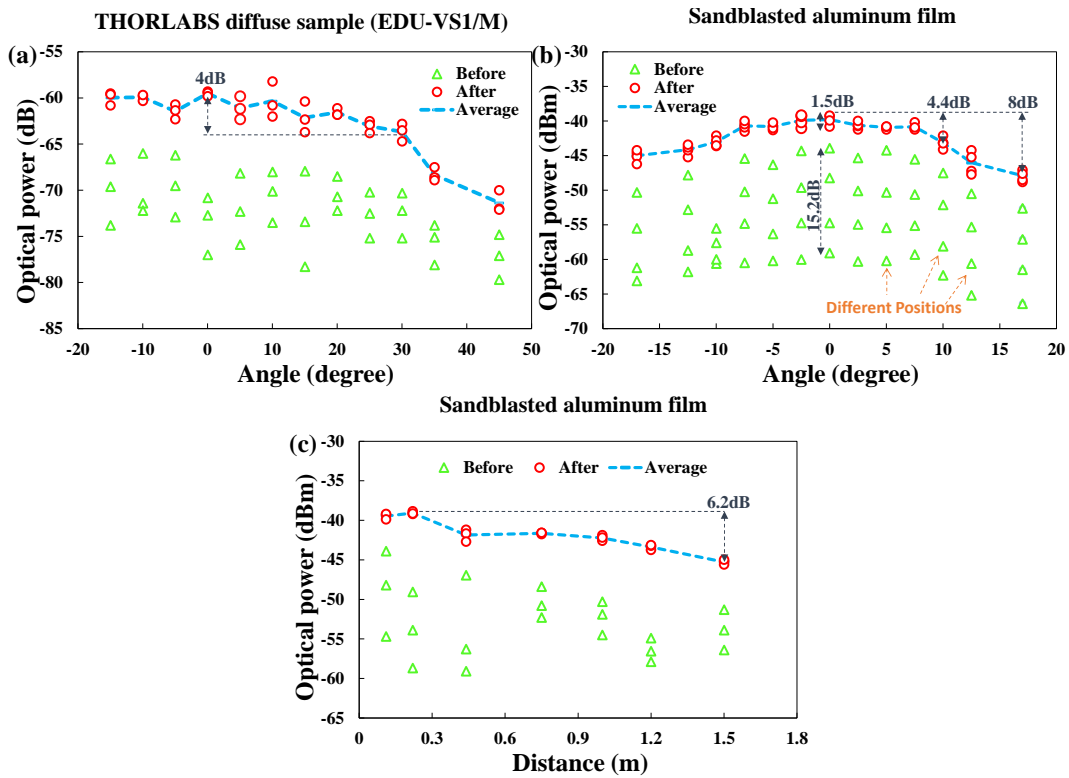


Fig. 6.5 (a)-(b) The measured power versus various reflection angles before and after wavefront shaping by using the THORLABS standard diffuse sample and the sandblasted aluminum, respectively; (c) the measured power versus various distances before and after wavefront shaping.

To evaluate the effectiveness of CAO-Tx, we compare cases with and without wavefront shaping. We use the optical power arriving at the receiver as a figure of merit. The enhancement of received power induced by wavefront shaping is shown in Fig. 6.5. First, the optimization experiment is performed on the polystyrene screen. To explore the performance of focusing and beam steering (direction tuning), the optical power is measured at a 0.43-m distance for an angle ranging from -15° to 45° (offset to the principal reflection angle, similarly hereinafter). Each measurement is

performed at three different spots on the diffuse reflector, and the results are shown in Fig. 6.5 (a). It can be seen that the reflected power slightly decreases along with the angle increase, with a 4-dB half-angle range of $\sim 30^\circ$. Within this range, the enhanced intensity remains constant, as expected theoretically, and an average gain of 14 dB is achieved. The power before wavefront shaping fluctuates strongly due to the position change of the spot on the diffuse reflector. This effect is caused by a random speckle distribution of the scattered light. However, the optimized power is not impacted by this effect, showing position-independent.

A similar measurement is also performed on the sandblasted aluminum film. The distance between the diffuse reflector and the optical receiver is fixed at 0.11 m. The optical power is measured at an angular offset ranging from -17° to 17° . Each measurement is performed at four different spots on the diffuse reflector. Before wavefront shaping, the received power at 0° offset intensely fluctuates from -59.1 dBm to -43.9 dBm. In contrast, the received power can always be enhanced to a relatively stable level (1.5-dB fluctuation). An 11.7-dB average enhancement is observed (from -51.5 dBm to -39.8 dBm). When the receiver is located at a dark point (-59.1 dBm), a maximum gain of 18.3 dB can be obtained. This result proves that, even when the receiver is located at a dark spot, the wavefront-shaping algorithm can effectively refocus the diffusely reflected light to a receiver. A similar enhancement is obtained for other angles, in which the power after wavefront shaping is optimized to $\sim -42.8 \pm 0.8$ dBm for a -10° offset and $\sim -43.8 \pm 1.2$ dBm for a 10° offset.

Additionally, the distance between the reflector and the receiver is varied from 0.11 m to 1.5 m while keeping the receiver angle fixed at 0° . The measured power-to-distance curve is depicted in Fig. 6.5 (c). Again, we can see that, although the signal power decreases with the increasing distance, signal enhancement obtained by wavefront shaping is approximately constant.

The experimental results of these two diffuse materials prove the effectiveness of power enhancement in a diffuse link achieved by wavefront shaping. Because ceilings and walls are general diffuse-reflectors [179], this method is expected to be effective as well. Compared with the isotropically scattering polystyrene screen (enhanced power: -60 dBm @ 0.43 m in Fig. 6.5 (a)), the received power of the sandblasted aluminium has a 18-dB improvement (~ -42.2 dBm @ 0.44 m in Fig. 6.5 (c)). Although the angular coverage becomes narrower, the received power is much higher. Therefore, we use the sandblasted aluminum reflector in our data transmission experiment.

Record data rate over a diffused link:

In this experiment, a record 30-Gbit/s data rate is achieved in a diffused NLOS OWC system. Fig. 6.6 (a) presents the normalized optical spectra (normalized to the same noise level) before and after wavefront shaping to show the optical SNR improvement. The spectrum of the OBTB case without the free-space link serves as a reference with 43.12-dB normalized peak power. The peak values of the spectra before and after wavefront shaping are 3.50 dB and 22.92 dB with a 19.42-dB improvement. To evaluate the transmission performance, the Q factor as a

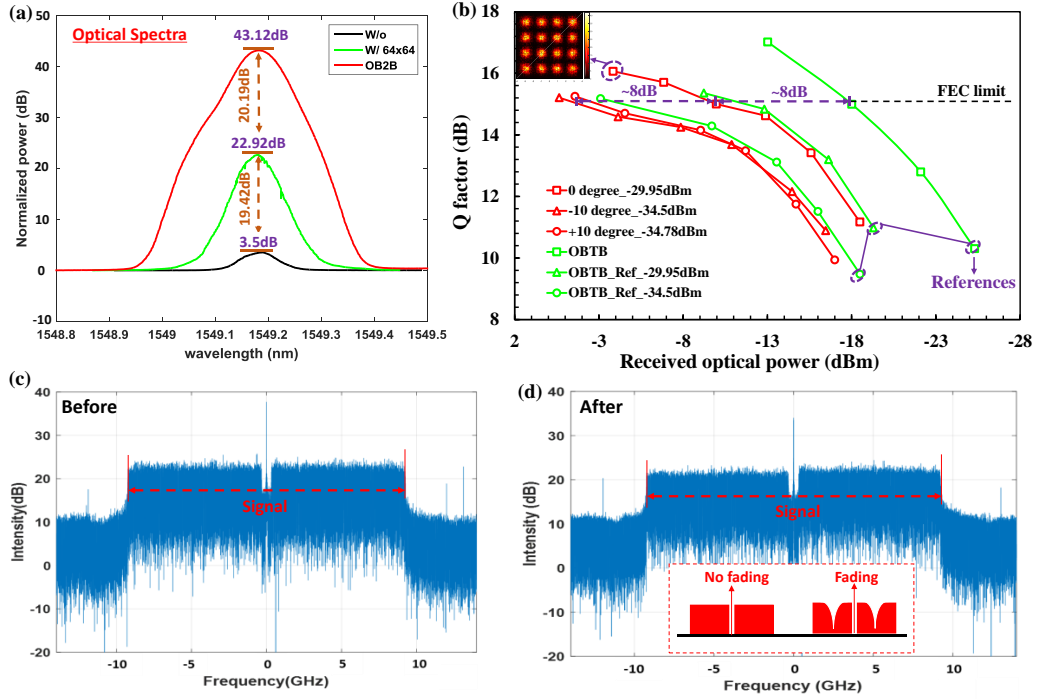


Fig. 6.6 (a) The measured optical spectra; (b) the measured Q factor as a function of the received power; (c) and (d) the RF spectra before (OBTB) and after wavefront shaping.

function of received power by adjusting a VOA is measured as shown in Fig. 6.6 (b). Here, the Q factor is defined as the electrical SNR [164]. 8×8 segments are further divided into 16×16 segments to achieve a higher power gain for the transmission. Compared to the incident power to the reflector (~ 10 dBm), the diffuse reflection sample introduces a >60 -dB loss (-50.9 dBm at the received collimator) at 0° offset, which greatly reduces power efficiency. After wave-front shaping, the power can be enhanced to -29.9 dBm with a 20.9 -dB gain. When the angle is shifted to $\pm 10^\circ$, the power is enhanced from -54.40 dBm and -52.10 dBm to -34.50 dBm and -34.78 dBm, respectively. Except for the curve of the default OBTB case (13.7 dBm after fibre), two more reference curves are measured for the OBTB cases, but with the power (after fibre) attenuated to -29.9 dBm (0°) and -34.5 dBm ($\pm 10^\circ$). We assess power penalties at the FEC threshold of 3.8×10^{-3} ($Q=15.17$ dB). Power penalties between focusing cases and their references (Reference (0°) and Reference $\pm 10^\circ$) are less than 1.5 dB. This suggests that the diffuse NLOS link does not introduce notable impairment. The power penalty between the case of 0° and the cases of $\pm 10^\circ$ is 8 dB, which is the same as the penalty between the OBTB case and the cases of Reference $\pm 10^\circ$. The 4.6 -dB power difference results in an 8 -dB power penalty when the received power is low (-30 dBm). This suggests that the improvement of received power by using CAO-Tx is critically important for diffuse NLOS links. Moreover, the received RF spectra, which are generated from the digital Fourier transform of the sampled OFDM signal, for the OBTB case (without the free-space link) and the diffuse focused case is shown in Fig. 6.6 (c) and 6.6 (d), respectively.

For wireless communication, a significant limit in an NLOS scenario is frequency fading, as depicted in the inset in Fig. 6.6 (d). Typical frequency spectra with (w/) and without (w/o) fading are located on the left and right sides, respectively. In a fading spectrum, the faded part usually causes serious inter-symbol interference in the time domain. Such interference plays a major role in the system performance degradation, rather than the low received power [180–182]. Compared with the OBTB case (shown in Fig. 6.6 (c)), no frequency fading is found for the focusing case (shown in Fig. 6.6 (d)). This absence of frequency fading can be attributed to the limited illuminated area on the diffuse reflector, causing negligible multiple path delays. The shaped wavefront is projected to a spot with a diameter of approximately 1.5 mm. Consequently, the time delay between the shortest and longest path from the transmitter cannot exceed 10 ps. For the OFDM signal used in our experiment, its cyclic prefix length is $1.333 \mu\text{s}$, which is much larger than the maximum time delay. Therefore, inter-symbol interference is not a limiting factor in the proposed system.

Analysis of the link performance:

In Table-I (in Fig. 6.7), system performance versus time is evaluated. The measurement is performed over three time periods (every 2 seconds) and each contains three Q calculations [164] (calculate every $9.6 \mu\text{s}$) at an angular offset of 0° . The results show that the Q factor fluctuates within a very small range of $<0.4 \text{ dB}$, which means the system is stable in time domain. Table-II describes the best performance when a receiver is located at 0° and $\pm 10^\circ$ respectively. When an angle offset increases by 10° , transmission performance declines and the Q value is just near the threshold of 3.8×10^{-3} ($Q=15.17 \text{ dB}$). Thus the experimentally demonstrated steered angle range is 20° . The constellations at different times and angles are shown in Fig. 6.5 to further evaluate the system's performance.

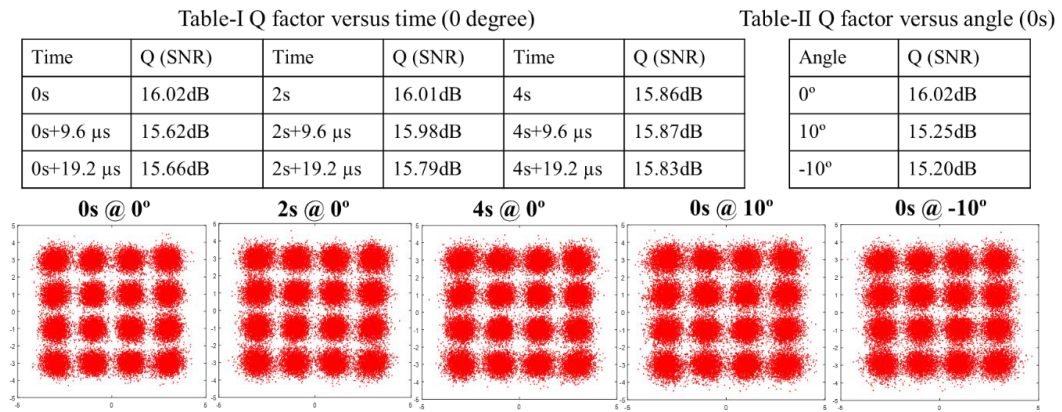


Fig. 6.7 The constellations at different measurement times and detection angles.

Then the Q-to-subcarrier distribution at the moment of 0 s is provided in Fig. 6.8. The subcarriers occupy a frequency range of 9.23 GHz (from -4.615 GHz to 4.615 GHz). Due to the bandwidth limit of the system and the low-frequency impact, the Q factor of some subcarriers is reduced. The system's Q factor is defined as the

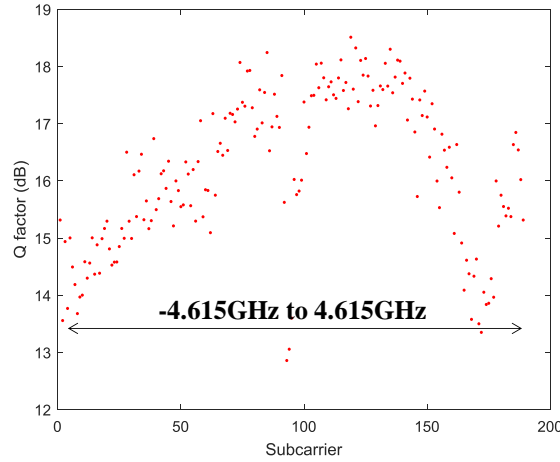


Fig. 6.8 Q factor versus subcarrier.

average value of all subcarriers, which determines the whole transmission capacity. The average Q factor is above the transmission limit of the QAM-16 signal.

6.1.4 Discussions

The angular range of beam focusing/steering:

In this experiment, we demonstrated the focusing of diffusely reflected light over an angular range of 20° using a sandblasted aluminum reflector. To achieve a larger angular range, we may either select a proper incident angle on the diffuse reflector through a mechanical scheme or use a more isotropically scattering sample. Using a more isotropically scattering sample, such as the polystyrene screen (Thorlabs EDU-VS1/M) or a white painted wall, will greatly extend the angular range of our method. However, larger angular coverage will also result in a higher loss of optical power.

Focus enhancement:

The fundamental limit here is the decrease in light intensity as the detector is moved further away from the diffuse reflecting surface. The intensity decrease can be compensated by optimizing for more SLM segments because the focus enhancement is proportional to N [177]. Recently, intensity enhancements as high as a factor of 100,000 have been reported [183]. Furthermore, the distance from the surface to the receiver can be shortened by projecting the SLM pattern on a reflecting surface close to the terminal devices. Besides, it is worth noting that the focus enhancement enabled by wavefront shaping will be roughly equal for both types of diffuse reflection materials, as is experimentally demonstrated in Fig. 6.5 (a) and (b).

Adaption to environment variation:

If the surface structure of the scattering ceiling or wall were to change, or any other change in the free-space path, such as airflow or dust particles, were to occur, a new SLM phase pattern can be updated using the wavefront shaping algorithm to re-establish a new NLOS link.

The speed of beam focusing/steering:

Separate controlling more SLM segments will increase the optimization time. In our experiment, the wavefront optimization of 8×8 segments, to enhance the optical power at the optical receiver, required approximately 400 seconds to complete. This optimization time is too long for most practical applications. However, by efficiently synchronizing the SLM and the detector, this process can become significantly faster. Additionally, here we used a liquid-crystal SLM with a maximum updating rate of 60 Hz, whereas alternatively, a digital mirror device could be used to modulate the wavefront of the light, which can be up to 3 orders of magnitude faster. Blochet et al. were able to optimize wavefronts at a rate of 4.1 kHz (0.244 ms per SLM segment) [184]. The potential of realizing the higher gain and faster optimization could meet the requirements of indoor applications. In indoor applications, diffuse reflectors (the ceiling and walls) are usually stable. Therefore, pre-scanning can help accelerate the beam focusing/steering process.

Optical spectral region for the proposed scheme:

Currently the spectral region of our method is limited by optical components, such as the SLM, collimators, and so on. In our experiment, the working spectral regions of these components are limited to a wavelength range of 1520-1620 nm. However, wavefront shaping has been widely investigated for visible and near-infrared light applications [177]. Our experimental setup can therefore easily be adjusted to work for a broader range of laser wavelengths.

Scaling up the data rate:

The net data rate of 30 Gbit/s can be further improved by using greater bandwidth or/and more advanced modulation formats. In our experiment, the modulated laser light had a bandwidth of 9.23 GHz. This is far below the upper limit on the bandwidth, which depends on the amount of time a light pulse spends in a scattering medium [171]. For strongly scattering samples, this time is on the order of picoseconds [185], which means that a modulated beam with a bandwidth of 100 GHz can still be efficiently focused without a large reduction in enhancement.

Implementation of an optical receiver:

As for the transceiver, the combination of IQ modulation and coherent detection is introduced to double the spectrum efficiency and raise detecting sensitivity. In practical applications, any modulating/detecting type is allowed as long as it can meet the requirements, such as cost, power responsivity, and available spectrum resource. The cost of coherent detection can be dramatically reduced by photonic integrated circuit technology for future applications [186].

6.1.5 Conclusion

In summary, a novel method of OWC for NLOS data transmission is proposed. By spatially modulating the light incident on a rough ceiling/wall, the diffusely reflected light to the OWC receiver is focused. The focusing capability of a diffusely reflected beam at distances of 0.11 m to 1.5 m is experimentally measured. A record-breaking 30-Gbit/s OFDM signal is transmitted over an indoor diffuse NLOS link

with a >17 -dB gain, in an angular range of 20° , and over a distance of 0.11 m from the diffuse reflector. The practical issues, such as the operation spectrum, coverage, environment adaption, focusing speed, higher data rate, and implementation of receivers, are discussed as well. We believe that this method, which breaks the NLOS limitation of OWC, will provide a new direction in this field.

6.2 Second generation beam-reconfigurable indoor NLOS OWC

A beam reconfigurable NLOS OWC system enabled by diffuse reflection focusing (DRF) brings a new idea [187]. Its key is to allocate diffuse reflection in a small area with wavefront shaping. Since the diffused area is limited, the multi-path effect is controlled at a very low level. Moreover, enabled by wavefront shaping, the diffused light beam can be focused and steered to the different terminal users. In the first generation implementation, a proof-of-concept is proposed and verified, but there are still many problems that need to be solved for realistic applications. The most significant issue is how to increase the speed of intensity optimization. A faster wavefront shaping algorithm is required to provide a real-time user-tracking NLOS communication system. Besides, the beam-steered angular range has to be wider for larger indoor spatial coverage. A significant performance improvement of the power enhancement is needed as well.

In this section, the previous work presented above is extensively extended, demonstrating a more realistic diffuse NLOS OWC system. This work is also based on narrow-beam-steered infrared light communication, in which light signals are brought only where and when needed. It can be more power-efficient and offers better privacy protection. By using a general (also standard) material—Thorlabs polystyrene screen (EDU-VS1/M), an average 18-dB-power-enhancement with a double-side angular-range of $>80^\circ$ is implemented over a 25-cm free-space link. The experimental results show significantly-high/-stable energy-efficiency-improvements. The highest 40-Gbit/s diffuse NLOS data rate, to the best of our knowledge, is achieved by using low-cost optical IM-DD and the OOK modulation format. As a key technique, the Transmission-Matrix (TM) algorithm enables a faster power-enhancement procedure with only 513 iterations, which shortens the focusing time to one-eighth of that in the first-generation indoor NLOS OWC.

6.2.1 Transmission matrix algorithm

As described in **Section 6.1**, the diffuse light is enhanced by using wavefront shaping, where the input beam is divided into N segments (connects to a vector T) that can be individually phase-modulated by using an SLM. Here, N is 256 (thus T is a 256×1 vector). The TM algorithm is utilized to find the optimized phase matrix (each pixel is in $0-2\pi$) for the transmitter-to-receiver power enhancement. This

phase-optimization is operated segment-by-segment. In the TM method, for each segment, the algorithm iteratively sets the phase retardation to 0, $2\pi/3$, and $4\pi/3$. Next, it measures the corresponding intensities at the m^{th} receiver's position as I_m^0 , $I_m^{2\pi/3}$, and $I_m^{4\pi/3}$. The transmission matrix elements can be estimated as equation 6.6 up to a multiplicative factor that can be eliminated as the factors are equal for all elements of the matrix [188].

$$t_{mn} = (2I_m^0 - I_m^{2\pi/3} - I_m^{4\pi/3})/6 + \sqrt{3}i(I_m^{2\pi/3} - I_m^{4\pi/3})/6 \quad (6.6)$$

By measuring the transmission matrix for certain receiving position of m , we can obtain the matching phase mask t'_{mn} (applied to the SLM screen) by calculating the conjugate transpose matrix of the transmission matrix t_{mn} . TM method is operated as follows:

1. For a given receiving position m , do steps 2–4 for all input channels;
2. Set the phase retardation of the segment n with respect to others to I_m^0 , $I_m^{2\pi/3}$, and $I_m^{4\pi/3}$;
3. Measure the I_m^0 , $I_m^{2\pi/3}$, and $I_m^{4\pi/3}$ intensities, respectively;
4. Set $t_{mn} = (2I_m^0 - I_m^{2\pi/3} - I_m^{4\pi/3})/6 + \sqrt{3}i(I_m^{2\pi/3} - I_m^{4\pi/3})/6$;
5. Set the SLM phase map according to the phases of t'_{mn} .

Normally, the TM algorithm only requires three measurements per segment to calculate the optimum phase map. But I_m^0 can be measured for all segments with a single measurement (all phases can be set to zero). The TM matrix will yield the optimum phase map after only $2N+1$ measurements. Here is 513.

6.2.2 Experimental setup

Figure 6.9 describes a 40-Gbit/s indoor NLOS OWC system enabled by CAO-Tx. In this experiment, a laser at 1550 nm is used as the optical source with 6-dBm output power. A 40-GBaud/s OOK signal is modulated onto the optical carrier by an SHF transceiver (SHF 46210C). The output signal is amplified via an EDFA (EDFA-1) to 10 dBm (the radiated power from collimator). Afterward, a PC (PC-1) and a polarizer are used to align the polarization state between the free-space light and the SLM. A collimated Gaussian beam is then incident on the SLM (HOLOEYE, PLUTO Phase Only SLM). 1024 pixels on the SLM screen are activated, which are further grouped into segments of 128×128 pixels, yielding a total of 16×16 segments. All pixels in a segment are simultaneously modulated by the same phase within 0 to 2π . After the phase modulation, a lens (Edmund Optics: ACH-NIR 50×150 NIR) is utilized to adjust the beam size onto a diffusion surface (e.g. ceilings or walls), which emulates the rough surface in an indoor scenario. Here, a standard material—Thorlabs polystyrene screen (EDU-VS1/M) is applied. Detailed information can be

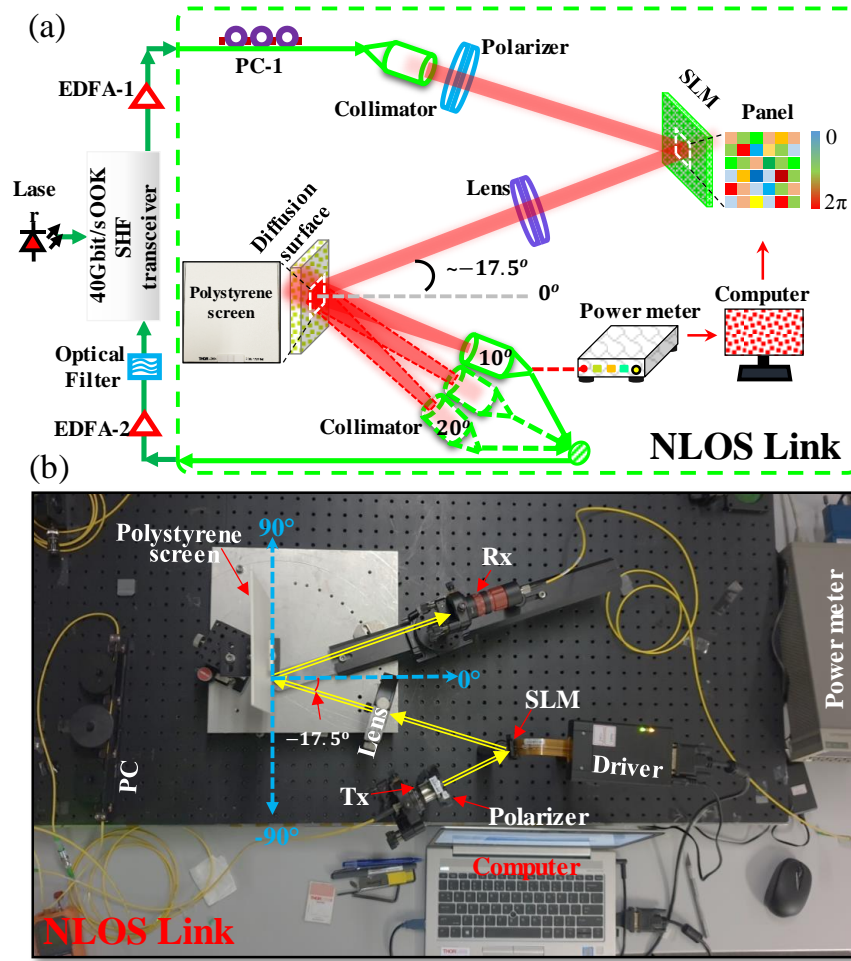


Fig. 6.9 (a) Experimental setup; (b) the photo of the NLOS link. EDFA: Erbium-doped Fibre Amplifier; PC: polarization controller; SLM: spatial light modulator; Tx: transmitter; Rx: receiver.

found on its website. The angle between the SLM-modulated beam and the normal of the diffusion surface is $\sim 17.5^\circ$, and we define the normal of the diffusion surface as 0° as shown in Fig. 6.9 (b). Thus the incident angle is defined as -17.5° . To match a fibre/waveguide-based high-speed photodetector, the diffusely reflected light is coupled into a single-mode fibre using a collimator (ZC618FC-C) which is 25-cm far from the surface. The receiving fibre is mounted on a movable stage, allowing an angle change. An optical power meter is used to provide feedback for the wavefront-shaping algorithm to enhance light intensity at the receiver. The received optical signal is pre-amplified via a second EDFA (EDFA-2) before detection. An optical filter is used to eliminate out-of-band noise. Finally, the signal is detected and processed in the SHF transceiver.

6.2.3 Results and discussions

Algorithm comparison:

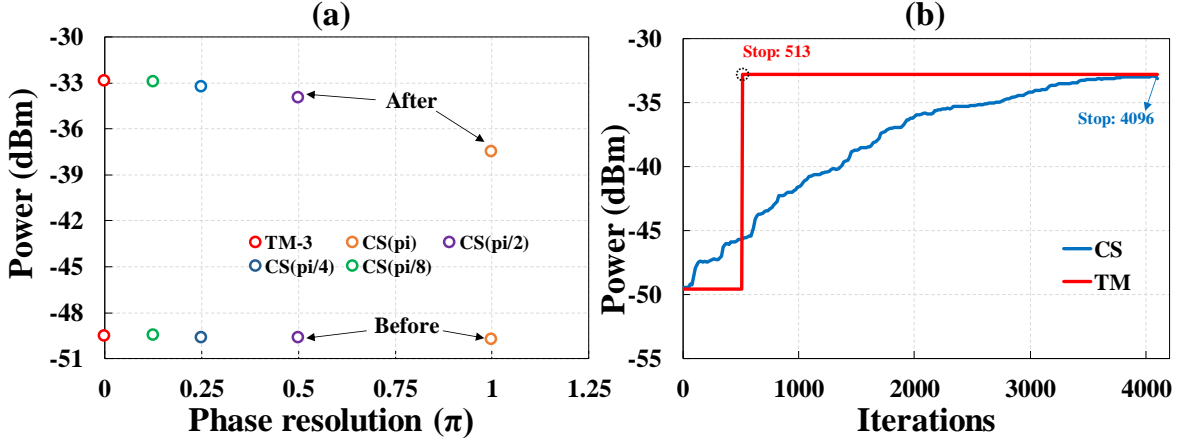


Fig. 6.10 The performance of the (a) enhancement; (b) time-consumption

In this part, we will discuss the speed and performance of the newly introduced TM algorithm by comparing it to the continuous sequential (CS) algorithm, which is widely used in optical wavefront shaping. Firstly, the activated area of the SLM screen is divided into 16×16 segments and each segment will do the phase-optimization. For the CS scheme, each segment is phase-modulated from 0 to 2π in increments of π , $\pi/2$, $\pi/4$, and $\pi/8$ respectively to search the power-optimized phase. Then repeat this procedure segment-by-segment until obtaining the completed 16×16 phase map, which is the final mask for a certain angle enhancement. The required number of iterations for single enhancement is 512, 1024, 2048, and 4096, respectively. Hence, the smaller the increment is used the slower the optimization will be. While, for the TM method, the required number of iterations is fixed at 513 ($2N+1$, if the matrix size is changed, this number will change as well.). The target phase is not obtained directly but obtained through calculation. In the experiment, five cases are compared under the same experimental conditions. Before enhancement, originally received power is -49.6 dBm. After that, the power is changed to -32.8 dBm (TM), -32.9 dBm (CS- $\pi/8$), -33.27 dBm (CS- $\pi/4$), -34.0 dBm (CS- $\pi/2$), and -37.5 dBm (CS- π), respectively. Obviously, TM and CS- $\pi/8$ have the almost same performance, under which the performance of the time-consumption is evaluated by using the number of iterations. As shown in Fig. 6.10 (b), TM only takes one-eighth of the time of CS- $\pi/8$'s.

Enhancement evaluation:

Enabled by the TM method, the optimization is explored in a large angular range ($>90^\circ$ single-side span) as presented in Fig. 6.9 (b). Using the parameters in **section 6.2.2**, the light intensity before and after enhancement is measured, sweeping a $>90^\circ$ range. Fig. 6.11 depicts the measured power before and after optimization with different incident angles. When the incident angle is fixed at -17.5° , the measured power before enhancement is random between -42.9 dBm and -62.2 dBm, which is mainly due to a diffusion-surface-caused random intensity pattern. After the enhancement, the power curve becomes very smooth with a measured 3-dB (from

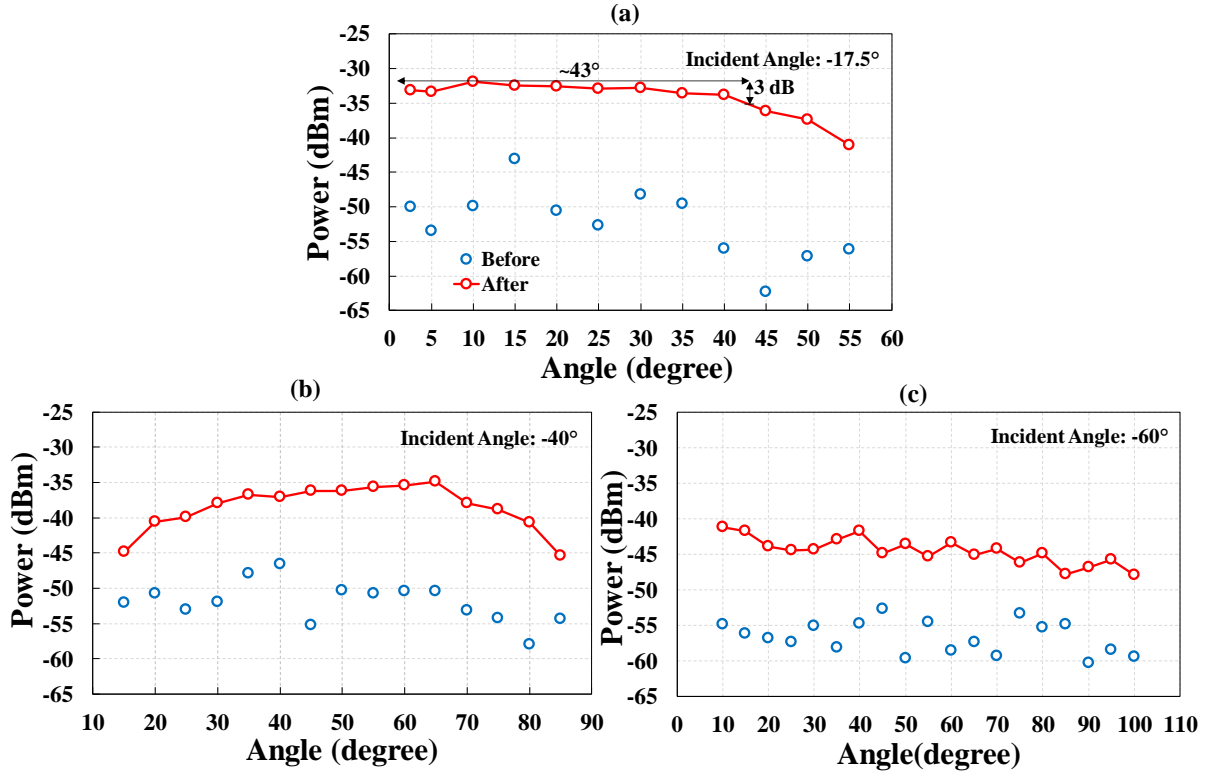


Fig. 6.11 The measured algorithm performance. The measured power enhancement performance (a) with -17.5° (b) with -40° (c) with -60° incident angles.

-32 dBm to -35 dBm) angular range of $>40^\circ$. The average intensity improvement is above 18 dB, which significantly improves the signal-to-noise ratio of a diffuse NLOS link. Then an incident angle of -40° and -60° is tested, respectively. The similar power enhancement can be obtained – an average power gain is 13.40 dB and 12.10 dB but with a loss increase of ~ 4 -dB and ~ 10 -dB, respectively. The angular range shifts towards a larger angle direction as well. Hence, properly increasing the incident angle can help extend the angular range. If we change the incident angle to their positive counterpart such as 17.5° , then a range from -43° to 0° can be also covered. This means the double-side coverage is at least $>80^\circ$.

Transmission investigation:

Finally, the data transmission is conducted at four receiving directions/angles (10° , 20° , 30° , and 40°) with -17.5° incident angle). BER curves are depicted in Fig. 6.12 (a). It is clear that the BER performance at the limit of 1×10^{-3} does not experience an apparent decrease when increasing the receiving angle (<0.4 dB). $>40^\circ$ single-side coverage range can be experimentally achieved at a 40-Gbit/s data rate. Fig. 6.12 (b) presents the optical spectra before and after enhancement at the receiver side.

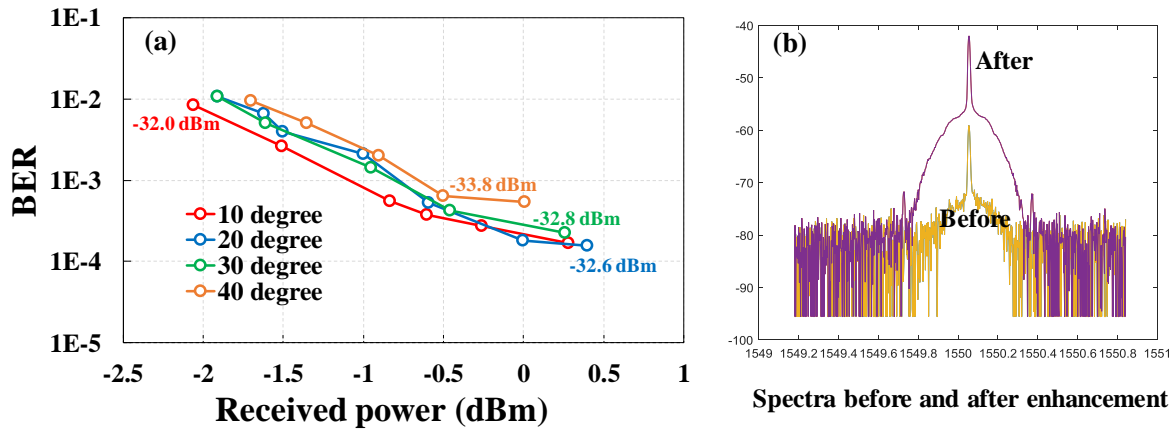


Fig. 6.12 (a) the measured BER-to-power curves at different receiving angles; (b) optical spectra before and after power enhancement.

6.2.4 Conclusion

A new record 40-Gbit/s (data rate) NLOS beam-steered OWC system by the proposed diffuse reflection focusing is experimentally implemented. Faster TM enhancement controlling algorithm is introduced with only 513 iterations. An average 18-dB-power-enhancement and a double-side-range of $>80^\circ$ are employed over a 25-cm free-space link. All these features exhibit its great potential for high-speed indoor wireless communications.

6.3 Chapter summary

Normally, current NLOS wireless communication for indoor applications is mainly based on the diffusely-reflected broadcast light, which does not address the diffusion mechanism itself. It is less energy-efficient and relatively low-speed. In this chapter, a breakthrough method, namely DRF, has been proposed, analyzed, experimentally demonstrated and discussed for the energy-efficient NLOS OWC. Using general material and wavefront shaping algorithm, a record 40-Gbit/s data rate is implemented for the first time, which provides a new idea to overcome the speed bottleneck for NLOS indoor wireless connectivity.

CHAPTER 7

FREE-SPACE OPTICAL FIELD MEASUREMENT SYSTEM

Free-space light is becoming more attractive due to its wide application in LiFi, OWC, and Lidar. The measurement of the free-space optical field radiated from a generator (e.g. free-space radiating lasers or gratings) is frequently required, not only its intensity but its phase response as well. Especially for optical antennas on-chip for optical beamforming or Lidar, the measurement of its field distribution is a significant evaluation of the performance. In terms of our research, direct motivation is the spatial FOV measurement of grating-based optical antennas on a tiny photonic chip, which requires a complicated system including both mechanical and optical designs. But the available commercial products do not exactly meet the requirements of the measurement. Therefore, we designed our own tool/equipment. In this chapter, I will show a system that can measure free-space optical patterns, introducing the functional design and parameters in detail. Then the characterization in an application in Lidar measurement is also presented.

7.1 System design

system parameters:

Fig. 7.1 depicts the optical free-space measurement system. At the bottom, it is a base that carries the whole architecture and weight. Inside the station, there is a central control unit with an interactive interface - a touch screen. Through the control panel, users can input their orders to control the turntable to rotate in the horizontal direction and the swing arm to sway in the vertical direction. It also supports mode switching between automatic and manually-controlled movement, which is discussed in the part of system control mode. In the center, it is a non-rotating central supporting platform that carries optical antennas (or chips) and their affiliated optical/mechanical architectures. The diameter of the platform is 400 mm and the height is tunable in a 110-mm range as shown in 7.1 (b). The required horizontal rotation is realized by a turntable under this platform. The turntable is drove by a 400-W servo motor which is further controlled by a programmable logic controller (PLC, Matsushita AFPXHC40T). It supports a full angular rotation of 0-360° with an accuracy of 0.4°. The turntable carries a 300-mm-high swing arm with two legs supporting a maximum $\pm 90^\circ$ adjustment in the vertical direction. This movement is implemented by another servo motor with an angular accuracy of 0.3°. At the right above, a tunable holder for optical detectors is mounted onto the swing arm. The holder can be adjusted to any position along the swingarm manually. The

height from the detector to the device under test (DUT) can be shifted between 150 mm to 260 mm for the pattern measurement at different distances. It should be pointed out that the DUT should be put at the center of the rotating axis of the swing arm as shown in Fig. 7.1 (the red-point position). Besides, two sensors are installed to prevent the turntable and the swing arm from going beyond the utmost positions.

At the beginning of our design, the probable applications were considered. First, the detector holder can be changed by other options such as a camera and a fibre-based collector. Moreover, the current holder can support different types of detectors. Considering the demand for a longer measurement distance, the swing arm is designed as a combination of three individual parts - two legs and a beam. The height of the swing arm can be extended by replacing longer legs. For some cases that require a single-leg swing arm with a larger operational space, the current structure can be changed using a single driving leg. The maximum load torque is 3.8 n·m. To protect the motor when the load is too heavy, the dual-leg architecture is needed.

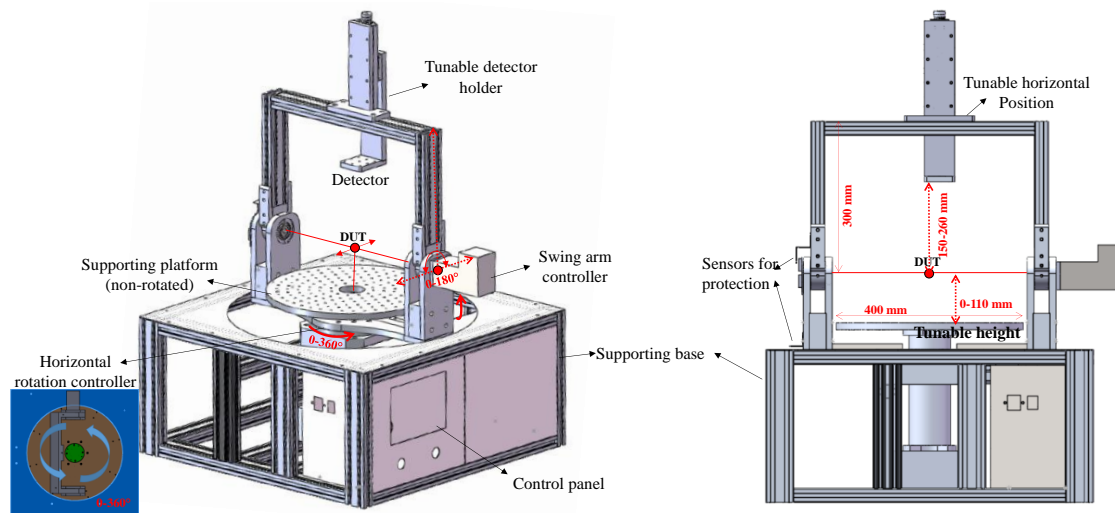


Fig. 7.1 The system setup.

system controlling mode:

The control of the optical field measurement system is implemented by two servo motors. Their controlling mode can be divided into three types, namely the automatic movement, the manual movement, and the joint movement. For the first two types, they are valid for the separate control of the turntable and the swing arm. In the automatic mode, a user needs to set a start position (angle) and a stop position (angle), then the servo motor can automatically move according to the set range. The moving speed is tunable with a maximum value of $10^\circ/\text{s}$. The manual control has a similar speed setting, but the user has to manually sweep a certain range. In addition, this measurement system can also support a joint movement of the two motors, which enables an automatic sweeping of a hemispherical surface.

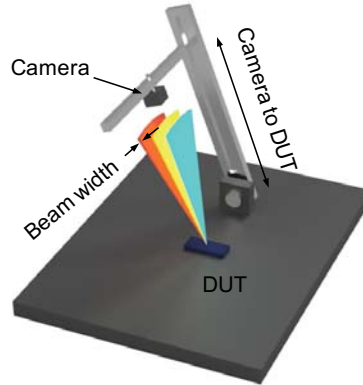


Fig. 7.2 Schematic of the measurement setup (illustrative, not-to-scale). The distance between the camera and the device under test is measured from the camera sensor to the wafer upper surface [189].

7.2 Characterization

The feasibility of the free-space optical field measurement system is proved in the measurement of InP-based grating antennas [189, 190]. This system is first applied to the direct far-field characterization of grating antennas on-chip as shown in Fig. 7.2. An infrared camera is utilized to capture the optical far-field image. It is mounted to a swing arm capable of $\pm 90^\circ$ swing at a 52-cm radius, and the chip is mounted at the rotation center. In this application, a single-leg swing arm is used to increase the distance between the detector and the DUT. By scanning the camera and stitching the captured images, a far-field pattern and a steer map can be obtained.

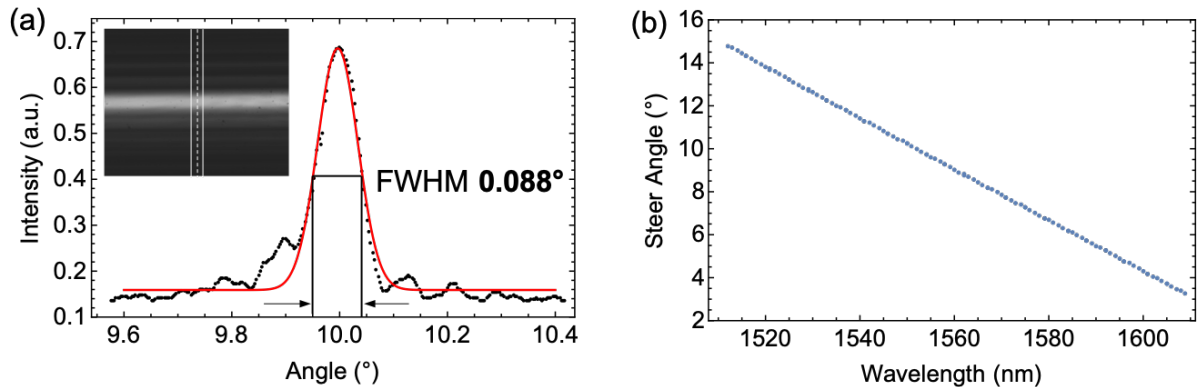


Fig. 7.3 Measured far-field pattern of the grating antenna. (a): Far-field beam profile (dotted) and gaussian fit (red line) showing a FWHM of below 0.1° . Inset: Original far-field image captured by the camera and the pixel-averaging region (white, illustrative). The cross-sectional beam profile was 5 pixel-averaged. (b): Steer map of the grating antenna by tuning the input wavelength. [190].

Antennas based on waveguide surface gratings is a type of optical phased arrays. The width of the emitted beam, quantified by the divergence angle at full width half maximum (FWHM), is a significant factor to evaluate the quality of the grating-based antenna. As shown in Fig. 7.3 (a), the FWHM obtained is 0.088° at $\sim 10^\circ$ angle,

combining with a steering range of $\sim 12^\circ$ by tuning the wavelength in a range of ~ 100 nm as presented in Fig. 7.3 (b). This experiment proves the effectiveness of the proposed optical field measurement system.

7.3 Chapter Summary

In conclusion, this chapter introduces a free-space optical field measurement system. By selecting different detectors, it supports multiple applications such as the pattern measurement of optical phased antennas and LED/laser sources. If the detector is an RF antenna, then field characterization of an RF antenna can be implemented as well. By using the designed system, a far-field measurement of an on-chip optical phased antenna is achieved.

SUMMARY AND FUTURE OUTLOOK

8.1 Summary

In this research work, efforts have been made towards innovative indoor wireless communication techniques realizing a very high capacity by means of advanced photonic methods. The explorations and achievements have been made by deploying several novel technologies including the mode/spatial multiplexing utilizing RF waves and the beam-steered LOS/NLOS communication utilizing optical waves. A free-space optical field measurement system is designed and experimentally verified as well.

The **first innovative technique** is the OAM multiplexing using RF waves. The key findings from the research in this direction are:

- **A bi-directional tunable integrated optical delay network for CAA-based RF-OAM activation** is proposed, simulated and experimentally demonstrated in this dissertation. Enabled by an imbalanced power-control, a compact 1-by-2 broadband time delay array is achieved with a 20-GHz double-sided bandwidth and a delay range continuously tunable over ± 13 -ps. The bi-directional tunable delay between two outputs is implemented by tuning a single phase-element, which enables a simpler controlling architecture. To the best of our knowledge, this is the first time that such a compact bi-directional ODN concept is proposed. As a basic building block, it can be used to build more complex true time delay networks for a high antenna-count RF-OAM generation. This work is presented in **Chapter 3**. Besides, it should be pointed out that, the novel bi-directional ODN can also be applied to generate the necessary delays for mm-wave beam steering in **Chapter 4**.
- A series of optical phased antenna arrays for broadband CAA-based RF-OAM activation is proposed and chip-designed in photonic integrated circuit technology in order to obtain broader band OAM modes.
 - **The optical 90° Hybrid-based passive phased array** is proposed to support the switch between three OAM modes of $l=0$ and $l=\pm 1$ by changing the optical wavelength. In this architecture, it enables a remote control without requiring any active controlling elements at the antenna side, which reduces the complexity of antennas. To obtain the optical phase shift and transfer it to RF signals, an optical filter on-chip is needed to split two phase-locked wavelengths before going into the passive phased

array. As to the filter design, two types are introduced – a filter utilizing cascaded MZIs (with different FSRs) and a filter utilizing MZI and ORRs. The former is a passive design with narrow bandwidth, while the latter is based on thermal optics (active control) with relatively higher bandwidth. Thus in terms of the whole network, the optical 90° hybrid-based phased array techniques are purely passive and half passive methods. Even for the half passive scheme, the active control needs to be set only once at the beginning of the system initialization.

- The other type is **the thermally-controlled phased array**. As a fully re-configurable scheme to support a higher antenna-count system, it can provide continuous phase shift and mitigate the phase error from fabrication. Two types of OAM mode switch – the thermal control and the wavelength control can be supported. By using the thermal controlling method, a user can access any supported OAM mode by the CAAs. But for the wavelength tuning mode, it is only valid for two modes – the positive and the counterpart negative ones. Similarly, the corresponding on-chip filter can be selected in the two types mentioned above. Thus such a kind of phased arrays requires frequent active-control. There will be a tradeoff between the supported number of OAM modes and the complexity of the antenna control.

The **second innovative technique** is the mm-wave beam steering utilizing integrated photonic tunable delay networks. The key findings from the research in this direction are:

- The first achievement is the realization of the looped-back AWG-based beam-former on-chip. It is a stepwise-tunable optical true-time delay network including a looped-back AWG and delay-offset waveguides. This work is based on photonic chip-level techniques aiming to implement a higher delay resolution per area, comprising the investigation of chip size reduction and the investigation of resolution increase from basic component designs to system designs.
 - First, by using a compact integrated technology – SOI photonic integrated circuits, a size-reduced transmission-type 5-by-5 AWG is experimentally implemented with a size of $367\ \mu\text{m}$ -by- $540\ \mu\text{m}$. Enabled by the integrated technology, the size-reduced basic component (AWG) can help improve the resolution density on-chip.
 - The second one is a further improvement on basic AWG design to reduce its footprint. In addition to the benefit of a similar compact integrated technology – IMOS photonic integrated circuits, a reflection-type architecture is introduced to the AWG design as well. Considering the double-fold reduction, the IMOS-based reflection-type AWG further shrinks the area on

a chip. By using high reflection photonic crystal reflectors, the reflection-type AWG is implemented with a size of $680 \mu\text{m} \times 190 \mu\text{m}$ and yields a performance of 6.7-dB insertion loss and 10-dB crosstalk attenuation. It enables a 35% size-reduced footprint at a cost of 1.1-dB extra loss compared with the traditional transmission-type AWG. The ultra-small 5.4-by-0.7 μm^2 PCR can realize $> 90\%$ reflectivity.

- Then an architecture improvement is made to double the delay resolution of the looped-back-AWG-based dual-port beamformer from the on-chip system-level. Enabled by extending the positive delay to its negative counterpart using the spatially-switching method, a doubled delay time resolution in a specially designed bi-directional beamformer can be obtained. It is fabricated in a generic InP platform and is experimentally characterized. The measured IL of the delay network is < 17.5 dB (a looped-back AWG (6.4 dB), a bi-directional hybrid coupler (7.94 dB) and a multimode interferometer (3 dB)). An imbalance of ~ 1 -ps between positive and negative delays has been implemented.
- Based on the spatially-switched dual-port beamformer, which requires an active control, an upgraded design is proposed for the purely passive target. By introducing an extra AWGR with two outputs connecting to the two spatially separate inputs of the beamformer mentioned above, a wavelength-tuned design is achieved with doubled delay resolution. It reduces the complexity of the antenna side.
- The proposed purely wavelength-tunable dual-port beamformer on-chip is evaluated in a 38-GHz mm-wave beam steering system with very high accuracy. It proves the effectiveness of the integrated optical mm-wave beamformer.

The **third innovative technique** is the beam-steered LOS communication utilizing optical waves. The key findings from the research in this direction are:

- The first improvement is the implementation of a crosstalk-mitigation scheme for the AWGR-based optical beam steering system. In this system, the 2D square-arranged output fibre array of an AWGR followed by a lens with high aperture can steer the optical beams from different fibres to different 2D directions. The spatial coverage is determined by the port-count of the AWGR. By creating polarization orthogonality between the odd and even channels, a very high crosstalk tolerance between spectrally overlapping AWGR channels can be achieved. Such overlap means higher spectral efficiency, which provides a new solution for a higher port-count AWGR because it can be implemented simply by reducing the spatial gap between output waveguides on a chip, which allows a low-complexity high port-count AWGR design. A 20-Gbit/s data rate OWC capacity using PAM-4 format has been obtained over 1.2-m free-space link. Moreover, the AWGR and the following 6-by-6 fibre array (100 μm spacing) are put into a photonic chip using the silicon photonic integration

technology, which allows an extremely small transmitter. Together with a size-reduced lens, the AWGR-based beam steerer can be made very compact.

- An energy-efficient optical beam steering scheme generating optical gratings on an SLM is proposed by using Polar coordinate (1D grating + angular rotation) instead of the traditional Cartesian coordinate (1D grating in horizontal + 1D grating in vertical). In polar coordinate, the angle rotation in an SLM is quasi-continuous in a range of full 2π . Based on the concept of the rotation gratings, a FoV of 18° is experimentally demonstrated by using a reflective SLM and a simple 1D grating. An optical wireless transmission speed of 40-Gbit/s is also implemented using OOK data over 1-km standard single-mode fibre and 0.5-m free space.

The **fourth innovative technique** is the beam-steered NLOS communication utilizing optical waves. The key findings from the research in this direction are:

- For the first time, a breakthrough solution for the long-term challenge of the indoor NLOS OWC has been proposed by using diffuse reflection (a rough surface) and an optical wavefront shaping technique. By spatially modulating the light incident on a rough ceiling/wall, the light diffusely reflected towards the receiver is focused. The focusing capability of a diffusely reflected beam at distances of 0.11 m to 1.5 m is experimentally measured. A record-breaking 30-Gbit/s OFDM signal is transmitted over an indoor diffuse NLOS link with a >17 -dB gain, in an angular range of 20° , and over a distance of 0.11 m from the diffuse reflector.
- Then the extensively improved NLOS OWC system is demonstrated by the proposed diffuse reflection focusing. In this work, the performance has been enhanced with a higher record 40-Gbit/s data rate, a faster TM enhancement controlling algorithm (requires only 513 iterations), a larger average 18-dB-power enhancement, a wider double-side-range of $>80^\circ$, and a longer 25-cm free-space link. All these features exhibit its great potential for high-speed indoor wireless communications.

Finally, a free-space optical field measurement system is designed and implemented in this dissertation. It can be used to measure the far field distribution of an optical free-space radiated antenna and an electrical antenna with flexible architecture adjustment such as measuring distance tuning and receiver replacement. The mechanical design is presented in detail and the effectiveness of the measurement system is verified in a far-field measurement of an on-chip optical phased antenna.

8.2 Future outlook

A number of points for future work regarding the **first technique** of the optically controlled OAM multiplexing using RF waves are:

- **To implement the photonic time-delay-based RF-OAM activation using a CAA**, tunable integrated optical delay arrays are needed. The following are the recommendations regarding future research directions:
 - (I) Utilize multiple individual integrated OTDLs to compose a multi-port delay array for a CAA, which is very simple but may increase the size of beamformer and cannot easily implement the bi-directional time delay; (II) Utilize the proposed concept of the more compact bi-directional ODN. The dual-port array needs to be extended to support the large antenna-count RF-OAM generation. The network layout has to be specially designed towards a larger-scale network, where the aspects of port-count, insertion loss, chip size, energy consumption, and bi-directional settings need to be considered. Further research on how to increase the tunable delay range and how to reduce the power imbalance between the two output ports is recommended. This may be achieved by properly setting the available bandwidth and the power split ratio. Besides, a CAA is another necessary element that can be newly designed or for which a commercial one can be selected. Then the system demonstration needs to be made to evaluate the feasibility of the time-delay-based RF-OAM activation.
- **For a higher quality RF-OAM mode** that requires broadband optical phased arrays, passive and active phased arrays are proposed for different application environments. The recommendations regarding future research directions are: Currently, the **optical 90° Hybrid-based passive phased array** can support a four-antenna system and thus three OAM modes. There are still several challenges. The first one is the phase error that may be caused by fabrication and imperfect designs. Thus the 90° Hybrid design needs to be improved. Normally there are two types – 4-by-4 MMI and a combination of individual 1-by-2/2-by-2 MMIs. For the former, it has more accurate phases but it is not easy to do the design. The latter is relatively easier and smaller but is more sensitive to fabrication errors [146]. The other challenge is the implementation of a complementary optical filter on-chip such as the interleaver and the cascaded MZI-based filter. The existing filters are recommended to be characterized and further structure/parameter changes may be required for better performance or different applications. For example, the filter should be able to have a very sharp spectral shape and a small FSR to split two closely spaced wavelengths. To provide more ports to a larger antenna-count (>4) CAA, how to enlarge the passive array dimension and support multi-mode switching is still a challenge. Fortunately, **the thermally-controlled phased array** can maintain the requirement of the scaled-up array. This fully reconfigurable scheme requires many active controls that might complicate the antenna side and reduce system stability. A better system controlling algorithm may help solve this problem. In terms of the heater-based thermal controller, its operational speed is very limited and thus it is hard to support high-speed applications. A faster phase shift will be a new trend, which can be solved

by replacing the thermal controller with a high-speed modulator. This might bring an even more complicated antenna, thus further research is needed.

Topics for future work regarding the **second technique** of the optically-controlled looped-back-AWG-based mm-wave beam steering are:

- **The performance of a single AWG** is essential for the optical mm-wave beam-former. Its parameters such as size, channel crosstalk, channel spacing, and port-count needed to be further improved. Since a large-scale 2D delay array is required for 2D mm-wave beam steering, the chip size needs to be densely integrated. Thus the reflection-type AWG using compact integrated technologies provides a promising solution. To increase the number of discrete delays, the AWG needs a higher port-count. This can be achieved by narrowing the channel spacing and/or increasing chip size. But it may affect other parameters such as increasing the channel crosstalk, hence the design of advanced AWGs needs to be further investigated.
- Besides, **the structure layout on system-level** requires further research. In this thesis, we only demonstrate the dual-port bi-directional 1D delay network. Extending the network from 1D to 2D is necessary for 2D mm-wave beam steering, which requires two types of AWG with different FSRs and each one is for a separate dimension. Taking the extension of the delay network into consideration, the design of the looped-back-AWG-based 2D delay network will be very different due to the impacts of wavelength misalignment, fabrication errors, system loss, power imbalance, and so on. Thermally-controlled compensation might help solve the misalignment problem. But more advanced (maybe more complicated) on-chip system-level circuits are needed to tackle problems of the loss and the power split ratio.
- **The transmitter realization combining the photonic beamformer and the electronic antenna sub-system** is the third aspect that needs to be paid more effort to. Normally, O/E conversion via a photodiode is done on a chip, and the connection can be done through wire bonding. But the antenna sub-system is separate and requires a large amount of work in the electrical domain such as the design of amplifiers and antennas.

Topics for future work regarding the **third technique** of the beam-steered LOS OWC are:

- For indoor OWC, **a transmitter with a large spatial coverage** is required for a realistic system. To increase the coverage of an AWGR-based 2D beam steering system, it requires a high port-count AWGR. By using the proposed crosstalk mitigation scheme in **Chapter 5**, the channel spacing of an AWGR can be reduced, which allows a higher port-count. Current commercial AWGRs aims at the telecom applications with wide channel spacing and small crosstalk. So

a port-count-increased AWGR can be designed by reducing channel spacing with higher crosstalk. Such an AWGR could increase the 2D coverage of the beam steering system without introducing apparent distortion to the signals. Moreover, the on-chip AWGR-based 2D beam steerer is proposed and being fabricated in IMEC platform, which enables a more compact transmitter. The chip measurement and the further system assembly (beam steerer and a small lens) and measurement need to be paid further efforts.

- **A receiver with wider FoV** is one of the most significant elements at the user side. In **Chapter 5**, the rotated-grating-based receiver with an 18° FoV is demonstrated. But the power loss is pretty high, which needs to be reduced via finer alignment and architecture improvement such as changing a reflection-type SLM and increasing the lens's aperture. Besides, a small photodiode array as a receiver can improve the FoV with relatively high bandwidth.

Topics for future work regarding the **fourth technique** of the beam-steered NLOS OWC are:

- **The beam reconfigurable NLOS OWC system** enabled by diffuse reflection focusing implemented in **Chapter 6** brings a breakthrough high-speed (40 Gbit/s) NLOS optical wireless communication for indoor. As a new research area, many technical issues need to be investigated. From the perspective of realistic applications, the first improvement should be on the speed of building the NLOS link (focus the diffuse light with high power optimization). Although, the Transmission Matrix algorithm has been applied and has an 8-times faster adjustment compared with the first-generation system, it still requires a faster rebuild of an NLOS link to keep tracking of the users' movement. More advanced techniques such as faster algorithms, pre-scanning, and faster equipment can be used to further accelerate this procedure. Further research is needed for the material selection of the diffuse reflector, which requires low cost and a high reflection ratio (reduced power loss). There is a tradeoff between the steered angular range of the NLOS link and the received optical power for a fixed incident angle. Normally, a larger angular range means a lower received power. Thus the angular coverage needs to be further discussed in future research. To increase the angular range without sacrificing received power, changing the incident angle of the light illuminated onto a rough surface mentioned in **Chapter 6** would help. The multi-transmitter architecture might also help to extend the spatial coverage. Another factor is the reach of the NLOS link, which is limited by the received power. Using a detector with higher sensitivity and reducing the length of the NLOS link by steering the light beam to the rough surface that is close to the user can enlarge its working distance. Based on a faster diffuse light focusing, the higher power enhancement (with inherent high time-consumption drawback) can be considered as an option for increasing the energy-efficiency of the NLOS

link. Of course, the transmission speed needs to be further increased by using higher bandwidth modulators, higher-order modulation formats, and more advanced DSP algorithms.

As to the optical field measurement system, higher accuracy of the mechanical movement is needed, which can be implemented by using a higher-quality servo motor. Besides, an extremely accurate optical alignment needs further research because it involves both careful optical alignment and mechanical alignment. Over-sampling and advanced DSP techniques might improve the alignment accuracy. The mechanical architecture still needs to be updated in order to support more complicated applications.

REFERENCES

- [1] V. Cisco, "Cisco visual networking index: Forecast and trends, 2018–2023," *White Paper*, vol. 1, 2020.
- [2] Huawei, "Huawei global industry vision," *White Paper*, vol. 1, 2019.
- [3] N. S. et al., "Light Communications for Wireless Local Area Networking," 2018. [Online]. Available: <https://futurenetworks.ieee.org/tech-focus/may-2018/light-communications-for-wireless-local-area-networking>
- [4] V. Pereira and T. Sousa, "Evolution of mobile communications: from 1g to 4g," *Department of Informatics Engineering of the University of Coimbra, Portugal*, 2004.
- [5] M. Meraj and S. Kumar, "Evolution of mobile wireless technology from 0g to 5g," *Int. J. Comput. Sci. Inf. Technol*, vol. 6, no. 3, pp. 2545–2551, 2015.
- [6] Qualcomm, "The Evolution of Mobile Technologies: 1G to 2G to 3G to 4G LTE | Qualcomm," 2014. [Online]. Available: <https://www.qualcomm.com/documents/evolution-mobile-technologies-1g-2g-3g-4g-lte>
- [7] J. A. del Peral-Rosado, R. Raulefs, J. A. López-Salcedo, and G. Seco-Granados, "Survey of cellular mobile radio localization methods: From 1g to 5g," *IEEE Communications Surveys & Tutorials*, vol. 20, no. 2, pp. 1124–1148, 2017.
- [8] wikipedia, "LTE (telecommunication)," 2014. [Online]. Available: [https://en.wikipedia.org/wiki/LTE_\(telecommunication\)](https://en.wikipedia.org/wiki/LTE_(telecommunication))
- [9] M. Z. Chowdhury, M. Shahjalal, M. Hasan, Y. M. Jang *et al.*, "The role of optical wireless communication technologies in 5g/6g and iot solutions: Prospects, directions, and challenges," *Applied Sciences*, vol. 9, no. 20, p. 4367, 2019.
- [10] A. Ijaz, L. Zhang, M. Grau, A. Mohamed, S. Vural, A. U. Quddus, M. A. Imran, C. H. Foh, and R. Tafazolli, "Enabling massive iot in 5g and beyond systems: Phy radio frame design considerations," *IEEE Access*, vol. 4, pp. 3322–3339, 2016.
- [11] K. David and H. Berndt, "6g vision and requirements: Is there any need for beyond 5g?" *IEEE Vehicular Technology Magazine*, vol. 13, no. 3, pp. 72–80, 2018.
- [12] F. Tariq, M. Khandaker, K.-K. Wong, M. Imran, M. Bennis, and M. Debbah, "A speculative study on 6g," *arXiv preprint arXiv:1902.06700*, 2019.
- [13] S. J. Nawaz, S. K. Sharma, S. Wyne, M. N. Patwary, and M. Asaduzzaman, "Quantum machine learning for 6g communication networks: State-of-the-art and vision for the future," *IEEE Access*, vol. 7, pp. 46 317–46 350, 2019.
- [14] R.-A. Stoica and G. T. F. de Abreu, "6g: the wireless communications network for collaborative and ai applications," *arXiv preprint arXiv:1904.03413*, 2019.
- [15] W. Saad, M. Bennis, and M. Chen, "A vision of 6g wireless systems: Applications, trends, technologies, and open research problems," *IEEE network*, 2019.

- [16] Finland, "Academy of Finland Communications: Academy of Finland selects first two competence clusters to the new Flagship Programme," 2019. [Online]. Available: <https://www.aka.fi/en/about-us/media/press-releases/2018/academy-of-finland-selects-first-two-competence-clusters-to-the-new-flagship-programme/>
- [17] E. Commission, "Quantum Technologies Flagship," p. January 20, 2020. [Online]. Available: <https://ec.europa.eu/digital-single-market/en/quantum-technologies>
- [18] wikipedia, "Wi-Fi," 2020. [Online]. Available: <https://en.wikipedia.org/wiki/Wi-Fi>
- [19] —, "IEEE 802.11b," 1999. [Online]. Available: https://en.wikipedia.org/wiki/IEEE_802.11b-1999
- [20] —, "IEEE 802.11a," 1999. [Online]. Available: https://en.wikipedia.org/wiki/IEEE_802.11a-1999
- [21] —, "IEEE 802.11g," 2003. [Online]. Available: https://en.wikipedia.org/wiki/IEEE_80211g-2003
- [22] —, "IEEE 802.11n," 2009. [Online]. Available: https://en.wikipedia.org/wiki/IEEE_802.11n-2009
- [23] —, "IEEE 802.11ac," 2013. [Online]. Available: https://en.wikipedia.org/wiki/IEEE_802.11ac
- [24] B. Bellalta, "Ieee 802.11 ax: High-efficiency wlans," *IEEE Wireless Communications*, vol. 23, no. 1, pp. 38–46, 2016.
- [25] wikipedia, "IEEE 802.11ad," 2012. [Online]. Available: https://en.wikipedia.org/wiki/IEEE_802.11ad
- [26] T. Baykas, C.-S. Sum, Z. Lan, J. Wang, M. A. Rahman, H. Harada, and S. Kato, "Ieee 802.15. 3c: The first ieee wireless standard for data rates over 1 gb/s," *IEEE Communications Magazine*, vol. 49, no. 7, pp. 114–121, 2011.
- [27] D. Vishwanath, A. Mckinnon, and Y. Bian, "Indoor digitalisation-the new era by small cells," *Huawei White Paper*, 2015.
- [28] C. Seker, M. T. Güneser, and T. Ozturk, "A review of millimeter wave communication for 5g," in *2018 2nd International Symposium on Multidisciplinary Studies and Innovative Technologies (ISMSIT)*. IEEE, 2018, pp. 1–5.
- [29] T. S. Rappaport, G. R. MacCartney, M. K. Samimi, and S. Sun, "Wideband millimeter-wave propagation measurements and channel models for future wireless communication system design," *IEEE Transactions on Communications*, vol. 63, no. 9, pp. 3029–3056, 2015.
- [30] A. M. Al-Samman, T. A. Rahman, M. Hindia, A. Daho, and E. Hanafi, "Path loss model for outdoor parking environments at 28 ghz and 38 ghz for 5g wireless networks," *Symmetry*, vol. 10, no. 12, p. 672, 2018.
- [31] F. Hossain, T. K. Geok, T. A. Rahman, M. N. Hindia, K. Dimyati, S. Ahmed, C. P. Tso, A. Rahman, and N. Ziela, "An efficient 3-d ray tracing method: prediction of indoor radio propagation at 28 ghz in 5g network," *Electronics*, vol. 8, no. 3, p. 286, 2019.
- [32] K.-C. Huang and Z. Wang, *Millimeter wave communication systems*. John Wiley & Sons, 2011, vol. 29.

- [33] J. Du Preez and S. Sinha, *Millimeter-wave antennas: configurations and applications*. Springer, 2016.
- [34] R. N. N. F. A. Ehab ALI, Mahamod ISMAIL, "Beamforming techniques for massive mimo systems in 5g: overview, classification, and trends for future research," *Front Inform Technol Electron Eng*, vol. 18, no. 6, pp. 753–772, 2020.
- [35] W. Roh, J.-Y. Seol, J. Park, B. Lee, J. Lee, Y. Kim, J. Cho, K. Cheun, and F. Aryanfar, "Millimeter-wave beamforming as an enabling technology for 5g cellular communications: Theoretical feasibility and prototype results," *IEEE communications magazine*, vol. 52, no. 2, pp. 106–113, 2014.
- [36] R. Bonjour, M. Singleton, S. A. Gebrewold, Y. Salamin, F. C. Abrecht, B. Baeuerle, A. Josten, P. Leuchtmann, C. Hafner, and J. Leuthold, "Ultra-fast millimeter wave beam steering," *IEEE journal of quantum electronics*, vol. 52, no. 1, pp. 1–8, 2015.
- [37] T. Koonen and Z. Cao, "Optically controlled 2d radio beam steering system," in *Microwave Photonics (MWP) and the 2014 9th Asia-Pacific Microwave Photonics Conference (APMP) 2014 International Topical Meeting on*. IEEE, 2014, pp. 389–391.
- [38] Z. Cao, X. Zhao, F. Soares, N. Tessema, and A. Koonen, "38-ghz millimeter wave beam steered fiber wireless systems for 5g indoor coverage: architectures, devices, and links," *IEEE Journal of Quantum Electronics*, vol. 53, no. 1, pp. 1–9, 2016.
- [39] A. Meijerink, C. Roeloffzen, L. Zhuang, D. Marpaung, R. Heideman, A. Borreman, and W. van Etten, "Phased array antenna steering using a ring resonator-based optical beam forming network," in *2006 Symposium on Communications and Vehicular Technology*. IEEE, 2006, pp. 7–12.
- [40] Z. Cao, N. Tessema, S. Latkowski, X. Zhao, Z. Chen, V. Moskalenko, K. Williams, H. Van Der Boom, E. Tangdiongga, and A. Koonen, "Integrated remotely tunable optical delay line for millimeter-wave beam steering fabricated in an inp generic foundry," *Optics letters*, vol. 40, no. 17, pp. 3930–3933, 2015.
- [41] B.-M. Jung, J.-D. Shin, and B.-G. Kim, "Optical true time-delay for two-dimensional x-band phased array antennas," *IEEE photonics technology letters*, vol. 19, no. 12, pp. 877–879, 2007.
- [42] B.-M. Jung and J. Yao, "A two-dimensional optical true time-delay beamformer consisting of a fiber bragg grating prism and switch-based fiber-optic delay lines," *IEEE Photonics Technology Letters*, vol. 21, no. 10, pp. 627–629, 2009.
- [43] Z. Cao, R. Lu, Q. Wang, N. Tessema, Y. Jiao, H. van den Boom, E. Tangdiongga, and A. Koonen, "Cyclic additional optical true time delay for microwave beam steering with spectral filtering," *Optics letters*, vol. 39, no. 12, pp. 3402–3405, 2014.
- [44] L. Zhuang, C. Roeloffzen, R. Heideman, A. Borreman, A. Meijerink, and W. van Etten, "Single-chip ring resonator-based 1x8 optical beam forming network in cmos-compatible waveguide technology," *IEEE Photonics Technology Letters*, vol. 19, no. 15, pp. 1130–1132, 2007.
- [45] M. A. Piqueras, G. Grosskopf, B. Vidal, J. Herrera, J. M. Martínez, P. Sanchis, V. Polo, J. L. Corral, A. Marceaux, J. Galière *et al.*, "Optically beamformed beam-switched adaptive antennas for fixed and mobile broad-band wireless access networks," *IEEE Transactions on Microwave Theory and Techniques*, vol. 54, no. 2, pp. 887–899, 2006.

- [46] T. Nagatsuma and G. Carpintero, "Recent progress and future prospect of photonics-enabled terahertz communications research," *IEICE Transactions on Electronics*, vol. 98, no. 12, pp. 1060–1070, 2015.
- [47] M. A. Akkaş, "Terahertz wireless data communication," *Wireless Networks*, vol. 25, no. 1, pp. 145–155, 2019.
- [48] R. Piesiewicz, T. Kleine-Ostmann, N. Krumbholz, D. Mittleman, M. Koch, J. Schoebei, and T. Kurner, "Short-range ultra-broadband terahertz communications: Concepts and perspectives," *IEEE Antennas and Propagation Magazine*, vol. 49, no. 6, pp. 24–39, 2007.
- [49] I. F. Akyildiz, J. M. Jornet, and C. Han, "Terahertz band: Next frontier for wireless communications," *Physical Communication*, vol. 12, pp. 16–32, 2014.
- [50] C. Jansen, S. Priebe, C. Moller, M. Jacob, H. Dierke, M. Koch, and T. Kurner, "Diffuse scattering from rough surfaces in thz communication channels," *IEEE Transactions on Terahertz Science and Technology*, vol. 1, no. 2, pp. 462–472, 2011.
- [51] B. Thidé, H. Then, J. Sjöholm, K. Palmer, J. Bergman, T. Carozzi, Y. N. Istomin, N. Ibragimov, and R. Khamitova, "Utilization of photon orbital angular momentum in the low-frequency radio domain," *Physical review letters*, vol. 99, no. 8, p. 087701, 2007.
- [52] F. Tamburini, E. Mari, A. Sponselli, B. Thidé, A. Bianchini, and F. Romanato, "Encoding many channels on the same frequency through radio vorticity: first experimental test," *New Journal of Physics*, vol. 14, no. 3, p. 033001, 2012.
- [53] G. Gibson, J. Courtial, M. J. Padgett, M. Vasnetsov, V. Pas'ko, S. M. Barnett, and S. Franke-Arnold, "Free-space information transfer using light beams carrying orbital angular momentum," *Optics express*, vol. 12, no. 22, pp. 5448–5456, 2004.
- [54] Z. Wang, N. Zhang, and X.-C. Yuan, "High-volume optical vortex multiplexing and demultiplexing for free-space optical communication," *Optics express*, vol. 19, no. 2, pp. 482–492, 2011.
- [55] J. Wang, J.-Y. Yang, I. M. Fazal, N. Ahmed, Y. Yan, H. Huang, Y. Ren, Y. Yue, S. Dolinar, M. Tur *et al.*, "Terabit free-space data transmission employing orbital angular momentum multiplexing," *Nature photonics*, vol. 6, no. 7, p. 488, 2012.
- [56] S. M. Mohammadi, L. K. Daldorff, J. E. Bergman, R. L. Karlsson, B. Thidé, K. Forozesh, T. D. Carozzi, and B. Isham, "Orbital angular momentum in radio—a system study," *IEEE transactions on Antennas and Propagation*, vol. 58, no. 2, pp. 565–572, 2009.
- [57] J. Capmany and D. Novak, "Microwave photonics combines two worlds," *Nature photonics*, vol. 1, no. 6, p. 319, 2007.
- [58] J. Yao, "Microwave photonics," *Journal of lightwave technology*, vol. 27, no. 3, pp. 314–335, 2009.
- [59] X. Gao, S. Huang, J. Zhou, Y. Wei, C. Gao, X. Zhang, and W. Gu, "Generating, multiplexing/demultiplexing and receiving the orbital angular momentum of radio frequency signals using an optical true time delay unit," *Journal of Optics*, vol. 15, no. 10, p. 105401, 2013.
- [60] X. Gao, S. Huang, Y. Song, S. Li, Y. Wei, J. Zhou, X. Zheng, H. Zhang, and W. Gu, "Generating the orbital angular momentum of radio frequency signals using optical-true-time-delay unit based on optical spectrum processor," *Optics letters*, vol. 39, no. 9, pp. 2652–2655, 2014.

- [61] K. Cui, G. Chen, Q. He, and Z. Xu, "Indoor optical wireless communication by ultraviolet and visible light," in *Free-Space Laser Communications IX*, vol. 7464. International Society for Optics and Photonics, 2009, p. 74640D.
- [62] T. Koonen, "Indoor optical wireless systems: technology, trends, and applications," *Journal of Lightwave Technology*, vol. 36, no. 8, pp. 1459–1467, 2018.
- [63] Z. Ghassemlooy, W. Popoola, and S. Rajbhandari, *Optical wireless communications: system and channel modelling with Matlab®*. CRC press, 2019.
- [64] D. C. O'Brien, L. Zeng, H. Le-Minh, G. Faulkner, J. W. Walewski, and S. Randel, "Visible light communications: Challenges and possibilities," in *2008 IEEE 19th International Symposium on Personal, Indoor and Mobile Radio Communications*. IEEE, 2008, pp. 1–5.
- [65] D. O'Brien, H. Le Minh, L. Zeng, G. Faulkner, K. Lee, D. Jung, Y. Oh, and E. T. Won, "Indoor visible light communications: challenges and prospects," in *Free-Space Laser Communications VIII*, vol. 7091. International Society for Optics and Photonics, 2008, p. 709106.
- [66] D. Karunatilaka, F. Zafar, V. Kalavally, and R. Parthiban, "Led based indoor visible light communications: State of the art," *IEEE Communications Surveys & Tutorials*, vol. 17, no. 3, pp. 1649–1678, 2015.
- [67] P. Hu, P. H. Pathak, A. K. Das, Z. Yang, and P. Mohapatra, "Plifi: Hybrid wifi-vlc networking using power lines," in *Proceedings of the 3rd Workshop on Visible Light Communication Systems*, 2016, pp. 31–36.
- [68] N. Saeed, S. Guo, K.-H. Park, T. Y. Al-Naffouri, and M.-S. Alouini, "Optical camera communications: Survey, use cases, challenges, and future trends," *Physical Communication*, vol. 37, p. 100900, 2019.
- [69] H. Chun, S. Rajbhandari, G. Faulkner, D. Tsonev, E. Xie, J. J. D. McKendry, E. Gu, M. D. Dawson, D. C. O'Brien, and H. Haas, "Led based wavelength division multiplexed 10 gb/s visible light communications," *Journal of lightwave technology*, vol. 34, no. 13, pp. 3047–3052, 2016.
- [70] S. Teli, W. A. Cahyadi, and Y. H. Chung, "Optical camera communication: Motion over camera," *IEEE Communications Magazine*, vol. 55, no. 8, pp. 156–162, 2017.
- [71] A. Gomez, K. Shi, C. Quintana, R. Maher, G. Faulkner, P. Bayvel, B. C. Thomsen, and D. O'Brien, "Design and demonstration of a 400 gb/s indoor optical wireless communications link," *Journal of Lightwave Technology*, vol. 34, no. 22, pp. 5332–5339, 2016.
- [72] Z. Cao, L. Shen, Y. Jiao, X. Zhao, and T. Koonen, "200 gbps ook transmission over an indoor optical wireless link enabled by an integrated cascaded aperture optical receiver," in *2017 Optical Fiber Communications Conference and Exhibition (OFC)*. IEEE, 2017, pp. 1–3.
- [73] F. Gomez-Agis, S. Van de Heide, C. Okonkwo, E. Tangdiongga, and A. Koonen, "112 gbit/s transmission in a 2d beam steering awg-based optical wireless communication system," in *2017 European Conference on Optical Communication (ECOC)*. IEEE, 2017, pp. 1–3.
- [74] A. Gomez, K. Shi, C. Quintana, M. Sato, G. Faulkner, B. C. Thomsen, and D. O'Brien, "Beyond 100-gb/s indoor wide field-of-view optical wireless communications," *IEEE Photonics Technology Letters*, vol. 27, no. 4, pp. 367–370, 2014.
- [75] A. Koonen and E. Tangdiongga, "Photonic home area networks," *Journal of Lightwave Technology*, vol. 32, no. 4, pp. 591–604, 2014.

- [76] G. P. Agrawal, *Fiber-optic communication systems*. John Wiley & Sons, 2012, vol. 222.
- [77] J. Courtial, R. Zambrini, M. R. Dennis, and M. Vasnetsov, "Angular momentum of optical vortex arrays," *Optics express*, vol. 14, no. 2, pp. 938–949, 2006.
- [78] X. Gao, S. Huang, Y. Wei, W. Zhai, W. Xu, S. Yin, J. Zhou, and W. Gu, "An orbital angular momentum radio communication system optimized by intensity controlled masks effectively: Theoretical design and experimental verification," *Applied Physics Letters*, vol. 105, no. 24, p. 241109, 2014.
- [79] S. Yu, L. Li, G. Shi, C. Zhu, X. Zhou, and Y. Shi, "Design, fabrication, and measurement of reflective metasurface for orbital angular momentum vortex wave in radio frequency domain," *Applied Physics Letters*, vol. 108, no. 12, p. 121903, 2016.
- [80] Q. Bai, A. Tennant, and B. Allen, "Experimental circular phased array for generating oam radio beams," *Electronics letters*, vol. 50, no. 20, pp. 1414–1415, 2014.
- [81] Y. Yan, G. Xie, M. P. Lavery, H. Huang, N. Ahmed, C. Bao, Y. Ren, Y. Cao, L. Li, Z. Zhao *et al.*, "High-capacity millimetre-wave communications with orbital angular momentum multiplexing," *Nature communications*, vol. 5, no. 1, pp. 1–9, 2014.
- [82] F. E. Mahmoudi and S. D. Walker, "4-gbps uncompressed video transmission over a 60-ghz orbital angular momentum wireless channel," *IEEE Wireless Communications Letters*, vol. 2, no. 2, pp. 223–226, 2013.
- [83] X. Gao, M. Zhao, M. Xie, M. Lei, X. Song, K. Bi, Z. Zheng, and S. Huang, "2d optically controlled radio frequency orbital angular momentum beam steering system based on a dual-parallel mach–zehnder modulator," *Optics letters*, vol. 44, no. 2, pp. 255–258, 2019.
- [84] B. Liu, J. Liu, P. Chen, and S. Yu, "Photonic demultiplexer for radio frequency orbital-angular-momentum signals," in *2015 Opto-Electronics and Communications Conference (OECC)*. IEEE, 2015, pp. 1–3.
- [85] J. Huang, Z. Cao, X. Zhao, X. Zhang, Y. Liu, Y. Xiang, G. Gerini, and T. Koonen, "Optical generation/detection of broadband microwave orbital angular momentum modes," *Journal of Lightwave Technology*, 2019.
- [86] Y. Wang, J. Li, L. Huang, Y. Jing, A. Georgakopoulos, and P. Demestichas, "5g mobile: Spectrum broadening to higher-frequency bands to support high data rates," *IEEE Vehicular technology magazine*, vol. 9, no. 3, pp. 39–46, 2014.
- [87] A. L. A. Y. Company, "5G NR mmWave outdoor and indoor deployment strategy," 2019. [Online]. Available: <https://www.qualcomm.com/media/documents/files/deploying-5g-nr-mmwave-for-indoor-outdoor.pdf>
- [88] —, "Feasibility of Mobility for 28 GHz millimeter-wave Systems," 2018. [Online]. Available: <https://images.samsung.com/is/content/samsung/p5/global/business/networks/insights/white-paper/feasibility-of-mobility-for-28-ghz-millimeter-wave-systems/Feasibility-of-Mobility-for-28-GHz-millimeter-wave-Systems.pdf>
- [89] Z. Cao, Q. Ma, A. B. Smolders, Y. Jiao, M. J. Wale, C. W. Oh, H. Wu, and A. M. J. Koonen, "Advanced integration techniques on broadband millimeter-wave beam steering for 5g wireless networks and beyond," *IEEE journal of quantum electronics*, vol. 52, no. 1, pp. 1–20, 2015.
- [90] L. Yaron, R. Rotman, S. Zach, and M. Tur, "Photonic beamformer receiver with multiple beam capabilities," *IEEE Photonics Technology Letters*, vol. 22, no. 23, pp. 1723–1725, 2010.

- [91] F. Soares, F. Karouta, E. Smalbrugge, M. Smit, J. Lopez, A. Enard, N. Vojdani *et al.*, "An inp-based photonic integrated beamformer for phased-array antennas," in *Integrated Photonics Research*. Optical Society of America, 2004, p. IFB2.
- [92] E. J. Murphy, T. F. Adda, W. J. Minford, R. W. Irvin, E. I. Ackerman, and S. B. Adams, "Guided-wave optical time delay network," *IEEE Photonics Technology Letters*, vol. 8, no. 4, pp. 545–547, 1996.
- [93] J. Xie, L. Zhou, Z. Li, J. Wang, and J. Chen, "Seven-bit reconfigurable optical true time delay line based on silicon integration," *Optics express*, vol. 22, no. 19, pp. 22 707–22 715, 2014.
- [94] R. L. Moreira, J. Garcia, W. Li, J. Bauters, J. S. Barton, M. J. Heck, J. E. Bowers, and D. J. Blumenthal, "Integrated ultra-low-loss 4-bit tunable delay for broadband phased array antenna applications," *IEEE Photonics Technology Letters*, vol. 25, no. 12, pp. 1165–1168, 2013.
- [95] X. Wang, L. Zhou, R. Li, J. Xie, L. Lu, K. Wu, and J. Chen, "Continuously tunable ultra-thin silicon waveguide optical delay line," *Optica*, vol. 4, no. 5, pp. 507–515, 2017.
- [96] G. Lenz, B. Eggleton, C. K. Madsen, and R. Slusher, "Optical delay lines based on optical filters," *IEEE Journal of quantum electronics*, vol. 37, no. 4, pp. 525–532, 2001.
- [97] M. S. Rasras, C. K. Madsen, M. A. Cappuzzo, E. Chen, L. T. Gomez, E. J. Laskowski, A. Griffin, A. Wong-Foy, A. Gasparyan, A. Kasper *et al.*, "Integrated resonance-enhanced variable optical delay lines," *IEEE photonics technology letters*, vol. 17, no. 4, pp. 834–836, 2005.
- [98] L. Zhuang, M. Hoekman, C. Taddei, A. Leinse, R. G. Heideman, A. Hulzinga, J. Verpoorte, R. M. Oldenbeuving, P. W. van Dijk, K.-J. Boller *et al.*, "On-chip microwave photonic beamformer circuits operating with phase modulation and direct detection," *Optics express*, vol. 22, no. 14, pp. 17 079–17 091, 2014.
- [99] N. Tessema, Z. Cao, J. Van Zantvoort, K. Mekonnen, A. Dubok, E. Tangdiongga, A. Smolders, and A. Koonen, "A tunable si₃n₄ integrated true time delay circuit for optically-controlled k-band radio beamformer in satellite communication," *Journal of Lightwave Technology*, vol. 34, no. 20, pp. 4736–4743, 2016.
- [100] L. Bliet, S. Wahls, I. Visscher, C. Taddei, R. B. Timens, R. Oldenbeuving, C. Roeloffzen, and M. Verhaegen, "Automatic delay tuning of a novel ring resonator-based photonic beamformer for a transmit phased array antenna," *Journal of Lightwave Technology*, vol. 37, no. 19, pp. 4976–4984, 2019.
- [101] R. Bonjour, S. A. Gebrewold, D. Hillerkuss, C. Hafner, and J. Leuthold, "Continuously tunable true-time delays with ultra-low settling time," *Optics express*, vol. 23, no. 5, pp. 6952–6964, 2015.
- [102] R. Bonjour, M. Singleton, S. A. Gebrewold, Y. Salamin, F. C. Abrecht, B. Baeuerle, A. Josten, P. Leuchtmann, C. Hafner, and J. Leuthold, "Ultra-fast millimeter wave beam steering," *IEEE journal of quantum electronics*, vol. 52, no. 1, pp. 1–8, 2016.
- [103] T. H. Maiman, "Stimulated optical radiation in ruby," *nature*, vol. 187, no. 4736, pp. 493–494, 1960.
- [104] N. Zheludev, "The life and times of the led—a 100-year history," *Nature photonics*, vol. 1, no. 4, p. 189, 2007.
- [105] D. M. Forin, G. Incerti, G. T. Beleffi, A. Teixeira, L. Costa, P. D. B. Andr , B. Geiger, E. Leitgeb, and F. Nadeem, "Free space optical technologies," in *Trends in Telecommunications Technologies*. IntechOpen, 2010.

- [106] A. K. Majumdar and J. C. Ricklin, *Free-space laser communications: principles and advances*. Springer Science & Business Media, 2010, vol. 2.
- [107] J. A. Simpson, B. L. Hughes, and J. F. Muth, "Smart transmitters and receivers for underwater free-space optical communication," *IEEE Journal on selected areas in communications*, vol. 30, no. 5, pp. 964–974, 2012.
- [108] M. Toyoshima, "Trends in satellite communications and the role of optical free-space communications," *Journal of Optical Networking*, vol. 4, no. 6, pp. 300–311, 2005.
- [109] J. C. Juarez, A. Dwivedi, A. R. Hammons, S. D. Jones, V. Weerackody, and R. A. Nichols, "Free-space optical communications for next-generation military networks," *IEEE Communications Magazine*, vol. 44, no. 11, pp. 46–51, 2006.
- [110] M. Ayyash, H. Elgala, A. Khreishah, V. Jungnickel, T. Little, S. Shao, M. Rahaim, D. Schulz, J. Hilt, and R. Freund, "Coexistence of wifi and lifi toward 5g: concepts, opportunities, and challenges," *IEEE Communications Magazine*, vol. 54, no. 2, pp. 64–71, 2016.
- [111] X. Huang, S. Chen, Z. Wang, J. Shi, Y. Wang, J. Xiao, and N. Chi, "2.0-gb/s visible light link based on adaptive bit allocation ofdm of a single phosphorescent white led," *IEEE Photonics Journal*, vol. 7, no. 5, pp. 1–8, 2015.
- [112] K. Werner, "Higher visibility for leds," *IEEE spectrum*, vol. 31, no. 7, pp. 30–34, 1994.
- [113] G. Pang, T. Kwan, H. Liu, and C.-H. Chan, "Optical wireless based on high brightness visible leds," in *Conference Record of the 1999 IEEE Industry Applications Conference. Thirty-Forth IAS Annual Meeting (Cat. No. 99CH36370)*, vol. 3. IEEE, 1999, pp. 1693–1699.
- [114] Y. Tanaka, T. Komine, S. Haruyama, and M. Nakagawa, "Indoor visible communication utilizing plural white leds as lighting," in *12th IEEE International Symposium on Personal, Indoor and Mobile Radio Communications. PIMRC 2001. Proceedings (Cat. No. 01TH8598)*, vol. 2. IEEE, 2001, pp. F–F.
- [115] T. Komine and M. Nakagawa, "Fundamental analysis for visible-light communication system using led lights," *IEEE transactions on Consumer Electronics*, vol. 50, no. 1, pp. 100–107, 2004.
- [116] Y. Wang, L. Tao, X. Huang, J. Shi, and N. Chi, "8-gb/s rgby led-based wdm vlc system employing high-order cap modulation and hybrid post equalizer," *IEEE Photonics Journal*, vol. 7, no. 6, pp. 1–7, 2015.
- [117] R. X. Ferreira, E. Xie, J. J. McKendry, S. Rajbhandari, H. Chun, G. Faulkner, S. Watson, A. E. Kelly, E. Gu, R. V. Penty *et al.*, "High bandwidth gan-based micro-leds for multi-gb/s visible light communications," *IEEE Photonics Technology Letters*, vol. 28, no. 19, pp. 2023–2026, 2016.
- [118] H. Haas, L. Yin, Y. Wang, and C. Chen, "What is lifi?" *Journal of lightwave technology*, vol. 34, no. 6, pp. 1533–1544, 2015.
- [119] S. Rajagopal, R. D. Roberts, and S.-K. Lim, "Ieee 802.15. 7 visible light communication: modulation schemes and dimming support," *IEEE Communications Magazine*, vol. 50, no. 3, pp. 72–82, 2012.
- [120] S. Dimitrov and H. Haas, *Principles of LED light communications: towards networked Li-Fi*. Cambridge University Press, 2015.
- [121] HHI, "HHI LiFi product," 2020. [Online]. Available: <https://www.hhi.fraunhofer.de/en/departments/pn/products-and-solutions/indoor-lifi-systems.html>

- [122] wikipedia, "Eye safety," 2019. [Online]. Available: https://en.wikipedia.org/wiki/Laser_safety
- [123] T. Koonen, K. Mekonnen, Z. Cao, F. Huijskens, N. Q. Pham, and E. Tangdiongga, "Ultra-high-capacity wireless communication by means of steered narrow optical beams," *Philosophical Transactions of the Royal Society A*, vol. 378, no. 2169, p. 20190192, 2020.
- [124] A. Koonen, "IEEE Photonics Society Webinar: Optical Wireless Systems: Technology, Trends and Applications," 2018. [Online]. Available: <https://www.photonicsociety.org/education-careers/webinars/webinar-archive>
- [125] K. Schulmeister, "Concepts in dosimetry related to laser safety and optical-radiation hazard evaluation," in *Laser and Noncoherent Light Ocular Effects: Epidemiology, Prevention, and Treatment*, vol. 4246. International Society for Optics and Photonics, 2001, pp. 104–116.
- [126] K. Wang, A. Nirmalathas, C. Lim, and E. Skafidas, "High-speed duplex optical wireless communication system for indoor personal area networks," *Optics Express*, vol. 18, no. 24, pp. 25 199–25 216, 2010.
- [127] —, "4×12.5 gb/s wdm optical wireless communication system for indoor applications," *Journal of Lightwave Technology*, vol. 29, no. 13, pp. 1988–1996, 2011.
- [128] —, "Experimental demonstration of optical wireless indoor localization system with background light power estimation," in *2015 Optical Fiber Communications Conference and Exhibition (OFC)*. IEEE, 2015, pp. 1–3.
- [129] P. Brandl, S. Schidl, A. Polzer, W. Gaberl, and H. Zimmermann, "Optical wireless communication with adaptive focus and mems-based beam steering," *IEEE Photonics Technology Letters*, vol. 25, no. 15, pp. 1428–1431, 2013.
- [130] K. Liang, H. Shi, S. J. Sheard, and D. C. O'Brien, "Transparent optical wireless hubs using wavelength space division multiplexing," in *Free-Space Laser Communications IV*, vol. 5550. International Society for Optics and Photonics, 2004, pp. 80–87.
- [131] C. Oh, E. Tangdiongga, and A. Koonen, "Steerable pencil beams for multi-gbps indoor optical wireless communication," *Optics Letters*, vol. 39, no. 18, pp. 5427–5430, 2014.
- [132] —, "42.8 gbit/s indoor optical wireless communication with 2-dimensional optical beam-steering," in *2015 Optical Fiber Communications Conference and Exhibition (OFC)*. IEEE, 2015, pp. 1–3.
- [133] T. Koonen, J. Oh, K. Mekonnen, Z. Cao, and E. Tangdiongga, "Ultra-high capacity indoor optical wireless communication using 2d-steered pencil beams," *Journal of Lightwave Technology*, vol. 34, no. 20, pp. 4802–4809, 2016.
- [134] T. Koonen, J. Oh, A. Khalid, K. Mekonnen, M. T. Vega, Z. Cao, and E. Tangdiongga, "2d beam-steered high-capacity optical wireless communication," in *2016 IEEE Photonics Society Summer Topical Meeting Series (SUM)*. IEEE, 2016, pp. 132–133.
- [135] A. Khalid, A. Koonen, C. Oh, Z. Cao, K. Mekonnen, and E. Tangdiongga, "10 gbps indoor optical wireless communication employing 2d passive beam steering based on arrayed waveguide gratings," in *2016 IEEE Photonics Society Summer Topical Meeting Series (SUM)*. IEEE, 2016, pp. 134–135.
- [136] A. Koonen *et al.*, "High-capacity optical wireless communication using awg router for 2-dimensional ir beam steering," in *Proc. OECC*, 2017.

- [137] T. Koonen, F. Gomez-Agis, F. Huijskens, K. A. Mekonnen, Z. Cao, and E. Tangdionga, "High-capacity optical wireless communication using two-dimensional ir beam steering," *Journal of Lightwave Technology*, vol. 36, no. 19, pp. 4486–4493, 2018.
- [138] A. Khalid, P. Baltus, A. Dommele, K. Mekonnen, Z. Cao, C. Oh, M. Matters, and A. Koonen, "Bi-directional 35-gbit/s 2d beam steered optical wireless downlink and 5-gbit/s localized 60-ghz communication uplink for hybrid indoor wireless systems," in *Optical Fiber Communication Conference*. Optical Society of America, 2017, pp. Th1E–6.
- [139] Z. Dong, K. Cui, G. Chen, and Z. Xu, "Non-line-of-sight link performance study for indoor visible light communication systems," in *Free-Space Laser Communications X*, vol. 7814. International Society for Optics and Photonics, 2010, p. 781404.
- [140] J. B. Carruthers and J. M. Kahn, "Modeling of nondirected wireless infrared channels," *IEEE transactions on communications*, vol. 45, no. 10, pp. 1260–1268, 1997.
- [141] G. Cossu, R. Corsini, and E. Ciaramella, "High-speed bi-directional optical wireless system in non-directed line-of-sight configuration," *Journal of Lightwave Technology*, vol. 32, no. 10, pp. 2035–2040, 2014.
- [142] P. W. Berenguer, D. Schulz, J. Hilt, P. Hellwig, G. Kleinpeter, J. K. Fischer, and V. Jungnickel, "Optical wireless mimo experiments in an industrial environment," *IEEE Journal on Selected Areas in Communications*, vol. 36, no. 1, pp. 185–193, 2017.
- [143] A. E. Willner, Y. Ren, G. Xie, Y. Yan, L. Li, Z. Zhao, J. Wang, M. Tur, A. F. Molisch, and S. Ashrafi, "Recent advances in high-capacity free-space optical and radio-frequency communications using orbital angular momentum multiplexing," *Philosophical Transactions of the Royal Society A: Mathematical, Physical and Engineering Sciences*, vol. 375, no. 2087, p. 20150439, 2017.
- [144] W. Shieh, H. Bao, and Y. Tang, "Coherent optical ofdm: theory and design," *Optics express*, vol. 16, no. 2, pp. 841–859, 2008.
- [145] E. Ip, A. P. T. Lau, D. J. Barros, and J. M. Kahn, "Coherent detection in optical fiber systems," *Optics express*, vol. 16, no. 2, pp. 753–791, 2008.
- [146] S.-H. Jeong and K. Morito, "Novel optical 90° hybrid consisting of a paired interference based 2×4 mmi coupler, a phase shifter and a 2×2 mmi coupler," *Journal of lightwave technology*, vol. 28, no. 9, pp. 1323–1331, 2010.
- [147] Y. Xie, Z. Geng, L. Zhuang, M. Burla, C. Taddei, M. Hoekman, A. Leinse, C. G. Roeloffzen, K.-J. Boller, and A. J. Lowery, "Programmable optical processor chips: toward photonic rf filters with dsp-level flexibility and mhz-band selectivity," *Nanophotonics*, vol. 7, no. 2, pp. 421–454, 2017.
- [148] L.-W. Luo, S. Ibrahim, A. Nitkowski, Z. Ding, C. B. Poitras, S. B. Yoo, and M. Lipson, "High bandwidth on-chip silicon photonic interleaver," *Optics express*, vol. 18, no. 22, pp. 23 079–23 087, 2010.
- [149] M. K. Smit and C. Van Dam, "Phasar-based wdm-devices: Principles, design and applications," *IEEE Journal of selected topics in quantum electronics*, vol. 2, no. 2, pp. 236–250, 1996.
- [150] D. Dai, X. Fu, Y. Shi, and S. He, "Experimental demonstration of an ultracompact si-nanowire-based reflective arrayed-waveguide grating (de) multiplexer with photonic crystal reflectors," *Optics letters*, vol. 35, no. 15, pp. 2594–2596, 2010.

- [151] E. G. Loewen and E. Popov, *Diffraction gratings and applications*. CRC Press, 2018.
- [152] J. J. van der Tol, Y. Jiao, L. Shen, A. Millan-Mejia, V. Pogoretskii, J. P. van Engelen, and M. K. Smit, "Indium phosphide integrated photonics in membranes," *IEEE Journal of Selected Topics in Quantum Electronics*, vol. 24, no. 1, pp. 1–9, 2017.
- [153] L. Liu, G. Roelkens, J. Van Campenhout, J. Brouckaert, D. Van Thourhout, and R. Baets, "Iii-v/silicon-on-insulator nanophotonic cavities for optical network-on-chip," *Journal of nanoscience and nanotechnology*, vol. 10, no. 3, pp. 1461–1472, 2010.
- [154] M. Paniccia, M. Morse, and M. Salib, "Silicon photonics," *Springer, Berlin*, 2004.
- [155] S. Assefa, F. Xia, and Y. A. Vlasov, "Reinventing germanium avalanche photodetector for nanophotonic on-chip optical interconnects," *Nature*, vol. 464, no. 7285, pp. 80–84, 2010.
- [156] Y. Vlasov, W. M. Green, and F. Xia, "High-throughput silicon nanophotonic wavelength-insensitive switch for on-chip optical networks," *Nature photonics*, vol. 2, no. 4, p. 242, 2008.
- [157] D. Van Thourhout, J. Van Campenhout, P. Rojo-Romeo, P. Regreny, C. Seassal, P. Binetti, X. Leijtens, R. Notzel, M. Smit, L. Di Cioccio *et al.*, "A photonic interconnect layer on cmos," in *33rd European Conference and Exhibition of Optical Communication*. VDE, 2007, pp. 1–2.
- [158] A. W. Fang, H. Park, O. Cohen, R. Jones, M. J. Paniccia, and J. E. Bowers, "Electrically pumped hybrid alginas-silicon evanescent laser," *Optics express*, vol. 14, no. 20, pp. 9203–9210, 2006.
- [159] V. Pogoretskiy, J. P. van Engelen, J. J. van der Tol, and Y. Jiao, "Towards a fully integrated indium-phosphide membrane on silicon photonics platform," in *Nanophotonics and Micro/Nano Optics IV*, vol. 10823. International Society for Optics and Photonics, 2018, p. 1082308.
- [160] J. van der Tol, J. Pello, S. Bhat, Y. Jiao, D. Heiss, G. Roelkens, H. Ambrosius, and M. Smit, "Photonic integration in indium-phosphide membranes on silicon (imos)," in *Integrated Optics: Devices, Materials, and Technologies XVIII*, vol. 8988. International Society for Optics and Photonics, 2014, p. 89880M.
- [161] C. K. Madsen and J. H. Zhao, *Optical filter design and analysis*. Wiley New York, 1999.
- [162] A. Rigny, A. Bruno, and H. Sik, "Multigrating method for flattened spectral response wavelength multi/demultiplexer," *Electronics Letters*, vol. 33, no. 20, pp. 1701–1702, 1997.
- [163] S. Pathak, M. Vanslembrouck, P. Dumon, D. Van Thourhout, and W. Bogaerts, "Optimized silicon awg with flattened spectral response using an mmi aperture," *Journal of Lightwave Technology*, vol. 31, no. 1, pp. 87–93, 2013.
- [164] J. Armstrong, "Ofdm for optical communications," *Journal of lightwave technology*, vol. 27, no. 3, pp. 189–204, 2009.
- [165] KyliA, "KyliA DWDM MUX," 2020. [Online]. Available: sup.xenya.si/sup/info/kylia/DWDM_MUX_kylianics.pdf
- [166] H. Takahashi, S. Suzuki, K. Kato, and I. Nishi, "Arrayed-waveguide grating for wavelength division multi/demultiplexer with nanometre resolution," *Electronics letters*, vol. 26, no. 2, pp. 87–88, 1990.
- [167] F. Feng, I. H. White, and T. D. Wilkinson, "Free space communications with beam steering a two-electrode tapered laser diode using liquid-crystal slm," *Journal of lightwave technology*, vol. 31, no. 12, pp. 2001–2007, 2013.

- [168] D. G. Leyva, B. Robertson, C. J. Henderson, T. D. Wilkinson, D. C. O'Brien, and G. Faulkner, "Cross-talk analysis in a telecentric adaptive free-space optical relay based on a spatial light modulator," *Applied optics*, vol. 45, no. 1, pp. 63–75, 2006.
- [169] A. Gomez, C. Quintana, G. Faulkner, and D. O'Brien, "Point-to-multipoint holographic beam-steering techniques for indoor optical wireless communications," in *Broadband Access Communication Technologies X*, vol. 9772. International Society for Optics and Photonics, 2016, p. 97720Q.
- [170] C. Oh, J. Kim, J. Muth, S. Serati, and M. J. Escuti, "High-throughput continuous beam steering using rotating polarization gratings," *IEEE Photonics Technology Letters*, vol. 22, no. 4, pp. 200–202, 2009.
- [171] A. P. Mosk, A. Lagendijk, G. Lerosey, and M. Fink, "Controlling waves in space and time for imaging and focusing in complex media," *Nature photonics*, vol. 6, no. 5, pp. 283–292, 2012.
- [172] I. M. Vellekoop and A. Mosk, "Focusing coherent light through opaque strongly scattering media," *Optics letters*, vol. 32, no. 16, pp. 2309–2311, 2007.
- [173] R. Horstmeyer, H. Ruan, and C. Yang, "Guidestar-assisted wavefront-shaping methods for focusing light into biological tissue," *Nature photonics*, vol. 9, no. 9, p. 563, 2015.
- [174] J. Tang, R. N. Germain, and M. Cui, "Superpenetration optical microscopy by iterative multiphoton adaptive compensation technique," *Proceedings of the National Academy of Sciences*, vol. 109, no. 22, pp. 8434–8439, 2012.
- [175] K. Dholakia and T. Čižmár, "Shaping the future of manipulation," *Nature Photonics*, vol. 5, no. 6, p. 335, 2011.
- [176] S. A. Goorden, M. Horstmann, A. P. Mosk, B. Škorić, and P. W. Pinkse, "Quantum-secure authentication of a physical unclonable key," *Optica*, vol. 1, no. 6, pp. 421–424, 2014.
- [177] I. M. Vellekoop, "Feedback-based wavefront shaping," *Optics express*, vol. 23, no. 9, pp. 12 189–12 206, 2015.
- [178] H. Yilmaz, W. L. Vos, and A. P. Mosk, "Optimal control of light propagation through multiple-scattering media in the presence of noise," *Biomedical optics express*, vol. 4, no. 9, pp. 1759–1768, 2013.
- [179] J. M. Kahn and J. R. Barry, "Wireless infrared communications," *Proceedings of the IEEE*, vol. 85, no. 2, pp. 265–298, 1997.
- [180] S. Kalita, R. Kaushik, M. Jajoo, and P. Sahu, "Performance enhancement of a multichannel uncoordinated code hopping dsss signaling scheme using multipath fading compensator," *Journal of Circuits, Systems and Computers*, vol. 25, no. 11, p. 1650145, 2016.
- [181] E. Biglieri, J. Proakis, and S. Shamai, "Fading channels: Information-theoretic and communications aspects," *IEEE Transactions on Information Theory*, vol. 44, no. 6, pp. 2619–2692, 1998.
- [182] P. Sahu and M. Singh, "Multi channel frequency hopping spread spectrum signaling using code m-ary frequency shift keying," *Computers & Electrical Engineering*, vol. 34, no. 4, pp. 338–345, 2008.
- [183] H. Yu, K. Lee, and Y. Park, "Ultrahigh enhancement of light focusing through disordered media controlled by mega-pixel modes," *Optics express*, vol. 25, no. 7, pp. 8036–8047, 2017.

- [184] B. Blochet, L. Bourdieu, and S. Gigan, "Focusing light through dynamical samples using fast continuous wavefront optimization," *Optics letters*, vol. 42, no. 23, pp. 4994–4997, 2017.
- [185] P. M. Johnson, A. Imhof, B. P. Bret, J. G. Rivas, and A. Lagendijk, "Time-resolved pulse propagation in a strongly scattering material," *Physical Review E*, vol. 68, no. 1, p. 016604, 2003.
- [186] M. Smit, J. Van der Tol, and M. Hill, "Moore's law in photonics," *Laser & Photonics Reviews*, vol. 6, no. 1, pp. 1–13, 2012.
- [187] Z. Cao, X. Zhang, G. Osnabrugge, J. Li, I. M. Vellekoop, and A. M. Koonen, "Reconfigurable beam system for non-line-of-sight free-space optical communication," *Light: Science & Applications*, vol. 8, no. 1, pp. 1–9, 2019.
- [188] S. Popoff, G. Lerosey, R. Carminati, M. Fink, A. Boccarda, and S. Gigan, "Measuring the transmission matrix in optics: an approach to the study and control of light propagation in disordered media," *Physical review letters*, vol. 104, no. 10, p. 100601, 2010.
- [189] Y. Wang, J. P. Van Engelen, S. Reniers, M. B. Van Rijn, X. Zhang, Z. Cao, V. Calzadilla, K. Williams, M. K. Smit, and Y. Jiao, "Inp-based grating antennas for high resolution optical beam steering," *IEEE Journal of Selected Topics in Quantum Electronics*, 2019.
- [190] Y. Wang, J. P. van Engelen, S. F. Reniers, M. B. van Rijn, X. Zhang, Z. Cao, V. Dolores-Calzadilla, K. A. Williams, M. K. Smit, and Y. Jiao, "High resolution grating antennas for beam steering on the imos platform," in *Asia Communications and Photonics Conference*. Optical Society of America, 2019, pp. M4B–5.

LIST OF PUBLICATIONS

Journal papers

1. **X. Zhang**, M. Zhao, Y. Jiao, Z. Cao and T. Koonen, "Integrated wavelength tuned optical mm-wave beamformer with doubled delay resolution," *Journal of Lightwave Technology*, (2020).
2. Z. Cao+, **X. Zhang**+, G. Osnabrugge+, J. Li, I. M. Vellekoop, and A. M. J. Koonen, "Reconfigurable beam system for non-line-of-sight free-space optical communication", *Light: Science & Applications*, 8 (1), pp. 69 (2019). (Co-firstauthor)
3. **X. Zhang**, C. Li, Y. Jiao, H. v. d. Boom, E. Tangdionga, Z. Cao, and A. M. J. Koonen. "Crosstalk-mitigated AWGR-based 2-D IR beam-steered indoor optical wireless communication system with a high spatial resolution.", *Journal of Lightwave Technology*, 37 (15), pp. 3713-3722(2019).
4. **X. Zhang**, J. V. Engelen, S. Reniers, Z. Cao, Y. Jiao, and A. M. J. Koonen, "Reflection-type AWG enabled by photonic crystal reflector on Indium-phosphide Membrane on Silicon platform", *Photonics Technology Letters*, 31 (13), pp. 1041-1044 (2019).
5. **X. Zhang**, Y. Liu, Z. Cao, F. Li, Z. Li, R. Ismaeel, G. Brambilla, Y. Chen, and A. M. J. Koonen, "40 Gb/s indoor optical wireless system enabled by a cyclically arranged optical beamsteering receiver", *Optics Letters*, 43 (4), pp. 723-726 (2018).
6. **X. Zhang**, Z. Cao, J. Li, D. Ge, Z. Chen, I. M. Vellekoop, and A.M.J. Koonen, "40-Gbit/s non-line-of-sight optical wireless connectivity for Industry 4.0.", Submitted to *Journal of Lightwave Technology* (2020).
7. **X. Zhang**, Z. Cao, J. V. Engelen, Y. Jao, and A.M.J. Koonen, "Single-element bidirectional broadband optical delay network.", In progress (2020).
8. **X. Zhang**, Z. Li, C. Li, M. Luo, H. Li, Cai Li, Q. Yang and S. Yu, "Transmission of 100-Gb/s DDO-OFDM/OQAM over 320-km SSMF with a single photodiode." *Optics Express*, 22(10), pp. 12079-12086 (2014).
9. **X. Zhang**, Z. Li, J. Li, C. Yu, A. P. T. Lau and C. Lu, "Low-cost coherent receiver for long-reach optical access network using single-ended detection.", *Optics Letters*, 39(18), pp. 5248-5250 (2014).

10. **X. Zhang**, J. Li, C. Li, M. Luo, H. Li, Z. He, Q. Yang, C. Lu and Z. Li, "Pilot-based blind phase estimation for coherent optical OFDM system.", *Optics Express*, 22(19), pp. 22888-22894 (2014).
11. J. Huang, Z. Cao, X. Zhao, **X. Zhang**, Y. Liu, Y. Xiang, G. Gerini, and A. J. M. Koonen, "Optical Generation/Detection of Broadband Microwave Orbital Angular Momentum Modes." *Journal of Lightwave Technology*, 38 (6), pp. 1202-1209 (2020).
12. M. Zhao, **X. Zhang**, K. Tran, H. Wen, Y. Xiang, Z. Cao, A.C.F. Reniers, and A. M. J. Koonen, "Integrated tunable phase shifter based on energy-conserved phase amplification and its application for RF-OAM generation", Submitted to *Journal of Selected Topics in Quantum Electronics* (2020).
13. C. Li, **X. Zhang**, E. Tangdiongga, X. Dai, C. Tsai, H. Wang, Y. Xiang, G. Lin, Z. Cao, and A. M. J. Koonen, "Cost-efficient half-duplex 10 Gbit/s all-optical indoor optical wireless communication enabled by a low-cost Fabry–Perot laser/photodetector." *Optics Letters* 44 (5), pp. 1158-1161 (2019).
14. Y. Wang, J. P. van Engelen, S. F. G. Reniers, M. B. J. van Rijn, **X. Zhang**, Z. Cao, V. Dolores-Calzadilla, K. A. Williams, M. K. Smit, Y. Jiao, "InP-based grating antennas for high resolution optical beam steering," *IEEE Journal of Selected Topics in Quantum Electronics* (2020).
15. M. Pang, **X. Zhang**, J. Li, and Z. Li, "Data-aided linear fitting blind phase estimation method for coherent optical OFDM system", *Photonic Network Communications*, 31, no. 2, 316-320 (2016).
16. J. Li, **X. Zhang**, Z. Li, X. Zhang, G. Li, and C. Lu, "Theoretical studies on the polarization-modulator-based single-side-band modulator used for generation of optical multicarrier." *Optics Express*, 24(12), 14087-14095 (2014).
17. C. Li, **X. Zhang**, H. Li, Cai Li, M. Luo, Z. Li, J. Xu, Q. Yang and S. Yu, "Experimental demonstration of 429.96-Gb/s OFDM/OQAM–64QAM over 400-km SSMF transmission within a 50-GHz grid." *Photonics Journal*, 6(4), 7200408 (2014).
18. J. Li, **X. Zhang**, and Z. Li, "Optical frequency comb generation by utilizing the three-branch-waveguide-interferometer-based single-side-band modulator with recirculating frequency shifting loop." *Optical Engineering*, 53(12), 12606 (2014).
19. Z. Li, T. Jiang, H. Li, **X. Zhang**, Cai Li, C. Li, R. Hu, M. Luo, X. Zhang, X. Xiao, Q. Yang and S. Yu, "Experimental demonstration of 110-Gb/s unsynchronized band-multiplexed superchannel coherent optical OFDM/OQAM system." *Optics Express*, 21(19), 21924-21931 (2013).

20. C. Li, H. Li, Q. Yang, M. Luo, **X. Zhang**, R. Hu, Z. Li, Wei Li, and S. Yu. "Single photodiode direct detection system of 100-Gb/s OFDM/OQAM-64QAM over 80-km SSMF within a 50-GHz optical grid." *Optics Express*, 22, no. 19, 22490-22497 (2014).

Conference contributions

1. **X. Zhang**, Z. Cao, G. Osnabrugge, J. Li, I. Vellekoop, and A. M. J. Koonen. "Non-line-of-sight beam-steered optical wireless communication (Conference Presentation)." In *Broadband Access Communication Technologies XIV*, vol. 11307, pp. 113070F. International Society for Optics and Photonics (2020).
2. **X. Zhang**, C. Li, Y. Jiao, H. van den Boom, E. Tangdionga, Z. Cao, and A. M. J. Koonen. "Crosstalk-free AWGR-based 2-D IR beam steered optical wireless communication system for high spatial resolution." In *Optical Fiber Communication Conference*, pp. Th1F-5. Optical Society of America (2019).
3. **X. Zhang**, M. Zhao, Y. Lei, K. A. Williams, X. J. M. Leijtens, Y. Jiao, S. Huang, Z. Cao, and A. M. J. Koonen. "An Integrated Stepwise Tunable Optical mm-wave Beam Former with Doubled Delay Resolution." In *2018 European Conference on Optical Communication (ECOC)*, pp. 1-3. IEEE (2018).
4. **X. Zhang**, Y. Tian, X. Deng, X. Lu, Z. Cao, and A. M. J. Koonen. "Inter-Subcarrier Phase Scrambling for PAPR Reduction in IM-DD OFDM System." In *Asia Communications and Photonics Conference*, pp. S3C-5. Optical Society of America (2017).
5. **X. Zhang**, Z. Li, C. Li, M. Luo, H. Li, Cai Li, Q. Yang and S. Yu, "100-Gb/s DDO-OFDM/OQAM transmission over 320-km SSMF with a single photodiode." in *Proc. OECC* (2014), 611-612.
6. **X. Zhang**, J. Li, and Z. Li, "SSBI cancellation method for IMDD-OFDM system with a single photodiode." in *Proc. PIERS* (2014), Session 2P15 SC3, 976.
7. **X. Zhang**, J. Li, C. Li, M. Luo, H. Li, Z. He, Q. Yang, C. Lu, and Z. Li, "Pilot-based blind phase estimation method for coherent optical OFDM." In *Proc. ICOCN* (2014), Suzhou, China. (Invited talk)
8. Y. Wang, J. P. van Engelen, S. F. G. Reniers, M. B. J. van Rijn, **X. Zhang**, Z. Cao, V. Dolores-Calzadilla, K. A. Williams, M. K. Smit, Y. Jiao, "High Resolution Grating Antennas for Beam Steering on the IMOS Platform," *2019 Asia Communications and Photonics Conference (ACP)*, Chengdu, China, pp. 1-3 (2019).

9. A. Trinidad, N. Tessema, **X. Zhang**, Z. Cao, E. Tangdiongga, and A. M. J. Koonen. "Evaluation of PAM-4, DMT, and Nyquist-SCM for Multi-Gbps Transmission on Bandwidth-Limited ORR-Based Beamformer." In 2018 European Conference on Optical Communication (ECOC), pp. 1-3. IEEE (2018).
10. Z. Cao, **X. Zhang**, Ivo Vellekoop, and A. M. J. Koonen. "Non-Line-of-Sight Beam Reconfigurable Optical Wireless System for Energy-Efficient Communication." In 2018 European Conference on Optical Communication (ECOC), pp. 1-3. IEEE (2018).
11. Z. Cao, **X. Zhang**, X. Zhao, L. Shen, X. Deng, X. Yin, and A. M. J. Koonen. "Millimeter wave beam steered fiber-wireless systems for 5G indoor coverage: Integrated circuits and systems." In Asia Communications and Photonics Conference, pp. S4D-1. Optical Society of America (2017).
12. C. Li, **X. Zhang**, H. Li, Cai Li, M. Luo, Z. Li, J. Xu, Q. Yang and S. Yu, "Experimental demonstration of 429.96-Gb/s OFDM/OQAM- 64QAM transmission over 400-km SSMF on the 50 GHz ITU-T Grid." In Proc. OECC (2014), 1046-1048.
13. Chao Li, **X. Zhang**, H. Li, Cai Li, T. Jiang, M. Luo, X. Zhang, Z. Li, X. Xiao, Q. Yang and S. Yu, "Experimental Demonstration of a Single Channel 44.7 Gb/s Coherent Optical Dual-polarization 256-QAM OFDM/OQAM Transmission." in Proc. ACP (2013), pp: AF4C.2.
14. M. Pan, **X. Zhang**, J. Li, and Z. Li. "Mixed-polar-amplitude-modulation pilot-based blind phase estimation for coherent optical OFDM system." In 2015 14th International Conference on Optical Communications and Networks (ICOON), pp. 1-3. IEEE, 2015.
15. S. Li, J. Wang, **X. Zhang**, L. Zhu, C. Li and Q. Yang, "Demonstration of simultaneous 1-to-34 multicasting of OFDM/OQAM 64-QAM signal from single gaussian mode to multiple Orbital Angular Momentum (OAM) modes." in Proc. ACP (2013), PDP: AF2E.5.
16. H. Li, Q. Yang, C. Li, **X. Zhang**, C. Li, T. Jiang, M. Luo, X. Zhang, Z. Li, and S. Yu. "Optical OFDM/OQAM for the future optical communication." In Asia Communications and Photonics Conference, pp. AW4H-5. Optical Society of America, 2014.

Patents

1. System and method for optical receiver, United States Patent, Patent No. US20170048002A1, Granted: May 1, 2018. <https://patents.google.com/patent/US20170048002/un>

CURRICULUM VITAE

Xuebing Zhang started working towards the Ph.D. degree at the Technische Universiteit Eindhoven (Eindhoven University of Technology, **TU/e**) in 2016. He received his B. Eng. (cum laude) degree in Telecommunication majoring in Communication Engineering from Harbin Engineering University in Harbin, China (2012). He received his M.Eng. (cum laude) degree in Optical Engineering from Jinan University in Guangzhou, China (2015). During his master study, he has been working for one and a half year in optical fibre communication system from State Key Laboratory of Optical Comm. Technologies and Networks, Wuhan, China. Since 2015, he has been working for around one year at HongKong Polytechnic University as a research assistant. He is currently pursuing the Ph.D. degree with the Electro-Optical Communications Group, TU/e. His research interests include integrated photonics circuits, microwave photonics, and optical wireless communication.

He is a recipient of a Graduate Student Fellowship from the IEEE Photonics Society 2019 (granted yearly to only 10 recipients all over the world). He is inventor of one granted US patent.

ACKNOWLEDGMENTS

I started my Ph.D. at Eindhoven University of Technology on 1st July 2016. When writing this part, it is almost reaching the end of my Ph.D. I would like to take this opportunity to thank everyone who has made this Ph.D. possible.

First of all, I would like to thank my supervisors, especially to my first promoter Prof. Ton Koonen, for the opportunity to do a Ph.D. in the national Gravity (Zwaartekracht) program in ECO group. Your knowledge and enthusiasm continuously motivated me in my work. I would also thank my co-promoter, Dr. Zizheng Cao, for your precious guidance, comments, and encouragement. As the daily supervisor, you gave me so many suggestions not only on my Ph.D. work but also on my daily life. Then I would like to thank the thesis committee including the reserved member Dr. Eduward Tangdionga for your insightful comments/suggestions that definitely lead to a better thesis.

My appreciation goes to the work collaborators Ivo and Gerwin from Twente University (Netherlands), Juhao from Peking University (China), Prof. Wim and Yanlu from Ghent University (Belgium), Prof. Xinlun and Lifeng from Sun Yat-sen University (China). You helped me a lot with idea discussion, experimental device support, design guidance, and chip fabrication. My sincere gratitude also goes to Yuqing and Jorn from TU/e for your precious suggestions on my IMOS chip design and fabrication.

In my four-year Ph.D. work, I've got countless help from our secretary – Jose, especially her kind suggestions and help for the preparation of my Ph.D. defense. Thanks, Jose! I've always been grateful in group plenary talk from other experts including Nicola, Oded, Chigo, Patty, Sonia, and Eduward.

I would like to give my sincere gratitude to my officemates - Mahir, Haotian, Ailee, Yu (Lei), Mehedi, Fu and Bruno for your kind help and encouragement, to friends who gave me precious help and suggestions on my work – Wang, Netsanet, Xunwei, Teng, Lei, Jianou, Mingyang, Fulong, Bin (Shi), Yu (Zhao), Xinran, Ketema, Joanne, Chenhui, Liuyan, Simone, Chao, and Cristif from ECO group, and Weiming, Longfei, and Dan from PHI group. My gratitude also goes to my friends who gave me a lot of help in the past four years – Ye, Xiong, Qiang, Shuli, Weigang, Lu, Bitao, Xiaotao, and Bin (Chen).

Finally, I come to my family especially to my parents, my girlfriend, and my brother. Without your supports and accompany, it was difficult for me to fix the attention on my Ph.D. work. Mom and dad, you always told me to work more when I was young. As you wish, I worked hard and gained so much – persistence and success. I always believe I have a super-brother – he gave me powerful supports on both work (advice) and life (money), even advice on how to do a Ph.D. Thank you, my brother - Dr. Xuequan. In the end, I would say I was so lucky that I found my

'girl-right' – Keyu. Here, my deepest gratitude goes to my girlfriend Keyu for your support and understanding in the last year of my Ph.D. research.